Shear-wave Splitting in Reflection Surveys: Theory, Methods and Case Studies

by

Xiangyang Li

B.Sc.(Hons) Geophysics 1982,
Changchun Geological Institute

M.Sc. Applied Geophysics 1984,
Beijing Graduate School of East China Petroleum Institute

Thesis submitted for the degree of Doctor of Philosophy
Department of Geology and Geophysics
University of Edinburgh
March 1992

I hereby declare that this thesis has been composed by myself and that the work described is entirely my own unless explicitly stated in the text.

Xiangyang Li

To

My family, Taohua and Xian, and my parents

ABSTRACT

Over the last decade, the use of multi-component seismic reflection data to study shear-wave splitting has become increasingly common within the hydrocarbon industry to determine the crack geometry of oil reservoirs. Thus, it is important to investigate the characteristics of, develop processing techniques for, and carry out case studies of shear-wave splitting in reflection surveys.

I have examined the effects of anisotropic symmetry, particularly orthorhombic symmetry, on velocity variations and moveouts of split shear-waves in vertical off-symmetry planes. I have also examined the effects of crack orientation changing with depth on reflection and transmission coefficients of split shear-waves. These theoretical developments in understanding shear-wave splitting in reflection surveys are described in Chapters 2 and 3.

Complex component analysis was developed as an alternative to polarization analysis for displaying and identifying shear-wave splitting in large seismic datasets. This complex component analysis allows the calculation of instantaneous amplitudes and instantaneous polarizations for two-component seismic data and of shear-wave splitting sections and polarization logs for four-component data. Four field seismic datasets, including a two- and a four-component VSPs, a reflection shot data matrix and a two-component crosshole survey, have been used to verify and illustrate the technique, as described in Chapters 4 and 5.

A linear-transform technique was developed as an alternative to rotation analysis for quantifying and processing shear-wave splitting in seismic data. This linear-transform technique allows various attributes to be measured, including the polarizations and time delays of split shear-waves and downhole

geophone orientation. It also allows time series of the split shear-waves to be separated deterministically and such separation can be made before stacking in reflection surveys. Three field datasets including a zero-offset VSP, an offset VSP and a reflection shot data matrix, have been used to verify and illustrate the technique, as described in Chapter 6.

Chapter 7 presented three integrated case studies of shear-wave splitting in reflection surveys. The datasets were acquired by Amoco Production Company in Dimmit, La Salle, and Frio Counties in South Texas and include three reflection lines with different azimuths in areas of varying oil production. I showed that the use of complex component analysis and linear transform techniques can simplify the processing sequence for shear-wave data in the presence of anisotropy and allows the generations of both stacked amplitude and stacked polarization sections of split shear-waves. The stacked polarization section can be used not only for identifying lateral variation of polarizations, but also for better imaging the subsurface structures. I also showed that the variation of anisotropy in the areas where the three lines were shot can be broadly correlated with oil production in the corresponding areas.

ACKNOWLEDGEMENTS

I would like to express my sincere gratitude to my supervisor, Professor Stuart Crampin, for his time and efforts in supporting and guiding my studies throughout the past four years, his kindness for encouraging and allowing me to travel to various meetings and conferences, his concerns about improving my English, and above all, his help in making life easy in Edinburgh for me and my family. Also I must thank him for all his hard work in initiating and directing the Edinburgh Anisotropy Project, which financed my research work, and without which this work would have been impossible.

I must thank the members of staff at the Global Seismology Research Group (GSRG) of the British Geological Survey (BGS), for their helpfulness and tolerance in various matters. Dr. Chris W. Browitt (head of GSRG) allowed me to use all the facilities in his group, and provided vital information and made critical phone calls for the extension of my UK residence visa and visa applications for overseas travel. Angela Muir (GSRG secretary) and Terry Turbitt (once the acting head of GSRG) have tolerated my continuous interference in their office for stationary, fax, and signatures. Charlie Fyfe, who shares the office with me, answered phone calls and took messages for me, and above all, helped me to use the LEX word processing system, without which all my reports, papers and this thesis could not have been written. I also thank David Booth, Russ Evans and John Lovell for many useful discussions.

I am very grateful to my colleagues and fellow students in the Edinburgh Anisotropy Project and in GSRG. Colin MacBeth made many constructive criticisms about my processing techniques. Phil Wild has put up with and tried to meet my increasing demands for disk storage space and computing power. Gareth Yardley processed the Lost Hills and Devine VSPs for testing

my processing techniques, from which part of Chapters 5 and 6 was made possible. Gareth also made numerous useful comments on my work. Iain Bush provided the processed Paris Basin VSP, and Greg Turner provided the processed crosshole data in Chapter 5. Enru Liu, Gareth Yardley, Min Lou, Xinwu Zeng, Iain Bush, David Campden and Heiner Igel had shared their computer programs with me. I am also grateful to Gareth Yardley, Phil Wild, Gerhard Graham, John Lovell, Colin Macbeth, and Helen Rowlands for their valuable time in proof reading this thesis.

I am particularly indebted to Mike Sankey in Marine Geophysics of BGS for his patience and time in helping me to used the SKS reflection data processing package. His colleague, Joe Bullat also offered me his experience with SKS. Professor Zoltan Hajnal, University of Saskatchewan, Canada, gave me useful advice in processing the reflection data in Chapter 7 and offered me his experience in colour displays of seismic attributes during his visit to Edinburgh. I am also very grateful to all the staff in the NCS (NERC Computing Service). In particular, I thank Siobhan Gilliland and Jane Robertson for their patience in dealing with my tapes and plots; Hugh Gough and Katrine Smalley for finding disk space for me; and Graeme Atkinson for solving various hardware and software bugs.

I thank Professor Ken M. Creer, Department of Geology and Geophysics, for accepting me as his student. I also thank the staff in the Faculty of Science for backdating my registration. I must thank the Chinese State Education Commission and the British Council for sending me abroad in 1987 under the Sino-British Friendship Scholarship Scheme (SBFSS) and supporting me in my first year in Edinburgh. In particular, I thank Ding Wubao, Du Wenqing, and Liang Yingnan in the Education Section of Chinese Embassy in London, George Morrison, my programme officer in the Edinburgh Office of the British Council, and his colleagues in London Headquarter. I must also thank my colleagues and employer in the East China Petroleum Institute (ECPI) and in the China National Petroleum Company for

encouraging and approving my stay abroad. In particular, I thank Professors Dong Minyu, Du Shitong, Li Chengchu, Liu Zhongyi, Yu Kangyi, Pan Zhenliang, Huang Longji, and Zhang Yiwei, in the Exploration Department of ECPI, Mr. Mao Xudong and Professor Lu Jimeng in the international office of ECPI.

I also thank NERC (Natural Environment Research Council) for awarding me a studentship in 1989. My studentship was administrated by the University Support Section in NERC, and their assistances in the payment and distribution of my grant are acknowledged. My studentship was funded by Edinburgh Anisotropy Project, and I gratefully acknowledge the following sponsors:

Amoco Production Company
British Geological Survey
BP/Britoil
Conoco
Chevron
Japan National Oil Corperation
Mobil
Occidental
Offshore Supply Office
Seismograph Services Ltd
Shell
Texaco

In particular, I thank British Petroleum plc for providing the VSPs in Chapter 6, and Amoco Production Company for providing the reflection data in Chapter 7. I must also thank Mike Mueller in Amoco for his patience and time in answering my inquiries, Sue Raikes in BP for her useful discussions with me, and Joe Reilly in Mobil for sending me his preprints about optimum stacking and anisotropic residues.

I am very grateful for the opportunity which this thesis has given me to record my thanks to all the colleagues and friends who helped me and my family throughout the past four years in Edinburgh. In particular, Stuart and Roma helped me to furnish the council house when my family just arrived Edinburgh. David Petrie and Gareth Yardley helped me and my family moving round. My fellow Chinese friends, Enru, Yun, Min, Linyuan, Xinwu, Hui in BGS; Daoning, Min, Tongchun, Shulan, Lujian, Xianglan, Zhengxin, Xiaoyan in Herriot-Watt University; and Xiangkang in the Department of Mechanical Engineering helped and accompanied me and my family on various occasions.

Last, but not least, I thank my wife, Taohua, for her continuous support to my work. I apologize to Taohua and my daughter Xian for many absent evenings. I also thank my parents for supporting my continuous education and encouraging me to go abroad.

CONTENTS

PAPERS ATTACHED TO BACK COVER

Li, X.-Y. and Crampin, S., 1990. Case studies of complex component analysis of shear-wave splitting. *60th Annual International Meeting & Exposition, Society of Exploration Geophysics, 23-27 September, 1990, San Francisco, Expanded Abstracts* **2**, 1427-1430.

Li, X.-Y. and Crampin, S., 1991a. Linear-transform technique for analyzing shear-wave splitting in four-component seismic data. *61st Annual International Meeting & Exposition, Society of Exploration Geophysics, 10-14 November, 1991, Houston, Expanded Abstract* **1**, 51-54.

Li, X.-Y. and Crampin, S., 1991b. Complex component analysis of shear-wave splitting: theory. *Geophysical Journal International* **107**, 597-604.

Li, X.-Y. and Crampin, S., 1991c. Complex component analysis of shear-wave splitting: case studies, *Geophysical Journal International* **107**, 605-613.

CHAPTER ONE

INTRODUCTION

1.1 BACKGROUND INFORMATION

The study of seismic waves propagating through the Earth has greatly improved our understanding of the Earth's interior, and has developed into one of the most important subjects in earth sciences. Using seismic waves, seismologists have been able to understand the mechanism of earthquakes and begin to monitor them, while exploration geophysicists have been able to characterize many complex geological structures and hydrocarbon reservoirs. However, most theory has been developed around the propagation of *P*-wave in isotropic solids, and for a long time this dominated the study of seismic waves (Aki and Richards 1980; Crampin 1981).

Just over 10 years ago, Keith and Crampin (1977), and Crampin (1978, 1981) established the theoretical and computational aspects of shear-waves propagating through anisotropic solids. They identified the potential importance of shear-wave splitting in both earthquake and exploration seismology. Their work was based on earlier identification and numerical calculation of surface waves in an anisotropic upper mantle (Crampin 1966, 1970, and a number of associated papers). Some years later, Crampin *et al.* (1980, 1985), Booth *et al.* (1985) and Buchbinder (1985) for the first time positively observed shear-wave splitting above small earthquakes. During 1986, Crampin *et al.* (1986) first reported shear-wave splitting in hydrocarbon reservoirs in a VSP in the Paris Basin, and Alford (1986b), Lynn and Thomsen (1986), and Willis *et al.* (1986) reported shear-wave splitting in reflection surveys.

Since then, the phenomenon of shear-wave splitting has attracted considerable interest in earthquake seismology (Peacock *et al.* 1988; Crampin *et al.* 1990; Shih and Meyer 1990; and many others), and in exploration seismology (Martin and Davis 1987; Squires, Kim and Kim 1989; Winterstein and Meadows 1990; Li and Crampin 1991a; and many others). Recently, the degree of shear-wave splitting in reflection surveys and VSPs has been correlated with oil production (Brodov *et al.* 1990; Davis and Lewis 1990; Lewis *et al.* 1991), and the relative amplitudes of the faster and slower split shear-waves have been used to determine the lateral variations of crack density in cracked reservoirs (Mueller 1991). Since most hydrocarbon reservoirs contain inclusions and display some form of shear-wave splitting (Willis *et al.* 1986), these studies may have wide implications for hydrocarbon exploration and production (Crampin 1987; Crampin and Lovell 1991).

The study of seismic wave propagation in anisotropic media can be traced back to more than ninety years ago. Love (1903) described transverse isotropy, a special case of anisotropy with hexagonal symmetry. Cholet and Richards (1954) and Richards (1960) introduced elliptical anisotropy, a special case of transverse isotropy assuming the wavefronts to be ellipsoids of revolution. Note that such elliptical anisotropy has not been confirmed by observations. Postma (1955) and Backus (1962) showed that periodic sequences of thin layers, each of which is isotropic, are effectively transversely isotropic with a vertical symmetry axis for long wave lengths. Since then there have been many publications on seismic wave propagation in transversely isotropic media in the literature (Berryman 1979; Levin, 1978, 1979; Daley and Hron, 1979; Helbig 1983). As the effects of anisotropy are small and difficult to detect in one-component *P*-wave seismic data (Krey and Helbig 1956; Crampin and Radovich 1982; Winterstein 1990), the relevance of anisotropy to hydrocarbon exploration and development was not widely recognized.

The use and study of shear-waves has also been reported throughout the history of the development of seismology. In 1943, Horton (1943) described the use of seismic shear-waves in exploration applications. Ricker and Lynn (1950) reported the use of mode converted shear-waves from the near-surface. Jolly (1956) and White *et al.* (1956) carried out extensive experiments in the use of *SH*-waves in exploration applications. However, the conclusion of these studies was largely negative because of limitations in instrumentation. The most positive result was the increased understanding of shear-wave propagation.

As digital recordings and large vibroseis sources became available during the late 1970's, interest in shear-wave exploration was revived. Several large experiments in shear-wave exploration were carried out during the late 1970's and earlier 1980's by a group of oil companies (McCormack and Tatham 1991), and some results were published in the literature (Tatham 1982; Ensley 1984; Winterstein and Hanten 1985; etc.). However, most of these studies were either restricted to special structure mapping, or limited to the use and the correlation of Vp/Vs ratios with variation in lithology.

The new insight into the behaviour of shear-waves in anisotropy media and the observations of shear-wave splitting in the Earth's crust made by Crampin and his co-authors opened new aspects in shear-wave exploration. During the late 1980's, multi-component reflection data have been acquired in a number of different areas for studying shear-wave anisotropy (Alford 1986b; Winterstein 1986; Squires *et al.* 1989; Murtha 1989; Muller 1991). Three-dimensional multi-component reflection data were also acquired for characterizing fractured reservoirs (Lewis 1989; Davis and Lewis 1990; Kramer 1991; Kramer and Davis 1991; Lewis *et al.* 1991), and the three-dimensional image of reservoir heterogeneity was obtained through the study of shear-wave splitting. Thus, studying the characteristics of shear-wave splitting in reflection surveys and developing techniques for processing and interpreting shear-wave splitting correctly, are certainly of great importance for shear-wave exploration.

1.2 AIMS AND OVERVIEW OF THIS THESIS

The aims of this thesis are: 1) to investigate the behaviour of split shear-waves propagating in anisotropic media with hexagonal and orthorhombic symmetry and in media where crack orientations may change with depth; 2) to investigate the use of colour displays of shear-wave attributes such as instantaneous polarization and instantaneous amplitude for displaying and interpreting shear-wave splitting in seismic sections; 3) to refine techniques for processing multi-component shear-wave seismic data in the presence of anisotropy in order to obtain the best stacked sections while preserving the characteristics of shear-wave splitting; and 4) to carry out case studies to verify the techniques and examine the role of shear-wave splitting in characterizing fractured reservoir.

Backus (1965) and Crampin (1977) used analytical equations for determining approximate phase-velocity variations in symmetry planes of a weakly anisotropic solid. Recent observations (Bush and Crampin 1987, 1991; Kramer 1991; Kramer and Davis 1991) showed that sedimentary thin-layer anisotropy is often combined with crack anisotropy forming orthorhombic anisotropy. In such media if a survey line is at an intermediate angle to the crack orientation, the vertical acquisition plane is not a symmetry plane. In Chapter 2, Backus's (1965) and Crampin's (1977) results are extended into the off-symmetry plane of a weakly anisotropic solid with orthorhombic symmetry.

Thomsen (1988) described the reflection coefficients of split shear-waves at an interface separating a thin layer anisotropic medium and an anisotropic medium containing a single set of vertical cracks, and identified the importance of studying the differential amplitudes of the faster and slower split shear-waves. However, the crack orientation in the near surface may differ from those at depth (Douma *et al.* 1989; Kerner *et al.* 1989, Squires *et al.* 1989; Crampin 1990; Winterstein and Meadow 1990, 1991a, 1991b). Chapter 3 examines effects on reflection coefficients in media where crack strike

changes with depth in order to interpret the variation of amplitudes in reflected shear-waves correctly.

Crampin and Radovich (1982), Evans (1984) and Booth and Crampin (1985) investigated some basic characteristics of shear-wave splitting in surface recordings. Split shear-waves recorded at the surface are significantly different from those recorded in the subsurface. The split shear-waves may interact with converted waves at the free surface (Evans 1984; Booth and Crampin 1985) and at internal interfaces (Liu and Crampin 1990). These effects are more severe in surface reflection surveys than in VSPs (Yardley and Crampin 1991). Stacking traces without allowing for these effects may degrade shear-wave polarizations (Li and Crampin 1989). Thus processing techniques which are capable of handling these problems need to be developed.

In the past, analysis of shear-wave splitting has relied principally on the detailed visual examination of individual polarization diagrams (polarization analysis; Crampin 1985b; Crampin and Booth 1985) and on the rotation of horizontal recording axes (rotation analysis; Alford 1986b; Thomsen 1988). These techniques are both time-consuming when attempting to analyze shear-wave splitting in large seismic data sets, and rotation analysis is not suitable for identifying abnormal polarization variations caused by surface or internal shear-wave windows, or other forms of noise. To overcome the problem, I developed two alternative techniques: complex component analysis (Li and Crampin 1991c, 1991d) and a linear-transform technique (Li and Crampin 1991b, 1992a).

Complex component analysis calculates instantaneous amplitudes and polarizations for two-component seismic data, and shear-wave splitting sections (SWS-sections) and polarization logs for four-component data, and displays them in traditional time-versus-offset colour sections, in which any polarization anomalies can be continuously followed both vertically and laterally (Li and Crampin 1990b, 1990d, 1991c, 1991d). Chapter 4 describes the principles of

complex component analysis and verifies the technique with full-wave synthetic seismic data. Chapter 5 illustrates the application of the technique using field datasets including a two- and four-component VSP, a reflection shot data matrix, and a crosshole dataset.

The linear transform technique transforms the seismic data by four linear transforms so that the complicated shear-wave motions are linearized in a wide variety of circumstances. The technique is very flexible, and can be used to analyze non-orthogonal split shear-waves and datasets where downhole geophone orientations are not known. In reflection surveys, the time series of split shear-waves can be separated before stacking which simplifies the sequence for processing reflection data in the presence of anisotropy. The linear-transform technique can also be extended to media where crack orientation changes with depth (Li and Crampin 1991b, 1992a). Note that because recorded polarizations of split shear-waves are determined by the anisotropy in the structure within a wavelength or two of the recording site (Crampin and Lovell 1991), the polarizations of shear-waves seen on the surface recordings may not be the polarization at depth in the zones of interest, if the crack orientation changes with depth. Chapter 6 describes the theory of the linear transform technique and illustrates it with several field datasets.

To further verify the use of complex component analysis and the linear-transform technique and to investigate the use of shear-wave splitting in characterizing fracture reservoirs, three case studies of shear-wave splitting in reflection surveys are described in Chapter 7. The datasets were acquired by Amoco Production Company in Dimmit, La Salle, and Frio Counties in South Texas in 1986, and included three reflection lines with different azimuths in areas of varying oil production. These studies confirm that the processing sequence for shear-wave reflection data in the presence of anisotropy can be simplified by the use of complex component analysis and the linear transform technique. Both stacked amplitude and stacked polarization sections of split shear-waves can be generated. Shear-wave events in the amplitude sections

obtained by linear transform technique are of better quality than those obtained by conventional rotation technique. The stacked polarization section can be used, not only for identifying lateral variation of polarizations which are often associated with lateral variation of crack geometry, but also for better imaging subsurface structures. These studies also show that the variation of anisotropy in the areas where the three lines were shot can be broadly correlated with oil production in the immediate neighbourhood.

CHAPTER TWO

APPROXIMATIONS TO SHEAR-WAVE VELOCITY AND MOVEOUT EQUATIONS IN ANISOTROPIC MEDIA

ABSTRACT

Backus and Crampin used approximate analytical equations for estimating velocity variations in symmetry planes in weakly anisotropic media. I examine the extension of these equations into off-symmetry planes in weakly anisotropic solids including orthorhombic symmetry. These modified equations are good approximations up to 10% anisotropy for propagation in symmetry planes for all three body waves (*qP*-, *qSH*-, and *qSV*-waves), but are only valid up to 6% anisotropy in off-symmetry planes.

I also obtain analytical moveout equations for the reflection of *qP*, *qSH*, and *qSV* waves from a single interface in both symmetry and off-symmetry planes. The moveout equation consists of two terms: a hyperbolic moveout and a residual moveout, where the residual moveout is proportional to the amount of anisotropy and the spread length of acquisition geometry. Numerical moveout curves are computed for a range of anisotropic materials to verify the analytical moveout equations.

2.1 INTRODUCTION

Velocity variations in symmetry planes in hexagonal anisotropic media with either a vertical (PTL-anisotropy) or a horizontal (EDA-anisotropy) symmetry axis have been well studied (Backus 1965; Crampin 1977; Levin

1978, 1979; Thomsen 1988; Sena 1991; Berge 1991; and many others). Recent observations (Bush and Crampin 1991; Kramer 1991; Kramer and Davis, 1991) suggest that the anisotropy in most sedimentary basins is a combination of PTL-anisotropy and EDA-anisotropy yielding orthorhombic symmetry (called CLA-anisotropy), and most multi-component shear-wave datasets (Alford 1986b; Squires et al. 1989; Mueller 1991; and many others) were acquired in vertical off-symmetry planes. This chapter examines the effects of such CLA-anisotropy and plane symmetry on the estimation of velocity variations and moveouts of split shear-waves.

Backus (1965) determined approximate equations for the variations of *qP* velocity over a plane in a weakly anisotropic solid in terms of linear combinations of the elastic constants. Crampin (1977) derived similar expressions for shear-waves propagating in planes of a weakly anisotropic solid. Crampin (1982) showed that these equations are only valid for propagation in planes of mirror symmetry. Levin (1978, 1979) and Helbig (1983) discussed *qP*-wave velocity variations and travel time equations in a transversely isotropic medium with a vertical symmetry axis (which is referred to as PTL-anisotropy, see Crampin 1989). They particularly studied the problem in PTL medium with elliptical velocity dependence and with horizontal layering; Uren et al. (1990) extended Levin and Helbig's results into an elliptical anisotropic media with dipping layering. Byun et al. (1989) obtained a general and skewed hyperbolic moveout relation for *qP* wave in weakly PTL-anisotropy. Thomsen (1986, 1988) discussed shear-wave moveouts in a crack-induced anisotropic medium (which is referred to EDA-anisotropy, also see Crampin 1989); Li and Crampin (1990a, 1990c) studied the dynamic and kinematic features of shear-waves in a horizontally stratified Earth with EDA-anisotropy; Sena (1991) extended these results into multilayered media.

However, most of these results are only strictly valid in symmetry planes of weakly anisotropic solids. This restriction may not cause severe problems in PTL-anisotropy in which all vertical planes are symmetry planes, but may

cause problems in media with EDA- or CLA-anisotropy. If a survey line runs at an oblique angle to the crack strike in a survey area with EDA- or CLA-anisotropy, the acquisition plane in a multi-component reflection survey is an off-symmetry plane.

Here, I extend the results of Backus (1965) and Crampin (1977) into off-symmetry plane of a weakly anisotropic solid. I then examine their accuracy over a range of anisotropic materials with PTL-, EDA-, and CLA-anisotropy. Based on the analytical velocity equations, I then derive analytical moveout equations in symmetry and off-symmetry planes for reflections of *qP*, *qSH* and *qSV* from a single interface, and verify the equations by numerical results. Some of the results in this Chapter were presented in the Fourteenth United Kindom Geophysical Assembly (UKGA-14) in Plymouth (Li and Crampin 1990a); and the Fourth International Workshop on Seismic Anisotropy in Edinburgh (Li and Crampin 1990c).

2.2 ANALYTICAL VELOCITY EQUATIONS

Consider a weakly anisotropic solid with three mutually-orthogonal symmetry planes (note that any two orthogonal symmetry planes necessarily imply a third mutually-orthogonal symmetry plane, Crampin 1984a). In a medium with a combination of PTL- and EDA-anisotropy (CLA-anisotropy), planes parallel and perpendicular to the crack strike and the mutually-orthogonal plane are symmetry planes. Suppose the ray geometry of a source-receiver configuration in a reflection survey is as shown in Figure 2.1, where it is assumed that there is PTL-, EDA-, or CLA-anisotropy and that the horizontal plane is a symmetry plane. The survey line is at an angle α to the crack strike, where ϕ is the ray angle measured from vertical, and $v(\phi)$ is the group velocity (ray velocity) of an arbitrary wave. I study the variation of $v(\phi)$ and the travel time from O to G reflected at R. The travel time equation is also referred to as moveout equation. Note that in an anisotropic medium, directions of phase- and group-velocity may be not colinear, so that except in

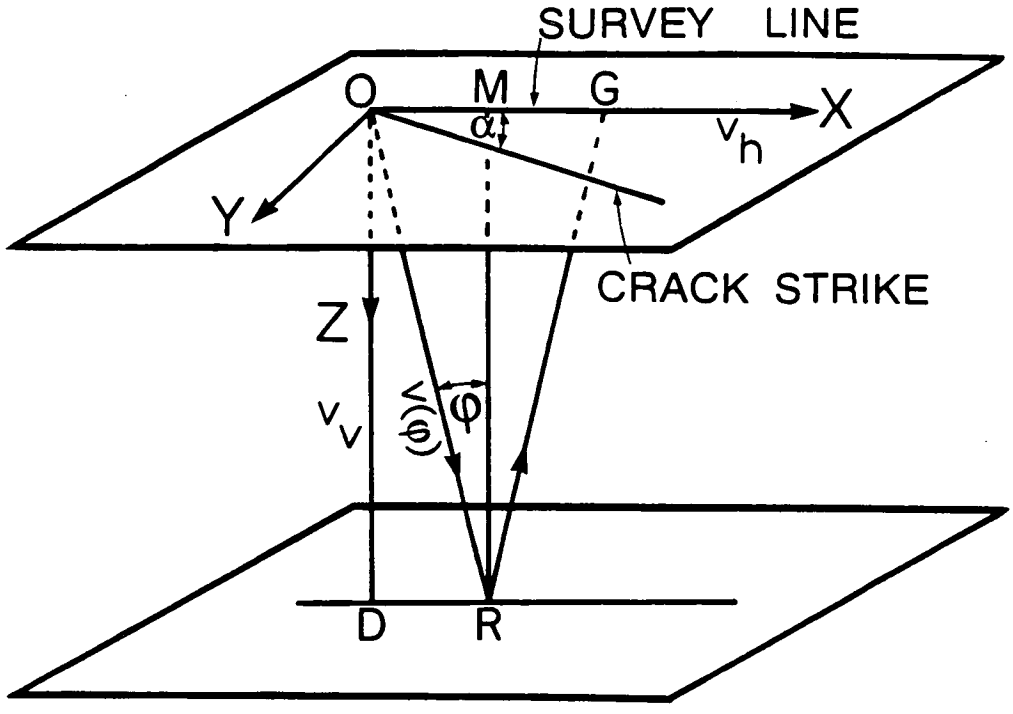

Figure 2.1. Diagram showing the acquisition geometry and coordinate system. A survey line on the surface is at α angle to the crack strike. v_h is the horizontal velocity travelling along the survey line, and v_v is the vertical velocity travelling at vertical incidence. $v(\phi)$ is the ray velocity and ϕ is the incidence angle. Note that these variables can be considered as for an arbitrary *qP*-, *qSH*-, or *qSV*-wave.

particular symmetry directions, seismic rays may deviate from the direction of phase propagation. However, for weakly anisotropic media, this ray deviation is small (Crampin 1981; Shearer and Orcutt 1985). Thus the ray geometry in Figure 2.1 is still a good approximation.

2.2.1 Basic theory

In an anisotropic medium, there are three body waves in each direction of phase propagation. For weakly anisotropic media, the three body waves are a quasi-compressional wave, and two quasi-shear waves (*qP*, *qS1* and *qS2*). [We shall also use the notation *qSH* and *qSV* to include waves which have nearly *SH*- and *SV*-wave particle motion.] The phase velocities of these three waves are solutions of the Kelvin-Christoffel equations (Musgrave 1970; Auld 1973; Crampin 1981). These solutions are rational functions of the elastic constants and direction cosines, and are sufficiently complicated to have little analytical application except in computer programs. However, in a symmetry plane of a weakly anisotropic medium, the phase velocities of the three body waves can be written as (Backus 1965; Crampin 1977, 1981):

$$\begin{aligned}
\rho v^2_{qP} &= A + B_c\cos 2\theta + B_s\sin 2\theta + C_c\cos 4\theta + C_s\sin 4\theta; \\
\rho v^2_{qSV} &= D + E_c\cos 4\theta + E_s\sin 4\theta; \text{ and} \\
\rho v^2_{qSH} &= F + G_c\cos 2\theta + G_s\sin 2\theta;
\end{aligned} \tag{2-1}$$

where

$$\begin{aligned}
A &= [3(c_{3333}+c_{1111}) + 2(c_{1133}+2c_{1313})]/8; \\
B_c &= (c_{3333} - c_{1111})/2; \\
B_s &= (c_{1333} + c_{3111}); \\
C_c &= [c_{3333}+c_{1111} - 2(c_{1133}+2c_{1313})]/8; \\
C_s &= (c_{1333} - c_{3111})/2; \\
D &= [c_{3333}+c_{1111} - 2(c_{1133}-2c_{1313})]/8; \\
E_c &= - C_c;
\end{aligned}$$

$E_s = - C_s$;
$F = (c_{2323} + c_{1212})/2$;
$G_c = (c_{2323} - c_{1212})/2$;
$G_s = c_{1223}$;

where ρ is the density; v_{qP} is the phase velocity of the *qP* wave, v_{qSH} and v_{qSV} are the phase velocities of the quasi shear-waves with polarizations parallel (*qSH*) and perpendicular (*qSV*) to the plane of variation, and θ is the incidence angle of phase propagation measured from the vertical axis. Note that here I examine velocity variation in a vertical plane as in Crampin and Radovich (1982), while Crampin (1977) considered variation over a horizontal plane. If $\theta = 0°$ is also a plane of mirror symmetry, the sine terms in equations (1) vanish, giving rise to the reduced equations (Crampin 1981).

However, what is usually observed in both field and laboratory experiments is the ray or group velocity of energy propagation, which is generally in a direction different from the direction of phase propagation. ϕ is used to represent the incidence angle of energy propagation (Figure 2.1), and θ to represent the incidence angle of phase propagation. At anisotropic/anisotropic interfaces, it is the ray behaviour that determines the point where the reflection or transmission occurs, but it is Snell's law applied to the phase velocity that determines the angle of reflection or transmission. In a symmetry plane, the relations between ϕ and θ, group velocity $v(\phi)$ and phase velocity $v_P(\theta)$ are simple (Postma 1955; Krey and Helbig 1956):

$$v^2(\phi) = v^2{}_P(\theta) + [v'_P(\theta)]^2; \text{ and}$$
$$\tan\phi = [v_P(\theta)\sin\theta + v'_P(\theta)\cos\theta]/[v_P(\theta)\cos\theta - v'_P(\theta)\sin\theta]; \qquad (2\text{-}2)$$

where $v'_P(\theta) = dv_P(\theta)/d\theta$ is the derivative of $v_P(\theta)$.

2.2.2 Approximate equation for $v(\phi)$

The expression for $v(\phi)$ can be obtained by substituting equation (2-1) into equation (2-2). However, as demonstrated by Crampin and Kirkwood (1981), Thomsen (1986), and others, in a symmetry plane of a weakly anisotropic medium, $v(\phi)$ and ϕ bear a similar relation to the energy propagation as $v(\theta)$ and θ do to the phase propagation. Hence:

$$\rho v^2(\phi) = a + b\cos 2\phi + c\sin 2\phi + d\cos 4\phi + e\sin 4\phi \qquad (2\text{-}3)$$

for any body waves; where a, b, c, d, and e are constants which can be expressed as linear combinations of elastic constants, if the anisotropy is weak (Crampin and Radovich 1982). Again, if $\phi = 0°$ is normal to a symmetry plane, the sine terms in equation (2-3) vanish. Dividing equation (2-3) by ρ gives:

$$v^2(\phi) = a' + b'\cos 2\phi + c'\sin 2\phi + d'\cos 4\phi + e'\sin 4\phi; \qquad (2\text{-}4)$$

where a', b', c', d', and e' are constants. Note that equation (2-4) is a general expression for all three body waves.

For studying moveout, the variation of $v^{-2}(\phi)$ is always used. Noting that ratios b'/a', c'/a', d'/a', and e'/a' are less than $p/100$, where p is the maximum percentage of velocity anisotropy (Crampin and Radovich 1982), $v^{-2}(\phi)$ can be represented by a Taylor expansion of these ratios. Taking the first two terms (the zero order and the first order) and making some suitable manipulations give:

$$v^{-2}(\phi) = a_0 + a_1\cos\phi + a_2\cos^2\phi + a_3\cos^3\phi + a_4\cos^4\phi; \qquad (2\text{-}5)$$

where a_i ($i = 0,1,2,3,4$) are constants. If c' and e' in equation (2-4) are zero, a_1 and a_3 in equation (2-5) will also be zero.

2.2.3 Validility

The above equations are strictly valid only for symmetry planes as pointed out by Crampin (1977, 1982). In off-symmetry planes, they are often poor representations of the velocity variations (Crampin and Kirkwood 1981). There are only three symmetry planes in Figure 2.1, corresponding to $\alpha=0°$, $\alpha=90°$ and $z=0$. Thus, equations (2-3), (2-4) and (2-5) are only strictly valid in the vertical acquisition planes $\alpha=0°$ and $90°$.

In most cases, as demonstrated below, the violation of the above equations in off-symmetry planes is due to the fact that the coefficients in the above equations can no longer be expressed as the linear combinations of elastic constants. Thus, in off-symmetry planes, the above equations may still be used to model the variation of phase and group velocities in an optimum sense, when the coefficients are determined numerically by least square fitting, thus sacrificing the physical significance of the coefficients as a linear combination of the elastic constants.

2.3 VERIFICATION OF ANALYTICAL EQUATIONS

Equation (2-5) is directly related to travel time equations. Given an anisotropic material, the velocity variations of $v^{-2}(\phi)$ of the three body waves can be calculated numerically. To demonstrate that equation (2-5) can be used in off-symmetry planes corresponding to $\alpha\neq0°$ and $90°$, and that to what amount of anisotropy equation (2-5) is valid, a least square fitting techniques is used to determine the goodness of fit. Fitting equation (2-5) to the numerical results by least square fitting, I can determine the coefficients of a_i ($i=0,1,2,3,4$), and examine the average relative error between the analytical velocity and the numerical velocity. For this purpose, I introduce:

$$\delta = (v_1 - v_2)/v_1;$$

$$e = (1/N) \sum_i |V(\phi_i) - v(\phi_i)|/V(\phi_i);$$

$$\varepsilon = e/\delta. \qquad (2\text{-}6)$$

δ is defined as the amount of differential shear-wave anisotropy of a material; where v_1 and v_2 are the velocities of the faster and slower split shear-waves at vertical incidence for EDA- and CLA-materials and at horizontal incidence for PTL-materials; e is the average error of analytical velocity $v(\phi)$ given by equation (2-5) relative to the numerical velocity $V(\phi)$, N is the number of incidence angles over the range 0° - 90°; ε is the ratio of average relative error to the amount of differential anisotropy.

The accuracy of equation (2-5) is judged in two ways. The first way is plotting out the analytical and numerical velocities against incidence angles, and directly comparing them to examine the overall fitness. The second way is by ε-criteria. If $\varepsilon << 0.1$, that is the error introduced by equation (2-5) is much less than a tenth of the amount of anisotropy (δ), then equation (2-5) is a good representation, and the error introduced by equation (2-5) to the velocities can be neglected; otherwise, if $\varepsilon \geq 0.1$, that is, the error introduced by equation (2-5) is comparable with the amount of anisotropy, then equation (2-5) is a poor representation.

Equation (2-5) is examined over a range of anisotropic materials including pure PTL-anisotropy, pure EDA-anisotropy and a combination of PTL- and EDA- anisotropy leading to CLA-symmetry. Tables 2.1, 2.2 and 2.3 summarize the parameters of these materials, the materials in Table 2.3 being obtained by cracking the corresponding materials in Table 2.1 with the crack density used in Table 2.2. Note that the materials are selected to give a range of percentage of anisotropy, and that the *P*-wave velocity of the isotropic matrix varies from 2.0 km/s to 4.0 km/s and covers the range from sandstone to granite. More details of the behaviour of such materials are given by Wild

TABLE 2.1: Elastic constants of PTL-anisotropy (in 10^9 Pa), where c_{ijkl} for $i, j, k, l = 1, 2, 3$, are elements of the elastic tensor (Crampin 1981), and density is 2.6g/cm^3. The bracketed constants (c_{ij}) are the alternative two-suffix notation for the elastic constants. Note that the materials are selected to represent typical rocks in sedimentary basin, and that the *P*-wave velocity of the isotropic matrix varies from 4.0 km/s to 2.5 km/s, covering the range from granite to sandstone.

Material name	Percentage anisotropy	c_{1111} (c_{11})	c_{3333} (c_{33})	c_{3311} (c_{13})	c_{2323} (c_{44})	c_{1212} (c_{66})
A1	2%	41.378	39.690	15.186	12.418	12.785
A2	4%	38.904	36.097	13.819	11.353	12.051
A3	6%	36.556	32.400	12.400	10.251	11.375
A4	9%	34.342	28.632	10.954	9.116	10.754
A5	12%	32.272	24.835	9.509	7.949	10.182
A6	17%	30.345	21.060	8.060	6.784	9.669
A7	22%	28.576	17.369	6.644	5.631	9.210
A8	28%	26.977	13.833	5.297	4.505	8.802
A9	26%	25.553	10.530	4.030	3.450	8.450

TABLE 2.2: Elastic constants of EDA-anisotropy (in 10^9 Pa), and density is 2.6 g/cm^3. Similar to Table 2.1, the materials are selected to represent typical rocks in sedimentary basin, and the *P*-wave velocity of the isotropic matrix varies from 2.0 km/s to 4.0 km/s, covering the range from sandstone to granite. Notation as in Table 2.1.

Material name	Crack density	c_{1111} (c_{11})	c_{3333} (c_{33})	c_{3311} (c_{13})	c_{2323} (c_{44})	c_{1212} (c_{66})
C01	0.01	13.159	13.162	4.387	4.387	4.288
C02	0.02	16.240	16.249	5.419	5.414	5.172
C05	0.05	19.627	19.659	6.538	6.557	5.849
C07	0.07	27.365	27.452	9.129	9.150	7.801
C09	0.09	27.338	27.449	9.120	9.150	7.457
C10	0.10	27.324	27.447	9.125	9.150	7.293
C15	0.15	31.571	31.819	10.518	10.620	7.589
C20	0.20	43.593	50.959	18.835	14.951	24.878

TABLE 2.3: Elastic constants (in 10^9 Pa) of orthorhombic CLA-anisotropy formed from cracking the PTL-materials in Table 2.1 with the crack density used in Table 2.2, and density is 2.6 g/cm^3. Notation as in Table 2.1.

TABLE 2.3:

Material Name	Percentage Anisotropy	c_{1111} (c_{11})	c_{1122} (c_{12})	c_{1133} (c_{13})	c_{2222} (c_{22})	c_{2233} (c_{23})	c_{3333} (c_{33})	c_{2323} (c_{44})	c_{3131} (c_{55})	c_{1212} (c_{66})
A1C01	2%	41.347	15.796	15.174	41.374	15.181	39.686	12.418	12.144	12.503
A2C02	3%	38.849	14.782	13.801	38.895	13.813	36.092	11.353	10.857	11.525
A3C05	6%	36.436	13.761	12.363	36.536	12.390	32.396	10.251	9.173	10.177
A4C07	8%	34.191	12.782	10.923	34.311	10.954	28.651	9.116	7.811	9.205
A5C09	11%	32.090	11.858	9.509	32.222	9.542	24.917	7.952	6.536	8.341
A6C10	14%	30.136	10.988	8.146	30.260	8.176	21.288	6.791	5.482	7.743
A6C15	16%	30.063	10.959	8.122	30.249	8.167	21.281	6.791	4.960	6.938
A7C10	17%	28.315	10.209	6.909	28.418	6.932	17.897	5.648	4.582	7.348
A7C15	18%	28.253	10.184	6.890	28.408	6.925	17.892	5.648	4.163	6.591
A8C10	19%	26.592	9.571	5.901	26.677	5.919	14.933	4.544	3.717	6.942
A7C20	21%	28.192	10.160	6.872	28.399	6.918	17.888	5.648	3.822	5.911
A8C20	24%	26.491	9.530	5.873	26.661	5.909	14.929	4.544	3.150	5.602
A9C20	28%	24.853	9.092	5.220	24.989	5.246	12.648	3.533	2.549	5.258

and Crampin (1991). The three different types of anisotropy are discussed separately in following sections.

2.3.1 PTL-anisotropy

There is no azimuthal variation in PTL-anisotropy with vertical axis of symmetry. All vertical planes are symmetry planes, and the behaviour is independent of angle α. Thus theoretical speaking, equation (2-5) is expected to be a good representation for all three body waves in all vertical planes.

Table 2.1 shows the differential shear anisotropy and the elastic constants of 9 pure PTL-anisotropy. The degree of anisotropy varies from 2% to 36%. Figure 2.2 shows the comparison of numerical velocities $V(\phi)$ and analytical velocity $v(\phi)$ given by equation (2-5) against incidence angle for materials A5 (Figure 2.2a) and A8 (Figure 2.2b). A5 corresponds to 12% PTL-anisotropy, and A8 corresponds to 28%. As shown in Figures 2.2a and 2.2b, the numerical velocities of the *qP*-wave are plotted out as dots, those of the *qSV*-wave as crosses, and those of the *qSH*-wave as diamonds; the solid lines through the corresponding marks represent the corresponding analytical velocities given by equation (2-5). Hereafter, these marks and notations will be applied to all the figures of the paper. Figure 2.2a shows that for 12% PTL-anisotropy, the analytical results match the numerical results very well for all the three body waves, and equation (2-5) is a good representation for 12% PTL-anisotropy. But Figure 2.2b, shows that for 28% PTL-anisotropy, equation (2-5) is not a very good representation for *qP*- and *qSV*-waves, but it is still good for *qSH*-waves. In general, the overall quality of the match is

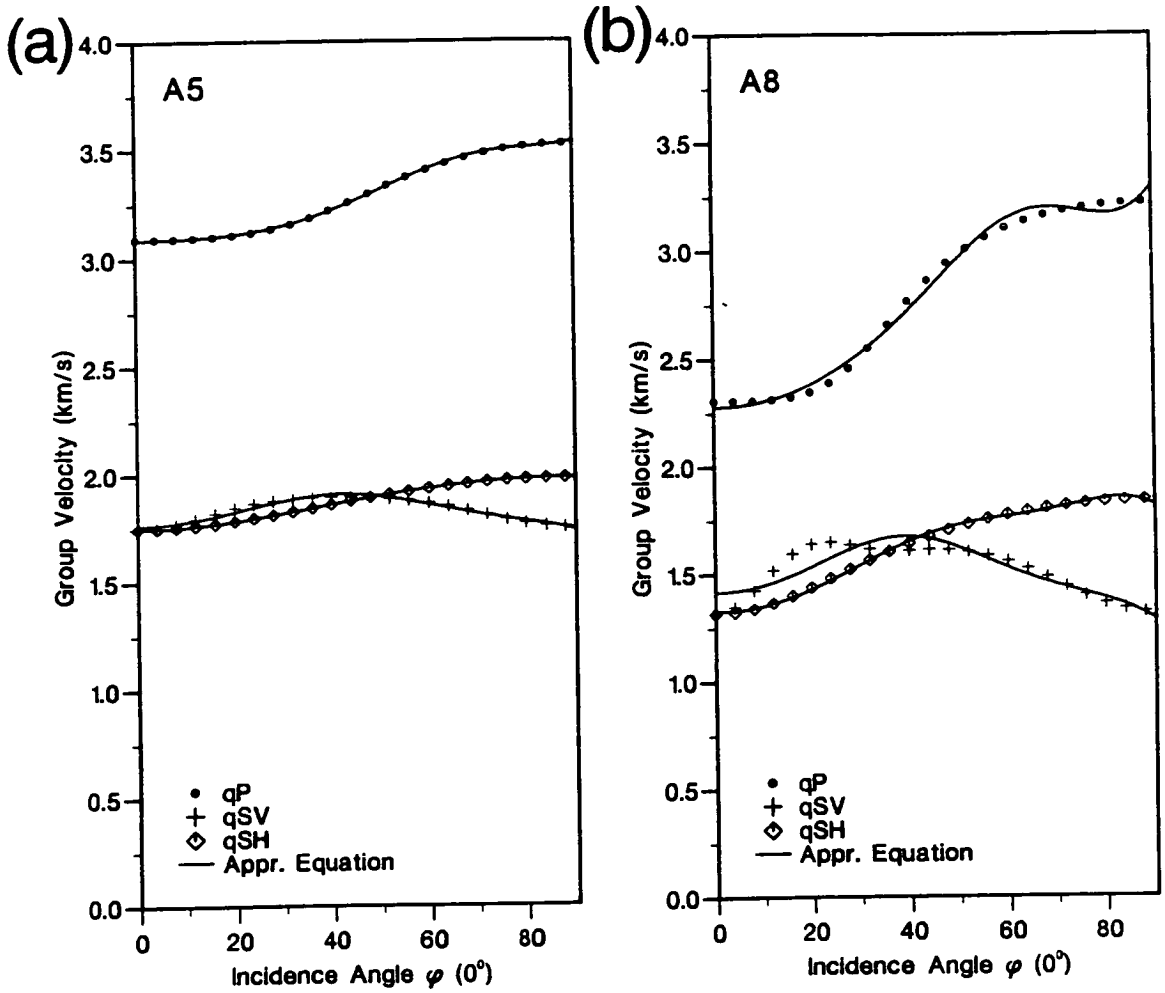

Figure 2.2. Comparison of numerical and analytical velocities for materials with PTL-anisotropy, where properties are independent of the azimuth α. The black dots are the numerical velocity of *qP*-waves, crosses are those of *qSV*-waves, and diamonds of *qSH*-waves. The solid lines through the corresponding marks are the analytical velocities. a) Material A5 with 12% PTL anisotropy; (b) material A8 with 28% anisotropy.

decreasing as anisotropy increases.

Next I examine the ε-criteria. I apply equation (2-5) to all the materials shown in Table 2.1, and calculate and plot the error ratio ε against the degree of anisotropy δ in Figure 2.3. Figure 2.3 shows that the error ratio increases as the amount of anisotropy increases. Although up to 36% PTL-anisotropy, the error ratio is still below the 0.1 for *qP*- and *qSH*-waves, it is not suggested that equation (2-5) is a good representation for *qP*- and *qSH*-waves up to 36% PTL-anisotropy. Take the error ratio of *qSH*-wave at 28% PTL anisotropy as a threshold. [Because equation (2-5) is only good for *qSH*-wave up to 28% PTL anisotropy, as shown in Figure 2.2b.] The error ratio close to this threshold is at 22% anisotropy for *qP*-wave, and at 9% anisotropy for qSV-waves (Figure 2.3). Note that at 12% anisotropy, the error ratio of *qSV*-wave is also very close to the threshold. Thus, to sum up, equation (2-5) is a good representation for velocity variations up to 22% PTL anisotropy for *qP*-wave, 28% anisotropy for *qSH*-wave, and 10% for *qSV*-wave, or up to at least 10% PTL-anisotropy for all three body waves. These results agree with Levin (1978, 1979) in his earlier study of seismic velocities in PTL-anisotropic media.

2.3.2 EDA-anisotropy

Table 2.2 shows the differential shear anisotropy and the elastic constants of seven pure EDA-materials. The amount of anisotropy varies from 1% to 20%, (crack density from 0.01 to 0.20). There are azimuthal variations in

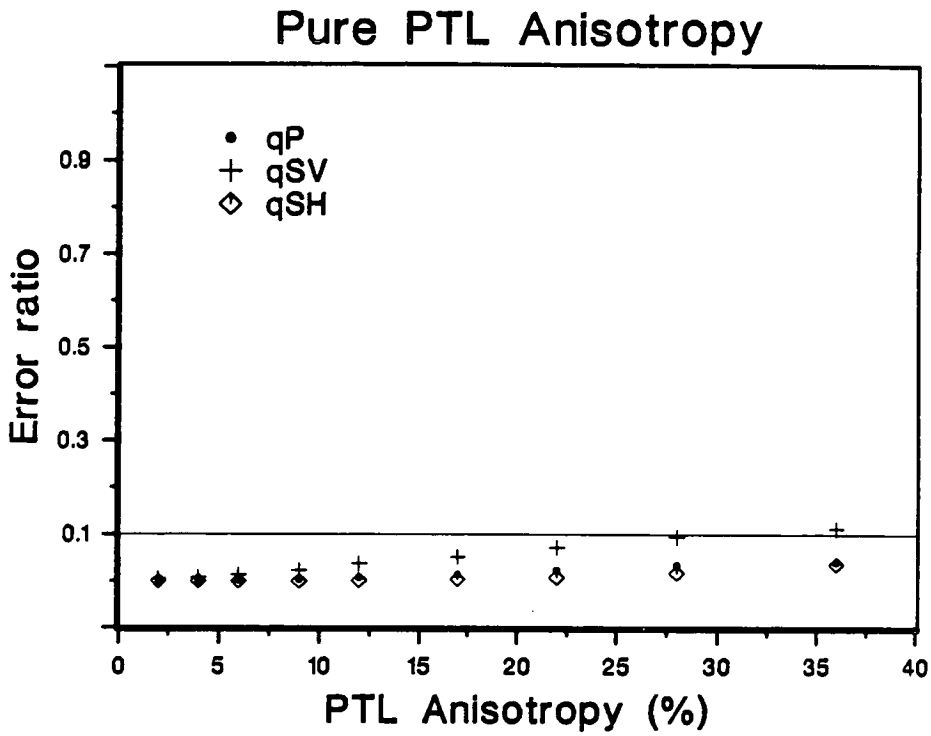

Figure 2.3. Error ratio ε against the amount of *PTL*-anisotropy.

EDA-anisotropy, that is, the velocity varies with α, the line azimuth angle measured from the crack strike. To examine the accuracy of equation (2-5) for representing the velocity variations of the three body waves in vertical acquisition planes, I consider two cases. Firstly, I choose plane $\alpha=30°$ and vary the amount of EDA-anisotropy, then I choose material C15 and vary the line azimuth angle α.

Following a similar sequence as in the previous discussion for PTL-anisotropy, I first examine the overall fit of the analytical to the numerical velocities. Figure 2.4 shows the comparison of the analytical approximate velocity $v(\phi)$ given by equation (2-5) with the numerical velocity $V(\phi)$ against incidence angle for materials C10 (Figure 2.4a) and C15 (Figure 2.4b) in off-symmetric plane $\alpha=30°$. C10 corresponds to crack density 0.10, about 10% shear-wave anisotropy; and C15 corresponds to density 0.15, about 15% shear-wave anisotropy. From Figure 2.4, it can be seen that the fit of the analytical to the numerical velocities is very good for both materials of C10 and C15 for *qP*-wave, is good for both materials for *qSH*-wave except near the point sigularity at about 70° incidence angle, and is not very good for both materials for *qSV*-wave.

The poor fit shown in Figure 2.4 for shear-waves is caused by the fact that the vertical plane in which the velocity variation is examined is an off-symmetry plane. In such off-symmetry planes, the rays are deviated and the polarizations of shear-waves are no longer strictly parallel or perpendicular to the plane of variation (Crampin 1981), particularly near the singularities.

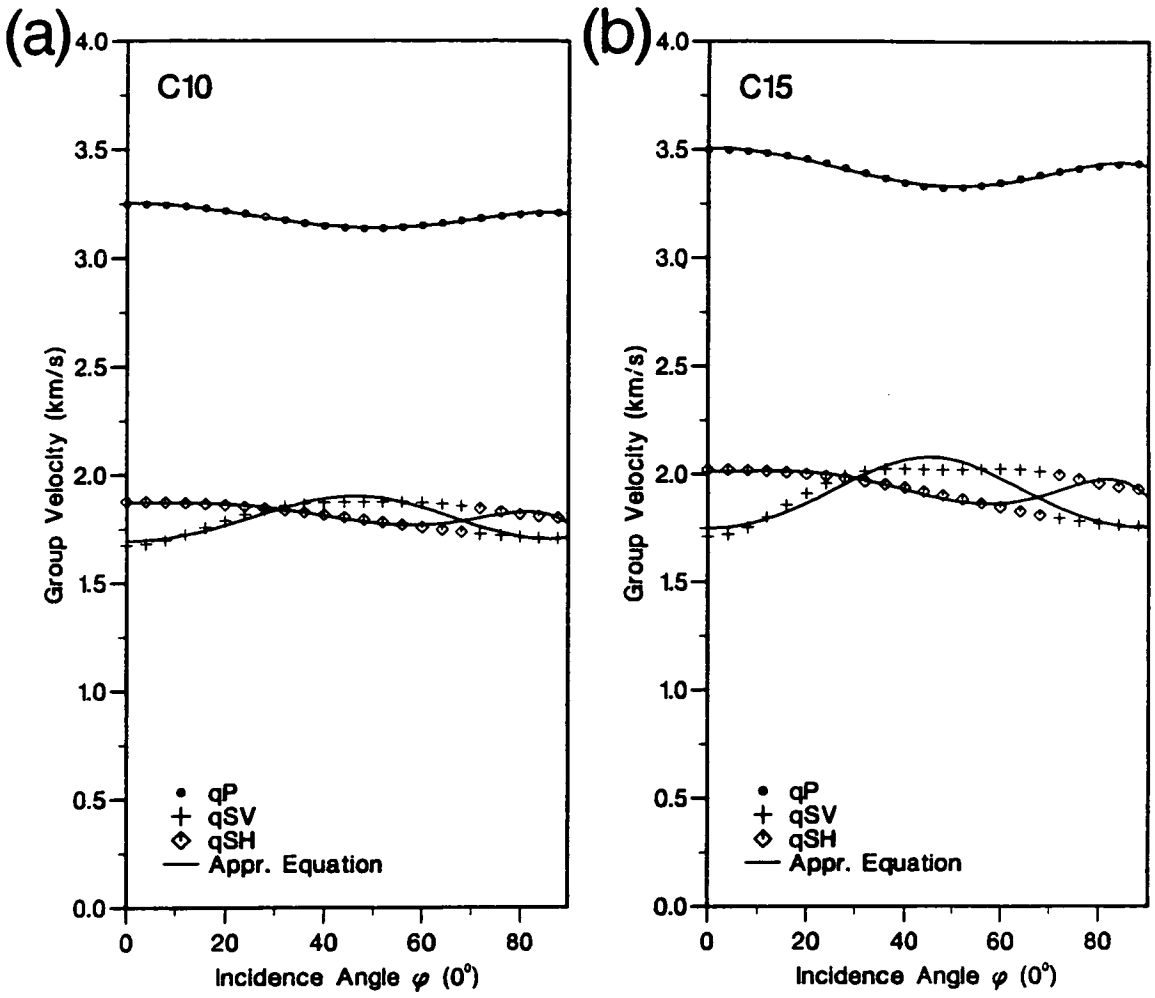

Figure 2.4. Same as Figure 2.2 but for materials with EDA-anisotropy. Line azimuth angle α equals 30°. (a) Material C10 with crack density 0.10, and about 10% shear-wave anisotropy; (b) material C15 with crack density 0.15 and approximately 15% anisotropy.

As a result, the shear-waves cannot be classified as *qSH* or *qSV* type. As shown in Figure 2.4, such classification will cause a sharp discontinuity at incidence angle about 70°. The misfit caused by the singularity at about 70° spreads over more than 20° in both Figures 2.4a and 2.4b for qSV-wave, and over more than 20° in Figure 2.4b but less than 10° in Figure 2.4a for *qSH*-wave. Thus, it can be said that equation (2-5) is a very good representation for up to 15% EDA anisotropy for *qP*-wave, is a good representation for up to 10% EDA-anisotropy for *qSH*-wave (although there some distortions at the singularities, these are small and may be neglected), and is not a good representation for *qSV*-wave at more than 10% EDA-anisotropy.

Next I examine the ε-criteria. Figure 2.5a shows the error ratio against the amount of EDA-anisotropy in off-symmetry plane $\alpha=30°$. Comparing Figure 2.5a with Figure 2.3 shows that the error ratios of *qP*-wave in Figure 2.5a are similar to those in Figure 2.3, but the error ratios of shear-waves in Figure 2.5a are slightly higher than those in Figure 2.3, which is caused by the distortions at the singularities as shown in Figure 2.4. Figure 2.5a shows that error ratios are all below the 0.1 line up to 15% EDA anisotropy for *qP*-and *qSH*-waves, but only up to 7% for *qSV*-wave. Similar to the case of PTL-anisotropy, take the error ratio of *qSH*-wave at 10% EDA-anisotropy as a threshold. For up to 15% EDA-anisotropy, the error ratios of *qP*-wave are below the threshold, and at about 5% and 7% anisotropy, the error ratios of *qSV*-wave are close to the threshold (Figure 2.5a). Thus, it can be said that at line azimuth 30°, equation (2-5) is good up to 15% EDA-anisotropy for

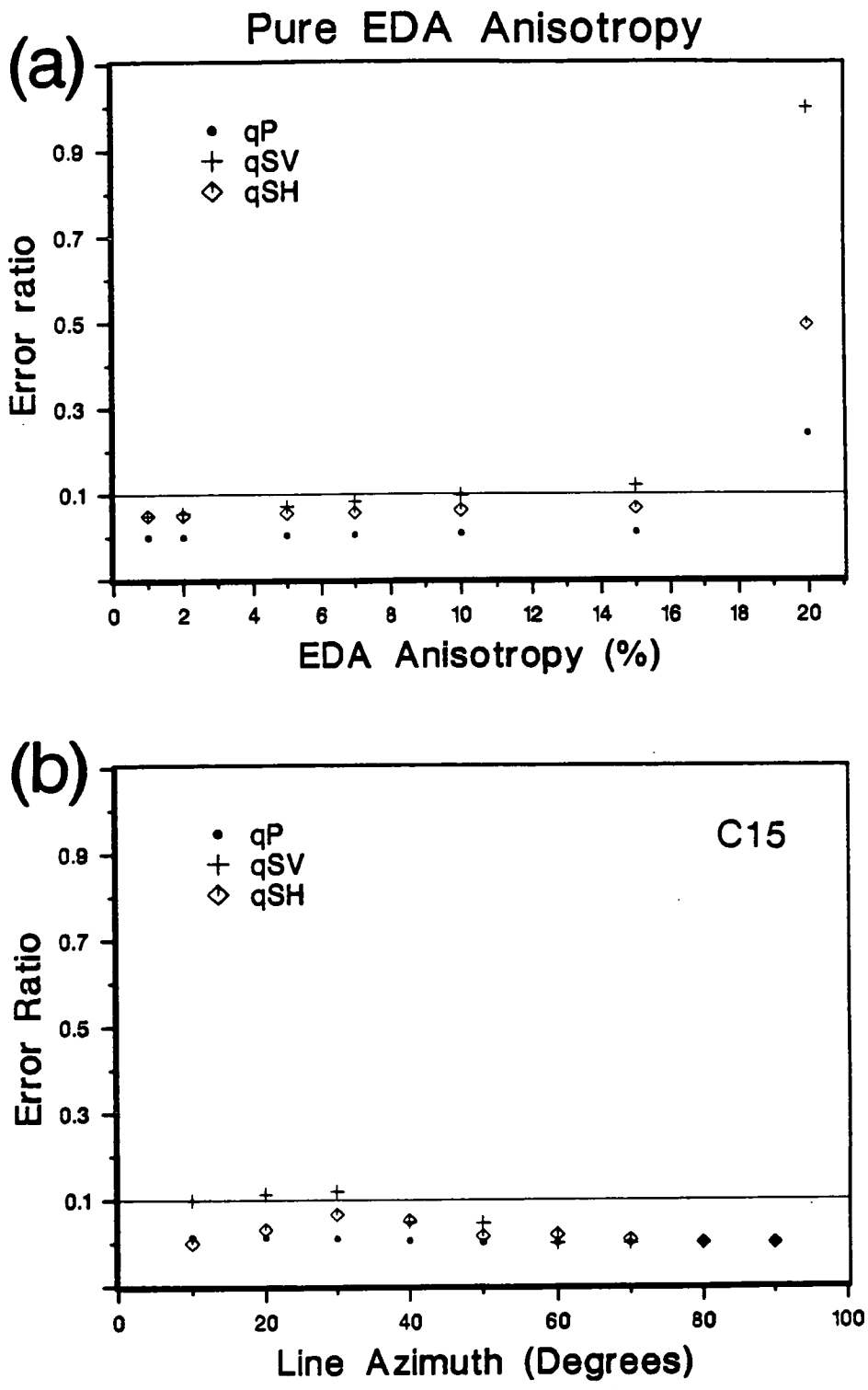

Figure 2.5. (a) Error ratio ε against the amount EDA-anisotropy with line azimuth $\alpha = 30°$; (b) error ratio ε against line azimuth angle α for material C15.

qP-wave, up to 10% anisotropy for *qSH*-wave, and 6% for *qSV*-wave. This is also true for other line azimuths as demonstrated in Figure 2.5b.

Figure 2.5b shows the error ratio against line azimuth for material C15. As the azimuth increases from 0° to 90°, the error ratio increases until $\alpha=30°$, then decreases. Line azimuth $\alpha=30°$ appears to have the largest error ratio over all the azimuths for material C15. Similar features can be expected for other EDA-materials because they have the same symmetry and can be described in similar ways using Hudson's theory (Hudson 1981, 1982).

2.3.3 Orthorhombic CLA-anisotropy

Table 2.3 shows the 13 orthorhombic materials used in this study. Figures 2.6 and 2.7 are same as Figures 2.4 and 2.5, but for CLA-materials. As shown Figure 2.6, both for materials A3C05 (6%) and A5C09 (11%), the curves of the analytical results match the numerical results very well for *qP*- and *qSH*-waves, although there are some distortions at the singularities of the shear-waves; the match for *qSV*-waves is good for material A3C05 in Figure 2.6a, but is not good for A5C09 in Figure 2.6b. Take the error ratio of *qSH*-wave at 6% CLA-anisotropy (A3C05) in Figure 2.7a as a threshold. The error ratios are close to the threshold up to 18% CLA-anisotropy for *qP*-wave (dots), 14% anisotropy for *qSH*-wave (diamonds), and 6% for *qSV*-wave (crosses). Note that comparing with variation of error ratio ε in PTL- and EDA-anisotropy (Figures 2.3 and 2.5a), the variation in CLA-anisotropy (Figure 2.7a) is more scattered and does not increase monotonically as the

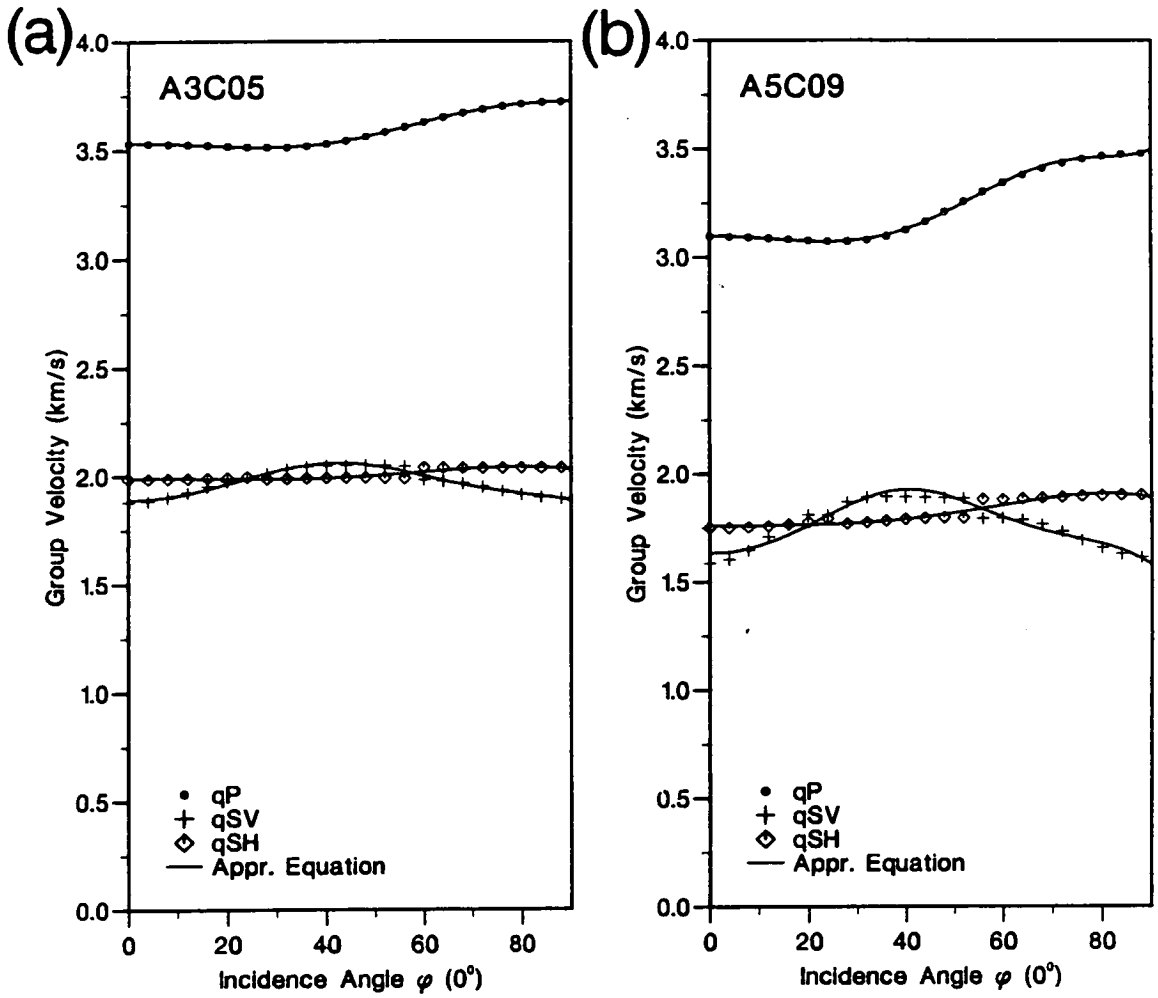

Figure 2.6. Same as Figure 2.2, but for materials with orthorhombic CLA-anisotropy formed from a combination of PTL- and EDA-anisotropies. The plane of variation is at $\alpha = 30°$. (a) Material A3C05 with 6% PTL-anisotropy and crack density 0.05, giving rise to about 6% orthorhombic anisotropy; (b) material A5C09 with 12% PTL-anisotropy and crack density 0.09, giving rise to about 11% orthorhombic anisotropy.

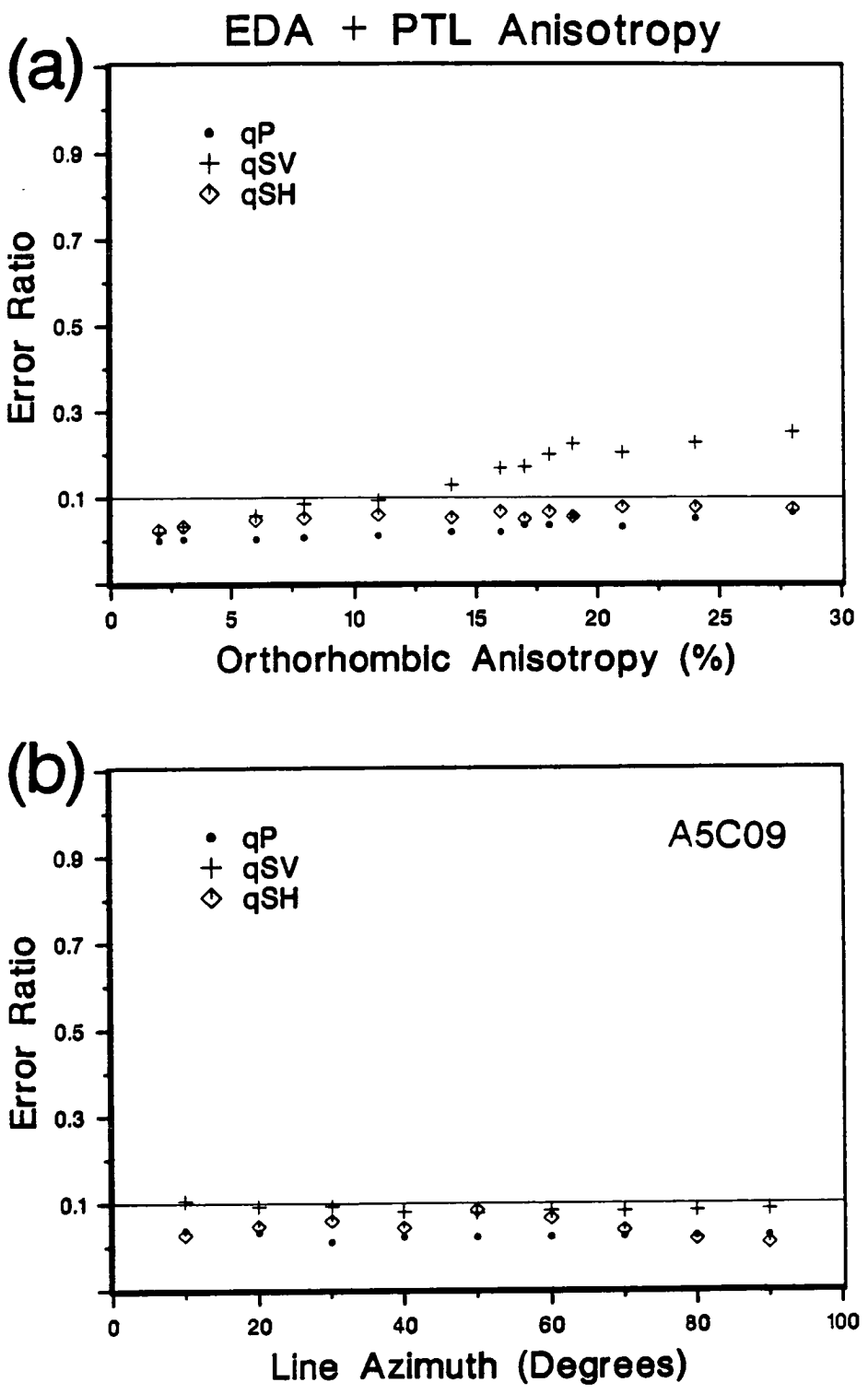

Figure 2.7. Same as Figure 2.5, but for orthorhombic CLA-anisotropy.

anisotropy increases, because a higher class of symmetry (orthorhombic symmetry) is involved.

Figure 2.7b shows the error ratio against line azimuth for materials A5C09 (about 11% anisotropy). The error ratios never exceed 0.1 for all three body waves and for all line azimuth angles, but the variations are also more complicated compared with Figure 2.5b. For *qP*- and *qSV*-waves, variation of ε is small as line azimuth varies; but for *qSH*-wave, the variation appears significant from about 0.05 at 90° to about 0.1 at 50°. As the anisotropy exceeds 11%, the largest error ratio for *qSH*-wave may exceed 0.1. Thus, to sum up, it can be said that equation (2-5) is good up to 18% CLA-anisotropy for *qP*-wave, 11% anisotropy for *qSH*-wave, and 6% for *qSV*-wave.

2.4 MOVEOUT EQUATION

Now I derive the moveout equation. As shown in Figure 2.1, x is the source-receiver distance OG, and z is the depth of the reflector OD. The travel time t from O to G reflected at R can be written as:

$$t^2 = 4z^2/(v(\phi)\cos\phi)^2. \qquad (2\text{-}7)$$

As demonstrated in Appendix A, substituting equation (2-5) into (2-7), the moveout equation can be written as:

$$t^2 = \begin{cases} t^2_h + t^2_r & \text{if } v_{nmo} \geq v_h; \\ t^2_h - t^2_r & \text{if } v_{nmo} < v_h; \end{cases} \tag{2-8}$$

where

$$t^2_h = t^2_0 + x^2/v^2_{nmo}; \tag{2-9}$$

$$t^2_0 = 4z^2/v^2_v; \tag{2-10}$$

$$t^2_r = x^2/v^2_{nmo}\delta^2_a \sin^2\phi; \text{ and} \tag{2-11}$$

$$\delta^2_a = |v^2_{nmo}/v^2_h - 1|. \tag{2-12}$$

Equation (2-8) shows that the travel time t from O to G via R in an anisotropic medium as shown in Figure 2.1 can be separated into two terms t_h and t_r, where t_h is a hyperbolic moveout as shown in equation (2-9), and t_r is a residual moveout. Equation (2-11) shows that t_r is the product of three terms. Term x/v_{nmo} is a conventional moveout term; δ_a in equation (2-12) is a measure of the apparent velocity anisotropy in the medium; $\sin\phi$ is a measure of the spread factor of the geometry. If the incidence angle is small (or x is small), then $\sin\phi$ is small, and t_r will be small. Also if the anisotropy is small, then t_r will be small. To sum up, t_r is a residual moveout related to the amount of anisotropy of the medium and the spread factor of the geometry.

To evaluate these equations, I compute synthetic moveout curves using the numerical velocities shown in the previous section. I assume a single 1000m thick anisotropic bed having a horizontal lower interface and calculate reflection arrival times for surface receiver with offsets from 0m to 2350m (the largest

incidence angle is about 50°) from a source also on the surface. I plot t^2 against x^2, then fit equation (2-9) (the hyperbolic moveout) to the t^2-x^2 data as a first order approximation, and fit equation (2-8) (hyperbolic moveouts plus residues) as a second order approach. The moveout velocity is the square root of the reciprocal of the absolute value of the initial slope of a t^2-x^2 curve (Thomsen 1988).

Figures 2.8, 2.9, and 2.10 show t^2-x^2 plots for velocities of the materials in Figures 2.2, 2.4 and 2.6, respectively. The numerical t^2-x^2 curves of *qP*-waves wave are plotted as black dots, those of *qSV*-waves as crosses, and those of *qSH*-waves as diamonds. The first order $t^2{}_h$-x^2 curves of *qP*- and *qSH*-waves are both plotted as dash lines, and the second order ($t^2{}_h \pm t^2{}_r$)-x^2 curves of the three body waves are all plotted as solid lines. Note that the first order $t^2{}_h$-x^2 curve of *qSV*-waves is not plotted, because the moveout of the *qSV*-wave decreases as offset increases at small offsets in Figures 2.8, 2.9 and 2.10, resulting in a negative initial slope at the corresponding t^2-x^2 curves in Figures 2.8, 2.9 and 2.10. Then it is obvious that in these cases the t^2-x^2 of *qSV*-waves cannot be modelled by the first order $t^2{}_h$-x^2 curves, even for small offset. The results of three different types of anisotropy will be discussed separately.

2.4.1 PTL-anisotropy

Firstly, I examine *qP*-waves. As shown in Figure 2.8, for small offset range, the first order curve of *qP* is a good match to the black dots of the t^2 –

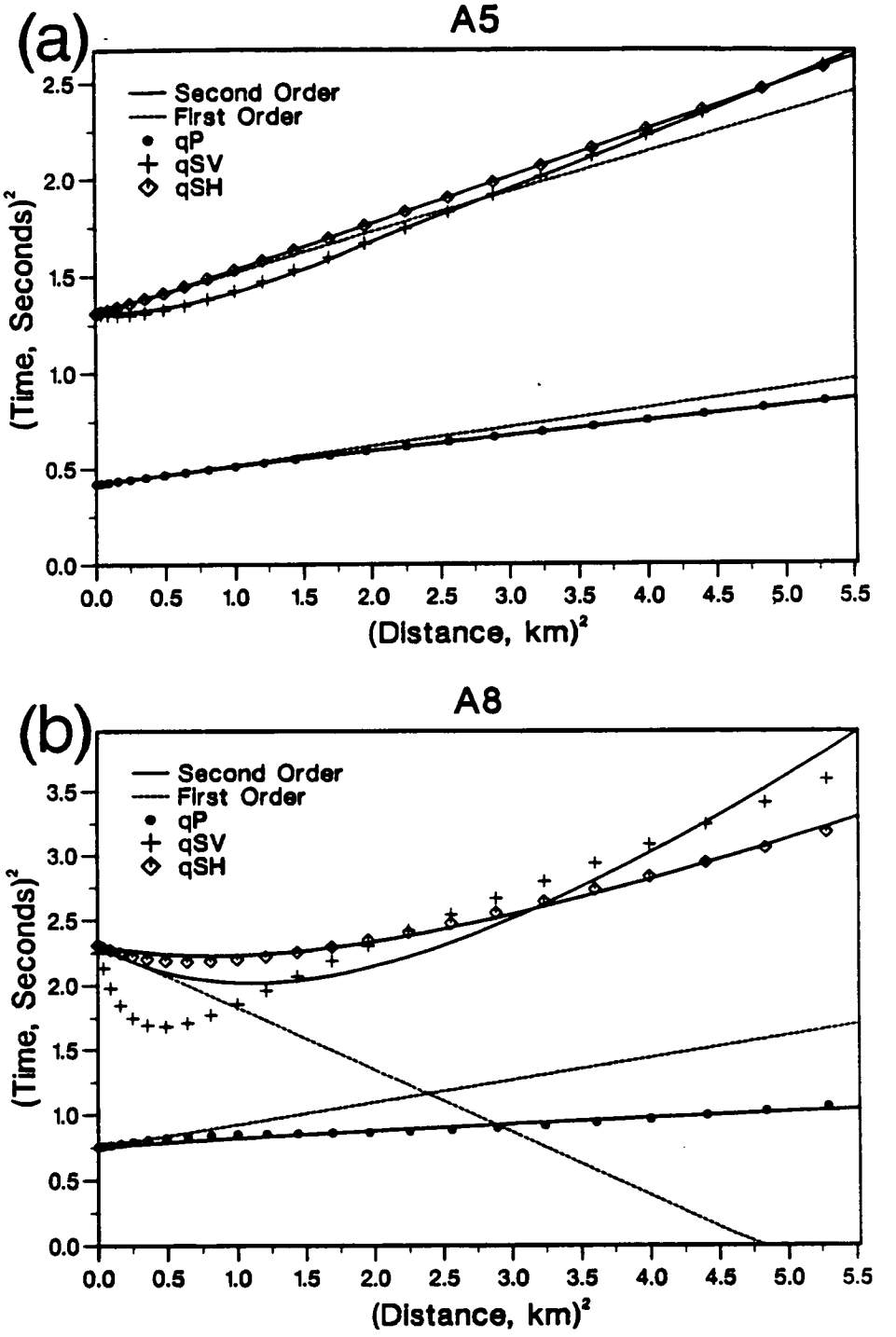

Figure 2.8. t^2-x^2 curves for PTL-anisotropy for the velocities of Figure 2.2 for a reflector at 1000m and a spread 0m to 2350m, corresponding to incidence angles 0° to 50° . The black dots are numerical results of *qP*-waves, crosses are those of *qSV*-waves, and diamonds are those of *qSH*-waves. The solid lines are the fit for second order equation (2-8), and dash lines are the fit for first order equation (2-9). The first order curves of *qSV*-waves are not plotted. (a) Material A5; (b) Material A8.

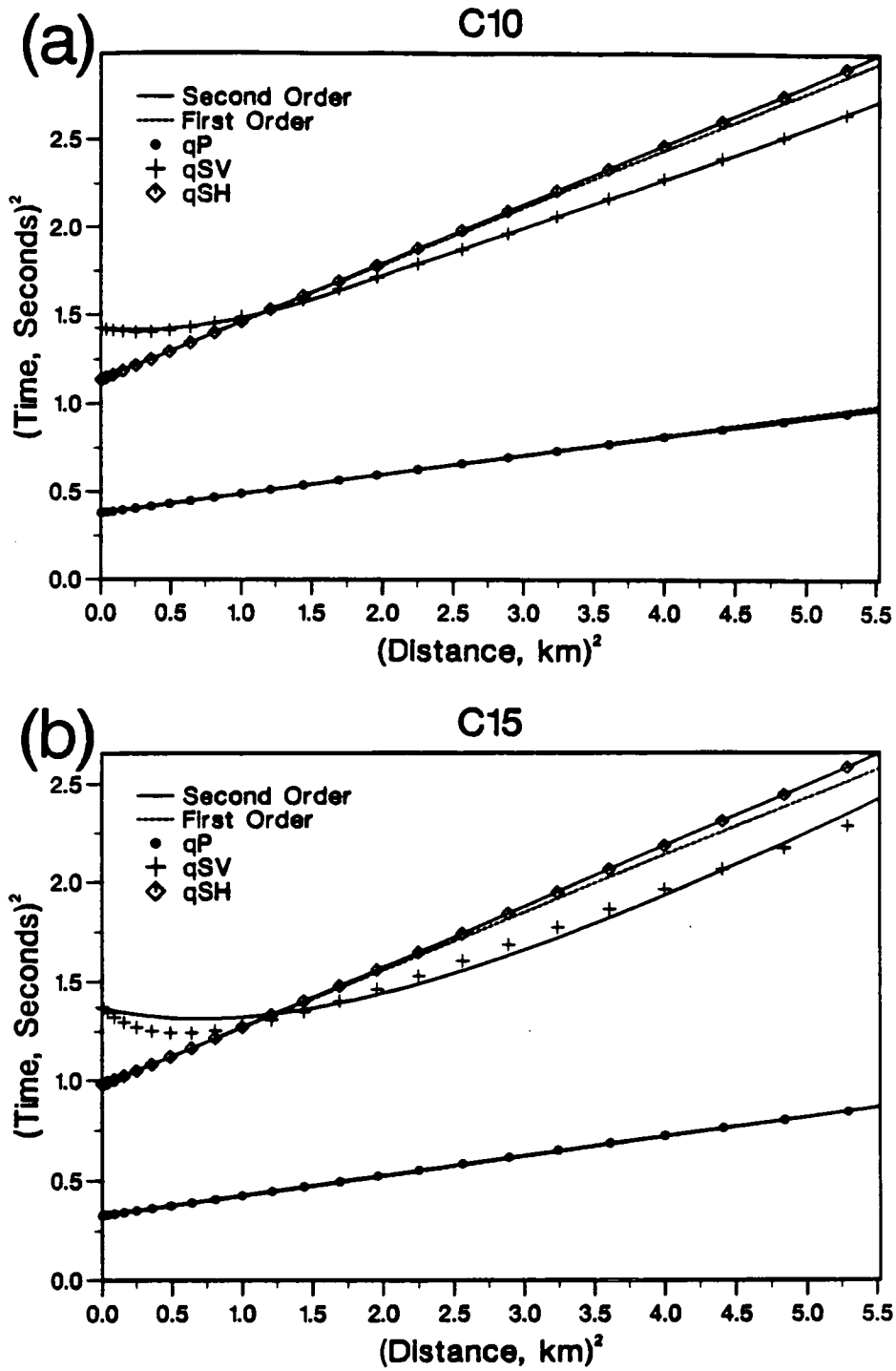

Figure 2.9. Same as Figure 2.8 but for EDA-anisotropy and velocity of Figure 2.4. Line azimuth angle $\alpha = 30°$. (a) Material C10; (b) Material C15.

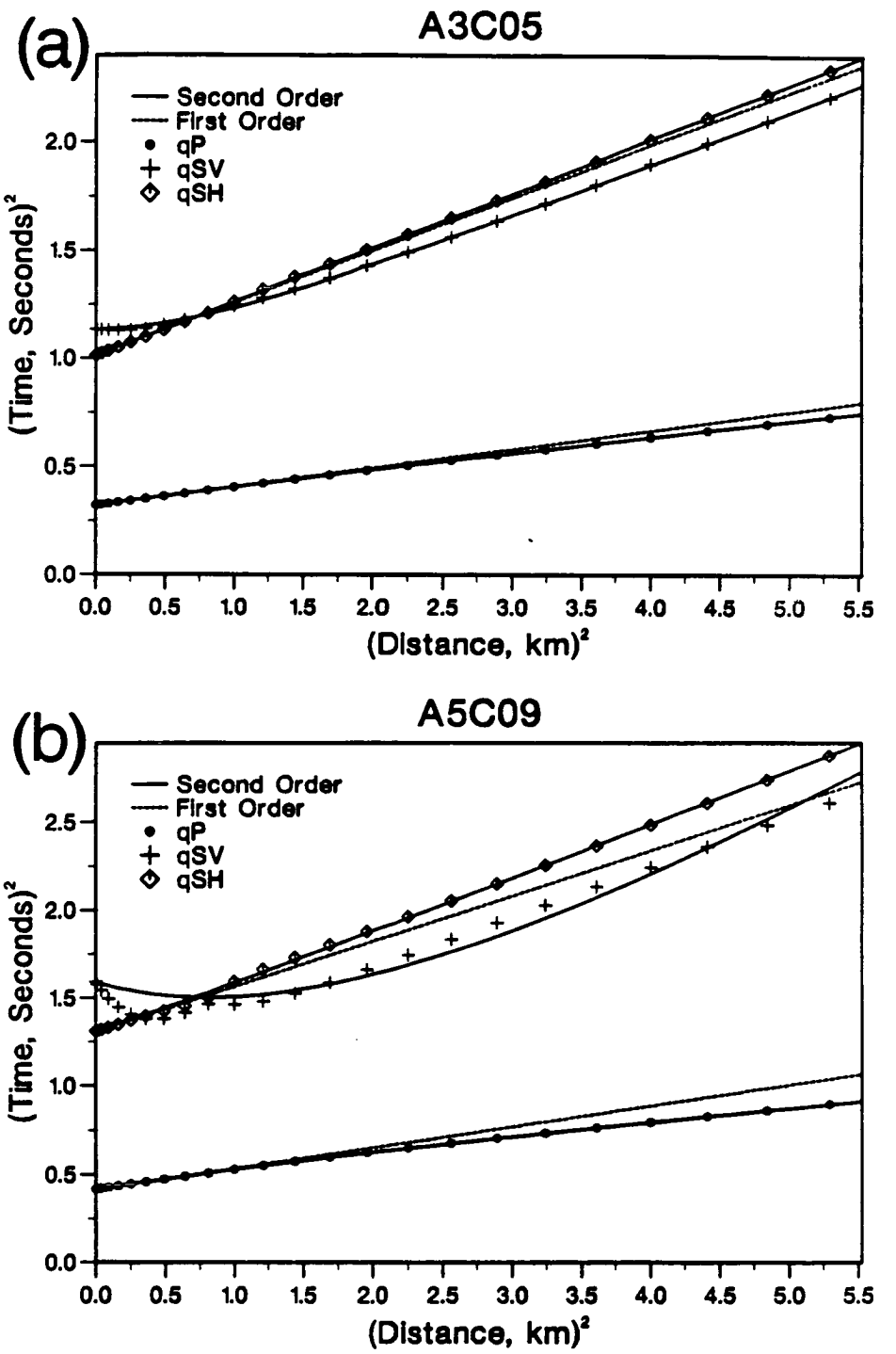

Figure 2.10. Same as Figure 2.9, but for orthorhombic CLA-anisotropy and velocity of Figure 2.6. Line azimuth angle $\alpha = 30°$. (a) Material A3C05; (b) Material A5C09.

x^2 curve, but this range decreases as anisotropy increases. For material A5 (12% anisotropy, Figure 2.8a), the range extends to about 1.5km^2 (offset 1.2km; about 31° of incidence angle ϕ). But for material A8 (28% anisotropy, Figure 2.8b), the range reduces to about 0.5km^2 (offset 0.7km; about 19° of incidence angle). In contrast, the second order curve (solid lines) almost exactly follows the black dots over the whole offset range in Figure 2.8a for material A5, and is only slightly deviated in Figure 2.8b for material A8.

Secondly, I examine *qSH*-waves. As in Figure 2.8a of material A5 demonstrated, the first order curves are good matches for small offsets ($x^2=1.2$km^2; $x=1.1$km; $\phi=29°$). But as in Figure 2.8b of material A8 has shown, the first order curve does not match the corresponding numerical results (the diamonds), because the moveout at small offset decreases with offset and leads to a negative initial slope. For material A5 (Figure 2.8a), the second order curve of the *qSH*-wave also follows the corresponding diamonds very closely over the whole offset range; for material A8 (Figure 2.8b), the match is slightly degraded but is still acceptable.

Thirdly, I examine the *qSV*-wave. For *qSV*-wave, however, the changes in the t^2-x^2 curves are quite dramatic. Both in Figures 2.8a and 2.8b, the moveout decreases with offset at near vertical incidence, hence, leads to a negative initial slope similar as the first order curve of *qSH*-wave (dash line) in Figure 2.8b of material A8. As a result, the first order curves do not match the numerical results at all, and the moveouts can no longer be represented by

a hyperbola even at small offset. The second order curve of *qSV* is a good match only for material A5 (Figure 2.8a).

2.4.2 EDA-anisotropy

Figure 2.9 shows the corresponding results for EDA-anisotropy. For the *qP*-wave, the first order and second order curves match the black dots for the whole offset range for both materials C10 (10% anisotropy) and C15 (15% anisotropy). This confirms that *q*P-wave is not sensitive to crack anisotropy. For the *qSH*-wave, the first order curves are a good match at small offsets both for C10 and C15 with offset ranges ($x^2=3.2\text{km}^2$; $x=1.8\text{km}$; $\phi=42°$) and ($x^2=2.2\text{km}^2$; $x=1.5\text{km}$; $\phi=36°$), respectively, and the second order curves are a good match over the whole offset range for both materials C10 and C15.

For *qSV*-waves, Figure 2.9 shows similar features as those of Figure 2.8. Firstly, the moveouts decrease with offset at small offsets, and the t^2-x^2 curves can no longer be modelled by the first order $t^2{}_h$-x^2 curves for both materials C10 and C15 (Figures 2.9a and 2.9b). Secondly, the second order curve is a good match to the numerical results only for material C10 (Figure 9a); for material C15, the matches are not very good at small offsets.

Note that distortions to the analytical results in Figure 2.4a appear at incidence angles large than 55°, and the spread shown Figure 2.9a has incidence angles less than 50°. Thus the distortions in Figure 2.4a have only a small effect on the second order curves in Figure 2.8a for both *qSH*- and

qSV-waves.

2.4.3 Orthorhombic CLA-anisotropy

Figure 2.10 shows the corresponding results for orthorhombic anisotropy. The overall features in Figure 2.10 are similar to those in Figures 2.8 and 2.9. For *qP*-waves, the first order curves in both Figures 2.10a and 2.10b are a good match to the black dots at small offsets - offsets less than about 2.7km^2 (offset 1.6km; about 39° of incidence angle ϕ) for material A3C05, and about 1.7km^2 (offset 1.3km; about 33° of ϕ) for material A5C09. The second order curves match to the black dots very well over the whole range of offsets and for both materials A3C05 and C5C09 (Figures 2.10a and 2.10b).

For *qSH*-waves, again, the first order curves match the diamonds at small offsets with a range of (x^2=3.0km^2; x=1.7km; ϕ=41°) for A3C05, and of (x^2=0.8km^2; x=0.9km; ϕ=24°) for A5C09, and the second order curves match to the diamonds over the whole offset range for both materials. For *qSV*-waves, the moveouts also decrease with offset at small offsets, thus the t^2-x^2 curves cannot be modelled by first order t^2_h-x^2 curves for both materials A3C05 and C5C09, and the second order curve shows good matches to the crosses only for material A3C05 (Figure 2.10a).

2.5 DISCUSSION

Approximately analytical equations can be used to estimate the velocity

variation in off-symmetry planes in weakly anisotropic solids including orthorhombic symmetry. The equations have forms shown as equations (2-3), (2-4) and (2-5). Results of the accuracy of the analytical equations related to the amount of anisotropy can be summarized as follows:

2.5.1 Accuracy of approximations for velocity variations

1. For *qSH*-waves, the approximate equations are good representations for up to 28% PTL-anisotropy, 10% EDA-anisotropy, and 11% CLA-anisotropy.

2. For *qP*-waves, the approximate equations are also good representations for up to 22% PTL-anisotropy, 15% EDA-anisotropy, and 18% CLA-anisotropy.

3. For *qSV*-waves, the approximate equations are good representations for up to 10% PTL-anisotropy, 6% EDA-anisotropy, and 6% CLA-anisotropy.

4. Within the above anisotropy limits, the approximate equations yield good representations of velocities in all vertical planes including off-symmetry directions.

2.5.2 Accuracy of approximations for moveouts

The analytical moveout equations for *P*- and shear-waves travelling in a weakly anisotropic medium can be obtained from the analytical velocity equations. The moveouts can be separated as hyperbolic moveouts and

residues. Analysis of numerical results shows the following:

1. For up to 28% PTL-anisotropy, 15% EDA-anisotropy (crack density 0.15), and 11% orthorhombic CLA-anisotropy, the moveout curve of qP-wave can approximately be modelled by a hyperbola (a straight line in t^2-x^2 plots) for incidence angle up to 20°. A modified moveout equation with an anisotropy residue term can model the moveout curve for the whole range of offsets up to 50° of incidence angle.

2. For at least 12% PTL-anisotropy, and for up to 15% EDA-anisotropy (crack density 0.15), and 11% CLA-anisotropy, the moveout curve of qSH-wave is still a hyperbola for incidence angle up to 20°. Again a modified moveout equation is valid for the whole range of offsets up to 50° of incidence angle and up to 28% PTL-anisotropy.

3. At 12% PTL-anisotropy, 10% EDA-anisotropy (crack density 0.10), and 6% CLA-anisotropy, the moveout of *qSV* wave can not be modelled by a hyperbolic curve. The moveout initially decreases when offset increases until about 15° of incidence angle. This decrease of moveout is caused by the increase of velocity as offset increases. But the modified moveout equation provides a good estimation of moveouts up to 12% PTL-anisotropy, 10% EDA-anisotropy (crack density 0.10), and 6% CLA-anisotropy for incidence angles up to 50°.

4. The decrease of moveout of *qSV*-waves is a good indicator of anisotropy in

horizontally layered media. The modified moveout equation can improve the estimation of velocities, and hence improve the results of stacking. Only if the velocity variation of different type of waves can be properly estimated, can identification of singularities, amplitude studies, and other interpretations of shear-wave anisotropy be carried out successfully in reflection surveys.

2.5.3 Limitations

The limitations of these approximations are severe:

1. The model for studying the moveout relation consists of only a single planar interface. This is clearly a poor representation of a realistic subsurface (Levin 1979), although the critical ideas revealed in this simple case may be also applicable to more complicated situations.

2. It should also be pointed out that before multilayering and dipping interfaces can be addressed, the different effects on shear-waves in reflection surveys caused by anisotropy and by structural variation must also be addressed. In some aspects, the effects of anisotropic variation and those of structural variation are very similar, particularly where residual moveouts are concerned.

Many other studies (Levin 1979; Uren *et al.* 1991; and others) investigating transverse isotropy with azimuthal isotropy (Crampin 1989) also have the above two restrictions. Note that all the vertical planes are symmetry

planes in azimuthal isotropic media, and in attempting to treat azimuthal anisotropy further limitations are introduced.

3. It must also be remembered that the notation *qSH*- and *qSV*-waves refers to waves which have closest to conventional *SH*- and *SV*-wave particle motion. In anisotropy, particle motion may deviate significantly from conventional motion (Crampin 1981), particularly in off-symmetry plane.

4. Finally, the resolution of the two split shear-waves into two separate entities the *qSH*- and the *qSV*-wave is a severe approximation. The places where the two split shear-waves appear to intersect, in Figures 2.2, 2.4, and 2.6, for example, are directions near point singularites, where split shear-waves may exchange energy and particle motions and are likely to have very disturbed propagation (Crampin 1991).

Sena (1991) investigated approximate travel time equations in azimuthal anisotropic media with hexagonal symmetry, while this study was being carried out. The above two limitations also exist in Sena's study (Sena 1991), although he did not point this out. Sena's results (Sena 1991) are only valid in symmetry planes. In the case of an off-symmetry plane and orthorhombic anisotropy, these approximations are certainly severe, as we demonstrated in this study. Although with all the limitations, these approximations can still be useful for providing guidelines for processing multi-component shear-wave data in the presence of anisotropy, they need to be verified by case studies.

2.6 CONCLUSIONS

Approximate velocity equations in symmetry planes of weakly anisotropic solids including orthorhombic symmetry are extended to off-symmetry planes to meet the needs of real data. The modified equations are good representations of velocity variations up to a significant amount of PTL-, EDA-, and orthorhombic CLA-anisotropy. However, waves in off-symmetry planes suffer more distortions in polarizations and phase and group velocities than waves in symmetry planes; and waves in anisotropic media with orthorhombic symmetry also suffer more distortions than waves in media with hexagonal symmetry.

The moveout of a *qP*-wave, or a *qSV* wave, or a *qSH* wave in a CMP gather, or a shot record, from a single interface of weak anisotropy can be separated into a hyperbolic moveout and a residual moveout. The residual moveout is proportional to the amount of anisotropy in the medium concerned, and to the spread length of the acquisition geometry. These equations can aid the processing and interpretation of multi-component shear-wave VSP and reflection data in the presence of anisotropy.

CHAPTER THREE

VARIATION OF REFLECTION AND TRANSMISSION COEFFICIENTS WITH CRACK STRIKE AND CRACK DENSITY IN ANISOTROPIC MEDIA

ABSTRACT

The variation of amplitude with crack geometry when the crack strike changes with depth has not been reported previously. In this chapter, I derive expressions for reflection and transmission coefficients of plane split shear-waves at vertical incidence at an interface separating two cracked media with different crack strikes. I examine the effects on these coefficients as crack strike and crack density vary. For interfaces with large velocity-contrasts (relative velocity change more than 50%), the effects of crack strike varying with depth on reflected waves are negligible. However, for interfaces with small velocity-contrasts (relative change less than 20%) , the effects cannot be neglected. In such cases, both the differential amplitude of the reflected faster and slower split shear-waves, and the amplitude ratio of the two off-diagonal elements in the reflected data matrix after separation of split shear-waves, contain information about the variation of crack strike and density. In contrast, effects of crack strike changing with depth on transmitted waves are more sensitive regardless of the velocity-contrast and the degree of anisotropy.

3.1 INTRODUCTION

The previous chapter studied the velocity variations and moveouts of split

shear-waves in anisotropic media. This chapter examines the effects of crack orientation changing with depth on reflection and transmission coefficients of split shear-waves (see also Li and Crampin 1992c).

Recent observations show that the differential amplitudes between the faster and slower split shear-waves in reflection surveys contain information about lateral variations of crack density in cracked reservoirs. (Mueller 1991). However, the variation of amplitude with crack geometry when the crack strike changes with depth has not been investigated previously.

Recently, observations of changing shear-wave polarizations with depth, which have been interpreted as indicating changes in crack strike in the subsurface, have been reported in the literature (Squires *et al.* 1989; Winterstein and Meadows 1991b). Other evidence also suggests that crack orientations in near surface structures may differ from those at depth (Douma, Den Rooijen and Schoking 1989; Kerner, Dyer and Worthington 1989; Crampin 1990). Thus, it is necessary to understand the variation of shear-wave amplitude and crack geometry in media where crack strike changes with depth in order to interpret the variation of amplitudes in reflected shear-waves correctly.

Variations of shear-wave amplitudes are frequently associated with variations of shear-wave reflection and transmission coefficients. Keith and Crampin (1977) gave a general numerical approach to the reflection and transmission of plane waves at the planar boundary between two anisotropic media. Daley and Hron (1979) obtained analytical solutions to the problem in elliptically anisotropic media, although in practice elliptical anisotropy rarely exists. Thomsen (1988) studied the problem at an interface separating a transversely isotropic medium with vertical axis of symmetry (which I shall refer to as PTL-anisotropy, see Crampin 1989), and a medium with a horizontal axis of symmetry (such as the EDA-anisotropy of stress-aligned vertical cracks, Crampin 1989). Spencer and Chi (1991) discussed the

implications of Thomsen's equations for measuring the degree of shear-wave anisotropy from the ratio of reflectivities of the faster and slower split shear-waves. Here, I calculate the reflection and transmission coefficients of plane shear-waves at a planar interface separating two cracked (anisotropic) media with different crack strikes (see also Li and Crampin 1992c).

It is difficult to interpret the variation of shear-wave amplitudes with offset in terms of anisotropy, because of inherent difficulties such as the shear-wave window at the surface (Booth and Crampin 1985) and the variation of polarization angles (Liu, Crampin and Yardley 1990). Much of the basic information about anisotropy in the reservoir layer is held in reflections at near-vertical incidence (Yardley, Graham and Crampin 1991). Similarly, observations of shear-wave amplitude variations with crack strike and crack density are also frequently restricted to near-vertical incidence (Mueller 1991). For these reasons, I only consider the case of vertical incidence. I derive the expressions of reflection and transmission coefficients, present a range of reflection and transmission coefficients, and discuss their behaviour as velocity-contrast, crack strike, and crack density vary.

Note that vertical incidence allows us to use plane wave approximations. This is important as plane-wave modelling of offset data can lead to serious inconsistencies with curved wavefronts from point sources (Liu and Crampin 1990). Although the effects of crack variations on curved wavefronts are important, it is much more complicated, and is beyond the scope of this present preliminary examination.

3.2 NOTATION

The terminology for anisotropy is that given by Crampin (1989). As shown in Figure 3.1, I assume a planar interface separating two media with vertical cracks and different crack strikes. When a plane shear-wave is incident perpendicular to an interface, the shear-wave splits typically into two

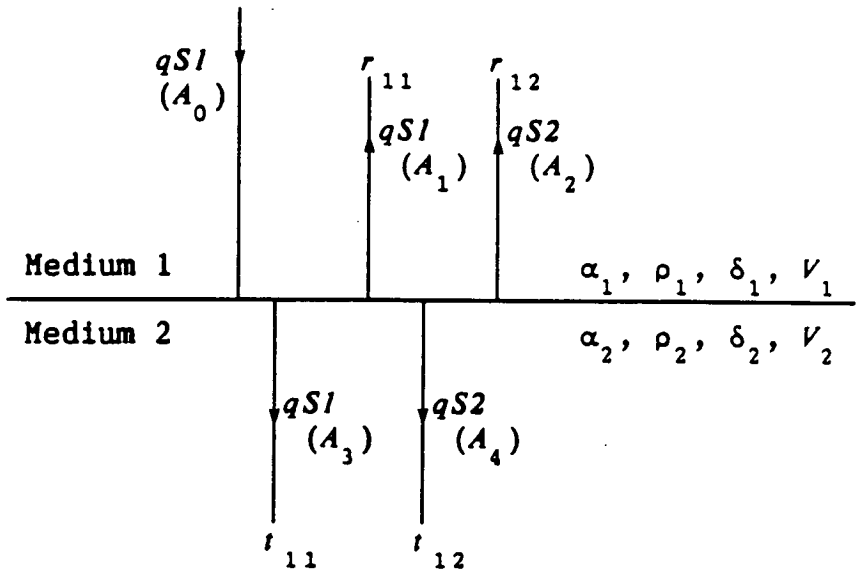

$$V_{11} = V_1$$
$$V_{21} = (1 - \delta_1/100)V_1$$
$$V_{12} = V_2$$
$$V_{22} = (1 - \delta_2/100)V_2$$
$$\Delta\alpha = \alpha_2 - \alpha_1$$

Figure 3.1. Diagram showing shear-wave reflection and transmission for a *qS1*-wave at vertical incidence at a single planar anisotropic/anisotropic interface. Notation as specified in text.

component phases, and faster and slower split shear-waves are both reflected and transmitted. I introduce the following notation, as illustrated in Figure 3.1.

qS1: faster split shear-wave, polarized parallel to the crack strike for nearly vertical propagation;

qS2: slower split shear-wave, polarized perpendicular to the crack strike for nearly vertical propagation;

A_0: amplitude of incident shear-wave, *qS1* or *qS2;*

A_1: amplitude of reflected *qS1*;

A_2: amplitude of reflected *qS2*;

A_3: amplitude of transmitted *qS1*;

A_4: amplitude of transmitted *qS2*;

r_{11}: reflection coefficient from *qS1* to *qS1*;

r_{12}: reflection coefficient from *qS1* to *qS2*;

r_{21}: reflection coefficient from *qS2* to *qS1*;

r_{22}: reflection coefficient from *qS2* to *qS2*;

t_{11}: transmission coefficient from *qS1* to *qS1*;

t_{12}: transmission coefficient from *qS1* to *qS2*;

t_{21}: transmission coefficient from *qS2* to *qS1*;

t_{22}: transmission coefficient from *qS2* to *qS2*;

V_1, V_2: shear-wave velocities of isotropic matrix of Medium 1 and 2, respectively;

V_{11}, V_{21}: velocity of *qS1* and *qS2*, respectively, in Medium 1;

V_{12}, V_{22}: velocity of *qS1* and *qS2*, respectively, in Medium 2;

α_1, α_2: crack strike of Medium 1 and 2, respectively;

δ_1, δ_2: percentage of differential shear-wave anisotropy in Medium 1 and 2, respectively;

$\Delta\alpha = \alpha_2 - \alpha_1$: difference in crack strike between Medium 1 and Medium 2;

ρ_1, ρ_2: density of Medium 1 and 2, respectively.

3.3 BASIC EQUATIONS

In vertical parallel cracks, the velocity of the faster split shear-wave, *qS1*, in the vertical direction equals the velocity of the uncracked formation (Crampin 1978, 1984b; Schoenberg and Douma 1988). I have:

$$\begin{aligned} V_{11} &= V_1; \\ V_{21} &= (1-\delta_1/100)V_1; \\ V_{12} &= V_2; \text{ and} \\ V_{22} &= (1-\delta_2/100)V_2. \end{aligned} \tag{3-1}$$

The percentage of differential shear-wave anisotropy, for thin cracks, is approximately equal to the crack density multiplied by 100 (Wild and Crampin 1991). With this approximation, I need not separate the concepts of crack density and degree of shear-wave anisotropy.

3.3.1 qS1 at vertical incidence

The four coefficients to be determined are r_{11}, r_{12}, t_{11}, and t_{12}, defined as:

$$\begin{aligned} r_{11} &= A_1/A_0; \\ r_{12} &= A_2/A_0; \\ t_{11} &= A_3/A_0; \text{ and} \\ t_{12} &= A_4/A_0; \end{aligned} \tag{3-2}$$

where A_0 is the amplitude of the incident faster split shear-wave. As shown in Appendix B, these coefficients can be written as:

$$r_{11} = \frac{1}{R_1}\left[\frac{(\rho_1 V_{11} - \rho_2 V_{12})}{(\rho_1 V_{21} + \rho_2 V_{12})}\cos^2\Delta\alpha + \frac{(\rho_1 V_{11} - \rho_2 V_{22})}{(\rho_1 V_{21} + \rho_2 V_{22})}\sin^2\Delta\alpha\right]; \tag{3-3}$$

$$r_{12} = -\frac{1}{R_1}\frac{\rho_1 V_{11}\ \rho_2(V_{12}-V_{22})}{(\rho_1 V_{21}+\rho_2 V_{12})(\rho_1 V_{21}+\rho_2 V_{22})}\ \sin 2\Delta\alpha; \tag{3-4}$$

$$t_{11} = \frac{1}{R_1}\frac{2\rho_1 V_{11}}{(\rho_1 V_{21}+\rho_2 V_{12})}\cos\Delta\alpha; \text{ and} \tag{3-5}$$

$$t_{12} = -\frac{1}{R_1}\frac{2\rho_1 V_{11}}{(\rho_1 V_{21}+\rho_2 V_{22})}\sin\Delta\alpha; \tag{3-6}$$

where

$$R_1 = \frac{(\rho_1 V_{11}+\rho_2 V_{12})}{(\rho_1 V_{21}+\rho_2 V_{12})}\cos^2\Delta\alpha + \frac{(\rho_1 V_{11}+\rho_2 V_{22})}{(\rho_1 V_{21}+\rho_2 V_{22})}\sin^2\Delta\alpha. \tag{3-7}$$

3.3.2 qS2 at vertical incidence

In this case, the four coefficients to be determined are r_{21}, r_{22}, t_{21}, and t_{22}, defined as:

$$\begin{aligned} r_{21} &= A_1/A_0; \\ r_{22} &= A_2/A_0; \\ t_{21} &= A_3/A_0; \text{ and} \\ t_{22} &= A_4/A_0; \end{aligned} \tag{3-8}$$

where A_0 is the amplitude of the incident slower split shear-waves. Again, as shown in Appendix B, these coefficients can be written as:

$$r_{22} = \frac{1}{R_2}\left[\frac{(\rho_1 V_{21}-\rho_2 V_{22})}{(\rho_1 V_{11}+\rho_2 V_{22})}\cos^2\Delta\alpha + \frac{(\rho_1 V_{21}-\rho_2 V_{12})}{(\rho_1 V_{11}+\rho_2 V_{12})}\sin^2\Delta\alpha\right]; \tag{3-9}$$

$$r_{21} = -\frac{1}{R_2}\frac{\rho_1 V_{21}\ \rho_2(V_{12}-V_{22})}{(\rho_1 V_{11}+\rho_2 V_{22})(\rho_1 V_{11}+\rho_2 V_{12})}\sin 2\Delta\alpha; \tag{3-10}$$

$$t_{21} = \frac{1}{R_2}\frac{2\rho_1 V_{21}}{(\rho_1 V_{11}+\rho_2 V_{12})}\sin\Delta\alpha; \text{ and} \tag{3-11}$$

$$t_{22} = \frac{1}{R_2}\frac{2\rho_1 V_{21}}{(\rho_1 V_{11}+\rho_2 V_{22})}\cos\Delta\alpha; \tag{3-12}$$

where

$$R_2 = \frac{(\rho_1 V_{21}+\rho_2 V_{22})}{(\rho_1 V_{11}+\rho_2 V_{22})}\cos^2\Delta\alpha + \frac{(\rho_1 V_{21}+\rho_2 V_{12})}{(\rho_1 V_{11}+\rho_2 V_{12})}\sin^2\Delta\alpha. \tag{3-13}$$

3.3.3 $\Delta\alpha = 0°$ and $\Delta\alpha = 90°$

$\Delta\alpha=0°$ and $\Delta\alpha=90°$ are two special cases that correspond to constant crack strike and an orthogonal change of crack strike with depth. In these two cases, the above equations can be simplified.

If $\Delta\alpha=0°$, I have:

$$\begin{aligned}
r_{11} &= (\rho_1 V_{11}-\rho_2 V_{12})/(\rho_1 V_{11}+\rho_2 V_{12});\\
r_{12} &= r_{21} = 0;\\
r_{22} &= (\rho_1 V_{21}-\rho_2 V_{22})/(\rho_1 V_{21}+\rho_2 V_{22});\\
t_{11} &= 2\rho_1 V_{11}/(\rho_1 V_{11}+\rho_2 V_{12});\\
t_{12} &= t_{21} = 0; \text{ and}\\
t_{22} &= 2\rho_1 V_{21}/(\rho_1 V_{21}+\rho_2 V_{22}).
\end{aligned} \tag{3-14}$$

These equations show that in a reflection survey, when a shear-wave

source is parallel or perpendicular to the crack strike in media with no change of crack orientation, the off-diagonal elements in the data matrix of a four-component survey (two orthogonally-polarized sources recorded by two orthogonally-polarized receivers) will be zero. This forms the basis of the technique of the Alford rotation (Alford 1986b) for processing shear-wave reflection data in the presence of anisotropy, where the sources and receivers are synchronously rotated to maximize the diagonal elements (r_{11} and r_{22}), or minimize the off-diagonal elements (r_{12} and r_{21}) in the data matrix. These equations also show that r_{11} and t_{11} are only dependent on the velocities of the faster shear-waves, and r_{22} and t_{22} are only dependent on the velocities of the slower shear-waves. Thus, the variation of percentage shear-wave anisotropy (or crack density) will only affect the variation of r_{22} and t_{22}, or the amplitudes of the slower split shear-waves.

If $\Delta\alpha = 90°$, I have:

$$
\begin{aligned}
r_{11} &= (\rho_1 V_{11} - \rho_2 V_{22})/(\rho_1 V_{11} + \rho_2 V_{22});\\
r_{12} &= r_{21} = 0;\\
r_{22} &= (\rho_1 V_{21} - \rho_2 V_{12})/(\rho_1 V_{21} + \rho_2 V_{12});\\
t_{11} &= t_{22} = 0;\\
t_{12} &= -2\rho_1 V_{11}/(\rho_1 V_{11} + \rho_2 V_{22}); \text{ and}\\
t_{21} &= 2\rho_1 V_{21}/(\rho_1 V_{21} + \rho_2 V_{12}).
\end{aligned}
\tag{3-15}
$$

This implies that after transmission, the incident faster or slower wave becomes the slower or faster wave in the lower medium. Thus, there will be a trend of decreasing time delay between the faster and slower shear-waves after transmission. This can be thought of as a negative time delay. Based on these assumptions, several authors (Squires *et al.* 1989; Davis and Lewis 1990) have interpreted negative time delays of split shear-waves as implying an orthogonal change in crack orientation. However, orthogonal changes of crack strike are not the only cause of negative time delays between split shear-waves; split shear-waves propagating either side of a shear-wave singularity may also

result in negative time delays (Crampin 1991). Since Wild and Crampin (1991) have suggested that singularities are common features of sedimentary basins, singularities may well be a common cause of orthogonal changes in shear-wave polarities. The expression for t_{12} shows that there is a 180° phase shift in the transmitted waves, whenever there is a 90° change of crack strike in the subsurface. Note also that:

$$(\rho_1 V_{11}-\rho_2 V_{22})/(\rho_1 V_{11}+\rho_2 V_{22}) > (\rho_1 V_{11}-\rho_2 V_{12})/(\rho_1 V_{11}+\rho_2 V_{12}); \text{ and}$$
$$(\rho_1 V_{21}-\rho_2 V_{12})/(\rho_1 V_{21}+\rho_2 V_{12}) < (\rho_1 V_{21}-\rho_2 V_{22})/(\rho_1 V_{21}+\rho_2 V_{22}); \qquad (3\text{-}16)$$

which imply that there will be larger differences in amplitudes between the reflected faster and slower split shear-waves for 90° changes of crack strike than for no change. Thus, observations of negative time delays together with larger differential amplitudes between faster and slower split shear-waves would confirm the interpretation of 90° change of crack strike in the subsurface. The r_{12} and r_{21} still remain zero, and the conditions required by the Alford rotation (Alford 1986b) are still satisfied.

3.4 BEHAVIOUR OF REFLECTION COEFFICIENTS

In the general case, where $\Delta\alpha \neq 0°$ and $\neq 90°$, I plot the amplitude coefficients against angle $\Delta\alpha$ (the difference in crack strike). These coefficients are also dependent on the density, the velocity, and the degree of shear-wave anisotropy, or crack density in the media concerned. To simplify the results, while still retaining generality, I consider models with the following parameters.

For convenience, I only consider the case where a shear-wave is incident from a low-velocity medium onto a high-velocity medium (low/high incidence case). In addition, since the percentage variation of rock density with depth is usually small, I assume that the density of Medium 1 is the same as the density of Medium 2.

Under these conditions I examine three cases. Firstly, I vary V_1 and V_2, and fix δ_1 and δ_2 as shown in Figures 3.2a and 3.2b. In Figure 3.2a, V_1 varies from 1.5km/s to 3.0km/s, and V_2 = 5.0km/s, so that the velocity-contrast decreases as V_1 increases. In Figure 3.2b, V_1 = 1.5km/s, and V_2 varies from 2.0km/s to 5.0km/s, so that the velocity-contrast increases as V_2 increases. In both Figures 3.2a and 3.2b, δ_1 = 2%, and δ_2 = 10%.

Secondly, I vary δ_1 and fix δ_2 but use two different velocity-contrasts, as shown in Figures 3.3a and 3.3b. Figure 3.3a shows the effects of a small velocity-contrast where V_1 = 1.5km/s and V_2 = 1.8km/s [relative velocity change: $\Delta V = |V_1-V_2|/V_2 < 20\%$], whereas Figure 3.3b has a large velocity-contrast where V_1 = 1.5km/s and V_2 = 3.0km/s (relative velocity change: ΔV = 50%). In both Figures 3.3a and 3.3b, δ_2 = 10%.

In the third case, I vary δ_2 and fix δ_1 and use the same velocities as those in Figures 3.3a and 3.3b. Figure 3.4a shows the effects of a small velocity-contrast ($\Delta V<20\%$), and Figure 3.4b shows a large velocity-contrast ($\Delta V=50\%$). δ_1 is fixed as 2% in both Figures 3.4a and 3.4b. In all three figures, crack strike difference $\Delta\alpha$ varies from 0° to 90°. The features in these figures can be summarized as follows.

3.4.1 Velocity-contrast

As shown in Figure 3.2, the variation in velocity-contrast affects r_{11} and r_{22} more than it does r_{12} and r_{21}. In Figure 3.2a, as V_1 varies from 1.5km/s to 3.0km/s (ΔV from 70% to 40%), values of r_{11} at $\Delta\alpha=0°$ decrease from 0.54 to 0.25, and those of r_{22} decrease from 0.51 to 0.22. Similar variations of r_{11} and r_{22} with velocity-contrast can be seen in Figure 3.2b. In contrast, both in Figures 3.2a and 3.2b, the four curves of r_{12} and r_{21}, corresponding to four different velocity-contrasts, are close to each other, and variation with velocity-contrast is small. r_{11} and r_{22} are an order of magnitude larger than

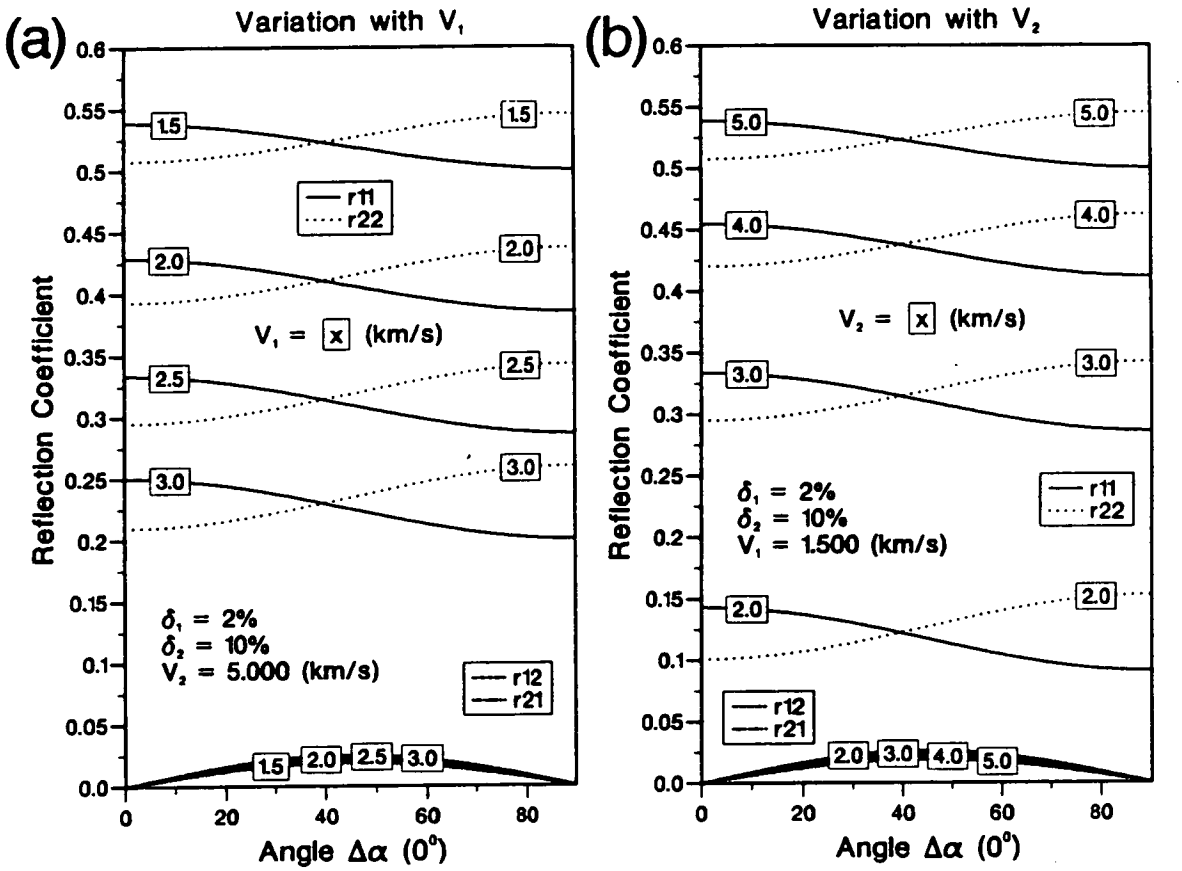

Figure 3.2. Reflection coefficients plotted against the difference in crack strike, $\Delta\alpha$, for different velocity-contrasts. (a) Variation for different values of V_1, where δ_1, δ_2, and V_2 are fixed; (b) variation for different values of V_2, where δ_1, δ_2, and V_1 are fixed.

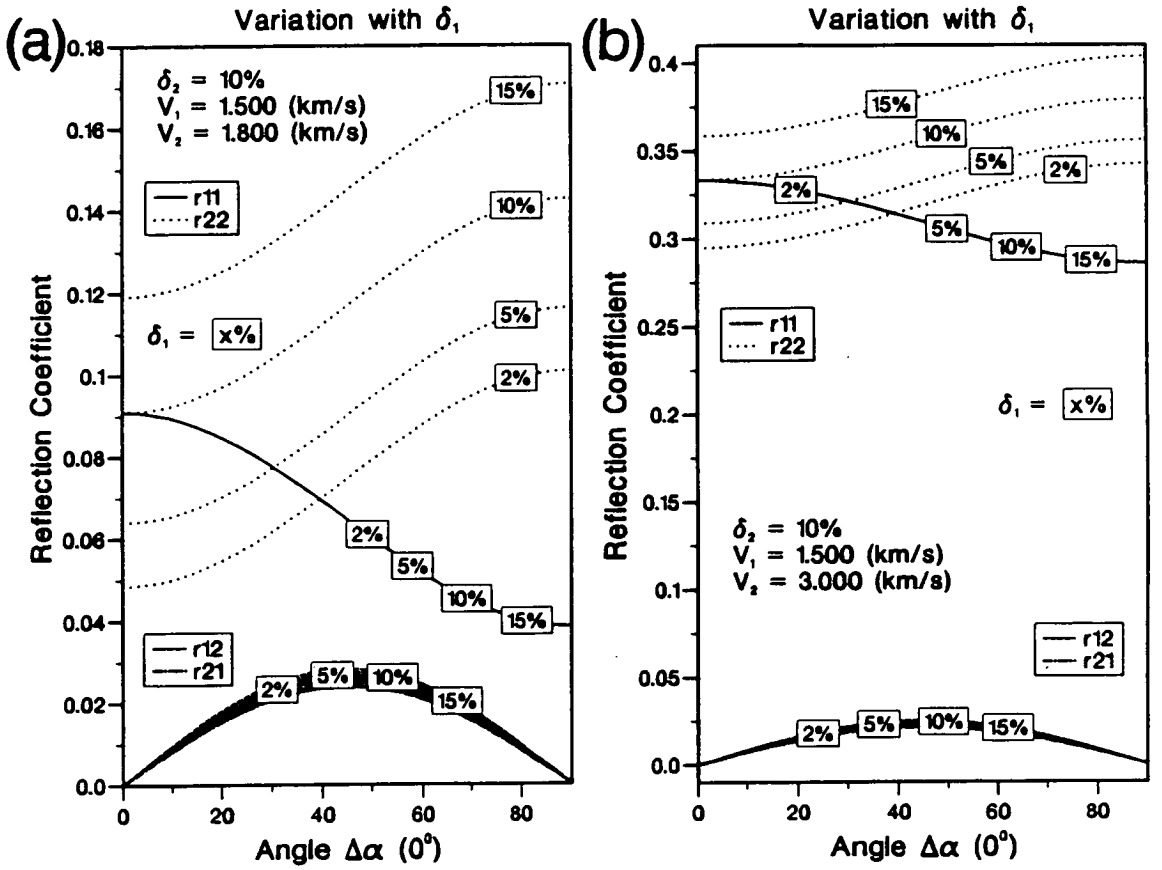

Figure 3.3. Reflection coefficients plotted against difference in crack strike, $\Delta\alpha$, as the degree of anisotropy in Medium 1, δ_1, varies, where the degree of anisotropy in Medium 2, δ_2, is fixed. (a) Small velocity-contrast: V_1=1.5km/s, V_2=1.8km/s; (b) large velocity-contrast: V_1=1.5km/s, V_2=3.0km/s.

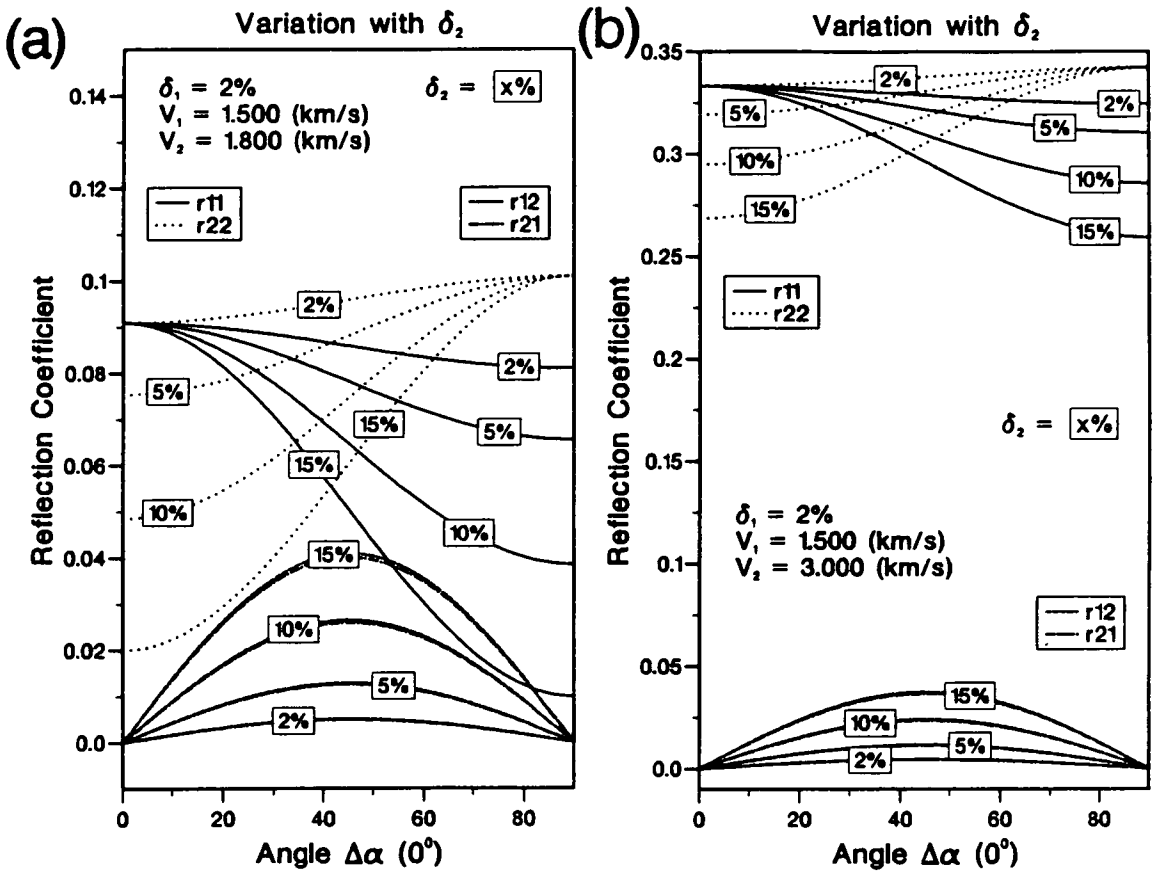

Figure 3.4. As in Figure 3.3, but for the variation of the degree of anisotropy in Medium 2, δ_2, where the degree of anisotropy in Medium 1, δ_1, is fixed. (a) Small velocity-contrast; and (b) large velocity-contrast, as in Figure 3.3.

r_{12} and r_{21}, particularly when the velocity-contrast is greater than 30%. The maximum value of r_{12} and r_{21} is only about 0.02 in Figures 3.2a and 3.2b, while the minimum value of r_{11} and r_{22} is about 0.2 in Figure 3.2a. The difference between r_{11} and r_{22} for a given $\Delta\alpha$ does not change very much as velocity-contrast changes.

3.4.2 Degree of differential shear-wave anisotropy

For a given velocity-contrast, r_{11} is independent of the degree of differential shear-wave anisotropy in medium 1 (δ_1), as shown Figure 3.3. The four curves of r_{11} in Figure 3.3, corresponding to four different values of δ_1, overlap each other. But r_{22} increases as δ_1 increases. In general, this will reduce the difference between r_{11} and r_{22} at $\Delta\alpha=0°$, but will increase the difference at $\Delta\alpha=90°$, as shown Figure 3.3. The change in δ_1 has negligible affect on r_{12} and r_{21}.

All the curves will be affected by change of anisotropy in medium 2, δ_2, as shown Figure 3.4. In general, as δ_2 increases, r_{11} and r_{22} decrease, and r_{12} and r_{21} increase. Thus differences between r_{11} and r_{12}, between r_{22} and r_{21} decrease, whereas the difference between r_{11} and r_{22} generally increases.

3.4.3 Difference in crack strike

As the difference between the crack strikes, $\Delta\alpha$, changes, all variations will be affected. Figures 3.2, 3.3, and 3.4 show that as $\Delta\alpha$ changes from 0° to 90°, r_{11} decreases, but r_{22} increases, and that the differential amplitude between r_{11} and r_{22} has different patterns of behaviour according to the values of δ_1 and δ_2. If $\delta_1=\delta_2$, the difference between r_{11} and r_{22} is zero at $\Delta\alpha=0°$, and monotonically increases as $\Delta\alpha$ increases, as shown by the curves for r_{11} and r_{22} corresponding to $\delta_1=10\%$ in Figure 3.3, and by curves corresponding to $\delta_2=2\%$ in Figure 3.4. If $\delta_1>\delta_2$, the difference of r_{11} and r_{22} monotonically increases as $\Delta\alpha$ increases, as shown by curves corresponding

to $\delta_1=15\%$ in Figure 3.3. If $\delta_1<\delta_2$, the difference first decreases as $\Delta\alpha$ increases until a critical angle at which $r_{11}=r_{22}$, then the difference increases as $\Delta\alpha$ passes the critical angle. If the velocity-contrast is large ($\Delta V>50\%$) and δ_2 is small (less than 5%), as shown in Figure 3.3, the variations of the coefficients with angle $\Delta\alpha$ are relatively small. Thus, the variation of crack strike with depth can be ignored in such cases.

As $\Delta\alpha$ changes, r_{12} and r_{21} first increase until $\Delta\alpha=45°$, then decrease as $\Delta\alpha$ exceeds 45°. Generally, $r_{12} \neq r_{21}$, if $\Delta\alpha\neq 0°$ and $\neq 90°$; the difference between r_{12} and r_{21} for a given velocity-contrast and given anisotropic parameters is small, as shown in Figures 3.2, 3.3 and 3.4, but not zero.

From equations (3-4) and (3-10), I obtain:

$$r_{21}/r_{12} = V_{21}/V_{11} = 1 - \delta_1, \text{ if } \Delta\alpha\neq 0 \text{ and } \neq 90°; \qquad (3\text{-}17)$$

where the ratio of r_{21} to r_{12} is related to the degree of differential shear-wave anisotropy in the upper medium of an interface.

In a four component shear-wave survey, r_{11} and r_{22} can be considered as the diagonal elements, and r_{12} and r_{21} as the off-diagonal elements in the data matrix after split shear-waves have been separated. [The separation is often made by rotating the intrumental axes into the natural coordinate system of the upper medium.] In the studies of anisotropy in reflection surveys reported so far (Alford 1986b; Thomsen 1988; Squires *et al.* 1989), such off-diagonal elements were ignored and treated as random noise. But equation (3-17) shows that, when crack strike changes with depth, it is possible to detect anisotropy by analyzing amplitudes of the off-diagonal elements after separation of split shear-waves.

3.5 BEHAVIOUR OF TRANSMISSION COEFFICIENTS

Similar discussions to those for reflection coefficients also apply to transmission coefficients. Figures 3.5, 3.6 and 3.7 show the corresponding results for the transmission coefficients to Figures 3.2, 3.3 and 3.4. The features can be summarized as follows.

3.5.1 Velocity-contrast

Figure 3.5 shows the variation of transmission coefficients with velocity-contrast; Figure 3.5a shows the variation with V_1, where δ_1, δ_2, and V_2 are fixed as 2%, 10% and 5.0km/s, respectively, and V_1 is chosen as 1.5, 2.0 and 3.0km/s; Figure 3.5b shows the variation with V_2, where δ_1, δ_2 and V_1 are fixed as 2%, 10% and 1.5km/s, and V_2 is chosen as 2.0, 3.0 and 5.0km/s. In Figure 3.5a, as V_1 varies from 1.5 to 3.0km/s, the velocity-contrast decreases, hence, the transmission coefficient at a given $\Delta\alpha$ increases; in Figure 3.5b, as V_2 varies from 2.0 to 5.0km/s, the velocity-contrast increases, and the transmission coefficient at a given $\Delta\alpha$ decreases.

3.5.2 Degree of shear-wave anisotropy

Figures 3.6 and 3.7 show the variation of transmission coefficients with percentage differential shear-wave anisotropy in the media. Figure 3.6 shows the variation with δ_1, where δ_2 is fixed as 15%, and V_1 and V_2 are 1.5 and 3.0km/s in 3.6a (high velocity-contrast: ΔV=50%) and are 1.5 and 5.0km/s in 3.6b (very large velocity-contrast: ΔV=70%). Figure 3.7 shows the variation with δ_2, where δ_1 is fixed as 2%, and V_1 and V_2 are the same as Figure 3.6. It can be seen that the value of t_{11} (solid lines) is independent of both δ_1 and δ_2 (Figures 3.6 and 3.7). This is because the faster shear-wave is only slightly affected by the cracks. Also Figure 3.6 shows that t_{12} (broken lines) is independent of δ_1, and Figure 3.7 shows that t_{21} (dotted-broken lines) is

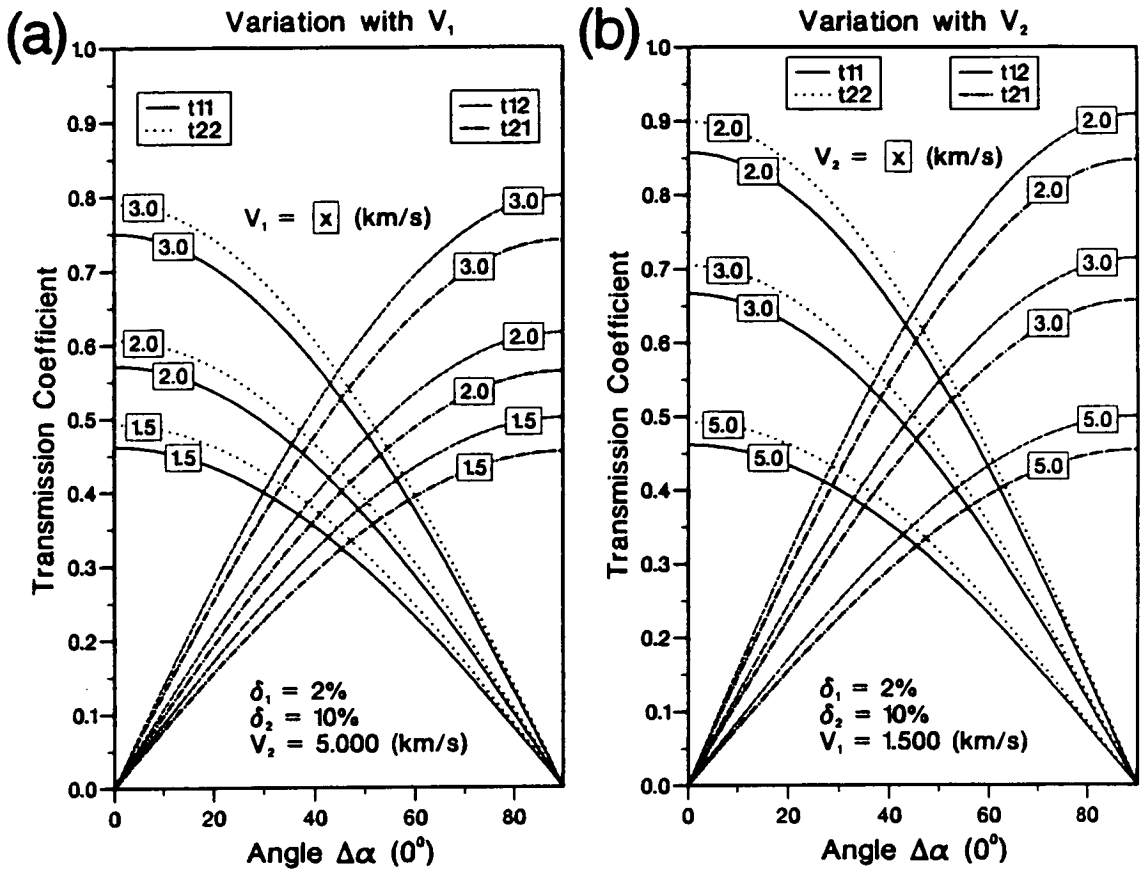

Figure 3.5. Transmission coefficients plotted against difference in crack strike, $\Delta\alpha$, for different velocity-contrasts. (a) Variation for different values of of V_1, where δ_1, δ_2, and V_2 are fixed; (b) variation for different values of V_2, where δ_1, δ_2, and V_1 are fixed.

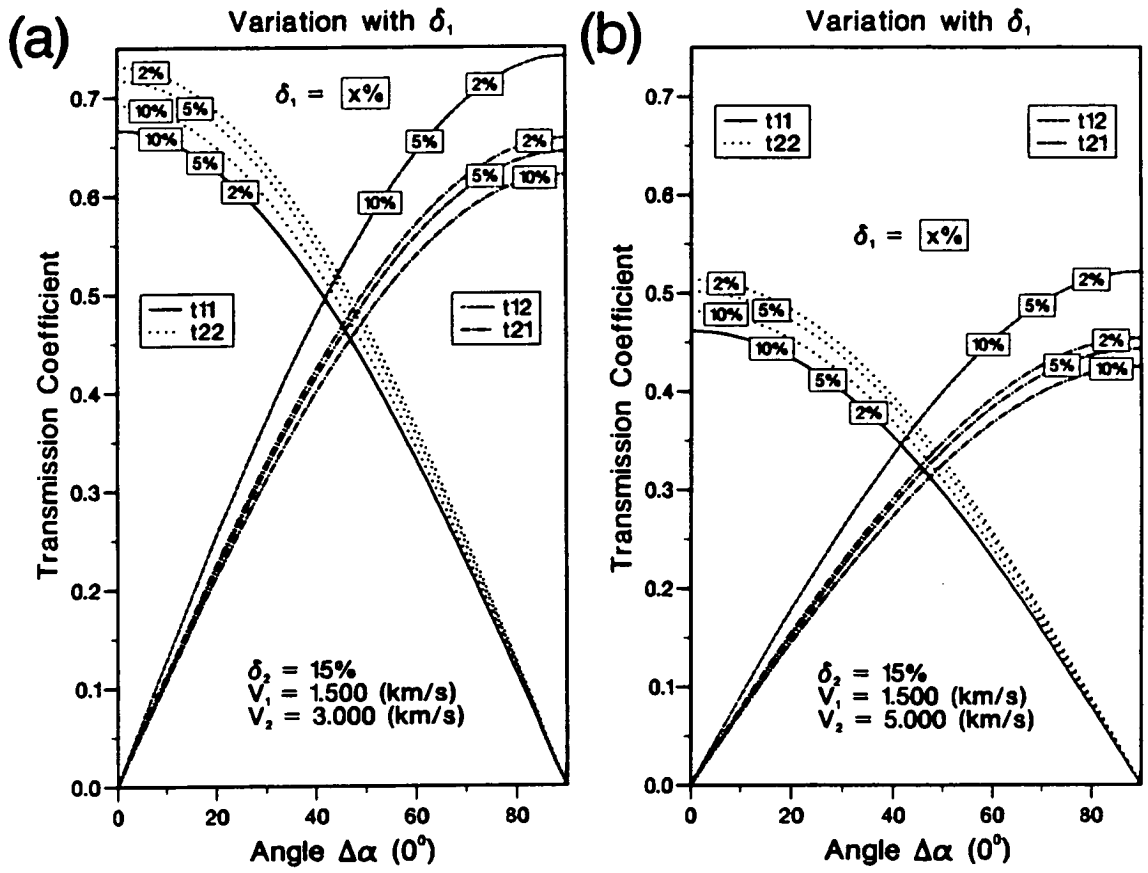

Figure 3.6. Transmission coefficients plotted against difference in crack strike, $\Delta\alpha$, for different degrees of anisotropy in Medium 1, δ_1, where the degree of anisotropy in Medium 2, δ_2, is fixed. (a) Large velocity-contrast: V_1=1.5km/s, V_2=3.0km/s; (b) very large velocity-contrast: V_1=1.5km/s, V_2=5.0km/s.

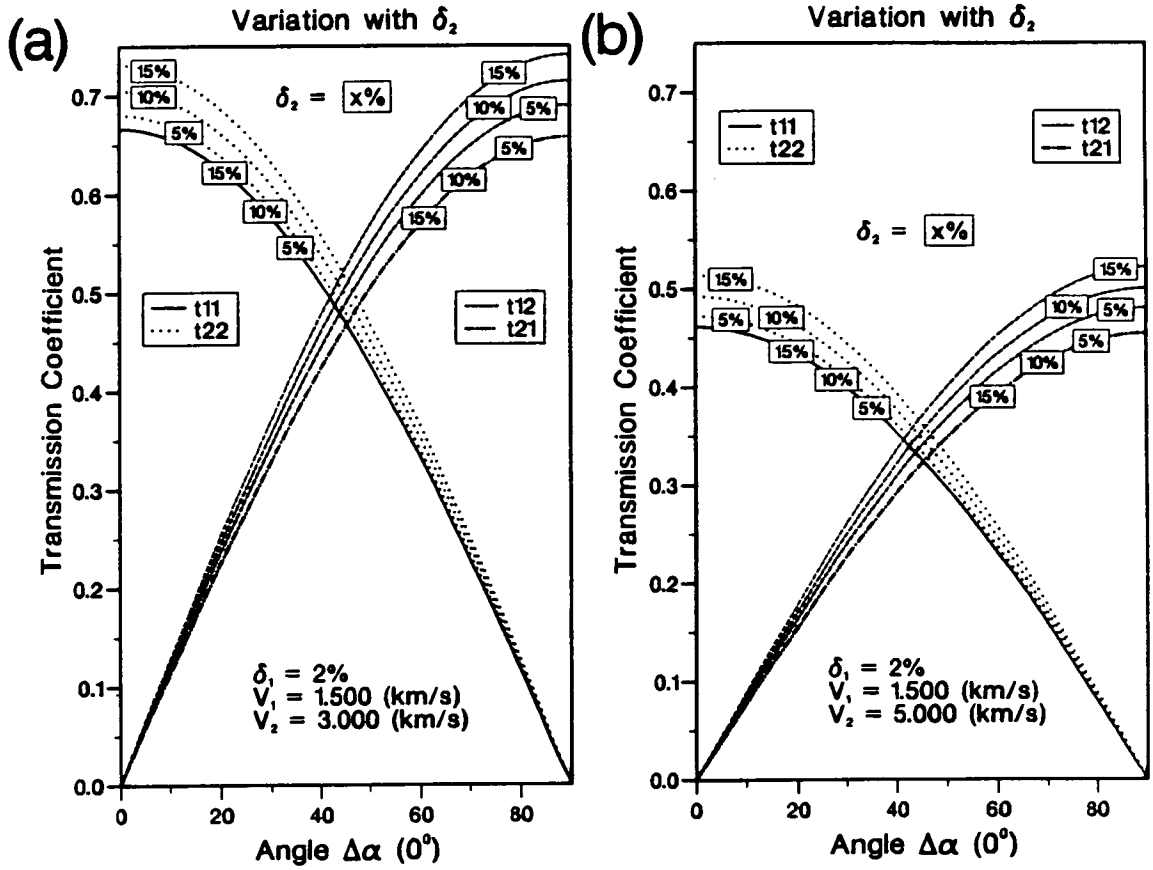

Figure 3.7. As in Figure 3.6, but for different degrees of anisotropy in Medium 2, δ_2, where the degree of anisotropy in Medium 1, δ_1, is fixed. (a) Large velocity-contrast, and (b) very large velocity-contrast, as in Figure 3.6

independent of δ_2. Both t_{22} (dotted lines) and t_{21} (dotted-broken lines) decrease as δ_1 increases (Figure 3.6), but increase as δ_2 increases (Figure 3.7).

3.5.3 Crack strike difference

Figures 3.5, 3.6 and 3.7 show that as $\Delta\alpha$ varies from 0° to 90°, t_{11} and t_{22} decrease from their maximum values to zero, but t_{12} and t_{21} increase from zero to their maximum values. There is also an amplitude difference between the transmitted faster and slower shear-waves. At $\Delta\alpha=0°$, t_{11} and t_{22} have maximum difference, and this difference gradually decreases as $\Delta\alpha$ increases. Compared with values of t_{11} and t_{22} themselves, this difference is relatively small, even when the velocity-contrast is very large ($\Delta V>70\%$) as in Figures 3.6b and 3.7b. For this reason, the differential amplitude between the transmitted faster and slower shear-waves is difficult to observe.

Figures 3.5, 3.6 and 3.7 also show that the transmission coefficients are more sensitive to the variation of the difference in crack strike than the reflection coefficients. If the crack strike difference $\Delta\alpha$ exceeds 20°, there will be significant energy in components t_{12} and t_{21} whose presence is diagnostic of the variation of crack strike with depth. Thus, analyzing amplitudes of transmitted split shear-waves in VSPs or crosshole surveys is likely to be a more reliable way for detecting variation of crack strike with depth than analyzing amplitudes of reflected shear-waves.

3.6 DISCUSSION AND CONCLUSIONS

I have shown that in addition to the polarization and time delay of split shear-waves, there are two other features which contain information about the variation of crack strike and crack density in shear-wave reflections when the velocity increases with depth. These are the differential amplitude between the faster and slower split shear-waves, and the presence of off-diagonal energy of

r_{21} and r_{12} in the data matrix after separation of split shear-waves. However, if the velocity-contrast of an interface is large (relative velocity change $\Delta V >$ 50%), the two features will not be very significant, compared with the diagonal energy in the data matrix after rotation, and may be considered as negligible. This suggests that if the velocity-contrast is large (more than 50%), the variation of crack strike with depth, and the difference between the faster and slower principal time series can be neglected. This is important for processing shear-wave data in the presence of anisotropy, because these two assumptions are used by most of the techniques for analyzing shear-wave splitting in multi-component shear-wave data (MacBeth and Crampin 1990).

However, if the velocity-contrast is small (relative change $\Delta V <$ 20%), these two features are significant and can be observed. In such cases, the current rotation techniques for studying anisotropy in multi-component shear-wave data may not be valid because their assumptions cannot be justified. Without taking into account the difference between r_{11} and r_{22} and the presence of r_{12} and r_{21}, rotation techniques will yield false results about anisotropy as demonstrated by MacBeth and Yardley (1991), although proper techniques can be developed based on these reflection coefficients (MacBeth, Li, Crampin and Mueller, 1992). Also I have shown that in such cases the ratio of r_{12} and r_{21} may give a good estimation of anisotropy in the upper layer of a reflection interface.

In contrast, the transmission coefficients are more sensitive to variations of crack strike regardless of the velocity-contrast. If the difference in crack strike between the upper and lower medium of an interface exceeds 20°, considerable energy will be converted to off-diagonal elements t_{12} and t_{21}. This suggests that variation of crack strike with depth can be more easily detected in transmitted shear-waves recorded in VSPs or crosshole surveys than in reflection surveys.

Moreover, transmission coefficients are generally larger than reflection

coefficients for a given configuration of layer parameters. In other words, most energy will transmit through interfaces except when the velocity-contrast is very large (more than 70%). This is similar to wave propagation in layered isotropic media. As a result, the difference between t_{11} and t_{22} is a relatively small percentage of their value, and the differential amplitude between the transmitted faster and slower split shear-waves is difficult to detect.

In summary, in order to evaluate shear-wave amplitude variations with crack strike and crack density, I have derived expressions for calculating plane shear-wave reflection and transmission coefficients at vertical incidence at an interface separating two cracked (anisotropic) media with different crack strikes. For an interface with high velocity-contrast (more than 50%), the crack-geometry information contained in the variation of reflection amplitude can barely be detected, and the effects of crack strike varying with depth can be neglected in processing shear-wave data in the presence of anisotropy. But for an interface with low velocity-contrast (less than 20%), such effects cannot be neglected in data processing. In such cases, analyzing the amplitude of the off-diagonal elements in the data matrix, after instrumental axes have been rotated to the natural coordinate system of the medium concerned, may be useful for extracting anisotropic information. In contrast, effects of crack strike changing with depth on transmitted waves are more sensitive, regardless of the velocity-contrast and the degree of anisotropy.

CHAPTER FOUR

COMPLEX COMPONENT ANALYSIS OF SHEAR-WAVE SPLITTING: THEORY

ABSTRACT

This chapter investigates the use of colour displays of seismic attributes for analyzing shear-wave splitting in multi-component seismic data. The horizontal components of a multi-component seismic survey can be directly taken as the real and imaginary parts of a complex component. This transforms multi-component data from conventional Cartesian coordinates to polar coordinates, and allows the calculation of instantaneous amplitude and instantaneous polarization. The technique is called complex component analysis. Wave motion can be represented by instantaneous attributes which show distinct features characteristic of the type of wave motion. Examination of monochrome and colour displays of these attributes can provide important quantitative information about the polarization and time delay of split shear-waves in multi-component VSPs and reflection surveys.

4.1 INTRODUCTION

In the past, analysis of shear-wave splitting has relied principally on the detailed visual examination of individual polarization diagrams (hodograms). Although it is reliable and straightforward for identifying shear-wave splitting in multi-component earthquake and VSP data, polarization analysis is less useful when attempting to analyse shear-wave splitting in large datasets from multi-component reflection surveys. In this chapter, I present a technique (Li

and Crampin 1990b, 1990d, 1991c, 1991d), which is called *complex component analysis*, to analyze shear-wave splitting in multi-component reflection and VSP surveys.

René *et al.* (1986) extended complex trace analysis (Taner and Sheriff 1977; Taner *et al.* 1979) to multi-component data. They defined the complex multi-component trace with real orthogonal components and imaginary (quadrature) components derived by application of the Hilbert transform to the corresponding real components. They then defined several polarization attributes including phase difference, reciprocal ellipticity and tilt angle. They applied the technique to multi-component walkaway seismic data to characterize ambient noise and source-generated waves.

Here, I directly define the two horizontal components of multi-component reflection and VSP surveys as the real and imaginary parts of a complex component. This transforms multi-component data from conventional Cartesian coordinates to polar coordinates, and allows the calculation of instantaneous amplitude and instantaneous polarization. These quantities, referred to as seismic attributes (following Taner *et al.* 1979), can be presented in conventional seismic time-versus-offset displays in which colour is used to quantify the polarizations of the shear-waves.

Three major applications of such complex component analysis can be envisaged:

1) Anisotropic interpretation. Attributes can assist in the rapid recognition and identification of shear-wave splitting in seismic sections, and in extracting shear-wave polarizations and delays from seismic data for interpretation in terms of the crack- and stress-geometry throughout the reservoir.

2) Stratigraphic interpretation. Seismic attributes provide further information about the location and analysis of faults, discontinuities, unconformities, and

other geological features, as demonstrated by Taner *et al.* (1979).

3) Hydrocarbon determination. Attributes can assist in identifying lateral variations of shear-wave polarizations, which may often be associated with lateral variations of fracture orientation and intensity, and preferential permeability. These features are directly associated with hydrocarbon accumulations in oriented cracks and fractures.

This chapter presents the theory of complex component analysis of shear-wave splitting, and demonstrates the significance of instantaneous attributes in identifying and evaluating shear-wave splitting. The application of the technique to field data is presented in Chapter Five.

4.2 CALCULATION AND SIGNIFICANCE OF A COMPLEX COMPONENT

4.2.1 Definitions

I assume a multi-component shear-wave dataset with the horizontal inline $x(t)$ and crossline $y(t)$ recording geometry shown in Figure 4.1. The horizontal displacement of a shear-wave (or, any seismic wave), with vector displacement Pt, amplitude $A(t)$ and angle to the inline direction $\theta(t)$, can be written as:

$$x(t) = A(t)\cos\theta(t); \text{ and} \tag{4-1}$$

$$y(t) = A(t)\sin\theta(t). \tag{4-2}$$

Thus, $x(t)$ and $y(t)$ can be considered as the real and imaginary parts of a complex signal $z(t) = x(t) + iy(t)$, where i is the square root of -1. In this way, the method of complex trace analysis of single component data (Taner and Sheriff 1977; Taner *et al.* 1979) can be extended to multi-component data without using the Hilbert transforms (René *et al.* 1986). Solving for A and θ for any x and y gives:

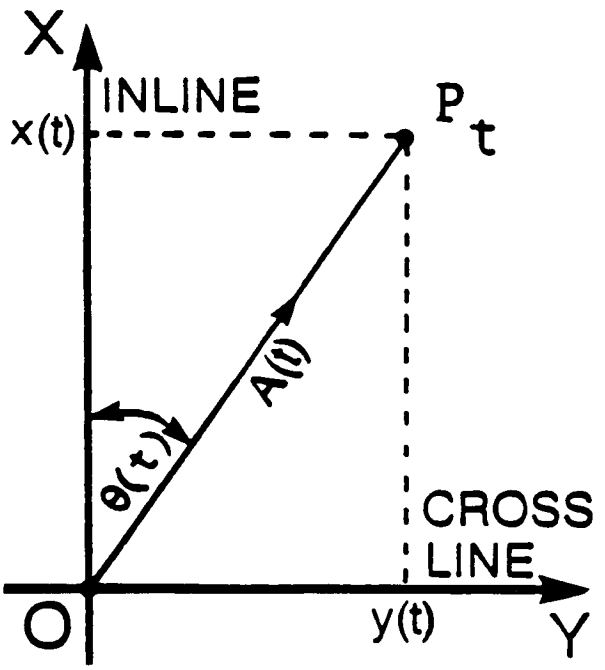

Figure 4.1. Diagram showing the coordinate system for complex component analysis. *P*t is the horizontal displacement of a shear-wave at time *t* with amplitude $A(t)$ and angle $\theta(t)$ to the inline direction, and $x(t)$ and $y(t)$ are the coordinates of the two horizontal components in a Cartesian coordinate system.

$$A(t) = [x^2(t) + y^2(t)]^{1/2} = |z(t)|; \text{ and} \tag{4-3}$$

$$\theta(t) = \arctan[y(t)/x(t)], \text{ defined for } \pm 180°; \tag{4-4}$$

where $A(t)$ is the *instantaneous amplitude*; and $\theta(t)$ is the *instantaneous polarization*.

4.2.2 Physical significance

In addition to the attributes described above, the wavetrain also contains information about instantaneous frequency, apparent polarity, energy distribution, and waveform, which can also be extracted from complex components (Taner *et al.* 1979; Huang 1989). Each piece of information has a particular significance and application in exploration seismology, and in reservoir characterization and development. Here, I shall only discuss instantaneous amplitude and instantaneous polarization.

Instantaneous amplitude.—The instantaneous amplitude in equation (4-3) is a measure of the distance between the moving particle and its equilibrium position. Instantaneous amplitude may have its maximum at points other than at peaks or troughs of the two individual horizontal components. Local maxima of instantaneous amplitude indicate the largest distance of the particle from its equilibrium position, and may help in identifying the onset of the shear-wave signal.

Instantaneous polarization.—The instantaneous polarization in equation (4-4) is a measure of the polarization direction of the moving particle relative to the polarization direction of the source. Since the polarization is independent of amplitude, it may give clear particle motion directions even for weak arrivals as long as they are coherent signals.

The variation of the instantaneous polarization of recorded split shear-waves represents the variation of the direction of the particle motion of the split shear-waves. The first arrival of the split shear-waves is polarized in a direction fixed by the raypath through the anisotropic rock (Crampin 1981), so that the instantaneous polarization tends to remain constant until the arrival of the slower split shear-wave. Thus the polarization display, and associated amplitude display, can help to identify and quantify shear-wave splitting in both seismic reflection and VSP datasets.

4.2.3 Represention of wave motion

Figures 4.2(a) and 4.2(b) show the seismograms and instantaneous amplitude and polarization attributes of eight typical wave motions: linear, elliptical, and shear-wave splitting with six different time delays. Figure 4.3 shows corresponding polarization diagrams (hodograms) of the particle motion. Since any shear-wave motion in the horizontal plane can be considered as either linearly, or elliptically polarized (or some combination thereof in shear-wave splitting), I first discuss these two characteristic types of wave motion.

Linear wave motion.— WM1 in Figures 4.2 and 4.3 show typical linear motion, that can be written as:

$$y(t) = x(t) \tan \alpha; \tag{4-5}$$

where $x(t)$ and $y(t)$ are the displacements in the x and y directions, respectively; α is the angle the polarization makes with the inline direction. In Figure 4.2, α is chosen as 160° measured from the initial polarization direction to the inline direction:

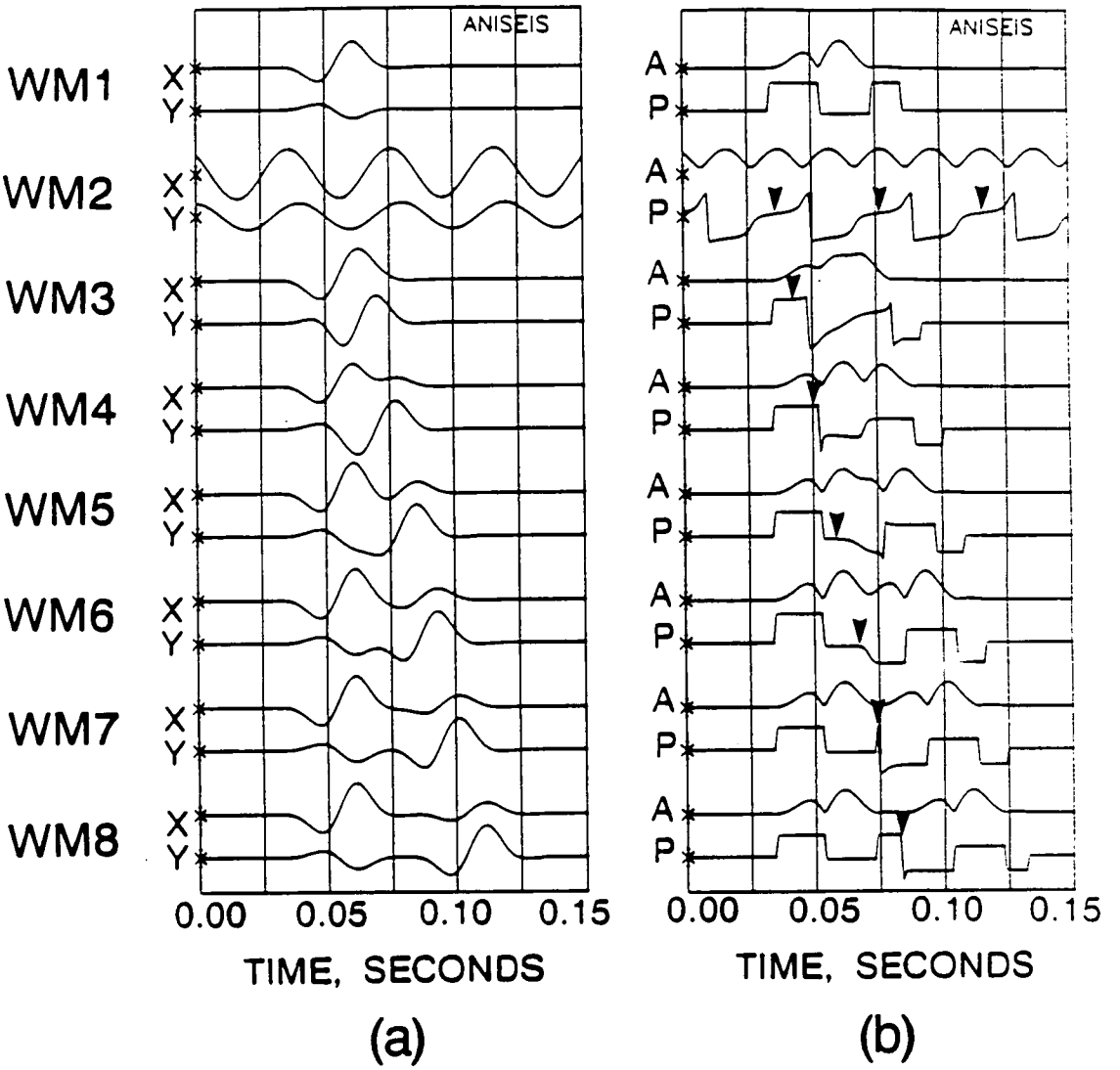

Figure 4.2. Seismograms and instantaneous attributes of eight typical wave motions, WM1 is linear motion, WM2 is elliptical, and WM3 to WM8 show shear-wave splitting with time delays increasing from 8 ms (WM3) to 48 ms (WM8) for a 40 Hz signal. (a) Horizontal component seismograms, *X* in-line and *Y* cross-line; (b) displays of instantaneous amplitude (A) and polarization (P). Arrows on WM2 mark the position of the effective polarization angle, and arrows on WM3 to WM8 mark the points where the polarization changes direction at the onset of the second split shear-wave arrival.

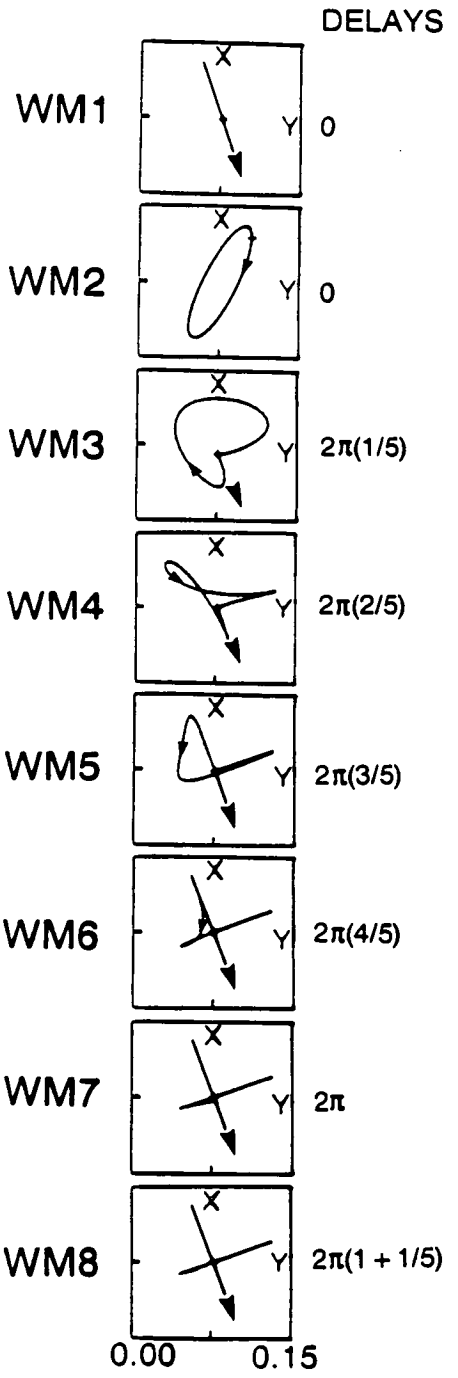

Figure 4.3. Polarization diagrams of the eight typical wave motions in Figure 4.2. The small arrows mark the direction of motion, and the large arrows mark the initial polarization directions.

$$\theta(t) = \begin{cases} \alpha = 160°, & x(t) < 0; \\ 0, & x(t) = 0; \\ \alpha - \pi = 160° - 180° = -20°, & x(t) > 0. \end{cases} \quad (4\text{-}6)$$

It can be seen that the instantaneous polarization of linear motion is a series of rectangular shapes. The important features to note are:

1) The height or depth of the initial rectangle from the base line is the polarization angle of the linear motion at that point, and the height or depth of the next rectangle is the polarization angle less 180°. Note that there is only one rectangle unless the signal is more than half a cycle long.

2) The width of the rectangle is the half period of the wave motion, independent of the number of cycles in the waveform (as long as the signal contains at least half a cycle). Thus, the angle of polarization given by the instantaneous polarization in Figure 4.2(b) is 160°, and the instantaneous amplitude has two local maxima. The final narrower rectangle in WM1, Figure 4.2(b), is a result of the low-amplitude tail of the wavelet used in Figure 4.2(a).

Elliptical motion.—The elliptical motion WM2 in Figures 4.2(a) and 4.3 can be represented by:

$$y(t) = a \sin\omega t \; ; \text{ and } x(t) = b \cos(\omega t + \phi) \; ; \quad (4\text{-}7)$$

where a and b are the peak amplitudes in x- and y-components (WM2, Figure 4.2a), respectively; ω is the angular frequency, here taken to be 2π x 40, say, for a 40 Hz signal, and ϕ is a phase shift, here taken to be 20°.

The elliptical motion in Figure 4.2(b) gives a varying instantaneous polarization of repeated characteristic shapes, which is called "semi-triangular". The polarization angle of the ellipse (the direction of semi-major axis, also

called the effective polarization angle) can be determined by combining the instantaneous polarization and amplitude displays. The maximum amplitude occurs when the particle displacement is at the long axis of the ellipse. Thus, the angle at the time where the amplitude has a local maximun is an effective polarization angle. (Note, however, that this is not usually coincident with the polarization directions of either of the split shear-waves.) There is also another feature which can be used to determine the polarization angle of the ellipse. When the particle motion is at the maximum, the polarization has a smooth variation which forms a step in the instantaneous polarization [marked with arrowhead in WM2, Figure 4.2(b)]. The polarization angle can be estimated from the amplitude of this step.

The features discussed above can be used to determine the type of wave motion. Wholly rectangular shapes indicate linear motion (or well separated split shear-waves), and semi-triangular shapes indicate some form of elliptical motion. Note that if black and white plots of instantaneous polarization, as in Figure 4.2(b), were to be routinely used to determine polarization angles, the polarization would need to be plotted at a larger scale so that the values of the polarization would be easily read. More effective displays will be discussed below.

4.3 SHEAR-WAVE SPLITTING

The most characteristic features of shear-waves in anisotropic structures are the polarization anomalies in the three-dimensional waveforms resulting from shear-wave splitting into phases which propagate with different polarizations and different velocities (Crampin 1978, 1981; Crampin and Booth 1985). The polarization patterns of shear-wave splitting can be represented by the interference of two linear motions with (typically) similar waveforms but different polarization directions and separated by a time delay. The interference of these signals results in a combination of linear and elliptical waveforms, or two linear waveforms if the time delay between the two split

shear-waves is large enough to separate the signals. The patterns of particle motion vary with the delay and particle-motion polarizations of the two split shear-waves.

I examine a variety of characteristic wavetypes. Without loss of generality, It is assumed that the two split shear-wave polarizations are polarized orthogonally.

4.3.1 Polarization patterns

The six polarization patterns, WM3 to WM8 in Figure 4.3, are characteristic of shear-wave splitting with a range of delays: from WM3 to WM8, the delay linearly increases from 8 ms to 48 ms on a 40 Hz signal (phase delays from 72° to 432°, respectively). At the onset of the faster split shear-waves, the polarizations are linear. At the onset of the slower shear-waves, the polarizations either change smoothly to elliptical motion or change abruptly to further linear motion in different directions, if the delays between the two split shear-waves are sufficiently large. When the delays between the split shear-waves are less than half a cycle [as in WM3 and WM4, Figure 4.3], the polarizations change smoothly with elliptical patterns of polarization, and the underlying characteristic cruciform patterns are barely discernible. As the delays increase beyond half a period (WM5 and WM6), the polarizations change more sharply, and the cruciform patterns become clearer. When the delays are equal to the period of the wave (WM7), or greater (WM8), the polarizations change abruptly, and the patterns are wholly cruciform.

4.3.2 Instantaneous attributes

Figure 4.2(b) shows corresponding instantaneous attributes of amplitude (A) and polarization (P) of the seismograms in Figure 4.2(a) and polarization diagrams in Figure 4.3:

WM3 and WM4.—The amplitude has three local maxima, and the polarization starts with a step equal to the polarization angle of the first arrival. The polarization then remains constant until the slower wave arrives, when it changes smoothly. If the change can be identified [marked by arrowheads in WM3 and WM4, Figure 4.2(b)], the arrival time and polarization direction of the slower split shear-wave and the delay between the two split shear-waves can also be determined. The overall feature of the instantaneous polarization of shear-wave splitting is a combination of rectangular and semi-triangular shapes.

WM5 and WM6.—The amplitude has four local maxima, and the polarization is again a combination of rectangular and semi-triangular shapes. The polarization change on arrival of the slower shear-wave has been marked by arrows in Figure 4.2(b), but is subtle and difficult to identify reliably.

WM7 and WM8.— The amplitude has four clear local maxima, and the polarization has wholly rectangular shapes. The polarization directions and the delay can be determined easily.

To summarize: as the delay increases, the number of local maxima of instantaneous amplitude increases, and the shape of instantaneous polarization changes from a combination of rectangular and semi-triangular shapes to a combination of purely rectangular shapes. Thus, shear-wave splitting can be identified from displays of instantaneous amplitude and polarization, and the polarization direction can be easily and accurately determined when the delays are sufficiently large. The delays are easy to determine when the delays are large, but may be difficult to determine when the delays are less than a cycle. The next section shows how, in this case, the use of colour displays of the attributes can be more informative.

4.4 COLOUR DISPLAYS

The use of colour in displaying seismic data has been shown to improve the perceptibility of subsurface features (Taner *et al.* 1979). Figure 4.4 shows the colour codes used for displays of instantaneous polarization in this paper. Code (a) contains a series of contrasting colours, useful for identifying the exact value of the polarization; and (b) a series of continuous colours, useful for recognizing shear-wave splitting in a larger scale. Note that the colours repeat every 180°. Thus, if the polarization values have a difference of $\pm 180°$, they will be coded with the same colour, allowing for the $\pm 180°$ difference between the positive and negative values of the polarization of linear motion.

Figure 4.5 is the colour display of Figure 4.2(b), showing the colour-coded polarization angle in the contrasting colours of code (a) superimposed on a wiggle trace of instantaneous amplitude. This type of display aids estimation of the parameters of shear-wave splitting:

1) The colour-coded polarization quantifies the polarization direction by reference to the colour key. For example WM1 is a wholly red colour, which represents $162° \pm 3°$ (or $-18° \pm 3°$), where I use the angle (colour) D to represent the range $D-3° < \text{to} \leq D+3°$. From the shape of the polarization curve the angle can be determined as $162° \pm 3°$.

2) The onset of the slower arrival can be easily identified by the change of the uniform (red) to the varying colours of elliptical motion in WM3 to WM7, or the uniform (black) colour representing perpendicular motion ($72° \pm 3°$ or $-108° \pm 3°$).

3) The difference between the linear motion, WM1 and the shear-wave splitting with a delay of more than a cycle, WM8, is clearly demonstrated by the colour. WM1 has a single colour which implies no change of polarization (or

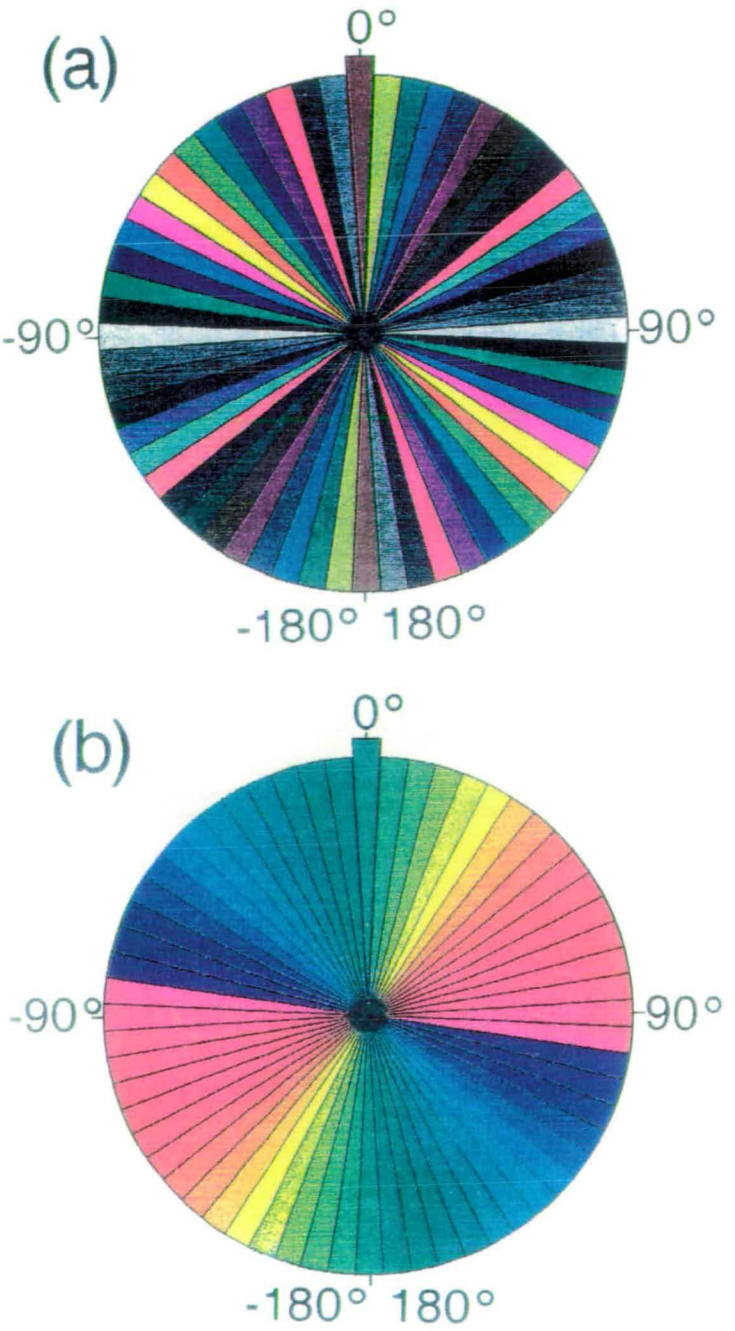

Figure 4.4. Colour codes for polarization displays: (a) contrasting colour-code; (b) continuous colour-code.

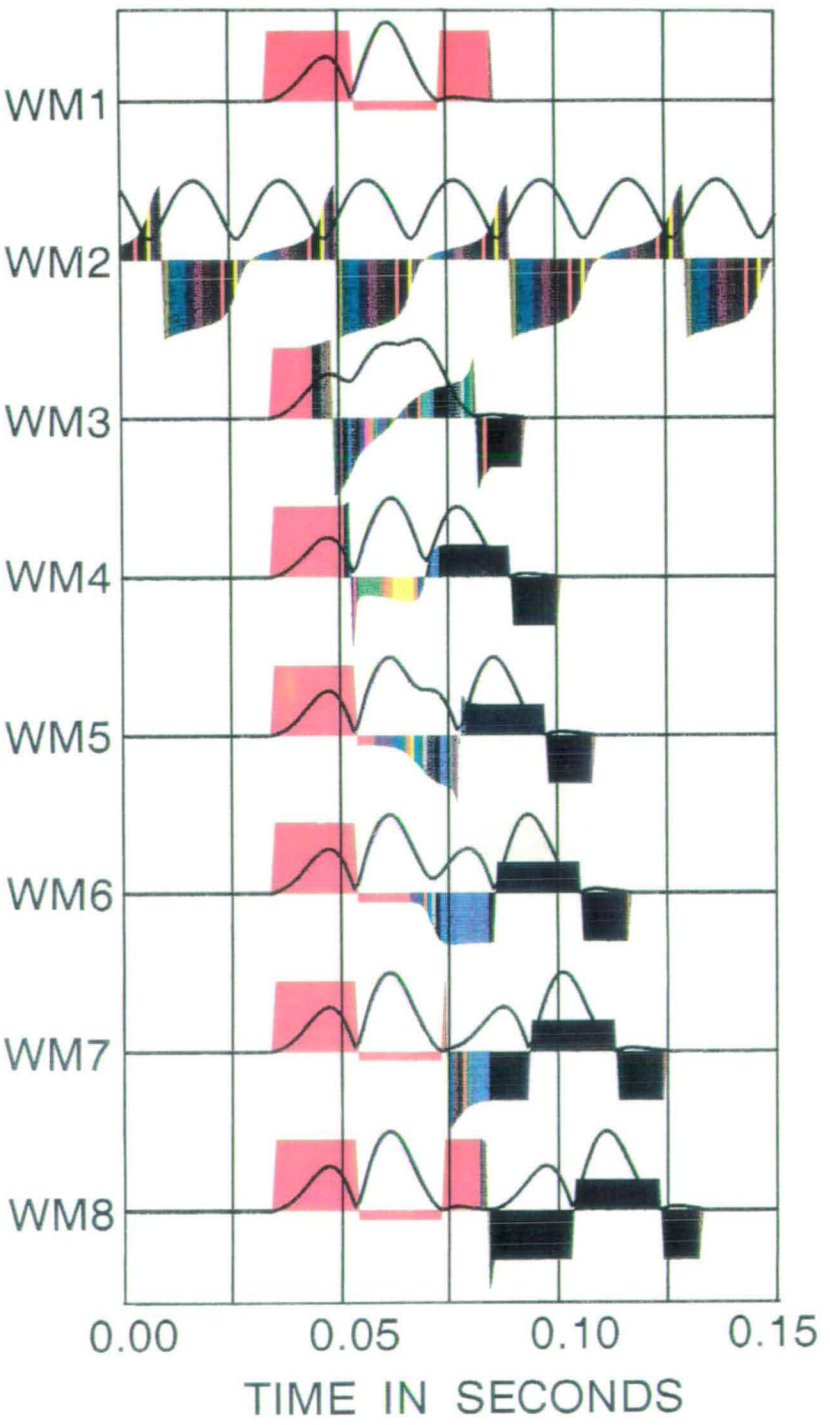

Figure 4.5. The colour-coded display of Figure 4.2(b), where a wiggle line of instantaneous amplitude is superimposed on the colour-coded instantaneous polarization.

a change of $\pm 180°$); whereas WM8 has two different colours (separated by approximately 90°), which implies two approximately orthogonal linear motions.

In applying these techniques to seismograms with incoherent or signal-generated noise, the use of the continuous colour code is recommended for identifying shear-wave splitting, although the contrasting colour code may be required for estimating values of polarization. In the following examples, the polarization is coded by the continuous code (b). Two examples are used to demonstrate the significance and application of instantaneous attributes to anisotropic interpretations.

4.5 APPLICATIONS

4.5.1 AMC model and data

The data used are a synthetic VSP and a CMP gather from the response of the Edinburgh Anisotropy Project (Wild 1990) to the Anisotropic Modelling Collaboration of Thomsen *et al.* (1989). A number of research groups are contributing to the Anisotropic Modelling Collaboration (AMC) to calculate full wave synthetic seismograms in specified VSPs and CMPs in a given anisotropic multilayered model (Thomsen *et al.* 1989). Figure 4.6(a), adapted from Wild (1990), shows a schematic diagram of Model 1 (AMC1) used in this study (note that only every second three-component geophone is marked in the figure). The crack strike is east-west in each anisotropic layer. The model features a strongly anisotropic layer from 1500 m to 2000 m depth, simulating highly fractured reservoir rocks.

The collaboration calculated a full nine-component (inline, crossline, and vertical sources recorded by inline, crossline, and vertical receivers) offset VSP, and a variety of nine-component reflection lines, as indicated in Figure 4.6(a). Only one source component, the inline component, of both the VSP,

Figure 4.6.

(a) The structure and geometry of the AMC model. The dots along survey lines represent every second geophone of 50 m geophone spacing.

(b) The two horizontal components of the VSP data for the inline source orientation. The offset is 500 m at an azimuth of N45°E. Note noise on the first five inline-source components. Some selected polarization diagrams are shown. Number on top-right corner of the polarization diagrams is the geophone number at the time interval marked below. Arrows drawn on particle motions are in the same notation as Figure 4.3. R1 to R4 are reflected shear waves from Layers L1 to L4, respectively. M1 to M4 are the multiples of the primary downward propagating shear-wave. The four particle motions on the left are selected from the primary downgoing shear-waves, and on the right from the reflected shear-waves.

(c) The two horizontal components of the reflection line at an azimuth of N45°E for the inline source orientation with some selected polarization diagrams. Symbols drawn on the diagrams have the same notation as (b). Those on the left are selected from the reflected shear-waves R1, R2, R3 and R4 at geophone 1 (near offset), and on the right from the same event-arrivals but at geophones at larger offsets where the polarizations have changed.

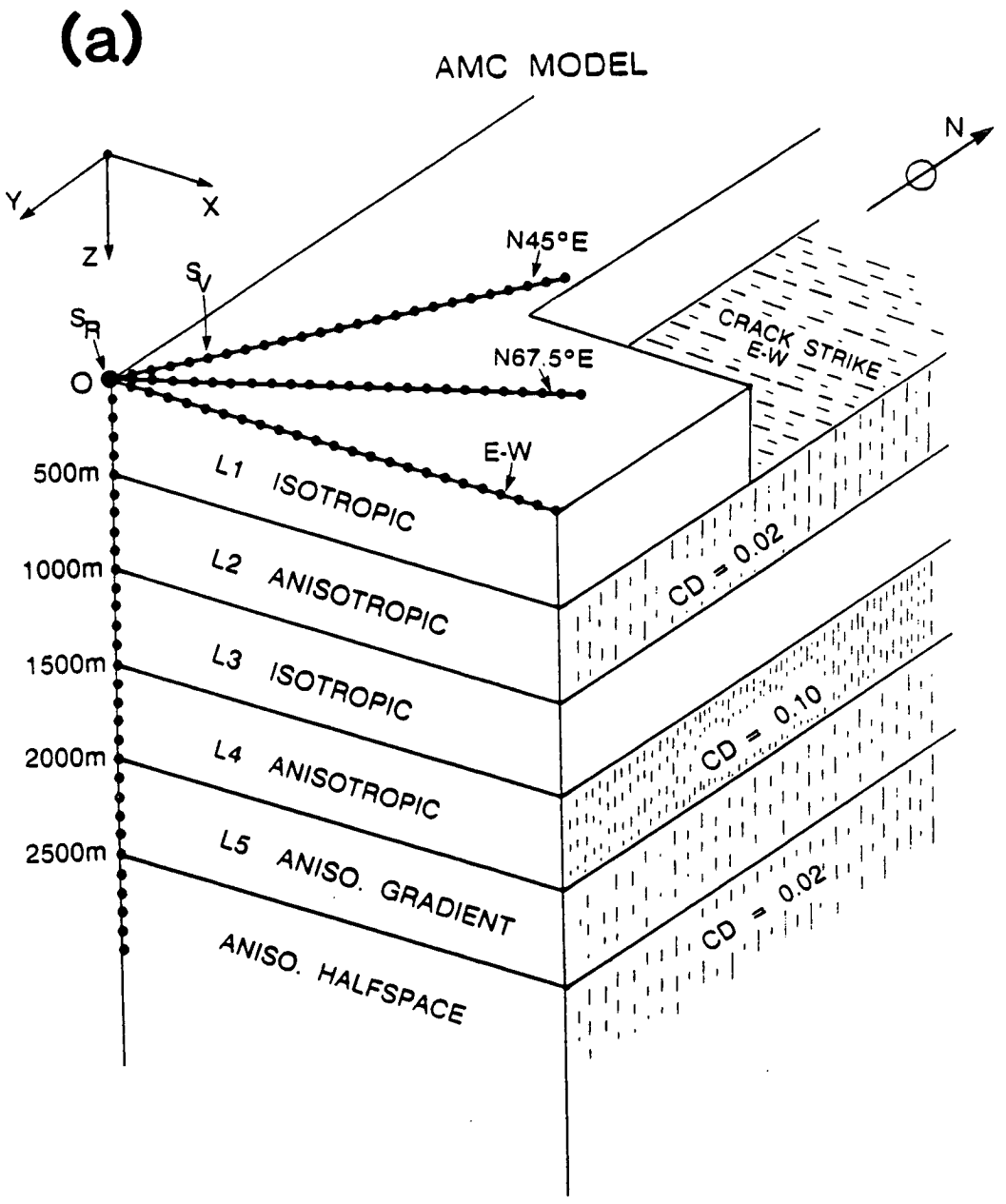
(a)
AMC MODEL
N
Y
X
Z
S_V
S_R
O
N45°E
N67.5°E
E-W
CRACK STRIKE E-W
500m
1000m
1500m
2000m
2500m
L1 ISOTROPIC
L2 ANISOTROPIC
L3 ISOTROPIC
L4 ANISOTROPIC
L5 ANISO. GRADIENT
ANISO. HALFSPACE
CD = 0.02
CD = 0.10
CD = 0.02

Figure 4.6a

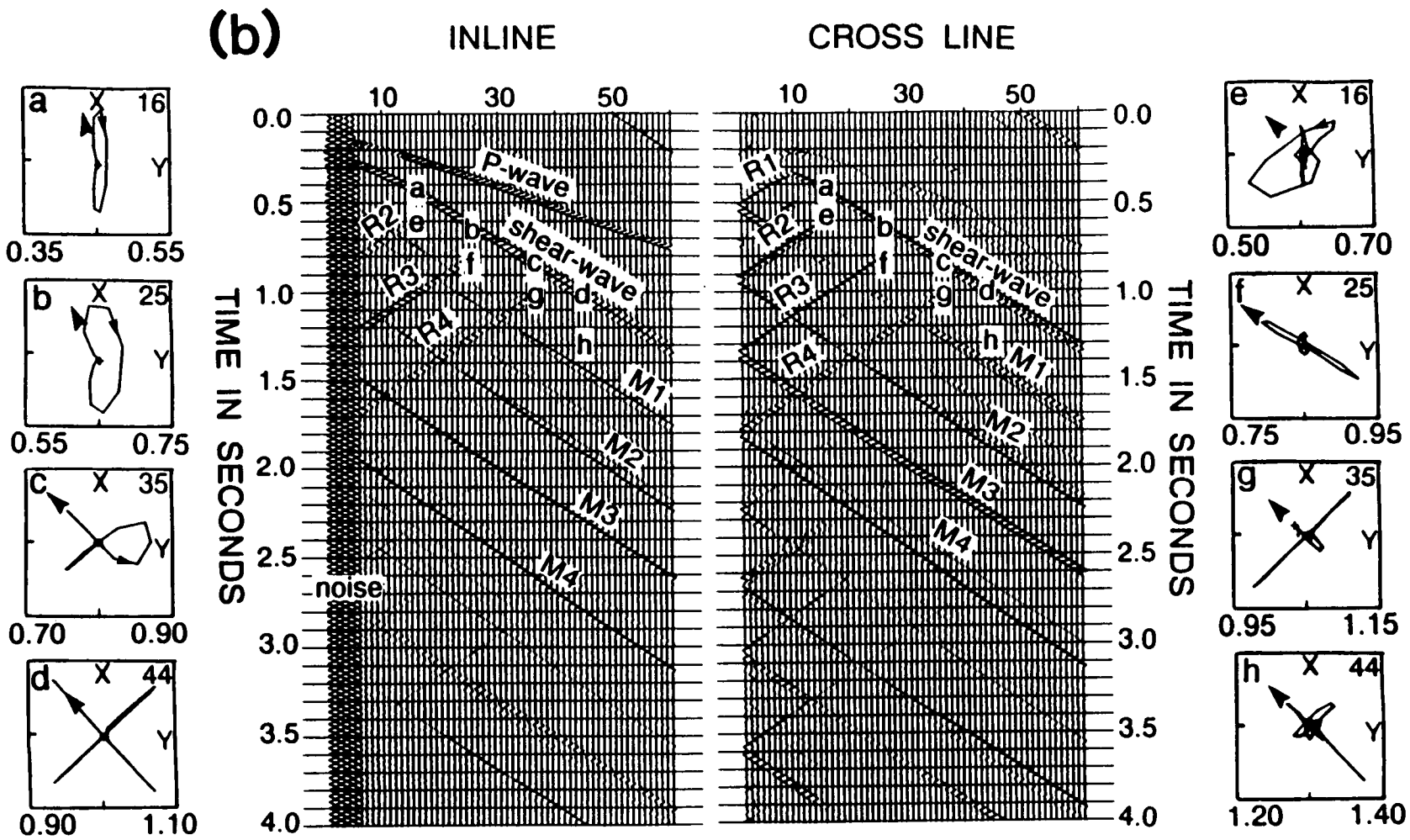
(b)
INLINE
CROSS LINE
10
30
50
0.0
0.5
1.0
1.5
2.0
2.5
3.0
3.5
4.0
TIME IN SECONDS
P-wave
shear-wave
R1
R2
R3
R4
M1
M2
M3
M4
noise
a
b
c
d
e
f
g
h
X
Y
16
25
35
44
0.35
0.55
0.55
0.75
0.70
0.90
0.90
1.10
0.50
0.70
0.75
0.95
0.95
1.15
1.20
1.40

Figure 4.6b

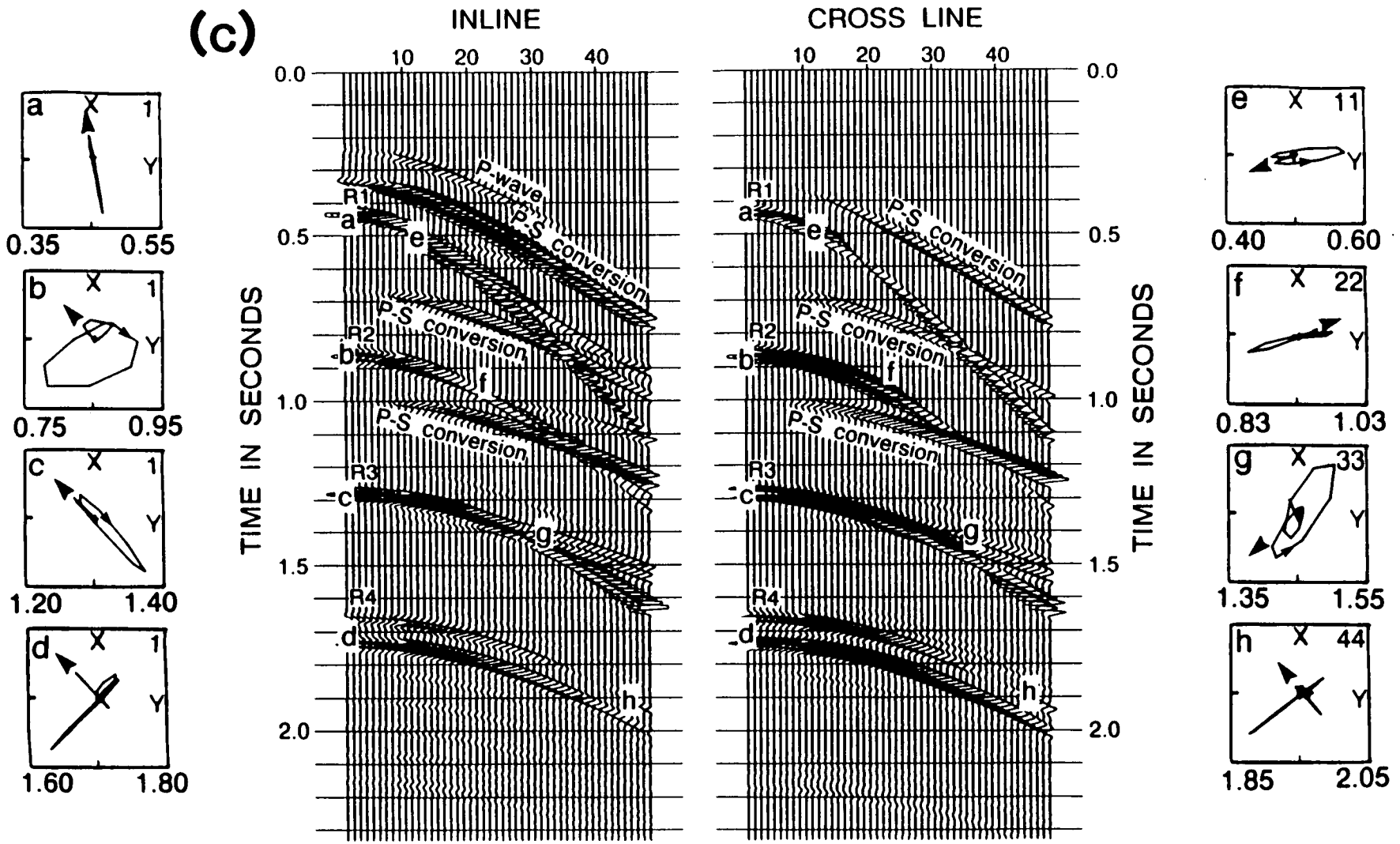
(c)
INLINE
CROSS LINE
10
20
30
40
0.0
0.5
1.0
1.5
2.0
TIME IN SECONDS
P-wave
P-S conversion
R1
R2
R3
R4
a
b
c
d
e
f
g
h
X
Y
1
11
22
33
44
0.35
0.55
0.75
0.95
1.20
1.40
1.60
1.80
0.40
0.60
0.83
1.03
1.35
1.55
1.85
2.05

Figure 4.6c

at an offset of 500 m and an azimuth of N45°E, and the 2400 m reflection line data, again at an azimuth of N45°E, are analyzed here. Figure 4.6(b) shows the two horizontal components of the VSP excited by the inline source located at S_V in Figure 4.6(a). Cruciform patterns of particle motion in the polarization diagrams from primary downgoing propagating shear-waves (polarization diagrams c and d) are observed within and below the simulated fractured reservoir (Layer L4); the delays between the downgoing shear-waves gradually increase with increasing geophone depth. Figure 4.6(c) shows the two horizontal components of the CMP gather excited by the inline source located at S_R in Figure 4.6(a). Polarization diagrams of the shear-wave reflection from the bottom of the reservoir (event R4; polarization diagrams d and g) have cruciform polarizations and show strong shear-wave splitting.

4.5.2 Analysis of the VSP

Figure 4.7 shows the colour-coded display for the instantaneous polarization of the VSP data in Figure 4.6(b), with a superimposed wiggle trace of instantaneous amplitude. The display contains a large amount of relatively easily interpretable information. A few major items in the interpretation of the display are summarized as follows:

1) Event A corresponds to the *P*-wave arrival in Figure 4.6(b). The whole waveform of the instantaneous amplitude is covered by a single green colour, implying linear motion with a polarization angle of $0° \pm 3°$ (or $\pm 180° \pm 3°$).

2) Event B is the direct shear-wave. Shear-wave splitting can be clearly identified by the shape of polarization curve containing two rectangles of blue ($132° \pm 3°$ or $-48° \pm 3°$) and orange ($42° \pm 3°$ or $-138° \pm 3°$) representing orthogonal or nearly-orthogonal motion. The polarization direction of the faster shear-wave is represented by the blue rectangle ($-48° \pm 3°$ or $132° \pm 3°$), and magnitude of the delay can be estimated from the duration of the blue rectangle. Below geophone 30, at the top of layer L4, the duration of the blue

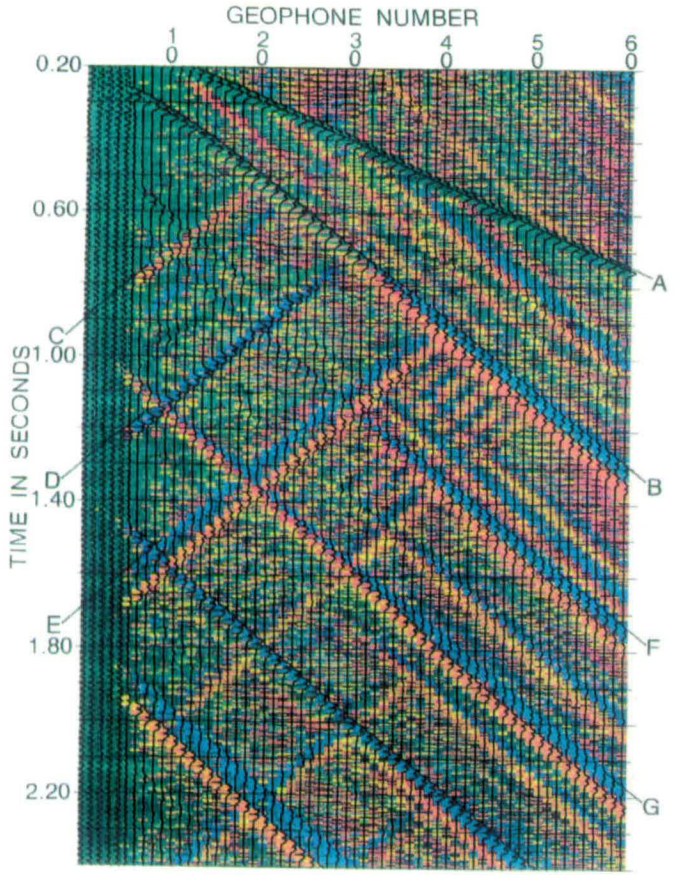

Figure 4.7. Colour display of instantaneous polarization and amplitude derived from the VSP data in Figure 4.6(b). The colour-coded instantaneous polarization is superimposed on wiggle lines of instantaneous amplitude. Letters A-G mark significant arrivals mentioned in the text.

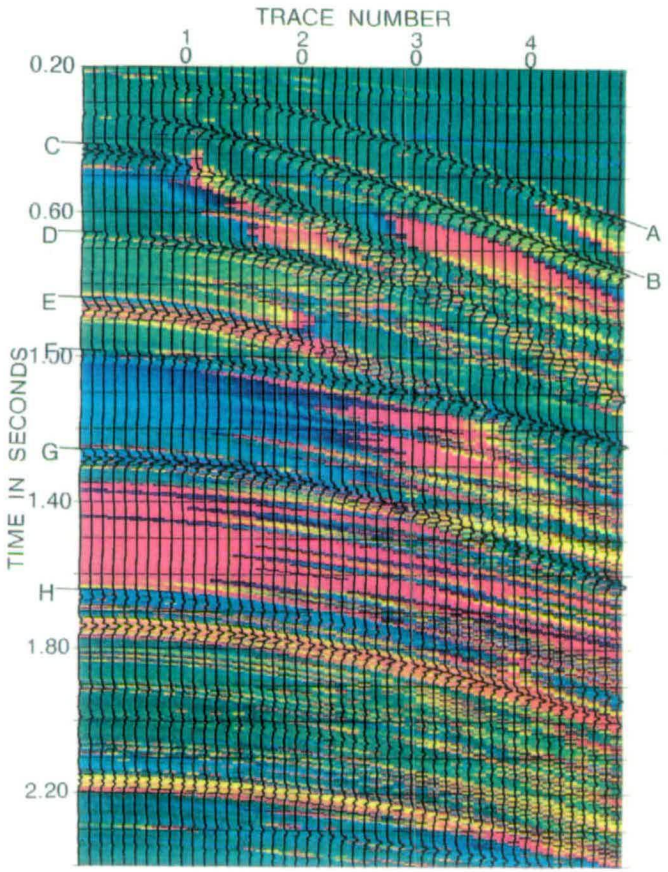

Figure 4.8. Colour displays of instantaneous polarization and amplitude derived from the CMP gathers of Figure 4.6(c). Letters A-H mark significant arrivals mentioned in the text.

rectangle gradually increases, showing the delay between the split shear-waves increasing with depth in the strongly anisotropic reservoir.

3) Event C corresponds to R2, a reflection from the bottom of L2. Shear-wave splitting can also be identified by the change of colours from blue to orange. Because the delay is small, this change is subtle and can only be clearly seen at geophones 9, 10, 11, and 12, where there is a narrow band of blue.

4) Event D corresponds to R3, a reflection from the bottom of L3. The blue rectangle covering the waveform indicates linear motion with a polarization angle of $132° \pm 3°$ (or $-48° \pm 3°$).

5) Event E corresponds to R4, a reflection from the bottom of L4. The waveforms of instantaneous amplitude are dominated by two rectangles of blue and orange, and the shear-wave splitting can be identified and parameters estimated as for the direct shear-wave.

6) Events F and G correspond to M1 and M2, respectively, multiples of the primary down shear-wave. The shape of the polarization curve and the variation of colour show the same features as those of the direct shear-wave.

4.5.3 Analysis of the CMP gathers

Figure 4.8 shows the instantaneous attributes of Figure 4.6(c) displaying colour-coded polarization data superimposed by wiggle lines of instantaneous amplitudes. The instantaneous attributes of CMP gathers have two applications.

Firstly, as discussed in the VSP data, the attributes of the CMP gathers can be used to identify the type of shear-wave motion in reflected waves, as follows:

1) Events A and F, describing the *P*-wave reflections from the bottom of layers L1 and L3, respectively, show linear motion as they are both dominated by a single light green (0°±3° or ±180°±3°) and dark green (174°±3° or -6°±3°) colours, respectively.

2) Events C and G (corresponding to R1 and R3, shear-wave reflections from the bottom of layers L1 and L3, respectively) are also linear motions at near offset and are dominated by one major colour: event C by the background green (0°±3° or ±180°±3°), and G by blue (132°±3° or -48°±3°).

3) Events E and H, corresponding to R2 and R4, are shear-wave reflections from the bottom of L2 and L4, respectively, and at near offsets both show shear-wave splitting which can be recognized by the shape of the polarization curve and the variation of colour from blue to orange. The polarization and delay can be determined in the same way as discussed for the VSP data. The delay of event E is small as indicated by the narrow blue rectangle, but the delay of event H is large as it traverses the strongly anisotropic L4 on both downgoing and upgoing rays.

Secondly, the attributes of CMP gathers contain information about the effective shear-wave window at the free surface (Booth and Crampin 1985) for each shear-wave reflection:

1) The polarization of shear-wave changes with offset, as demonstrated by the variation of colour. For example, event B (a *P-S* conversion from the bottom of layer L1) starts with background green colour at near offset, then changes to a light green at middle offset, and becomes yellow at far offset, indicating an approximate 30° change in polarization as the angle of incidence on the reflecting interface varies (Liu and Crampin 1990). In contrast, the polarization of the *P*-wave is relatively unaffected by the variation of offsets as shown by events A and F.

2) "Critical angles" at internal interfaces can also be identified, where one of the shear-waves has zero reflection amplitude as the offset increases (Liu and Crampin 1990). For incidence angles on the reflecting interface smaller than this angle, the colour of the instantaneous polarization remains constant (or only shows gradual change), but at the critical angle the colour indicates a 90° polarization (phase) change. For example, the change due to the critical angle for reflection from Layer 1 for event C is at geophone 12 (the colour suddenly changes from green to red, indicating a 90° change), and the critical angle for reflection from Layer 2 for event E is at geophone 22. Similarly, there are critical angles for event G at geophone 28, and elsewhere.

Effects of the shear-wave window are difficult to observe because of the interference of multiply reflected and converted waves. Note that effects of the first "critical angle" at internal reflections typically cause a comparatively simple change in polarization direction, and hence a change in the instantaneous polarization (Liu and Crampin 1990), whereas the shear-wave window at the surface usually causes much more complicated effects (Crampin and Booth 1985).

Identifying the offset at which the polarization of each shear-wave arrival changes polarity is important for stacking the CMP gather. Conventional stacking of split shear-waves, where the polarizations and delays change markedly with offset, will tend to distort and degrade the characteristics of the split shear-waves unless appropriate techniques are used (Li and Crampin 1989). Such changes of polarity occur both at critical reflections at internal interfaces (Liu and Crampin 1990), and at the surface shear-wave window (Booth and Crampin 1985).

4.6 DISCUSSION AND CONCLUSIONS

A technique has been proposed for the complex component analysis of shear-wave data by transforming the displacements from Cartesian to polar

coordinate systems. The large amount of information contained in the shear wavetrain (Crampin 1985b) can then be displayed in a form which is similar to many conventional time-versus-offset displays, and which could easily be assimilated into conventional stratigraphic analysis.

The VSP example shows how the technique can help in analyzing and estimating shear-wave splitting continuously as it varies with depth. The results of pre-stack reflection data show how shear-wave splitting can be traced along both time and offset directions, and reveals the potential for applying these techniques to field data, so that much of the stratigraphic and anisotropic interpretation can be made on a single display of complex attributes. Although, the instantaneous attributes were defined for vertical propagation, at wider angles they can be used to identify the various critical angles at the surface and at internal interfaces, which are critical for any stacking of shear-wave data in anisotropic structures (Li and Crampin 1989).

In conclusion, the treatment of the two horizontal components in multi-component shear-wave data as a complex variable allows convenient displays of instantaneous amplitude and polarization. The colour display of these attributes allows the identification of shear-wave splitting and permits estimates of shear-wave polarizations and delays in seismic sections. The examples in this chapter aim to demonstrate the concept of the complex component analysis of shear-wave splitting and the potential application of colour displays of instantaneous attributes. It is suggested that these colour displays provide a flexible format for recognising and parameterizing shear-wave splitting. Further developments and case studies are presented in Chapter Five (Li and Crampin 1990d, 1991d).

CHAPTER FIVE

COMPLEX COMPONENT ANALYSIS OF SHEAR-WAVE SPLITTING: CASE STUDIES

ABSTRACT

This chapter verifies the use of complex component analysis for analyzing shear-wave splitting by examining four case studies: a four-component single-offset VSP in the Lost Hills, Kern County; a multi-offset single-source two-component VSP in the Paris Basin; a four-component reflection-line in the Lost Hills; and an in-seam crosshole survey at German Creek Mine, Australia. In all cases, the polarization of the faster split shear-wave (or channel-wave) can be assessed from the colour coded record sections of the seismic attributes. In particular, the source-independent coherent polarization on the colour sections of the complex components of inline and crossline sources allows the shear-wave polarization angle to be determined without need for rotation of the instrument and source axes. In conclusion, complex component analysis can aid identification and estimation of shear-wave splitting from seismic sections, help stratigraphic interpretation, and simplify the processing sequence of multi-component reflection data in the presence of anisotropy.

5.1 INTRODUCTION

This chapter applies the complex component analysis techniques developed in Chapter Four (Li and Crampin 1990b, 1991c) to four field data sets: a four-component vertical seismic profile (VSP) in Lost Hills, Kern County, a two-component VSP in the Paris Basin, a four-component reflection profile in

Lost Hills, and a three-component in-seam (crosshole) seismic survey from the German Creek Mine, Australia. [Note that nine-component were recorded at the Lost Hills, however only four-components will be analyzed here.]

Seismic sections, displaying seismograms in time-versus-offset plots, accentuate the relative arrival times of the various phases, and analysis of such arrival times is the principal technique for stratigraphic interpretation. Polarization diagrams (hodograms), displaying the data in the displacement plane over an appropriate time window, stress the variation of the particle motions, and analysis of such particle motions is the principal technique for characterizing wave motion and analyzing shear-wave splitting.

Transformation of seismic data from one domain to another (time domain, frequency domain, FK-space, etc.) is common in seismic data processing. Complex component analysis transforms multi-component data from conventional Cartesian coordinates to polar coordinates in the horizontal plane (it can be extended to other planes). Such transformations retain the local significance of both the variation of waveforms and the variation of particle motion by calculating the instantaneous amplitude and instantaneous polarization. Such complex component analysis can be used to evaluate the effects of anisotropy in terms of the polarization of the leading split shear-wave and the delay between the two split shear-waves, and allows these parameters to be displayed in a similar form to conventional record sections.

Application of complex component analysis to field data confirms the theoretical promise in Chapter Four (Li and Crampin 1990b, 1991c), and reveals new insights into the technique. Here, I outline the calculation of complex components of four-component seismic data, discuss necessary pre-processing procedures, and present the four case studies.

5.2 CALCULATION OF COMPLEX COMPONENTS

The technique of complex component analysis of shear-wave splitting is presented in Chapter Four (Li and Crampin 1990b, 1991c), where the ideas were illustrated with two-component synthetic shear-wave data. However to study shear-wave splitting, multi-component receivers, and multi-component sources have been used to generate four-component (Alford 1986b; Thomsen 1988) and nine-component data sets (Squires *et al.* 1989).

Chapter Four (Li and Crampin 1990b, 1991c) defined complex component analysis for two-component shear-wave data. Here I apply these techniques to further multi-component data in three ways:

5.2.1 Comparison of X- and Y-sources

1. Calculate and display the complex components of inline- and crossline-sources separately by equations (4-1) to (4-4) in Chapter Four (Li and Crampin 1990b, 1991c). (Hereafter, inline, and crossline will be referred to as IL, and XL, respectively). Features which are diagnostic of shear-wave splitting or stratigraphic variation typically display systematic behaviour, so that data sets from orthogonally polarized source components are expected to display consistent features, which will enhance and confirm interpretations.

5.2.2 Shear-wave splitting section

2. Calculate and display the shear-wave splitting section (SWS-section). Let $\theta_x(t)$ and $\theta_y(t)$ be the instantaneous polarizations of the IL-, (x), and XL-, (y), source, respectively. The absolute differential polarization angle $d(t)$ between θ_x and θ_y can be calculated as:

$$d(t) = |\theta_x(t) - \theta_y(t)|. \qquad (5\text{-}1)$$

A filter operator $f(t)$ can be defined as:

$$f(t) = \begin{cases} 1 & \text{if } d(t) \leq d_0; \\ 0 & \text{if } d(t) > d_0; \end{cases} \tag{5-2}$$

where d_0 is a threshold value. The combined polarization $\theta(t)$ can be written as:

$$\theta(t) = [\theta_x(t) + \theta_y(t)]\, f(t)/2. \tag{5-3}$$

Equations (5-1), (5-2), and (5-3) show that $\theta(t)$ will specify any common polarization which appears on both IL- and XL-sections. The existence of a common polarization at the onset of the shear-wave arrival among different source orientations suggests shear-wave splitting, where the common polarization is the alignment of leading split shear-wave. Thus, $\theta(t)$ is called the instantaneous polarization of shear-wave splitting; and the corresponding display is called the shear-wave splitting section (SWS-section).

5.2.3 Polarization logs

3. Calculate and display the transformed complex component of IL- and XL-sources. For near vertical propagation through vertical parallel cracks with no crack orientation changes with depth, the four components can be written as (Thomsen 1988):

$$s_{11}(t) = qS1(t) \cos^2\theta + qS2(t) \sin^2\theta; \tag{5-4}$$

$$s_{22}(t) = qS1(t) \sin^2\theta + qS2(t) \cos^2\theta; \text{ and} \tag{5-5}$$

$$s_{12}(t) = s_{21}(t) = [qS1(t) - qS2(t)] \sin\theta\cos\theta; \tag{5-6}$$

where $qS1(t)$ and $qS2(t)$ are the faster and slower split shear-wave signals, $qS1$, and $qS2$, respectively. s_{ij} are the recorded seismograms, where i is the receiver component, and j is the source component; subscript 1 is the

IL-component, and 2 the XL-component; and θ is the crack strike measured from the IL-direction. Linear transforms of:

$$\xi(t) = s_{11}(t) - s_{22}(t); \text{ and} \tag{5-7}$$

$$\eta(t) = s_{12}(t) + s_{21}(t); \tag{5-8}$$

can be used to transform four-component data to two-component data. Equations (5-4), (5-5) and (5-6) give:

$$\tan 2\theta = \eta(t)/\xi(t); \tag{5-9}$$

showing that the instantaneous polarization of the two component data $\xi(t)$ and $\eta(t)$ is a measure of polarization of the leading split shear-wave, which is called the *polarization log*. In the absence of lithology- or layer-induced anisotropy, this instantaneous polarization is the strike of the cracks (or fractures) in the rockmass (Crampin 1981). Equation (5-9) can also be derived from the $\tan 4\theta$ expression of rotation angle based on the minimization of the sum of squares of the off-diagonal terms over a time window in the data matrix (Murtha 1988).

5.3 DATA PROCESSING

The aim of data processing is to improve data quality while preserving the characteristics of shear-wave splitting. Processing data prior to complex component analysis often involves:

1. Use of band-pass filtering to improve signal-noise ratio. If the passband is properly selected, by simple spectral analysis, for example, the characteristics of shear-wave splitting will not be affected (Campden 1990). Figure 5.1 shows the PDs of the down-going shear-wave in the Lost Hills VSP before [Figure 5.1(a)] and after [Figure 5.1(b)] a 2-25 Hz band-pass filtering, showing that the polarization is preserved.

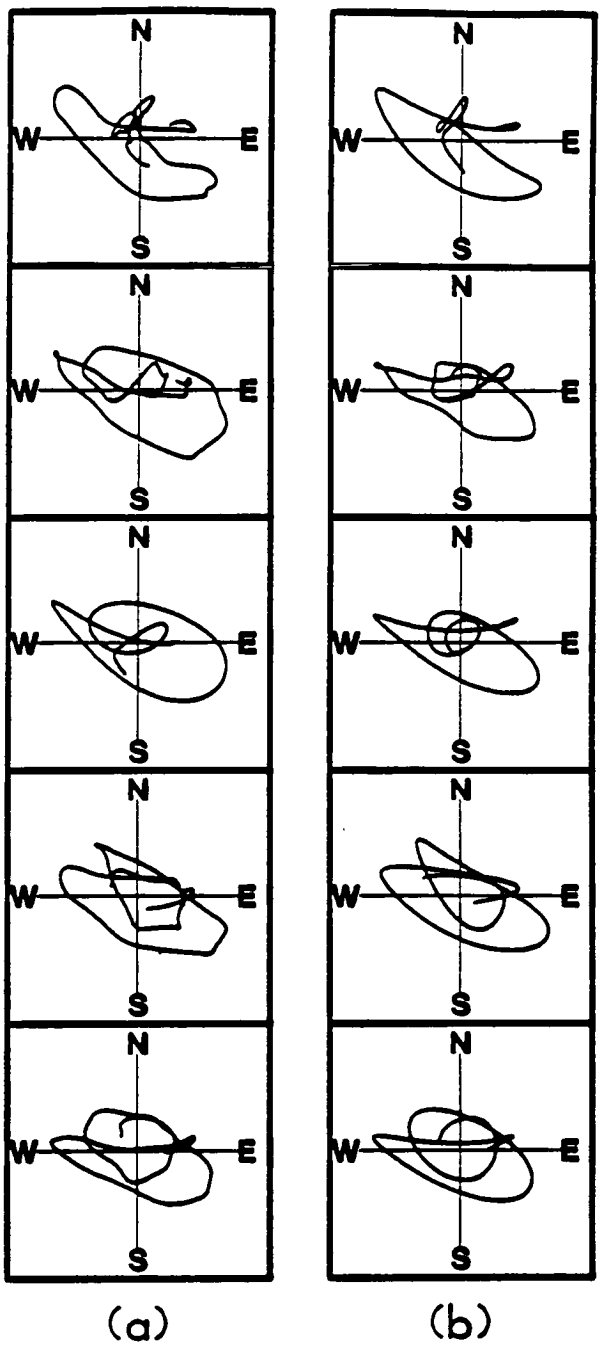

Figure 5.1. Polarization diagrams: (a) before and (b) after a 2-25 Hz bandpass filter. Data are from the Lost Hills VSP.

2. Use of FK-filtering to separate the up-going and down-going wave fields. The FK-filter is preferred for separating seismic wave fields without the degradation resulting from median-filters, or other separation methods (Campden 1990). Figure 5.2(a) shows PDs before FK- and median-filtering of the Paris Basin VSP data; Figure 5.2(b) shows PDs after FK-filtering, and Figure 5.2(c) after median-filtering. The PDs show almost no difference after FK-filtering, but have significant differences after median-filtering.

3. Use of polarization filtering to improve the image of colour-sections of complex components by muting-out noise with intermediate polarizations. Figure 5.3 shows the definition of polarization filter. Like a fan filter, it passes the principal- and orthogonal-polarizations, in order to preserve the characteristics of shear-wave splitting. The passband should be as wide as possible, around the principal- and orthogonal-polarizations. Selected PDs can be used to determine the passband. A front mute is often applied in conjunction with the polarization filter. Note that zero is a meaningful polarization value, and to implement the polarization filter, when $\theta(t)$ is outside the passband, I set $\theta(t)$ to a specific value which represents the backgound colour of display media. Also note that the improved colour image accentuates the principal polarizations, whether they are shear-waves, converted waves, or *P*-waves.

Figure 5.4(a) shows colour overlays of instantaneous amplitudes and polarizations from the Lost Hills VSP before applying polarization filters, where although polarization variations can be followed, the rainbow of colours may be misleading. From the PDs in Figure 5.4(b), it can be seen that the initial polarization is about N54°E±3°, and that an effective polarization (main ellipse) is about N42°W±3°. Thus a passband from N15°E to N75°E is appropriate. After applying the designed filter, the section accentuates the principal shear-wave polarizations [Figure 5.4(d)], from which the variation of polarization can be more easily followed.

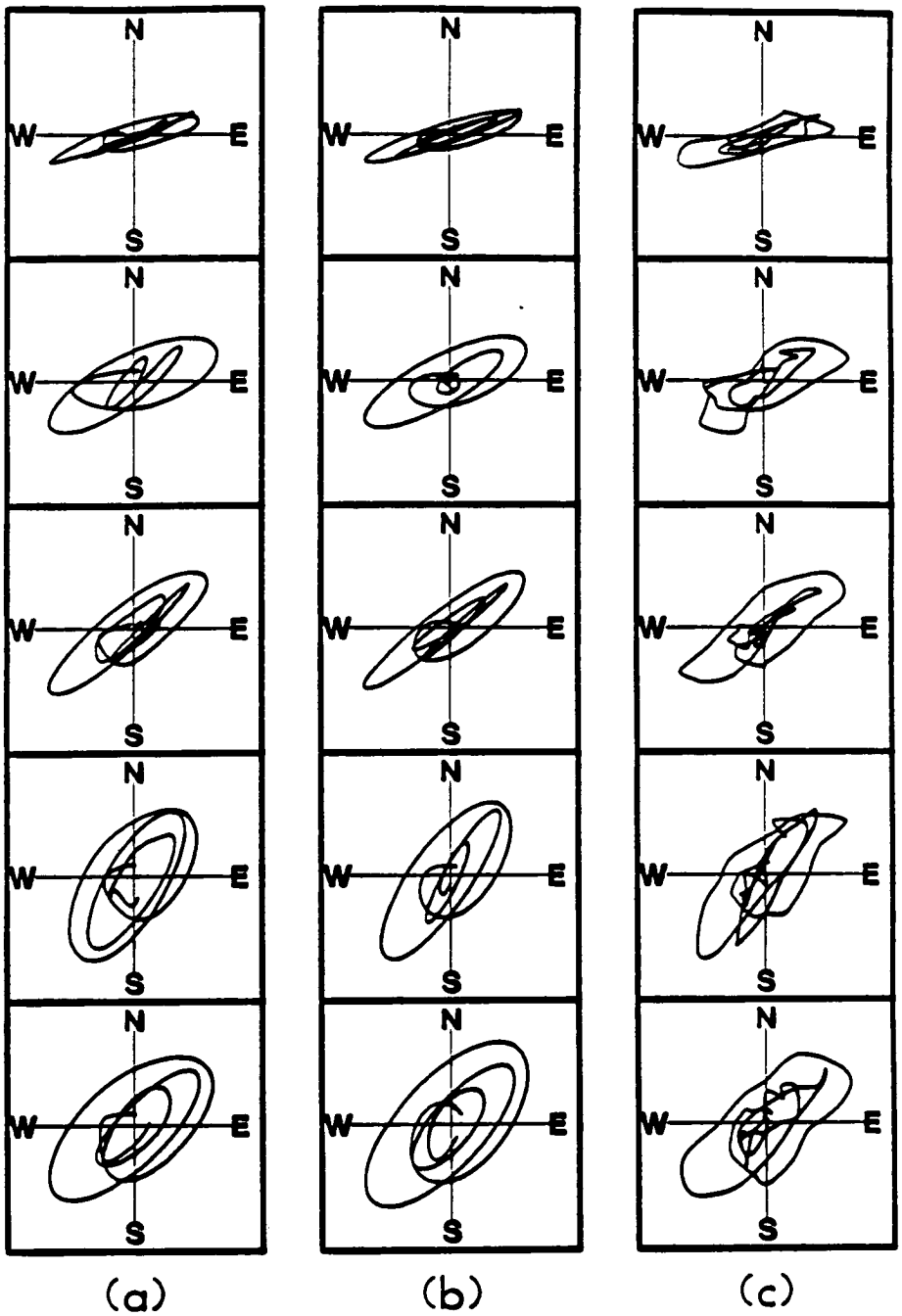

Figure 5.2. Comparison of FK-filter and median-filter: (a) PDs before FK- and median-filter; (b) PDs after FK-filter; and (c) PDs after median-filter. Data are from the Paris Basin VSP.

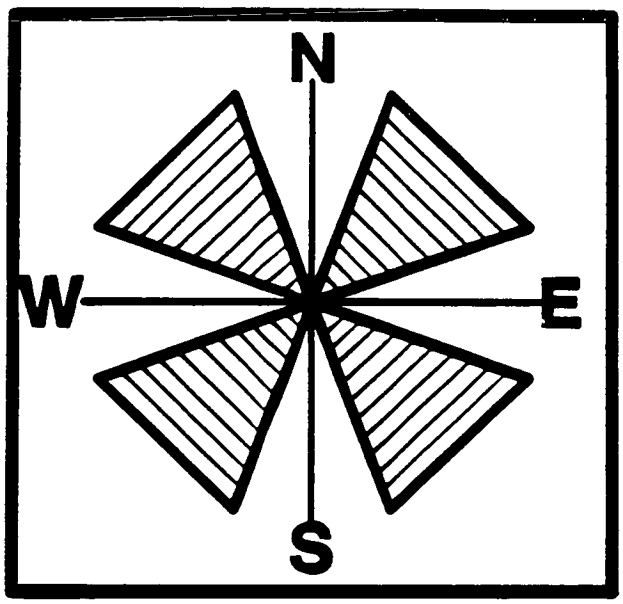

Figure 5.3. Geometry of polarization filter for north-south or east-west polarized shear-waves, where the polarizations within the shading areas are muted.

5.4 CASE STUDIES

Four field datasets are used to illustrate the application of complex component analysis in a variety of different recording situations.

5.4.1 Lost Hills four-component VSP

This example aims to illustrate the use of complex component analysis for analyzing shear-wave splitting for four-component VSP data. The Kim-Tech Lost Hills VSP is a total wavefield nine-component data set of high quality (Squires *et al.* 1989), but in this analysis only the four horizontal components will be used. Preliminary results from the shear-wave modelling of this data have been given by Yardley and Crampin (1990), and a full discussion of the data, geology and full-wave modelling is given by Yardley (1992). The two horizontal sources are oriented approximately north and east (N17°W and N73°E, Yardley 1992). The source offset is 500 ft (150 m) approximately west (N253°E, Yardley 1992) of the well and there are 42 geophones with 100 ft (30 m) spacing. The first geophone is located at a depth of 3600 ft (1100 m). Consequently, the incidence angle is comparatively small and most of the shear-wave energy is in the horizontal plane. The initial linear-motion can be observed in PDs of the primary shear-waves at most geophone depths [Figure 5.4(b)]. Note that terms such as north-south (NS-) source, and east-west (EW-) source are used for VSPs of small offset, where the IL- and XL- terms of the reflection survey are less relevant.

Figure 5.4(b) shows some selected colour PDs in which the particle motions are superimposed on colour pies which represent the colour scale used in this study. The initial polarization direction indicated by arrowheads is corresponding to a red-orange colour, indicating N54°E±3°.

Figures 5.4(c) and 5.4(d) show the attribute displays of the north-south and east-west sources, marked as NS- and EW-sections, respectively. At the

Figure 5.4. Processing the Kim-Tech Lost Hills VSP. (a) Colour section of the complex components of EW-source: instantaneous polarization superimposed on wiggle-lines of instantaneous amplitude of the north-south source of Lost Hill VSP before polarization filter. (b) Selected PDs of north-south source component in the horizontal plane with geographical coordinates, where the colour pie shows the colour scale used in this study. (c) Colour section of the instantaneous amplitude and polarization of NS-source; (d) Colour section of the instantaneous amplitude and polarization of EW-source; (e) SWS-section, which combines the common polarizations in the EW-section (c) and NS-section (d); (f) orientation logs of the EW- and NS-sections the of Lost Hill VSP.

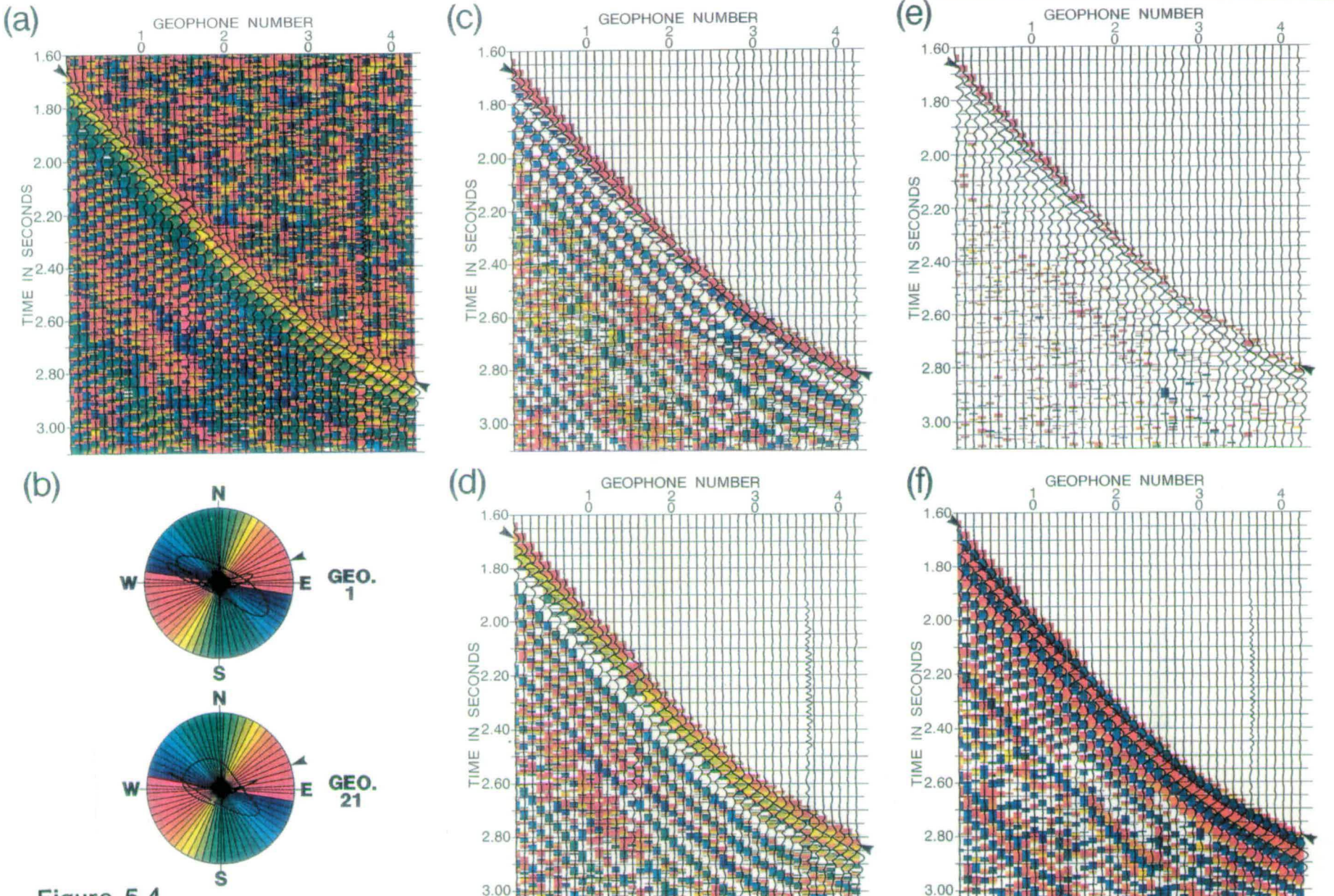
(a)
GEOPHONE NUMBER
10 20 30 40
TIME IN SECONDS
1.60 1.80 2.00 2.20 2.40 2.60 2.80 3.00
(c)
GEOPHONE NUMBER
10 20 30 40
TIME IN SECONDS
1.60 1.80 2.00 2.20 2.40 2.60 2.80 3.00
(e)
GEOPHONE NUMBER
10 20 30 40
TIME IN SECONDS
1.60 1.80 2.00 2.20 2.40 2.60 2.80 3.00
(b)
N
W
E
S
GEO. 1
N
W
E
S
GEO. 21
(d)
GEOPHONE NUMBER
10 20 30 40
TIME IN SECONDS
1.60 1.80 2.00 2.20 2.40 2.60 2.80 3.00
(f)
GEOPHONE NUMBER
10 20 30 40
TIME IN SECONDS
1.60 1.80 2.00 2.20 2.40 2.60 2.80 3.00

Figure 5.4

onset of the shear-wave, indicated by arrowheads, almost the same red-orange colour band appears on all geophones on both NS- and EW-sections. There are minor colour changes of about 6° in these first arrivals, which are believed to be due to the interference of split shear-waves (Yardley and Crampin 1990). [Note that errors in estimating tool orientation can also introduce such changes. For example, tool orientations from *P*-wave polarizations have errors of 5° to 10° (Kramer 1991). However, here the tool orientation is determined from gyroscope which has an error less than 1° (Yardley 1992).]

The existence of a similar colour band means the polarization of the onset shear-wave is fixed in space, independent of the source orientations, and is diagnostic of shear-wave splitting. Thus, the polarization of the faster split shear-wave is represented by the red-orange band, and the time delay between the split shear-waves by the duration of the band. This band is about 50 ms wide at the shallowest depths, and as depth increases, the duration of the band slightly decreases, indicating a decrease in the time delays. As mentioned above, the red-orange colour indicates N54°E±3°, which agrees with the results of Yardley and Crampin (1990).

A similar decrease in delays in a multi-offset VSP at a neighbouring site in the Lost Hills Field has been interpreted by Winterstein & Meadows (1990) as indicating a change in crack orientation with depth. Similarly, Squires *et al.* (1989) have interpreted a negative delay in a nine-component reflection survey through the Lost Hills site I am analyzing as a 90° change in crack orientation. However, shear-wave point singularities are believed to be commonly situated near vertical raypaths in sedimentary basins (Crampin 1991; Wild and Crampin 1991), as a result of combinations of matrix and crack anisotropies. Thus, an alternative explanation for the decrease in delays may be that the directions of the raypaths through a uniform crack orientation vary with depth so that they cross a point singularity. The raypaths in the upper layers have angles of incidence on one side of a point singularity and build up a delay, whereas the raypaths in the lower layers have angles of incidence on

the other side, with a nearly 90° change in effective polarization (Crampin 1991), and the delay would be reduced [for further details, see Yardley (1992)].

At the shear-wave onset in both Figures 5.4(c) and 5.4(d), the instantaneous polarization shows a constant band of colour, where the instantaneous polarizations have rectangular shapes. After this band, the instantaneous polarizations show a smooth change of colour, with semi-triangular shapes. These characteristic combinations of rectangular and semi-triangular shapes are diagnostic shear-wave splitting and confirm the theoretical results in Chapter Four (Li and Crampin 1990b, 1991c).

Figure 5.4(e) shows SWS-sections calculated from the NS-section [Figure 5.4(c)] and the EW-section [Figure 5.4(d)] using equations (5-1), (5-2) and (5-3), where only arrivals which have similar polarizations on both source sections are displayed. Following the onset of shear-waves, Figure 5.4e shows a red-orange colour band. The colour of the band represents the polarization of the faster split shear-wave, and the duration of the band represents the delay between the two split shear-waves.

Figure 5.4(f) shows the polarization logs from equations (5-7), (5-8) and (5-9). As with the SWS-sections, the red-orange colour at the onset of the shear-waves indicates the polarization of the faster split shear-waves, and the duration of the band indicates the delay, however, with this display, the interference of split shear-waves is separated. Figure 5.4(f) shows two simple polarizations: a red-orange polarization, the polarization of faster split shear-wave, and a blue polarization, the polarization of slower split shear-wave.

I have demonstrated three types of display for processing shear-wave splitting in four-component VSP data by complex component analysis: (1) colour sections of complex component attributes from different source orientations to examine the coherency and duration of instantaneous

polarizations; (2) SWS-sections; and (3) polarization logs.

5.4.2 Paris Basin two-component VSP

This Paris Basin VSP was a multi-offset single source VSP recorded on two horizontal geophones (Bush and Crampin 1987, 1991). Here, only the S1 offset at 272m will be processed. This case history is presented to demonstrate the application of complex component analysis to two-component seismic data. In addition to showing how complex component analysis can be used to interpret shear-wave splitting, I also show how it can aid stratigraphic interpretation. Preliminary processing included: applying a band pass filter of 5-50 Hz; an FK-filter to separate the down-going and up-going wave fields; and prior to display, applying a polarization filter of N15°E - N75°E.

Enlargements of the PDs in Figure 5.5(a) show a very small initial orientation of a blue colour, indicating N42°W±3°. This is less obvious than the first arrival in the Lost Hills VSP [Figure 5.4(b)] because of the smaller time delays in the Paris Basin data. The effective polarization (polarization of the main ellipse) changes from red (N78°E±3°) to orange yellow (N42°E±3°).

Figure 5.5(b) shows the instantaneous amplitude and polarization of the down-going wavefield. At the onset of the shear-wave, the polarization starts with a band of blue colour, indicated by arrowheads, which has a rectangular shape. The polarization colour smoothly changes following the constant blue band, and has semi-triangular shapes. These characteristic shapes suggest shear-wave splitting. This blue band and the following colour pattern changes appear at all geophone depths, showing consistency and coherency, which enhances the interpretation. The time delay and polarization can be interpreted from the blue band, which is about 20 ms wide and increases with depth. This example of two-component data analysis also confirms the theoretical promise in Chapter Four (Li and Crampin 1990b, 1991c).

Figure 5.5. Results of the Paris Basin VSP: (a) selected PDs in the horizontal plane with notation of Figure 5.4(b); (b) colour section of the instantaneous amplitude and polarization of down-going shear waves; (c) colour section of the instantaneous amplitude and polarization of up-going shear waves; and (d) VSP corridor stack (or VSP log) obtained by shifting up-going waves to two-way time and stacking.

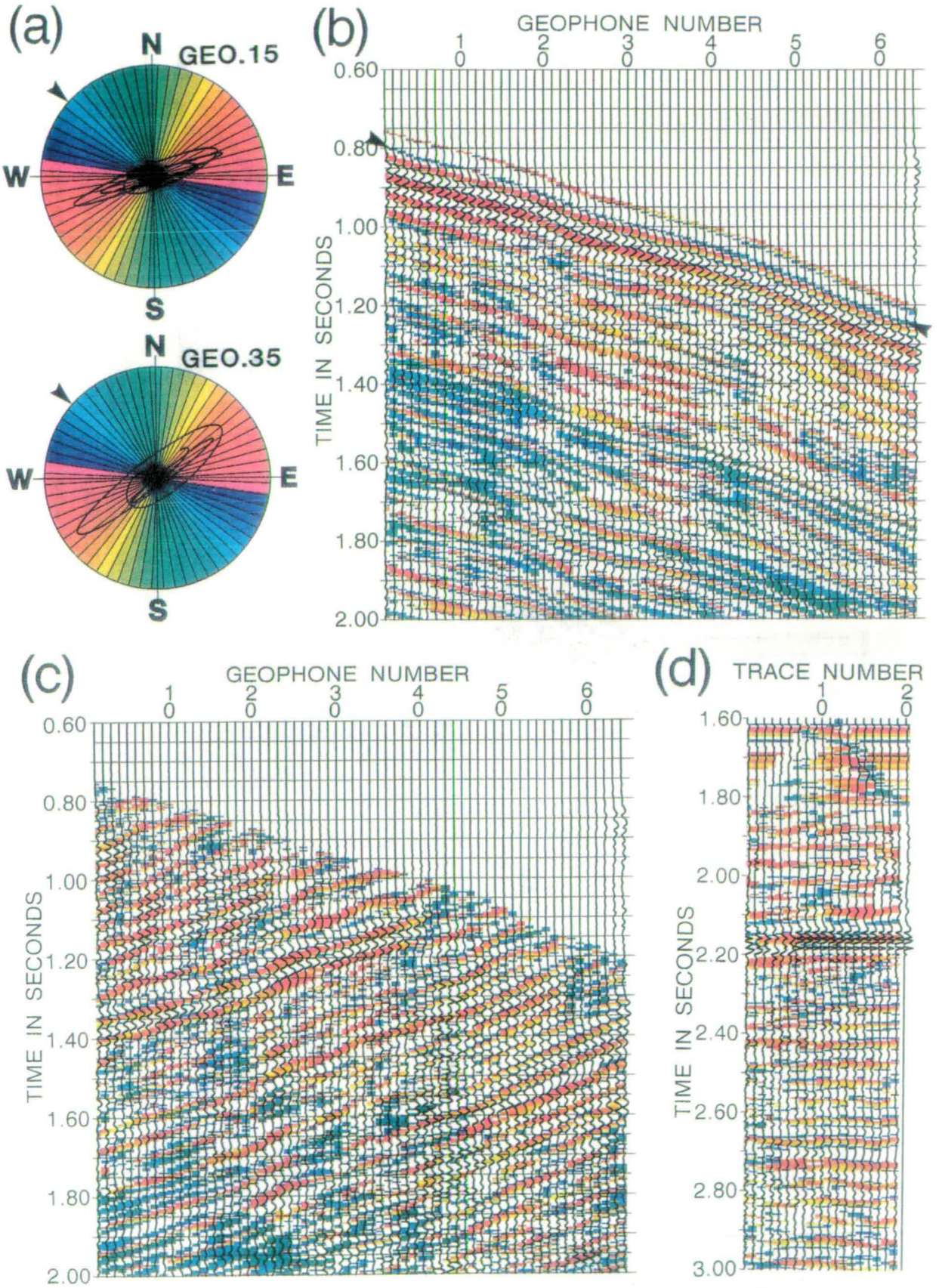
(a)
N
GEO.15
W
E
S
N
GEO.35
W
E
S
(b)
GEOPHONE NUMBER
10
20
30
40
50
60
TIME IN SECONDS
0.60
0.80
1.00
1.20
1.40
1.60
1.80
2.00
(c)
GEOPHONE NUMBER
10
20
30
40
50
60
TIME IN SECONDS
0.60
0.80
1.00
1.20
1.40
1.60
1.80
2.00
(d)
TRACE NUMBER
10
20
TIME IN SECONDS
1.60
1.80
2.00
2.20
2.40
2.60
2.80
3.00

Figure 5.5

Figures 5.5(c) and 5.5(d) demonstrate the application of complex component analysis in stratigraphic interpretation. Figure 5.5(c) shows the colour section of the instantaneous amplitude and polarization of the up-going wave field. Reflections from the same interface tend to have coherent polarizations at adjacent geophones when there is shear-wave splitting. [Reflections of shear-waves at isotropic/isotropic interfaces at wider offsets display systematic changes of polarization with incidence angle due to differences in the reflection coefficients of *SH*- and *SV*-wave components (Liu *et al.* 1990).] This coherency of polarization can help identify reflection events. As shown in Figure 5.5(c), the events can be easily identified and traced back to the reflectors following the variation of polarization colours. A variation of polarization from red (N78°E±3°) to yellow orange (N42°E±3°) can be observed from shallow reflections to deep reflections; Bush and Crampin (1987, 1991) modeled this as the effects of combination of thin-layer and crack anisotropy.

Processing the up-going wave field further, I shift to two-way time, and apply a corridor stack, to obtain the VSP log in Figure 5.5(d). Figure 5.5(d) shows instantaneous polarization superimposed on wiggle-lines of instantaneous amplitude. Colour displays of instantaneous polarization appear to display better continuity of shear-wave reflections than amplitude displays. In addition, the polarization offers additional criteria in correlating VSPs with stacked sections.

Thus, the characteristic shape and coherency of polarizations between adjacent geophones are the major criteria for interpreting shear-wave splitting in two-component VSP data. The coherency of polarizations also improves the continuity of reflection events and hence the image of subsurface structure.

5.4.3 Lost Hills reflection profile

Complex component analysis was applied to four-component relection profiles in the Kim-Tech Lost Hills dataset to analyze shear-wave splitting and aid stratigraphic interpretation. I examined the pre-stack common shot records. This avoids possible data degradation introduced by inappropriate data processing, such as stacking of varying shear-wave polarizations (Li and Crampin 1989). It also avoids possible source inconsistences in CMP gathers, such as unequal source strengths and different configurations of source arrays subject to acquisition conditions (Lewis 1989; Lewis *et al.* 1991). Prior to display I have applied a band pass filter and a fan polarization filter as in the Lost Hills VSP discussed above. The effects of these processing procedures on the charateristics of shear-wave splitting can be neglected if the choice of parameters is optimal.

Figure 5.6(a) shows the data matrix of a selected shot. *XX* stands for horizontal *X*-source (first *X*) and horizontal *X*-receiver (second *X*) component; *XY* stands for *X*-source and *Y*-receiver component; etc. A major reflection event can be identified at 1.60 seconds on the middle trace (trace 60), marked with A. Figure 5.6(b) shows some selected PDs, where shear-wave splitting can barely be identified from the PDs because of the interference of shear-wave and existence of noise. Figure 5.6(c) shows the colour section of the instantaneous amplitude and polarization calculated from *XX* and *XY*, which is called the *X*-section; Figure 5.6(d) shows the section from *YX* and *YY* (the *Y*-section). Figure 5.6(e) shows the polarization log. The features and interpretations of these sections are summarized below:

1. The shapes of polarization in Figures 5.6(c) and 5.6(d) are difficult to interpret. As a result, shear-wave splitting in reflection data cannot be analyzed in the same way as in VSP data. Similarly, PDs show few diagnostic features of shear-wave splitting.

Figure 5.6. Results of Lost Hill reflection survey: (a) data matrix of a selected record (record 137), and *X* stands for inline, and *Y* for cross-line; *XX* stands for *X*-source (first *X*) and *X*-receiver (second *X*), and *XY* for *X*-source and *Y*-receiver, etc. (b) selected PDs of *XX* and *XY* components; (c) *X*-section, the colour section of the instantaneous amplitude and polarization of *XX* and *XY*; (d) *Y*-section, that of *YX* and *YY*; (e) orientation logs.

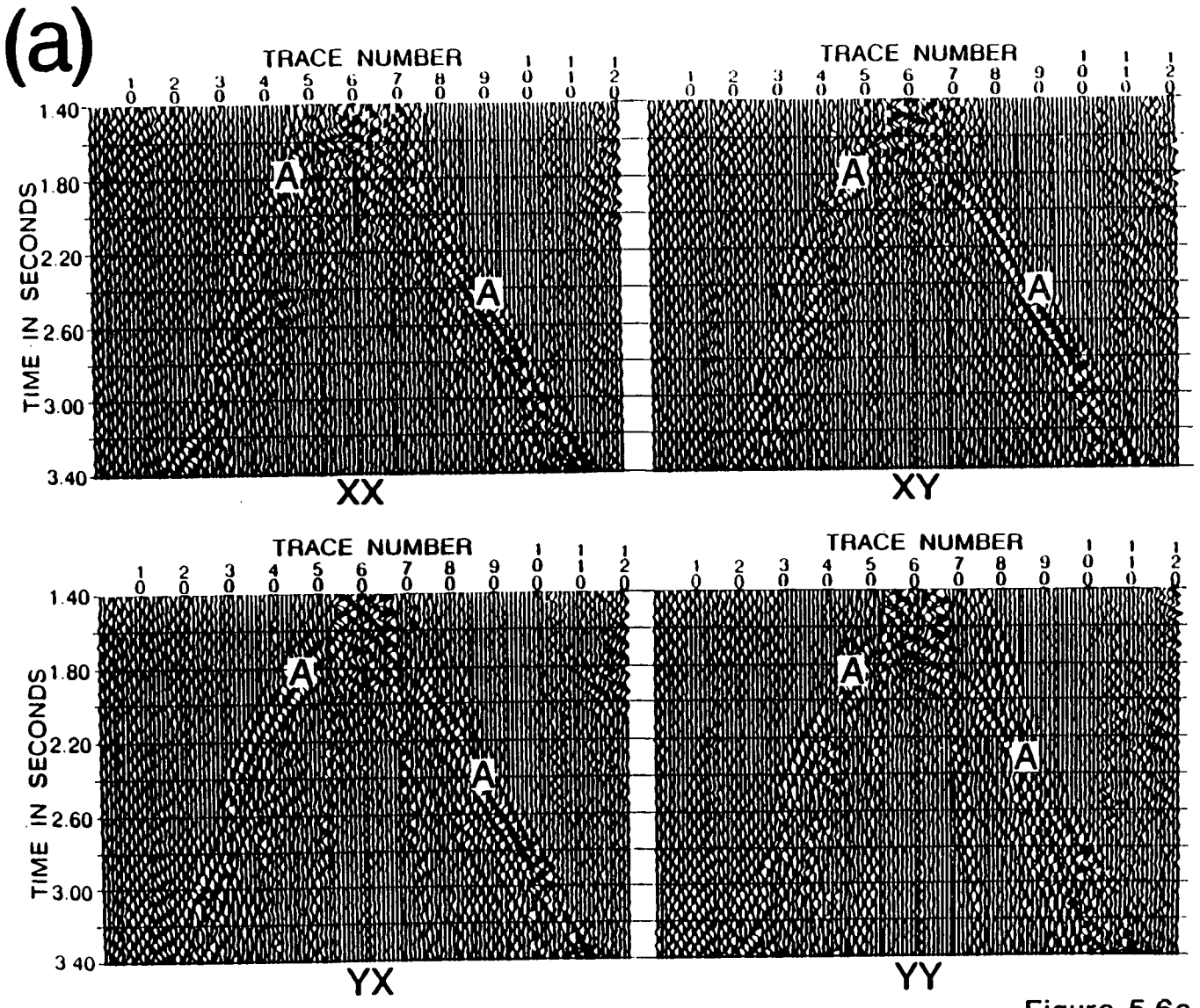
(a)
TRACE NUMBER
TIME IN SECONDS
1.40
1.80
2.20
2.60
3.00
3.40
A
XX
XY
YX
YY

Figure 5.6a

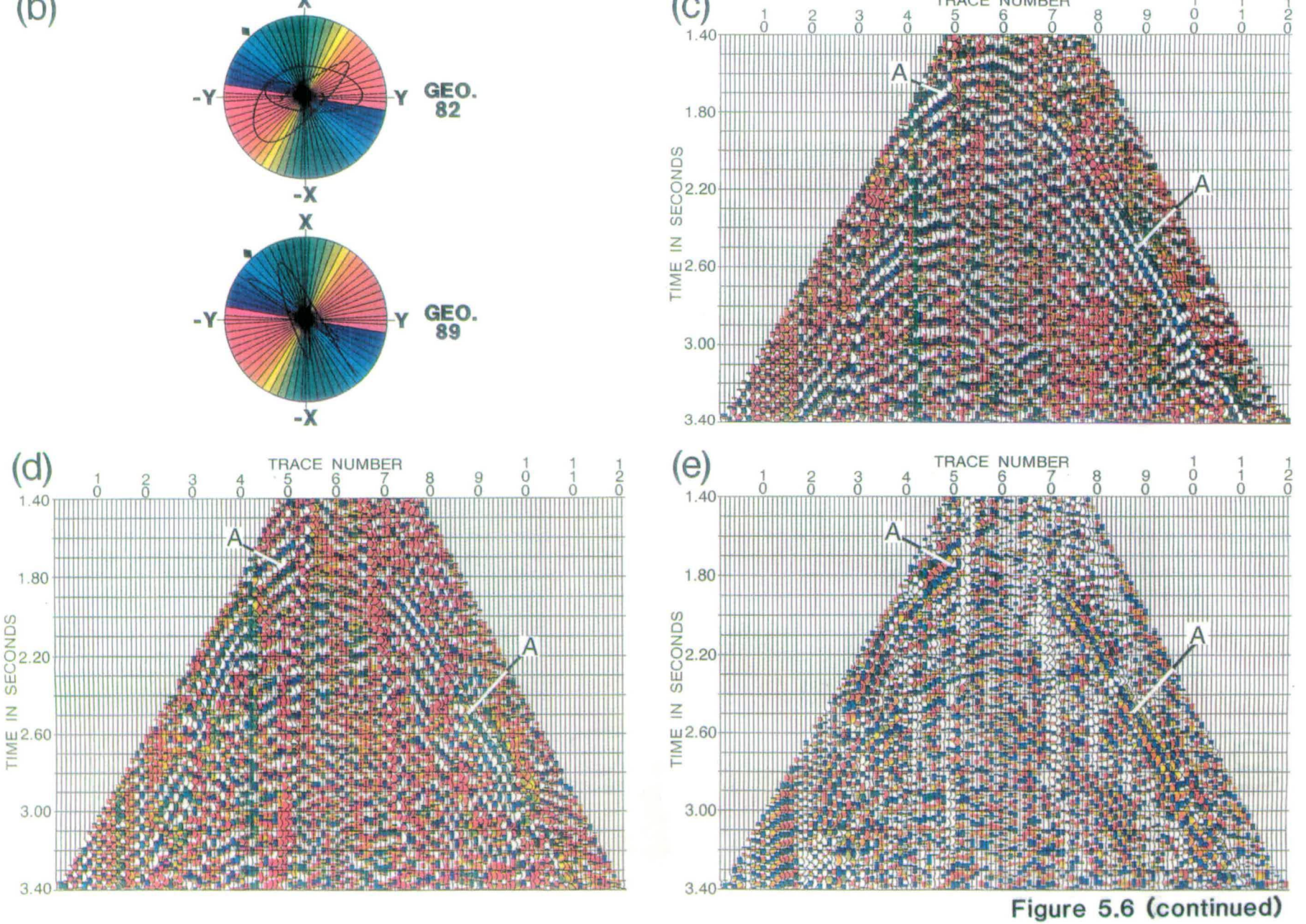

Figure 5.6 (continued)

2. Variations of polarization with incidence angle are also difficult to interpret. In noise-free data, as incidence angle reaches the internal shear-wave window of an interface (Liu and Crampin 1990), polarizations show sudden changes, which can be identified on the colour section of the complex component (Li and Crampin 1990b, 1991c), as described in Chapter Four. Sudden changes of individual polarization can easily be identified in real data, such as event A on the *Y*-section [Figure 5.6(d)] at trace 67, and trace 83. However, these changes are most likely to be caused by interference with ambient noise caused by air wave, groundroll, random noise, etc., but might also be caused by the effects of an internal shear-wave window (Liu and Crampin 1990). Since most of reflective interfaces are well below the surface, it is reasonable to assume that the angle of incidence is sufficiently small that all reflections are within internal shear-wave windows.

3. Although polarization variations of individual traces are difficult to interpret, Figures 5.6(c) and 5.6(d) show that polarizations of the same reflection events appear to be coherent, as is observed in VSPs. For example, event A of *X*-section [Figure 5.6(c)] has a coherent blue polarization on higher traces than 60 where the source is located. Because the interfaces are dipping (Squires *et al.* 1989), the arrivals for event A at lower traces than 60 are contaminated with the direct arrival. Coherent polarizations appear also on other events such as the event at 2.6 seconds and trace 35 at *X*-section [Figure 5.6(c)], etc. This coherency of polarizations helps to indentify shear-wave events, and Figures 5.6(c) and 5.6(d) show better continuity of reflection than Figure 5.6(a).

4. Figures 5.6(c) and 5.6(d) also show that there are coherent polarizations independent of source orientations on the two colour sections, as observed in VSPs. For examples, event A in the *Y*-section [Figure 5.6(d)] has the same coherent blue colour as in the *X*-section [Figure 5.6(c)]. There are several similar events. The same coherent colour (polarization) on different events, independent of source orientations, can most directly be interpreted as

indicating shear-wave splitting, and can be used to identify shear-wave splitting. The coherent colour represents the polarization angle of the leading shear-wave. In this case, the coherent colour is blue, indicating N42°W±3°. This observation can be used to determine the pre-stack rotation angles before synchronous rotation in processing multi-component reflection shear-wave data in the presence of anisotropy. Thus the processing of shear-wave data in the presence of anisotropy can be simplified by dropping post-stack rotation analysis which is now a conventional procedure for determining the rotation angle.

5. Figure 5.6(e) shows that polarization logs of the reflection data improve the continuity of reflection events and separate the interference of the split shear-waves. The variations of polarization in Figure 5.6(e) can be more easily followed than in Figures 5.6(c) and 5.6(d). The blue colour of the polarization of leading split shear-wave arrivals appears on all events, and the polarization of the slower split shear-wave can also be identified as a red-orange colour. Note there is a lateral change of anisotropy in the Lost Hills line; the polarizations of the leading split shear-wave at this shot position has a different orientation from those at location of VSPs, as was also found by Squires *et al.* (1989). The SWS-section of the reflection data is less informative than that of the VSPs, because of noise and shear-wave interference, and is not shown here.

To summarize, the attribute sections of reflection data have a more complex nature than those of VSPs. Characteristic rectangular shapes of polarizations are difficult to determine with confidence, hence analyzing shear-wave splitting in reflection data cannot be carried out in the same way as in VSPs. I am able to indentify shear-wave splitting and determine the polarization of leading split shear-waves, by examining the coherency of polarization between geophones and different source orientations. This makes it possible to determine polarization angles for pre-stack data without a post-stack rotation analysis. Polarization logs improve the continuity of reflection events and separate the interference of split shear-waves, allowing the

optimum rotation angle to be more easily determined. SWS-sections of reflection data are less informative than those of VSP data.

5.4.4 German Creek crosshole data

The example is given to demonstrate how complex component analysis can help examine polarization variation in crosshole surveys. This is an in-seam seismic dataset acquired from German Creek Mine in Australia. Figure 5.7(a) shows the acquistion geometry on the horizontal plane (Greg Turner, private communication). There are 33 source points, and two fixed 3-component geophones, marked as G1 and G2. The polarizations of wave modes received at the geophone are expected to be different at different source positions. By examining such variation of polarizations it is possible to locate the cleats and determine cleat directions in coal seams (Liu *et al.* 1989). To identify the type of wavemodes and to recognize the polarization variations, one often plots out seismograms and PDs of the horizontal components. In practice, this is time-consuming and difficult to keep objective. Complex component analysis can help overcome these difficulties.

Figure 5.7(b) shows the colour section of instantaneous polarizations superimposed on wiggle traces of instantaneous amplitude received at G1. Two modes can be identified with different characteristic colours. A is a *P*-wave mode, which has a constant green polarization (N0°E±3°) at all source positions. B is a shear-wave mode with a red polarization (N78°E±3°) at lower source numbers, but gradually changes to red-orange (N54°E±3°) at higher source numbers. Figure 5.7(c) shows the colour displays of waves received at G2. Wave mode A has yellow green polarizations (N18°E±3°) at lower source numbers, then changes to pure green polarization (N0°E±3°). Thus, mode A is *P*-wave mode, and the change of polarization is due to the change of angle of azimuth of the travel path. This crosshole dataset demonstrates that complex component analysis offers an easy way to examine polarization variations in many configurations.

Figure 5.7. Results of German Creek Mine data: (a) plan of acquisition geometry; (b) colour section of the instantaneous amplitude and polarization of the two horizontal components at geophone G1; (c) colour section of the instantaneous amplitude and polarization of the two horizontal components at geophone G2. Letters mark the significant events explained in the text.

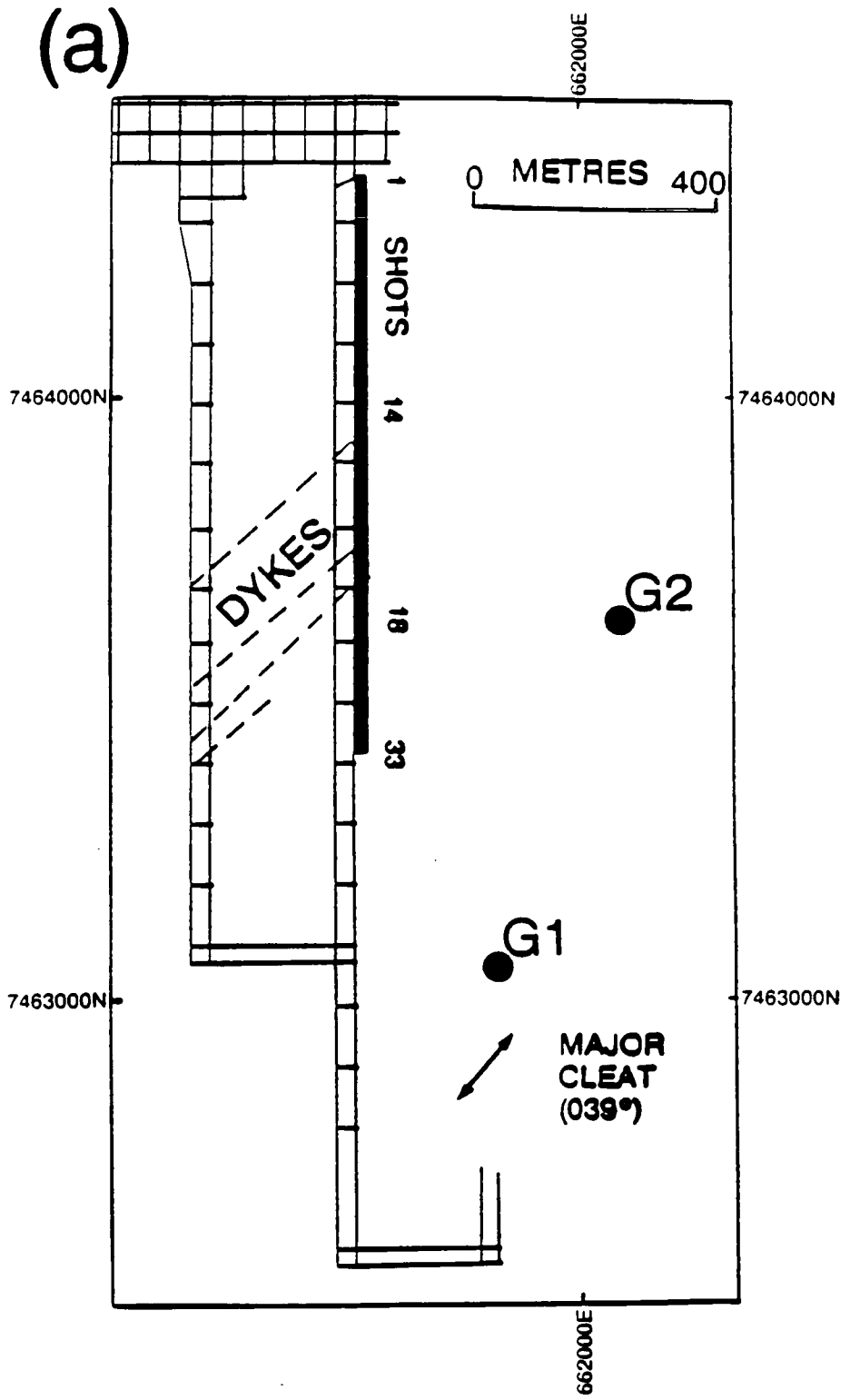
(a)
662000E
0 METRES 400
1
SHOTS
14
18
33
7464000N
7464000N
DYKES
G2
G1
7463000N
7463000N
MAJOR
CLEAT
(039°)
662000E

Figure 5.7a

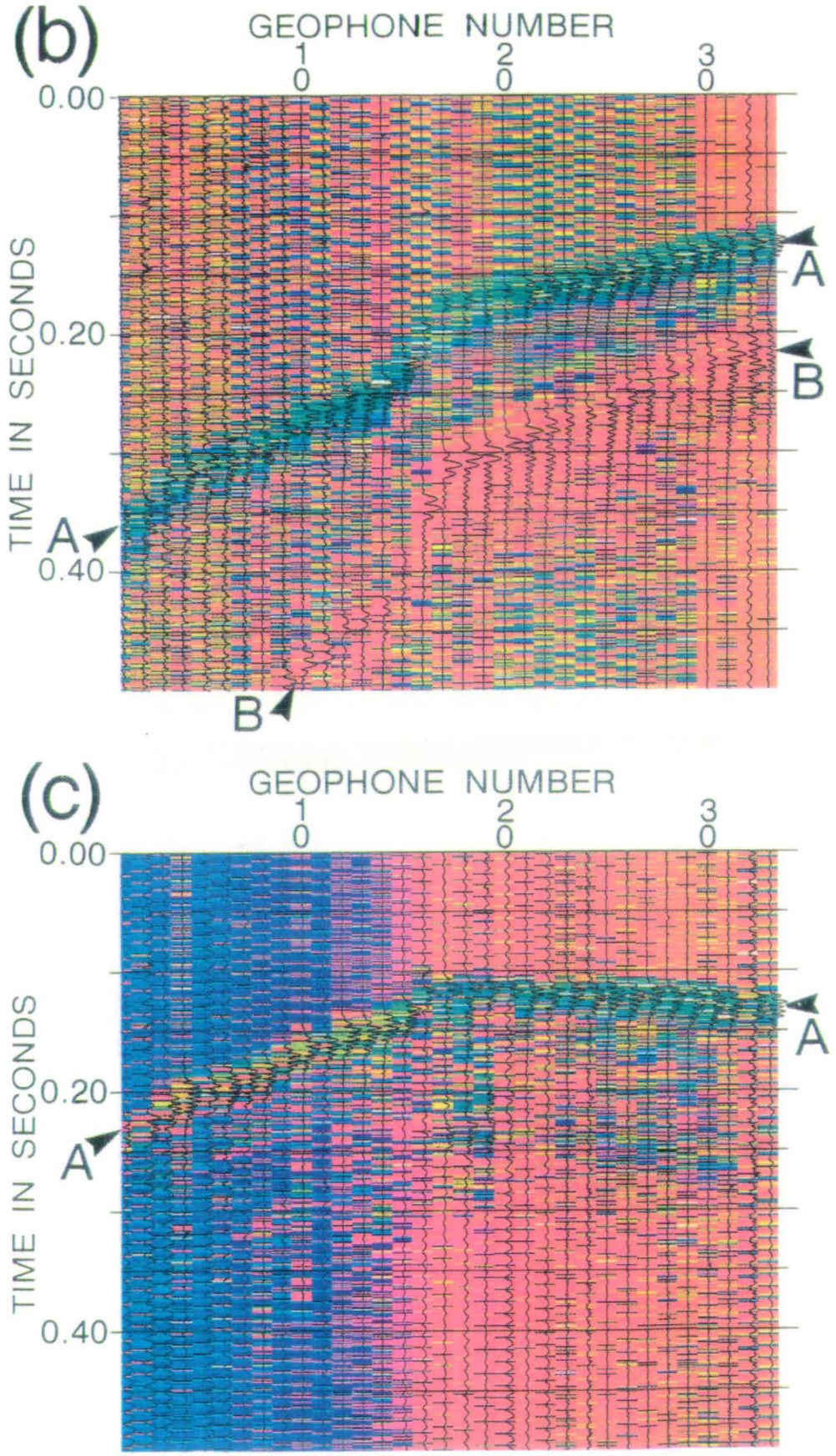

Figure 5.7 (continued)

5.5 DISCUSSION

The above case studies show the following phenomena:

1. The VSPs confirm that the instantaneous polarization of shear-wave splitting shows characteristic combinations of rectangular and semi-triangular shapes as predicted in Chapter Four (Li and Crampin 1990b, 1991c), which can be used to analyze shear-wave splitting in colour sections of complex components.

2. Complex component analysis is further developed for application to four-component seismic data. The Lost Hills VSP shows that calculating and displaying SWS-sections and polarization logs provides direct information about shear-wave splitting. In SWS-sections, shear-wave arrivals showing shear-wave splitting are characterized by a coherent colour band in which the colour represents the polarization of the leading shear-wave and the width of the band represents the delay between the split shear-waves. In polarization logs, the polarization of a split shear-wave is coded by colour plots, and the colour band of the leading split shear-wave represents the delay between the split shear-waves.

3. It is observed that the polarizations of split shear-waves are remarkably coherent. Consequently, complex component analysis is comparatively robust in the presence of noise.

The polarizations of the leading direct shear-wave in VSPs tend to be consistent, and coherent among adjacent geophones. In isotropic examples, the polarization is source dependent, whereas in anisotropy, it is fixed in the symmetry direction and independent of source orientatations.

The polarizations of reflected shear-waves are more complicated than VSPs, and are dependent on source and incidence angle. Outside the

shear-wave window, the polarizations are not coherent among adjacent traces regardless of source orientation and presence or absence of anisotropy. Within the shear-wave window at the free surface, in an isotropic rockmass, the polarizations are also varied and shear-wave polarizations are not usually orientated parallel to source axes (Liu *et al.* 1990); but in anisotropy, the polarizations are fixed and independent of source orientations. If the receiver axes are orientated parallel to source orientations, coherency of polarization among traces received within the shear-wave window can aid in identifying reflection events.

Techniques that take advantage of the coherency of signals are frequently robust in the presence of noise. A reasonable amount of noise could modify the polarization shape of individual geophone or trace, but barely disturb the coherent polarization variation as a whole. Thus, the behaviour of shear-waves as indicated by complex component analysis will be preserved in the presence of noise as demonstrated by the Lost Hills reflection data.

4. Complex component analysis of pre-stack data can be used to determine the rotation angle for source-geophone rotation for multi-component reflection data. Source-geophone rotation has now become a conventional processing procedure for multi-component reflection data, as demonstrated by Alford (1986b), Murtha (1989), Squires *et al.* (1989), and others. To apply source-geophone rotation, a post-stack rotation analysis (Alford 1986b; Squires *et al.* 1989) is often required to determine the optimum rotation angle. If post-stack rotation analysis is used, often the data have to be processed twice in order to get satisfactory results (Mike Mueller, Amoco, private communication). The data are first stacked without rotation to apply post-stack rotation analysis, then stacked again with pre-stack rotation using the angle determined from rotation analysis. Murtha (1988) derived an analytic $\tan 4\theta$ expression of rotation angle for reflection data without the rotation scanning procedure. This can also be achieved by complex component analysis.

The purpose of rotation analysis is to determine the optimum rotation angle which best separates the energy of the two shear-wave arrivals. The process depends on the coherency of the polarization. This optimum angle is the source-independent coherent polarization in the colour sections of complex components. Thus, instead of using post-stack rotation analysis, one can use complex component analysis of pre-stack data to determine the optimum rotation angle. It is only necessary to calculate the complex components and display colour sections, and to look for the coherent polarization that is independent of source orientation and that appears on all major reflection events. This procedure is much simpler than rotation analysis.

By calculating polarization logs, the interference of split shear-waves is resolved, and the determination of optimum angles for source-geophone rotation becomes more reliable, as demonstrated by the Lost Hills reflection data. There are two dominant coherent polarizations orthogonal to each other in logs. Thus, pre-stack rotation can be easily and efficiently implemented, and lateral variation of rotation angle along the survey line can be examined as one changes the location of polarization logs.

5. The German Creek crosshole data confirms that both variation of waveforms and variation of polarizations can be followed continuously either along time direction, or along offset direction as predicted in Chapter Four (Li and Crampin 1990b, 1991c), and complex component analysis provides a useful tool for cases where identification of wave types and recognition of polarization variations are essential.

6. In summary, complex component analysis is a simple, robust, and effective technique for analyzing shear-wave anisotropy in VSPs and reflection surveys. In the past, two methods have been used to examine shear-wave anisotropy in VSPs and reflection surveys: polarization analysis, and rotation analysis. Polarization analysis (analysis of polarization diagrams) relies principally on the shape of individual polarization pattern and is a straightforward technique;

while rotation analysis is mainly based on the coherency of whole polarizations and is relatively robust in the presence of noise. Both techniques are time-consuming. In contrast, complex component analysis allows both for the shape of individual polarization and the coherency of whole polarizations. Thus, complex component analysis retains the advantages of both techniques, but has fewer disadvantages. It is suggested that complex component analysis could well become a routine procedure in analyzing shear-wave anisotropy for VSPs and reflection surveys.

5.6 CONCLUSIONS

The field data confirm that instantaneous polarizations of shear-wave splitting have diagnostic shapes which are combinations of rectangular and semi-triangular shapes as described in Chapter Four (Li and Crampin 1990b, 1991c). The technique is developed for multi-source component seismic data. Four-component data can be used to calculate shear-wave splitting sections (SWS-sections) or transformed to calculate polarization logs. Complex component analysis of four-component shear-wave reflection data allows the optimum rotation angle between adjacent geophones and different sources to be determined before stacking without source-geophone rotation. Finally, polarizations of split shear-waves tend to be remarkably coherent. This coherency helps us to identify and estimate shear-wave splitting, and aids the stratigraphic interpretation of reflection events in VSPs and reflection surveys.

In conclusion, the theoretical promise in Chapter Four (Li and Crampin 1990b, 1991c) is confirmed by case studies, and complex component analysis can be further developed into four-component VSPs and reflection surveys. This technique of complex component analysis can aid identification and estimation of shear-wave splitting in VSPs and reflection surveys, help stratigraphic interpretation, and simplify the processing procedures for analyzing four-component reflection shear-wave data in the presence of anisotropy.

CHAPTER SIX

LINEAR-TRANSFORM TECHNIQUES FOR PROCESSING SHEAR-WAVE SPLITTING IN FOUR-COMPONENT SEISMIC DATA

ABSTRACT

Most published techniques for analyzing shear-wave splitting tend to be computing intensive, and make assumptions, such as the orthogonality of the two split shear-waves, which are not necessarily correct. This chapter presents a fast linear-transform technique for analyzing shear-wave splitting in four-component (two sources/two receivers) seismic data, which is flexible and widely applicable.

The four-component data are transformed by simple linear transforms so that complicated shear-wave motions are linearized in a wide variety of circumstances. This allows various attributes to be measured, including the polarizations of faster split shear-wave, and the time delays between faster and slower split shear-waves, as well as allowing the time series of the faster and slower split shear-waves to be separated deterministically. In addition, with minimal assumptions, the geophone orientations can be estimated for zero-offset VSPs, and the polarizations of the slower split shear-waves can be measured for offset VSPs. The time series of the split shear-waves can be separated before stack for reflection surveys. The technique has been successfully applied to a number of field VSPs and reflection data sets. Applications to a zero-offset VSP, an offset VSP, and a reflection dataset will be presented to

illustrate the technique.

6.1 INTRODUCTION

In the previous two chapters, I described complex component analysis for analyzing shear-wave splitting in seismic sections, where the polarizations and time delays of split shear-waves can be be interpreted visually from colour displays of instantaneous attributes. Here, I describe another technique for processing shear-wave splitting in seismic data, where large a amount of information about shear-wave splitting can be determined analytically.

The earliest techniques for processing shear-wave splitting were various types of rotation scanning. Alford (1986b) and Thomsen (1988) rotated the source and instrument axes of four-component data simultaneously (*synchronous source-geophone rotation*) to minimize the off-diagonal energy in the data matrix. Naville (1986) and Nicoletis et al. (1988) adopted a similar rotation procedure, but minimized off-diagonal elements in the propagation matrix. MacBeth and Crampin (1991a) minimized the spectral interference of two split shear-waves in the frequency domain. MacBeth and Crampin (1991b) adapted the *independent source-geophone rotation* technique of Igel and Crampin (1990) to an exploration context.

Most of these techniques tend to be computing intensive because of the rotation scanning procedure. In searching for more efficient techniques, Murtha (1989) developed an analytical expression for rotation angle in a specified time-window based on the technique of Alford (1986b) and Thomsen (1988). Guich (1989) further developed Murtha's technique into a statistical rotation procedure for three-dimentional multi-component shear-wave data. Li and Crampin (1990b, 1990d, 1991c, 1991d; also see Chapters 4 and 5) developed complex component analysis of shear-wave splitting.

All the above techniques (except complex component analysis) also make

assumptions, such as the orthogonality of the two split shear-waves, and that the crack strike in the rockmass is constant with depth, which are not necessarily correct. In searching for techniques which can deal with crack strike changing with depth, Winterstein and Meadows (1990, 1991a, 1991b) adapted the technique of Alford (1986b) and Thomsen (1988) into a layer-stripping procedure. However, the procedure still involves rotation scanning and is computing-intensive. [Note that more recently, analytical techniques for layer stripping and for monitoring acquisition system have been developed for zero-offset VSPs, where the orthogonality of split shear-waves can be assumed (Lefeuvre *et al.* 1991; Zeng and MacBeth 1992).]

Here, I present a new fast analytical technique, which is called the *linear-transform technique*, for analyzing shear-wave splitting in four-component seismic data (also see Li and Crampin 1991b; 1992a). I assume an acquisition geometry for four-component seismic data of two-horizontal sources and two horizontal receivers. The data are then transformed by simple linear transforms so that the complicated shear-wave motion is linearized in a wide variety of circumstances. The technique allows non-orthogonal split shear-waves for offset VSPs and reflection data, where the geophone orientation is known, and allows unknown downhole geophone orientation for zero-offset VSPs, where the orthogonality of the two split shear-waves can be assumed. The technique can be also extended into media where crack strikes change with depth.

A number of parameters can be determined by the linear-transform technique, including the polarizations of faster split shear-waves, the time delays between faster and slower split shear-waves, and the principal time series of faster and slower split shear-waves. In addition, the time series of split shear-waves can be separated before stack in reflection surveys. The technique has successfully applied to a number of field VSPs and reflection surveys, and will be illustrated with a zero-offset VSP, an offset VSP, and a reflection survey.

6.2 ASSUMPTIONS AND DEFINITIONS

6.2.1 Acquisition Geometry

Figure 6.1 shows the coordinate system with origin at the surface. Figure 6.1a shows the source geometry, where X and Y are two orthogonal source orientations, and **e1** and **e2** are two unit vectors representing the directions of faster and slower split shear-waves, respectively, for a given raypath, which are not necessarily orthogonal. **e1**, and **e2** are at angles of α' and β', respectively, from X-direction. Figure 6.1b shows the surface projection of the geophone geometry, where x and y are two orthogonal geophones, and **e1** and **e2** are same unit vectors as in Figure 6.1a, but are at angles α and β from the x-direction, respectively. All angles are measured clockwise from the X- and x-directions. Note that the geophone orientation in Figure 6.1b is different from the source orientation in 6.1a, and the medium between the source and the first geophone, and between successive geophones, is homogeneous with uniform distribution of cracks. Thus, any change in shear-wave polarization is assumed to occur at the levels of the geophones.

Figures 6.1a and 6.1b can be considered as typical VSP geometry. The geometry of reflection surveys can be considered as a special case of VSP geometry, where the source and geophone are all on surface and are orientated in the same direction. Hereafter, the geometry of VSPs and reflection surveys will not be treated separately, unless otherwise specified.

I further assume that the angle between the faster and slower split shear-waves is preserved throughout the homogeneous material. Consequently, overlaying Figures 6.1a and 6.1b, as shown 6.1c, gives:

$$\beta' - \alpha' = \beta - \alpha. \qquad (6\text{-}1)$$

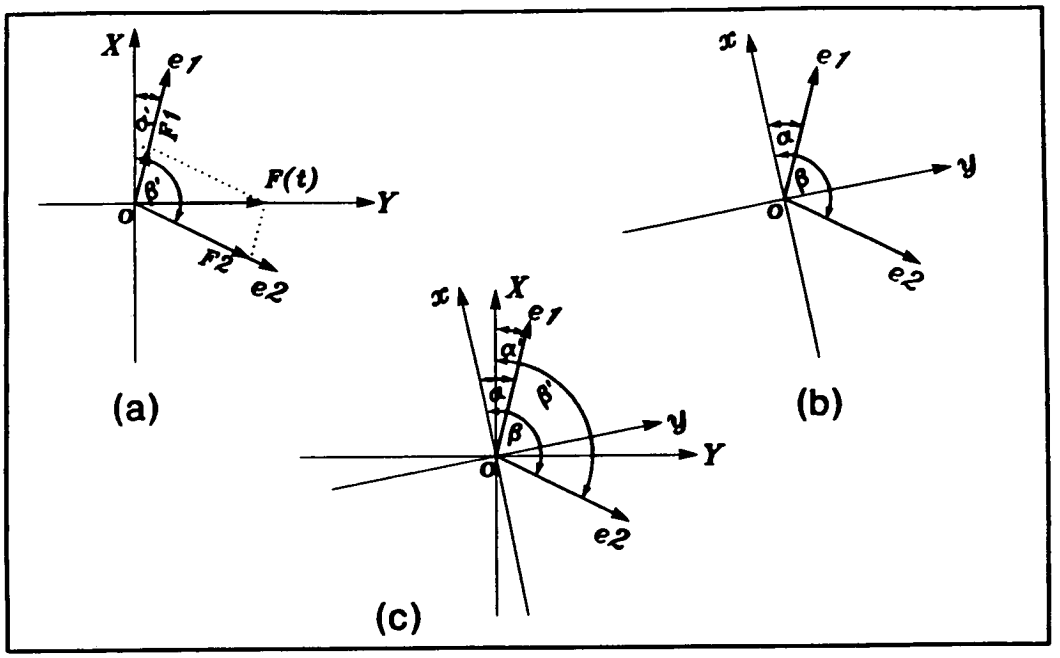

Figure 6.1. Diagrams showing the acquisition geometry and coordinate system in the horizontal plane. (a) Source geometry, where X and Y are two orthogonal sources with signature $F(t)$, **e1** and **e2** are the directions of faster and slower split shear-waves received at the geophone position, and **F1** and **F2** are two decompositions of the source vector **F**. (b) Geophone geometry, where x and y are two orthogonal geophones possibly in a different orientation from the sources, and **e1** and **e2** are same as (a). (c) Overlay of (a) and (b) for homogeneous medium where the effective shear-wave polarization does not change in the medium between the source and geophone.

6.2.2 Basic Assumptions

Anisotropy of the Earth.—It is assumed that anisotropy in the Earth is caused by stress-aligned fluid-filled inclusions (*EDA*-cracks), and the inclusions are uniformly distributed between the source and geophone. If this is satisfied the medium between the source and geophone is referred to as homogeneous. If the polarizations of the shear-waves change with depth, or angle of incidence, as reported by Winterstein and Meadows (1990, 1991a, 1991b) [and interpreted by them as implying changing crack orientations], the medium is called inhomogeneous. In such inhomogeneous anisotropy, it is possible to extrapolate the source downwards, as demonstrated by Winterstein and Meadows (1991b).

Source signature.—$F(t)$ is used to represent the signature of the source, which is assumed to be the same for both X- and Y-source orientations. This is an assumption in field acquisition, which many of the reported multi-component datasets appear to satisfy, at least approximately (Alford 1986b; Squires et al. 1989; Winterstein and Meadows 1990, 1991a, 1991b).

Geophone orientations.— The geophone orientation may change between different locations, particularly at different levels in VSPs, but for a given location the orientation is fixed for both X- and Y-sources. This requirement is again usually satisfied in field acquisition.

Polarizations of the split shear-waves.— The polarizations of the split shear-waves are fixed for a given raypath direction. This implies that the angles α', β', α and β are invariant over a time window which covers a specific shear-wave arrival, but may change for different arrivals as different raypaths are involved. These conditions are believed to be generally satisfied in most anisotropic materials.

Principle of superposition.— It is assumed that a source vector **F** with signature $F(t)$ can be decomposed into two subsources **F1** and **F2** along **e1** and **e2** with signatures $F1(t)$ and $F2(t)$, respectively (Figure 6.1a), and that the wave field excited by source vector **F** in the medium is equivalent to the wave field excited simultaneously by subsources **F1** and **F2**. This assumption is called the *principle of superposition*.

With the above assumptions, where α' and β' in Figure 6.1 are the angles of the faster and slower split shear-waves from X-direction, it gives (see Appendix C):

$$F1(t) = -F(t)\cos\beta'/\sin(\beta'-\alpha'); \text{ and}$$
$$F2(t) = F(t)\cos\alpha'/\sin(\beta'-\alpha'). \qquad (6\text{-}2)$$

The principal time series $qS1(t)$ of the faster split shear-wave is defined as the time series received at a receiver when the receiver and a source vector **F** with signature $F(t)$ are both polarized along **e1**. Similarly, the principal time series $qS2(t)$ of the slower split shear-waves is defined as the time series received when the receiver and the source vector **F** are both polarized along **e2**. The concept of the principal time series was introduced by Alford (1986b) and Thomsen (1988). Here I give an alternative geometrical definition.

I introduce two transformed time series $V1(t)$ and $V2(t)$ as the sum and difference, respectively, of the principal time series $qS1(t)$ and $qS2(t)$:

$$V1(t) = qS1(t) + qS2(t);$$
$$V2(t) = qS1(t) - qS2(t). \qquad (6\text{-}3)$$

6.3 THE LINEAR-TRANSFORM TECHNIQUE

6.3.1 Equations of four-component data

With the acquisition geometry in homogeneous anisotropic medium shown in Figure 6.1, and the principle of superposition, the *X*-source can be decomposed into subsources as shown Figure 6.1a. The amplitudes of the faster and slower split shear-waves excited by *X*-source can be written as (see Appendix C):

$$\begin{aligned} &qS1(t)\ \sin\beta'/\sin(\beta'-\alpha'); \text{ and} \\ &-qS2(t)\ \sin\alpha'/\sin(\beta'-\alpha'); \quad \text{respectively;} \end{aligned} \tag{6-4}$$

where $qS1(t)$, and $qS2(t)$ are the principal time series of faster, and slower split shear-waves, respectively; and α' and β' are the angles in Figure 6.1a and 6.1c.

The four-component time series $s_{ij}(t)$ is defined as the signal recorded from *X*- and *Y*-sources ($j = 1, 2$) on *x*- and *y*-geophones ($i = 1, 2$). The two geophone components $s_{11}(t)$ and $s_{21}(t)$ from the *X*-source can be written as:

$$\begin{aligned} s_{11}(t) &= [qS1(t)\ \sin\beta'\cos\alpha - qS2(t)\ \sin\alpha'\cos\beta]/\sin(\beta'-\alpha'); \text{ and} \\ s_{21}(t) &= [qS1(t)\ \sin\beta'\sin\alpha - qS2(t)\ \sin\alpha'\sin\beta]/\sin(\beta'-\alpha'). \end{aligned} \tag{6-5}$$

Similarly, the amplitudes of the faster and slower split shear-waves excited by *Y*-source are (see Appendix C):

$$\begin{aligned} &-qS1(t)\ \cos\beta'/\sin(\beta'-\alpha'); \text{ and} \\ &qS2(t)\ \cos\alpha'/\sin(\beta'-\alpha'); \end{aligned} \tag{6-6}$$

and the two components of $s_{12}(t)$ and $s_{22}(t)$ can be written as:

$$s_{12}(t) = [-qS1(t)\cos\beta'\cos\alpha + qS2(t)\cos\alpha'\cos\beta]/\sin(\beta'-\alpha'); \text{ and}$$
$$s_{22}(t) = [-qS1(t)\cos\beta'\sin\alpha + qS2(t)\cos\alpha'\sin\beta]/\sin(\beta'-\alpha'). \quad (6\text{-}7)$$

These are basic relations between the recorded components and the principal time series of split shear-waves. The equations could be solved by computer-intensive rotation scanning techniques, as suggested by Alford (1986b) and Thomsen (1988). Here, I apply linear transforms to the four-component datasets:

$$\xi(t) = s_{11}(t) - s_{22}(t); \quad (6\text{-}8)$$
$$\eta(t) = s_{21}(t) + s_{12}(t); \quad (6\text{-}9)$$
$$\zeta(t) = s_{11}(t) + s_{22}(t); \text{ and} \quad (6\text{-}10)$$
$$\chi(t) = s_{12}(t) - s_{21}(t). \quad (6\text{-}11)$$

Combining these various equations gives:

$$\xi(t) = [qS1(t)\sin(\alpha+\beta') - qS2(t)\sin(\alpha'+\beta)]/\sin(\beta'-\alpha');$$
$$\eta(t) = -[qS1(t)\cos(\alpha+\beta') - qS2(t)\cos(\alpha'+\beta)]/\sin(\beta'-\alpha');$$
$$\zeta(t) = [qS1(t)\sin(\beta'-\alpha) + qS2(t)\sin(\beta-\alpha')]/\sin(\beta'-\alpha'); \text{ and}$$
$$\chi(t) = -[qS1(t)\cos(\beta'-\alpha) - qS2(t)\cos(\beta-\alpha')]/\sin(\beta'-\alpha'). \quad (6\text{-}12)$$

[Linear transforms (6-8) and (6-9) were first used by Li and Crampin (1990b, 1990d; also see Chapter 5) to calculate polarization logs in reflection surveys, when the components of geophone and source were assumed to be orientated in the same direction, either in the acquisition geometry, or by subsequent rotation.]

There are six unknowns in five equations in equations (6-1) and (6-12); and there will be no exact solutions unless further constraints are introduced. I discuss two cases. The first is the case with orthogonally polarized shear-waves, as in zero-offset VSPs (or, stack sections), where the linear transform technique allows the orientations of downhole geophones to be determined.

The second is the case with non-orthogonally polarized shear-waves, as in offset VSPs, where the orientation of downhole geophones are known, from the polarization of *P*-arrival, for example, and the angle of separation of the split shear-waves can be determined, and the orthogonality of the split shear-waves can then be tested. A reflection survey can be considered as a special case of an offset VSP.

6.3.2 Orthogonal split shear-waves

I assume that the two split shear-waves in a crack-induced anisotropic medium are orthogonal to each other at vertical incidence, as in zero-offset VSPs, or the stacked sections in a reflection survey. [The orientation of the faster split shear-wave is often associated with the crack strike.] Noting that $\beta = \pi/2 + \alpha$ and $\beta' = \pi/2 + \alpha'$, equations (6-12) can be rewritten as:

$$\begin{aligned} \xi(t) &= [qS1(t) - qS2(t)] \cos(\alpha' + \alpha) \\ \eta(t) &= [qS1(t) - qS2(t)] \sin(\alpha' + \alpha) \end{aligned} \tag{6-13}$$

and

$$\begin{aligned} \zeta(t) &= [qS1(t) + qS2(t)] \cos(\alpha' - \alpha) \\ \chi(t) &= [qS1(t) + qS2(t)] \sin(\alpha' - \alpha) \end{aligned} \tag{6-14}$$

Equation (6-13) shows that the time series $V2(t) = qS1 - qS2$ represents linear motion in coordinate system (ξ, η) with angle $\alpha' + \alpha$ to the axis ξ, and equation (6-14) shows that time series $V1(t) = qS1 + qS2$ represents linear motion in coordinate system (ζ, χ) with angle $\alpha' - \alpha$ to the ζ axis. From the properties of linear motion in Appendix D, *V1* and *V2*, and $\alpha' + \alpha$ and $\alpha' - \alpha$ can be uniquely determined. Thus, $qS1 = (V1 + V2)/2$ and $qS2 = (V1 - V2)/2$, and α and α' can be determined, and the orientation of the geophone can be estimated from $\alpha - \alpha'$.

6.3.3 Non-orthogonal split shear-waves

In off-vertical incidence, the polarizations of the faster and slower split shear-waves in the horizontal plane may not be orthogonal. Such cases include offset-VSPs, and pre-stack data in reflection surveys, but non-orthogonally polarized shear-waves may also be present in zero-offset VSPs if the structure is not horizontal. [Note that there are two principal reasons for the non-orthogonality of shear-waves. The polarizations of split shear-waves along raypaths in directions without axial symmetry are not usually orthogonal (Crampin 1981), except in media with transverse isotropy, and in any case the orientations of non-vertically propagating shear-waves will be further distorted in the horizontal plane.]

In all cases of non-orthogonality, it is reasonable to assume that the orientation of geophone is the same as the source. This is usually true in reflection surveys. In offset VSPs, even without gyro data, the orientations of geophones can usually be determined from the polarization of *P*-waves, so that the horizontal recordings can be digitally rotated so that the axes of source and geophone do effectively coincide. If the orientation of the geophone is the same as the source, that is, $\alpha = \alpha'$, and $\beta = \beta'$, equations (6-12) can be re-written as:

$$\xi(t) = [qS1(t) - qS2(t)] \sin(\alpha+\beta)/\sin(\beta-\alpha); \text{ and}$$
$$\eta(t) = -[qS1(t) - qS2(t)] \cos(\alpha+\beta)/\sin(\beta-\alpha); \qquad (6\text{-}15)$$

and

$$\zeta(t) = qS1(t) + qS2(t); \text{ and}$$
$$\chi(t) = -[qS1(t) - qS2(t)] \cos(\beta-\alpha)/\sin(\beta-\alpha). \qquad (6\text{-}16)$$

Thus, time series $V1 = qS1 + qS2 = \zeta(t)$ is directly given by equation (6-16), and $V2 = qS1 - qS2$ can be determined as follows. I now introduce a

time series $U(t)$, satisfying:

$$U(t) = [qS1(t) - qS2(t)]/\sin(\beta-\alpha); \tag{6-17}$$

so that equations (6-15), (6-16), and (6-17) can be written as:

$$\begin{aligned}\xi(t) &= \quad U(t)\sin(\alpha+\beta);\\ \eta(t) &= -\,U(t)\cos(\alpha+\beta);\ \text{and}\\ \chi(t) &= -\,U(t)\cos(\beta-\alpha).\end{aligned} \tag{6-18}$$

Similarly, equations (6-17) and (6-18) show that $U(t)$ is also linear in coordinate system $(\xi, -\eta)$. Consequently, $V1 = qS1 + qS2$, $V2 = qS1 - qS2$, and angles $\alpha-\beta$ and $\alpha+\beta$ can also be estimated from linear transforms. Thus, the faster split shear-wave $qS1$ and polarization angle α, and the slower split shear-wave, $qS2$ and angle β can be directly determined. Angle $\beta-\alpha$ is the angle between the faster and slower split shear-wave and is a measure of the orthogonality of the split shear-waves.

In summary, instead of solving for $qS1$ and $qS2$ directly in zero-offset or wider-offset VSPs, after linear transforms, the time series of the split shear-waves, $qS1 = (V1 + V2)/2$ and $qS2 = (V1 - V2)/2$, can be separated directly, and their various polarizations measured, regardless of the orthogonality of split shear-waves.

6.4 VERIFYING THE LINEAR-TRANSFORM TECHNIQUE

To verify this technique, I demonstrate the linearity of the transformed time series in field VSPs, and apply the technique to a synthetic VSP, where the polarizations and amplitudes of the split shear-waves are known.

6.4.1 Linearity of V1 and V2

Equations (6-13) and (6-14) show that *V1* and *V2* are expected to have linear-motion in the transformed coordinate system for zero-offset VSPs. This is tested with field data in Figure 6.2, which shows polarization diagrams (PDs, or hodograms) in the horizontal plane of a zero-offset VSP from BP's test site at Devine, Texas. Figure 6.2a shows PDs of the in-line (*X*-) source (the particle motion of s_{11} and s_{21}), and Figure 6.2b shows PDs of the cross-line (*Y*) source (particle motion of s_{12} and s_{22}), at the same geophones. Shear-wave splitting is difficult to identify because the small delay between the two split shear-waves makes the motion elliptical. Figure 6.2c shows PDs of the transformed motions, *V2*(*t*) (particle motion of $\xi = s_{11} - s_{22}$ and $\eta = s_{12} + s_{21}$); and Figure 6.2d shows PDs of the transformed motions , *V1*(*t*) (particle motion of $\zeta = s_{11} + s_{22}$ and $\chi = s_{12} - s_{21}$). Almost all of the patterns of the transformed motions in the PDs of Figures 6.2c and 6.2d are essentially linear as expected, despite the ellipticity of the original particle motion.

Note that if the anisotropy is small, similar to the case of an isotropic medium, the orientations of PDs (the polarization direction of the main ellipse) of recorded shear-wave components at near vertical incidence will often preserve the orientations of the sources. Thus the orientations of PDs in Figures 6.2a and 6.2b are expected to be orthogonal for a given geophone level because PDs in 6.2a and 6.2b correspond to two orthogonal sources and time delay between the two split shear-waves, hence the anisotropy, are small. However, the orientations of transformed PDs in 6.2c and 6.2d are dependent on angles $\alpha' + \alpha$ and $\alpha' - \alpha$, respectively, as shown in equations (6-13) and (6-14). If geophone *x* direction happens to be close to **e1** in Figure 6.1b, angle α will be small and angles $\alpha' + \alpha$ and $\alpha' - \alpha$ will be close. Thus the orientations of the transformed PDs in this case will be almost parallel as shown in geophone 32, 39, and etc. in (c) and (d) of Figure 2. As α' (source *X*-direction) is fixed and α (geophone *x*-direction) varies with depth, the orientation of PDs of the transformed components in Figure 6.2c and 6.2d will

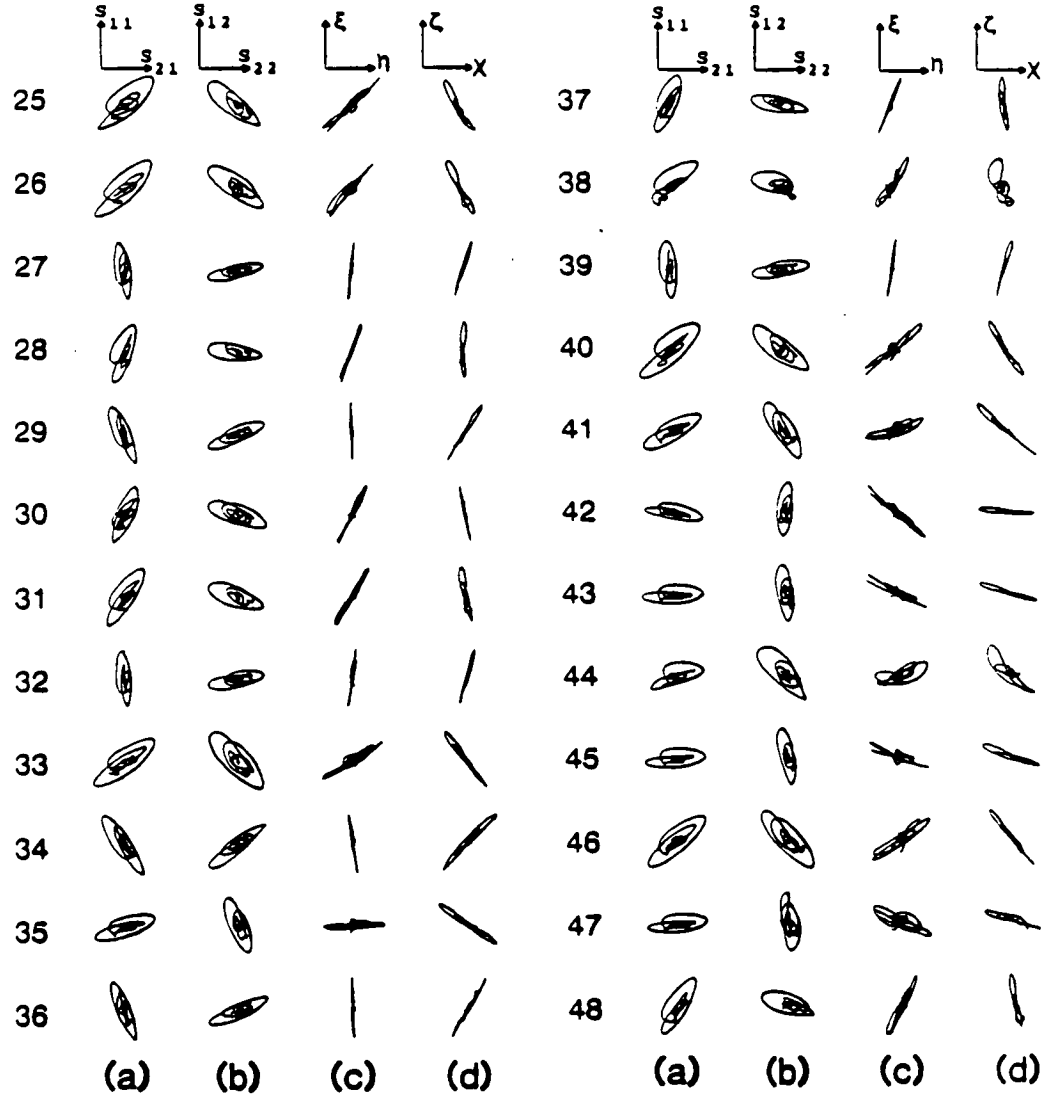

Figure 6.2. Polarization diagrams (PDs) of a zero-offset VSP from BP's test site at Devine, Texas, showing the linearity of the transformed motions: (a) in-line source (X-source), $s_{11}(t)$ and $s_{21}(t)$; (b) cross-line source (Y-source), $s_{12}(t)$ and $s_{22}(t)$; (c) transformed components, $\xi(t)=s_{11}(t)-s_{22}(t)$ and $\eta(t)=s_{12}(t)+s_{21}(t)$; and (d) transformed components $\zeta(t)=s_{11}(t)+s_{22}(t)$ and $\chi(t)=s_{12}(t)-s_{21}(t)$.

vary with depth.

Figure 6.3 shows similar PDs in the horizontal plane of an offset-VSP, also from Devine, Texas. Figures 6.3a and 6.3b show the polarizations of in-line and cross-line (*X*- and *Y*-) sources received at horizontal geophones, as in Figure 6.2. Again the recorded shear-motion is elliptical. Figure 6.3c shows PDs of the transformed motion of $V2(t)$ in coordinate system (ξ, η) from equations (6-15). Again the motion in Figure 6.3c is essentially linear. Note that the essentially linear motion of motion $V1(t)$ is already determined by equation (6-25), it is not shown here. Also note that in Figure 6.3, the geophones are rotated so that all the geophones are effectively orientated in the same direction as the sources, thus the orientations of the PDs in Figure 6.3 do not change with depth.

In summary, although the particle motion of shear-waves as recorded are frequently elliptical, the linear transforms of the sum and difference of the split shear-waves, *V1* and *V2*, respectively, are linear. Consequently, the time series of the split shear-waves can be directly separated by recombining *V1* and *V2*.

6.4.2 Testing with synthetic data

I test the technique for measuring the polarization, time-delay, geophone orientation, and orthogonality with synthetic data. The data are taken from the response of the Edinburgh Anisotropy Project to the Anisotropy Modelling Collaboration, VSP Model 1 (Thomsen et al. 1989). The VSP has a 500m offset, to a maximum depth of 2500m, but for the purposes of this analysis it is treated as a zero-offset, that is, the polarizations of the two split shear-waves in the horizontal plane are assumed to be orthogonal.

Figure 6.4a shows the comparison of measured and expected time delay between the split shear-waves; Figure 6.4b shows the comparison of measured and expected polarizations (where the top layer of the model is isotropic);

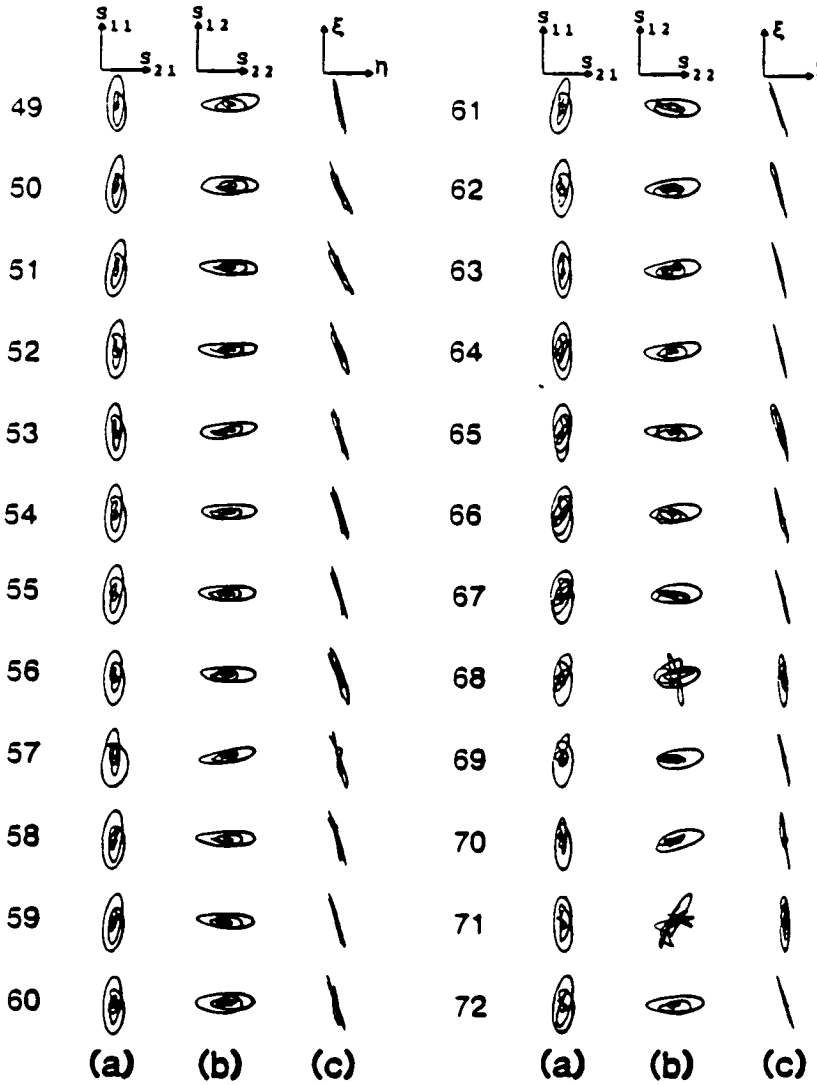

Figure 6.3. PDs of an offset VSP [offset 600 ft (190 m)], also from Devine, Texas, showing the linearity of the transformed motions: (a) in-line source, $s_{11}(t)$ and $s_{21}(t)$; (b) cross-line source, $s_{12}(t)$ and $s_{22}(t)$; and (c) transformed components $\xi(t)=s_{11}(t)-s_{22}(t)$ and $\eta(t)=s_{12}(t)+s_{21}(t)$.

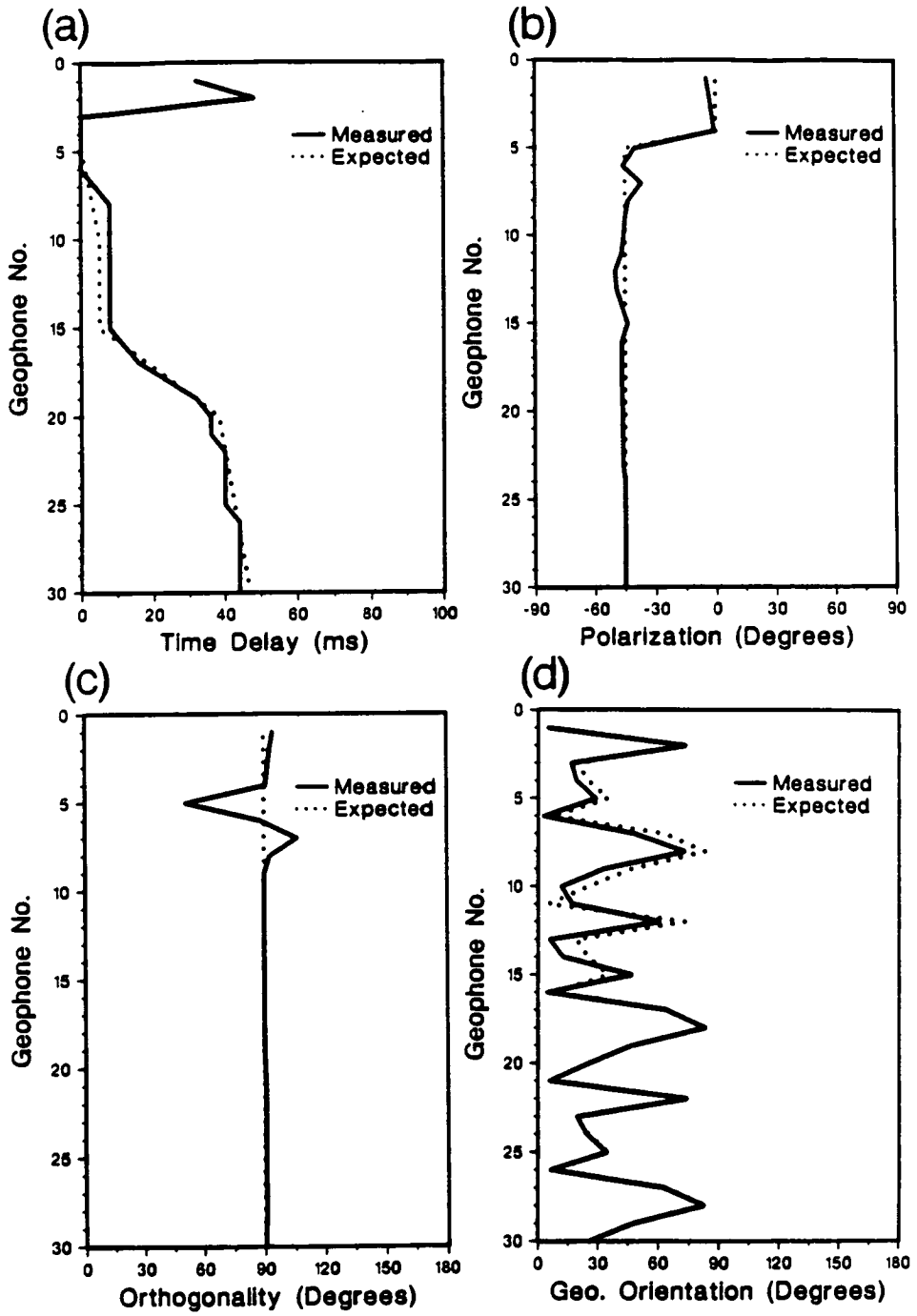

Figure 6.4. Test with synthetic AMC VSP data showing comparison of measured attributes (solid line) with expected values (dotted line): (a) time delay between the faster and slower split shear-waves; (b) polarization of the faster split shear-wave measured from the source *X*-direction. (c) orthogonality, angle between the faster and slower split shear waves; and (d) geophone orientation (*x*-direction) measured from *X*-source direction, where the expected values have been disturbed.

Figure 6.4c shows the measured and expected anlge of separation of the split shear-waves (orthogonality); and Figure 6.4d shows the comparison of the geophone orientation measured and known orientation, which has been deliberately modified for the purposes of the test. The match of measured to expected results for time delays (Figure 6.4a) is good, except for the top two geophones which are too close to the source and are noisy. The match for polarizations (Figure 6.4b) is good for all geophones. The match for orthogonalities is good, except for geophones 5 to 7 which are located at, or close to the isotropic/anisotropic interface where the time delay starts to build up as shown Figure 6.4a, and some interferences of split shear-waves exist. The match for geophone orientations is good for all geophones (Figure 6.4d), but for the top 15 geophones there are 10~15° differences between the measured and expected results, which is possibly due to the small time delays between the two split shear-waves for the top 15 geophones as shown in Figure 6.4a, and it is likely that there are some interferences of split shear-waves. Despite this, the overall match is good.

6.5 APPLICATIONS TO FIELD DATA

I now apply the technique to field datasets, zero-offset and wide offset VSPs from BP's test site at Devine, Texas, and a shot gather from the Kim-Tech Lost Hills reflection line. A full discussion of the Devine VSP, geology and interpretation is given by Raikes (1991) and Yardley (1992); and of the Lost Hills reflection data was given by Squires *et al.* (1989).

6.5.1 Zero-offset VSP

The technique has been applied with satisfactory results to a number of zero-offset VSPs, without gyro data so that geophone orientations are unknown. I choose a VSP from Devine as an example.

Figure 6.5a shows four-component seismic data matrix from a Devine

Figure 6.5. Results from the zero-offset VSP from Devine in Figure 6.2. (a) Four-component seismic data matrix showing four record sections $s_{11}(t)$, $s_{21}(t)$, $s_{12}(t)$, and $s_{22}(t)$; note that the gain applied to s_{21} and s_{12} is four times larger than the gain applied to s_{11} and s_{22}; (b) record section of faster and slower split shear-waves, $qS1(t)$ and $qS2(t)$, measured from data matrix (a); the same constant gain as used for components s_{11} and s_{22} was applied to components *qS1* and *qS2;* (c) measured time delay against depth; (d) measured polarization direction of faster split shear waves; and (e) comparison of geophone orientations (x-direction) estimated by the linear transform technique (solid line) and by visual examination of polarization diagrams, PDs (dotted line), where both attributes are measured from the source X-direction.

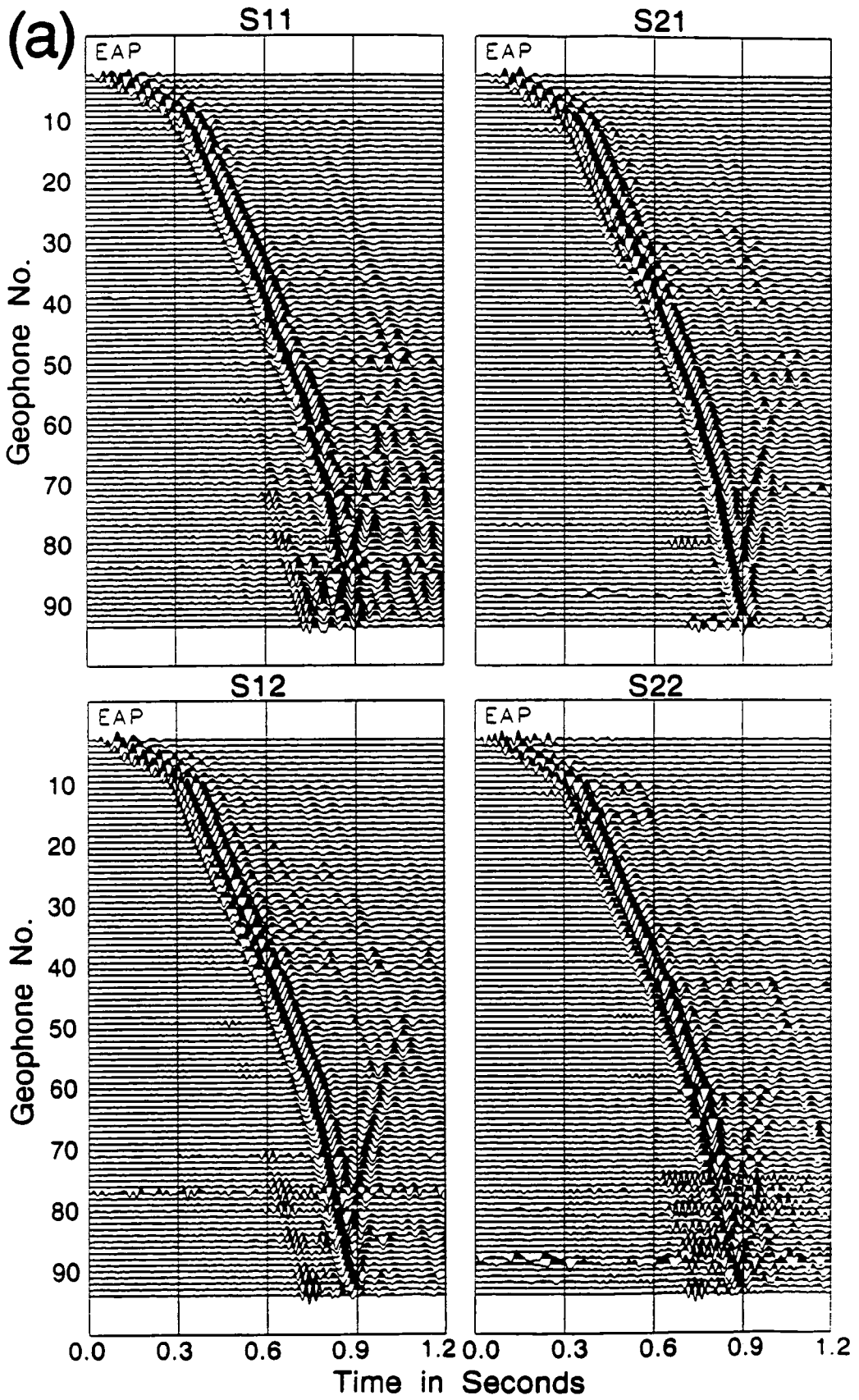
(a)
S11
S21
S12
S22
EAP
EAP
EAP
EAP
Geophone No.
Geophone No.
10
20
30
40
50
60
70
80
90
0.0
0.3
0.6
0.9
1.2
Time in Seconds

Figure 6.5a

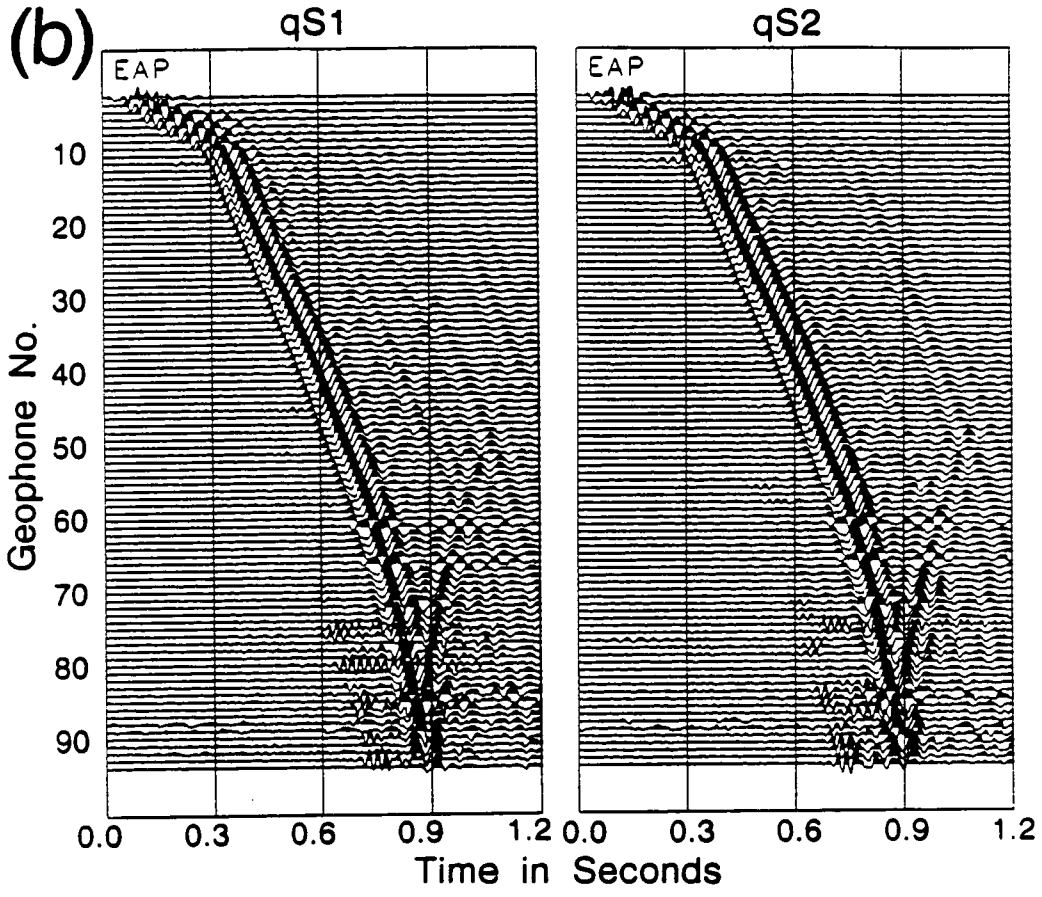
(b)
qS1
qS2
EAP
EAP
Geophone No.
10
20
30
40
50
60
70
80
90
0.0
0.3
0.6
0.9
1.2
0.0
0.3
0.6
0.9
1.2
Time in Seconds

Figure 6.5b

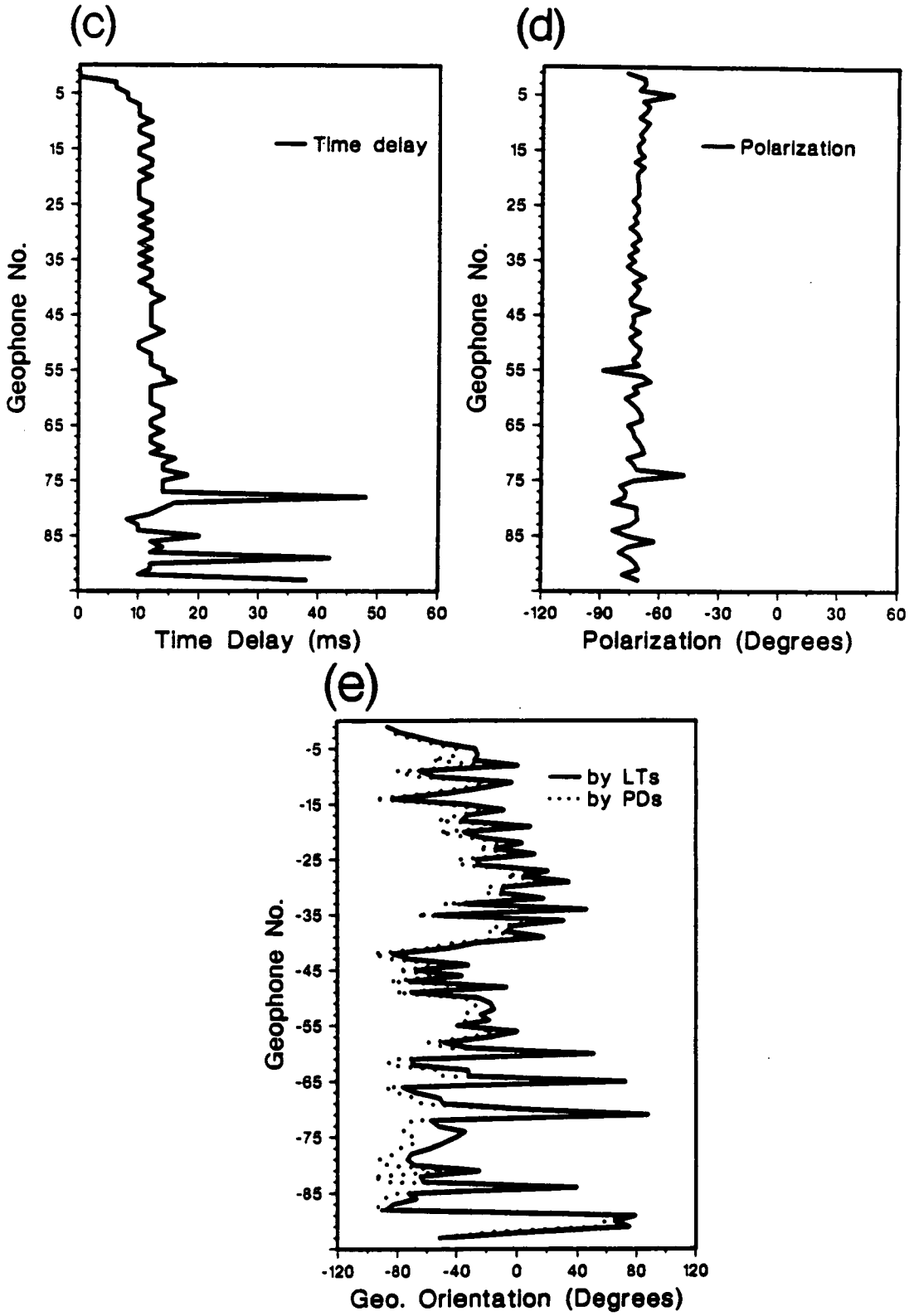
(c)
Time delay
Geophone No.
5
15
25
35
45
55
65
75
85
0
10
20
30
40
50
60
Time Delay (ms)
(d)
Polarization
Geophone No.
-120
-90
-60
-30
0
30
60
Polarization (Degrees)
(e)
by LTs
by PDs
Geophone No.
-5
-15
-25
-35
-45
-55
-65
-75
-85
-120
-80
-40
0
40
80
120
Geo. Orientation (Degrees)

Figure 6.5c

VSP, and Figure 6.5b shows the faster and slower split shear-waves separated by the linear transform technique. Note that in displaying Figure 6.5a, the gain applied to components s_{21} and s_{12} is four times larger than the gain applied to components s_{11} and s_{22} in order to show the variation of waveforms in component s_{21} and s_{12} clearly. Comparison of Figures 6.5a and 6.5b shows that the overall signal-to-noise ratio is slightly improved by the separation, with the direct shear arrivals being more consistent between geophone levels. Detailed comparison of the separated split shear-waves shows almost identical waveforms with a very small time delay.

Figure 6.5c shows the measured time delays. The trend of variation of the time delay agrees with a preliminary analysis based on PDs by Gareth Yardley (Yardley 1992). Figure 6.5d shows the polarization of leading split shear-wave, which is consistent between geophones with a gradually linear change of polarization angle with depth. This linear change of polarization angle with depth may represent some kind of crack orientation changing with depth, but may also represent the differential attenuations of faster and slower split shear-waves. The slower split shear-wave tends to be affected and attenuated more than the faster split shear-wave (Thomsen 1988; Mueller 1991). As depth increases, such attenuation of slower split shear-waves will increase, which results in a gradual change of polarization angle with depth. There are also other factors, such as, irregularities in field acquisition, which may cause polarization change. It is possible to separate these factors by full-wave forward modelling (Gareth Yardley, personal communication).

Figure 6.5e shows geophone orientations (x-direction measured from the X-source direction) determined by the linear transform technique (solid line) compared with those estimated from PDs (dotted line). There are 10~20° differences between the two kinds of measurements, for which there are two possible reasons. On one hand, when the time delay is small, measurements of geophone orientation by linear transform technique may yield 10~15° differences, as shown in the synthetic results of Figure 6.4d. On the other

hand, visual examination of polarization diagrams may easily introduce an error of 5~10°. Despite all these, the trend of the variation of the two kinds of measurements matches very well, and the results are generally acceptable.

6.5.2 Offset VSP

The technique has been applied to several offset VSPs from Devine BP, and elsewhere, where the geophone orientation is determined from the polarizations of *P*-waves. One example from Devine is presented. Figure 6.6a shows the seismic data matrix, and Figure 6.6b shows the separated split shear-waves. Same gains as used in Figure 6.5a and 6.5b were applied to display Figure 6.6a and 6.6b. Again the signal-to-noise ratio is improved, and the two split shear-waves are consistent in the separated data. Figure 6.6c compares the delay between the split shear-waves from assuming orthogonal measurements from equations (6-13) and (6-14), and the delay from allowing non-orthogonal shear-waves polarizations from equations (6-15) and (6-16). The time delays from assuming orthogonal and non-orthogonal polarizations are almost identical, presumably because the polarizations are nearly orthogonal. As in the zero-offset in Figure 6.5, the delays increase gradually with depth. Figure 6.6d shows the polarizations of the shear-waves and the estimated angle of separation. The measured polarizations are similar to those of the zero offset VSP (Figure 6.5d). The angle of separation of the two split shear-waves are about the 90° line, as expected from the comparison of the delays in Figure 6.6c.

6.5.3 Reflection survey

Again the technique has been applied to several reflection data sets, where the geophone orientation is same as the source orientation. A shot gather from the Kim-Tech Lost Hills reflection line is presented as an illustration.

Figure 6.7a shows the seismic data matrix, and Figure 6.7b shows the

Figure 6.6. Results from the offset VSP from Devine shown in Figure 6.3. The offset is 750 ft (190m). (a) and (b) have same notations as in Figures 6.5a, and 6.5b; the gain is also the same as in Figure 6.5a and 6.5b; (c) shows comparison of time delay measured using the orthogonal algorithm [equations (6-13) and (6-14)] (solid line); and using the non-orthogonal algorithm [equations (6-15) and (6-16)] (dotted line); and (d) shows the measured orthogonality, angle between the two split shear-waves (dotted line), and polarization angles of the faster split shear-waves (solid line), where both attributes are measured from source *X*-direction.

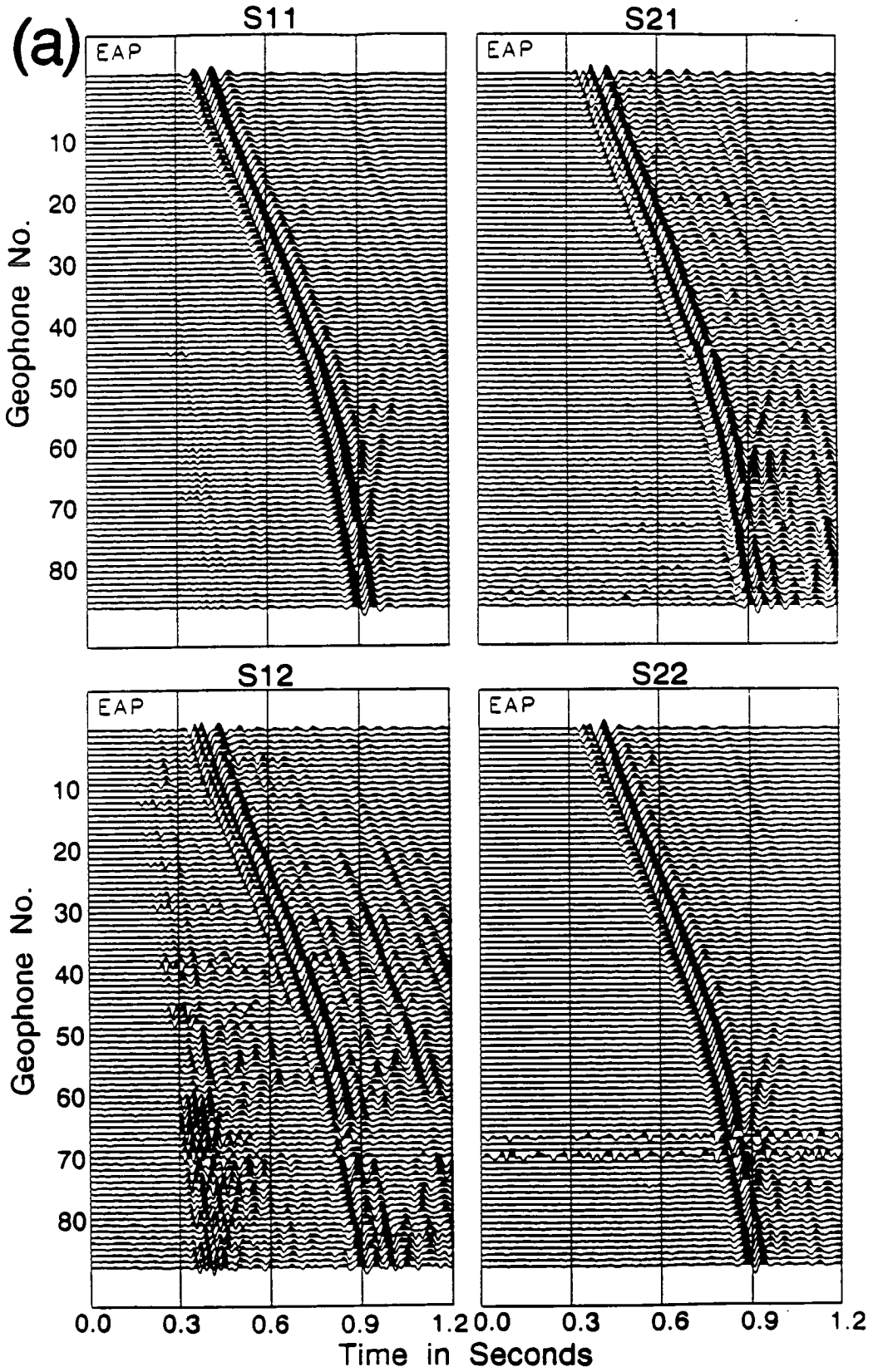
(a)
S11
S21
S12
S22
EAP
EAP
EAP
EAP
Geophone No.
Geophone No.
10
20
30
40
50
60
70
80
0.0
0.3
0.6
0.9
1.2
Time in Seconds

Figure 6.6a

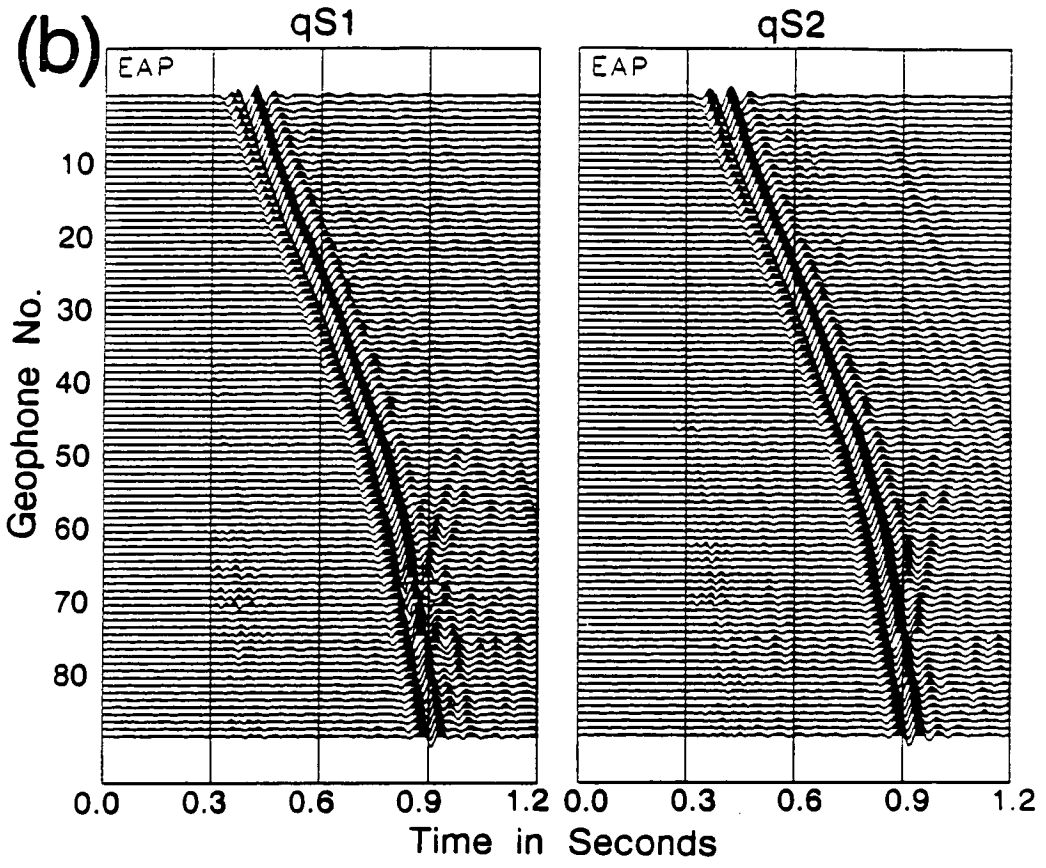
(b)
qS1
qS2
EAP
EAP
Geophone No.
10
20
30
40
50
60
70
80
0.0
0.3
0.6
0.9
1.2
0.0
0.3
0.6
0.9
1.2
Time in Seconds

Figure 6.6b

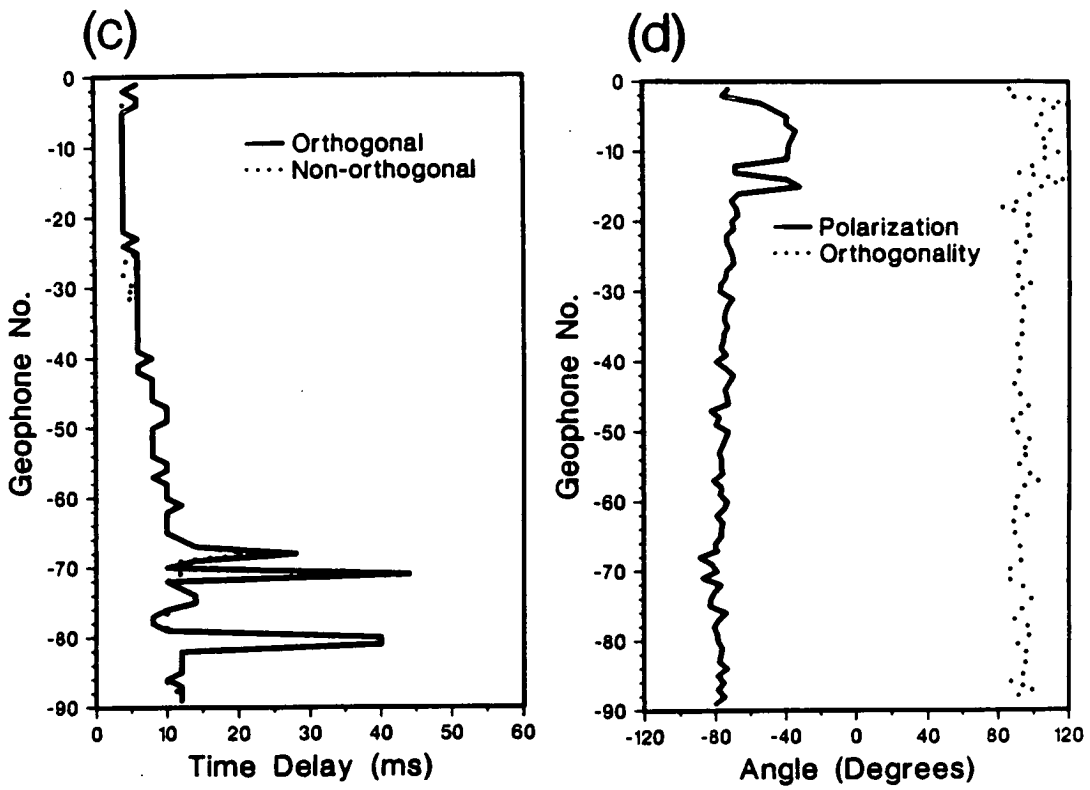
(c)
Orthogonal
Non-orthogonal
Geophone No.
0
-10
-20
-30
-40
-50
-60
-70
-80
-90
0
10
20
30
40
50
60
Time Delay (ms)
(d)
Polarization
Orthogonality
Geophone No.
-120
-80
-40
0
40
80
120
Angle (Degrees)

Figure 6.6c

Figure 6.7. Results from Lost Hills reflection data. (a) Four-component data matrix of a shot record from the Lost Hills dataset showing four record sections, $s_{11}(t)$, $s_{21}(t)$, $s_{12}(t)$, and $s_{22}(t)$; a constant gain was applied to all four components; (b) measured amplitude section of faster and slower shear-waves, $qS1(t)$ and $qS2(t)$; the same constant gain as (a) was used here; and (c) colour plot of polarization variations of split shear-waves.

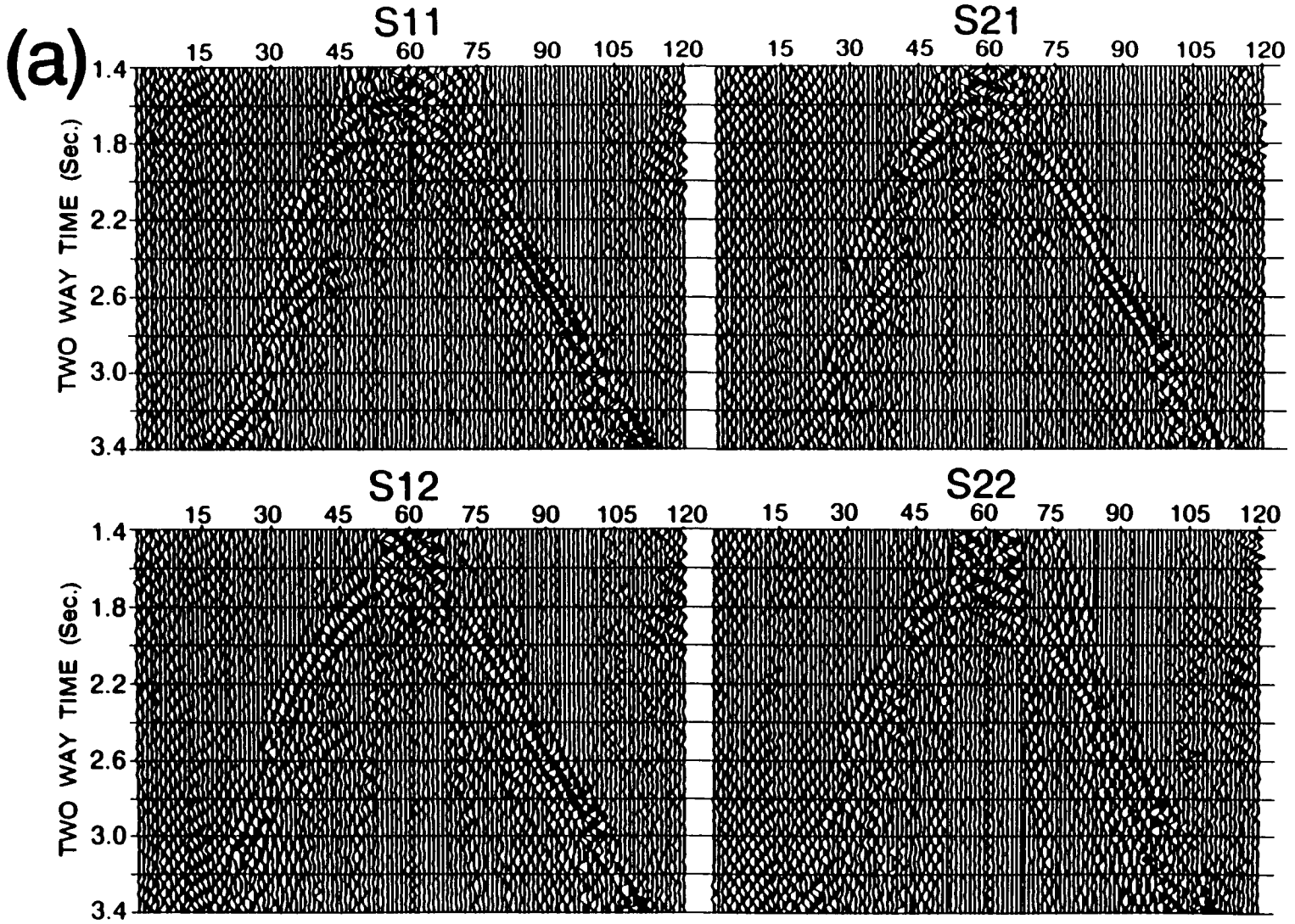
(a)
S11
S21
S12
S22
15 30 45 60 75 90 105 120
TWO WAY TIME (Sec.)
1.4
1.8
2.2
2.6
3.0
3.4

Figure 6.7a

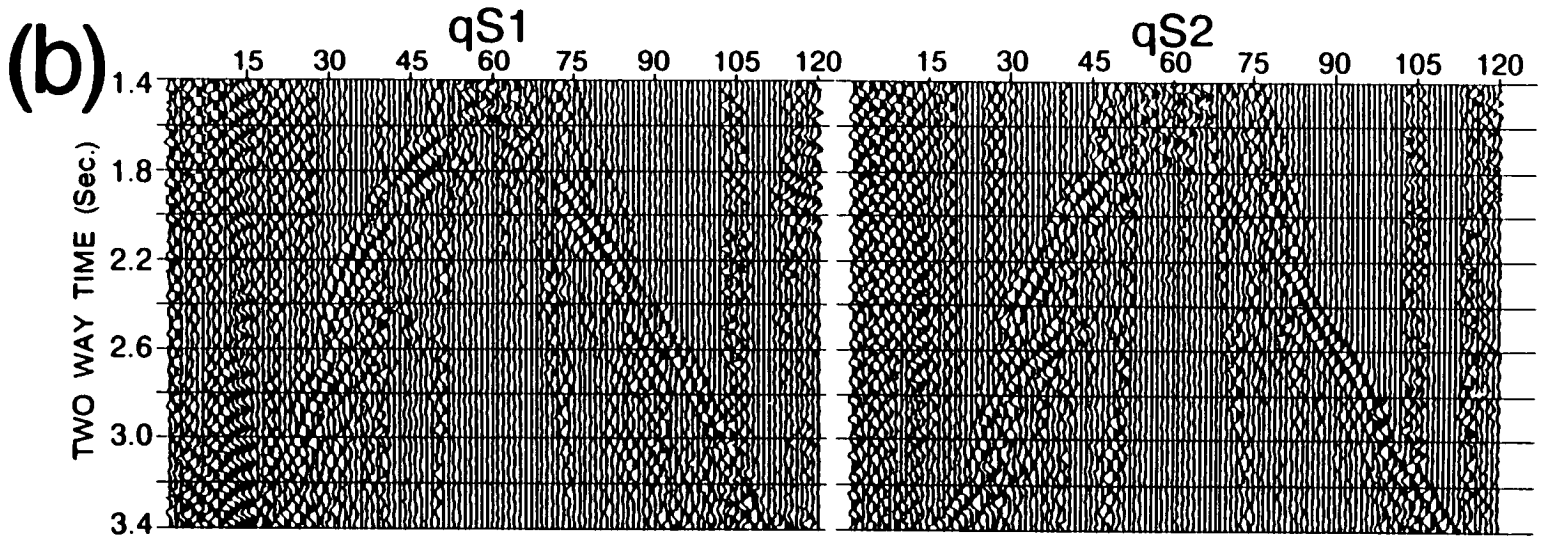
(b)
qS1
qS2
15 30 45 60 75 90 105 120
15 30 45 60 75 90 105 120
TWO WAY TIME (Sec.)
1.4
1.8
2.2
2.6
3.0
3.4

Figure 6.7b

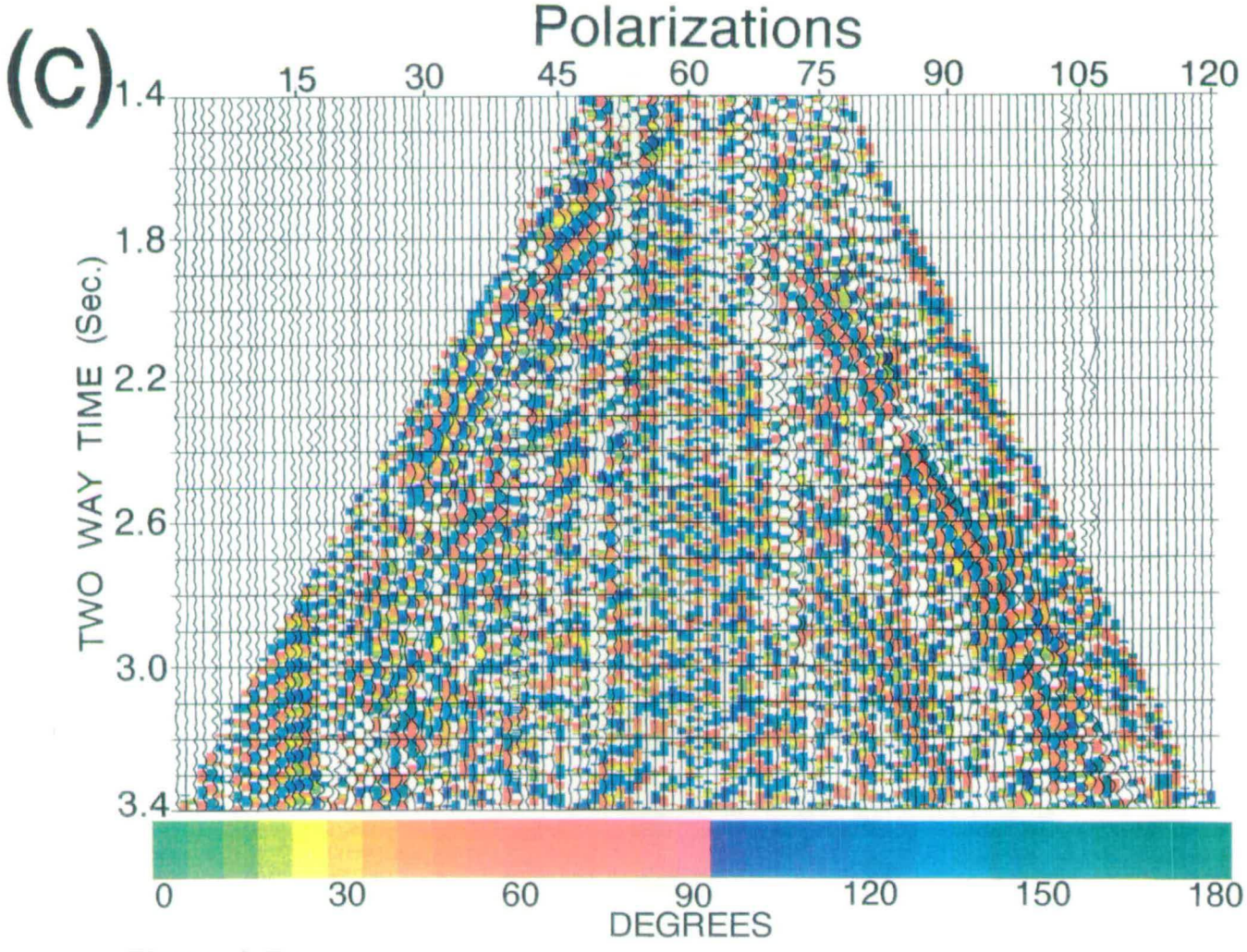
(c)
Polarizations
15
30
45
60
75
90
105
120
1.4
1.8
2.2
2.6
3.0
3.4
TWO WAY TIME (Sec.)
0
30
60
90
120
150
180
DEGREES

Figure 6.7c

separated split shear-waves. The continuity of events is improved in the separated data, and comparison of the faster and slower section shows a clear separation at the major reflection arrivals. A constant gain was applied to display Figure 6.7a and 6.7b.

Figure 6.7c shows a colour display of polarizations, using the complex component analysis described in Chapters 4 and 5 (also see Li and Crampin 1990b, 1990d, 1991c, 1991d). First, the variation of colour represents the variation of polarization. Two major colour events, blue and red-orange, can be identified in Figure 6.7c, which represent the polarizations of the faster and slower split shear-wave, respectively. The polarization angles of the faster and slower split shear-waves can be approximately estimated as 135° (blue) and 45° (red-orange). Second, the variation of polarization, represented by the colour, delineates reflection events clearly, and the continuity of wave events in Figure 6.7c is better than in the amplitude displays (Figure 6.7a and 6.7b).

6.6 DISCUSSION AND CONCLUSIONS

The above examples show that the polarizations and amplitudes of the faster and slower split shear-waves in VSPs and reflection surveys can be estimated by linear-transform techniques. I have only discussed the situation of a homogeneous anisotropic medium, that is, where the polarizations of the split shear-waves do not vary with depth. The technique can be extended to media where the effective polarizations changes with depth, and in this case one can either extrapolate the sources downwards into the lower layers, so that the medium between the extrapolated sources and the geophones is homogeneous, as demonstrated by Winterstein and Meadows (1991b), or one can deconvolve the lower geophone with upper geophone to remove the effects of the upper layer, as demonstrated by Zeng and Macbeth (1992), then perform linear transforms in the frequency domain.

This technique recognizes the linearity of the transformed shear-wave

motion in the transformed coordinate system. These (four) linear transforms are deterministic and can be efficiently implemented. It is suggested that two features of the linear-transform technique should be noted: (1) the speed and directness of the calculations; and (2) the remarkable consistency of the measurements of the attributes in the field datasets, as shown in Figures 6.5c, 6.5d, 6.5e, 6.6c, and 6.6d. Conventional methods employ a rotation scanning procedure (Alford 1986b) and tend to be computing intensive.

In conclusion, the linear-transform technique separates the faster and slower split shear-waves efficiently, and measures the parameters of shear-wave splitting with satisfactory accuracy in four-component seismic data. It is flexible and can be used in a variety of ways to treat both orthogonally and non-orthogonally polarized split shear-waves. The technique estimates the orientation of downhole geophones in zero-offset VSPs where the split shear-waves can be assumed, and measures the angle of separation of the two split shear-waves in offset-VSPs where the orientation of the geophones can be estimated by other techniques. In reflection survey, the faster and slower split shear-wave can be deterministically separated before stack, which simplifies the processing procedure of multi-component reflection data in the presence of anisotropy. Further complete case studies about the use of complex component analysis and the linear-transform technique in processing multi-component shear-wave reflection data are described in Chapter 7.

CHAPTER SEVEN

CORRELATION OF ANISOTROPY WITH OIL PRODUCTION: SHEAR-WAVE SPLITTING IN REFLECTION SURVEYS IN SOUTH TEXAS

ABSTRACT

In 1986, Amoco Production Company acquired multi-component shear-wave reflection data in South Texas to investigate the use of shear-wave splitting for characterizing fractured reservoirs. In this chapter, three lines of shear-wave data are processed and analyzed to further verify the use of complex component analysis and linear-transform techniques in processing shear-wave reflection data, and to demonstrate the correlation of variations in amplitudes and time delays of split shear-waves with fracture density and oil production in the survey area.

The three lines, 1 and 2 in Dimmit County, and 3 in Frio and La Salle Counties, were, respectively, parallel, perpendicular, and at about 39° to the regional fracture strike. The time delays of the split shear-waves measured from the stacked sections of the faster (*S1*) and slower (*S2*) split shear-waves of Line 1 are small, and events in both *S1* and *S2* sections have strong amplitudes and show good continuity. These features correlate with the absence of commercial production nearby. A trend of increasing time delays between split shear-waves measured from the *S1* and *S2* stacked sections of both Line 2 and Line 3 is observed. The events in the *S1* sections of both lines clearly show better continuity than the corresponding events in the *S2* sections. These

features correlate with the fact that Line 2 is close to and Line 3 is within major production fields. The trend of time delay variation along Line 3 also correlates with the distribution of producing oil wells along that line.

The use of the complex component analysis and the linear transform technique simplifies the processing sequence for shear-wave reflection data in the presence of anisotropy. It allows the generation of both stacked amplitude and stacked polarization sections of split shear-waves. Split shear-waves in the amplitude sections obtained by the linear transform technique are optimized in comparison with those obtained by conventional rotation techniques. The stacked polarization section can be used not only for identifying lateral variation of polarizations, which are often associated with lateral variation of crack geometry, but also for better imaging the subsurface structure, as demonstrated by Line 3.

7.1 INTRODUCTION

This chapter interprets shear-wave reflection data acquired in South Texas by Amoco Production Company (see also Li, Crampin and Mueller 1992). The study area includes Dimmit, Zavala, Frio, and La Salle Counties (Figure 7.1). The subsurface structures are essentially horizontal layers with structures parallel to those in the large Pearsall anticline in central Frio County (Layden 1976). Primary oil and gas plays in the area are in Cretaceous rocks including the Olmos Sandstone, San Miguel Sandstone, and Austin Chalk (Ames 1990). In the southwest of the area, oil and gas are produced from the Olmos Sandstone on trend with productions in North Webb County (Snedden and Kersey 1982). In the northeast, oil and gas are produced from the San Miguel Sandstones and the Austin Chalk on trend with productions in Zavala and Frio Counties (Layden 1976; Stapp 1977).

Of these major oil producing formations, the Austin Chalk has attracted continuous interest since the initial discovery of oil in the Chalk in the 1920's

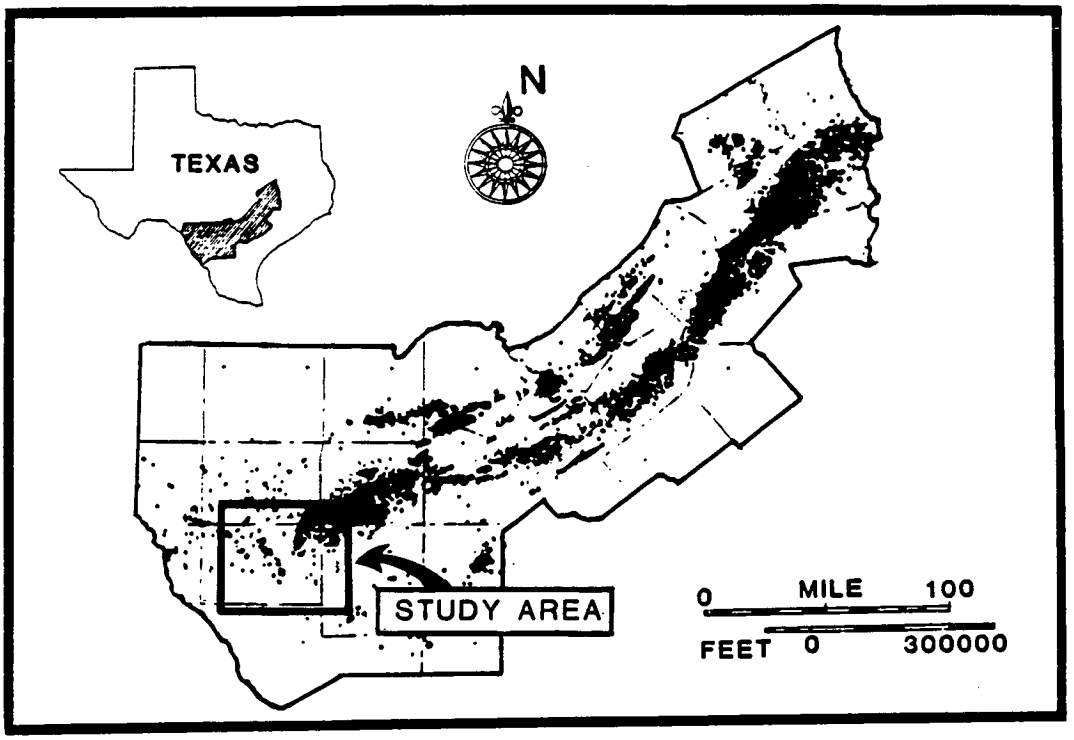

(a)

Figure 7.1. (a) Distribution of producing oil wells in the Austin Chalk, adapted from Scott (1977) and Mueller (1991). (b) Locations of the three reflection lines and oil wells (courtesy of Amoco Production Company).

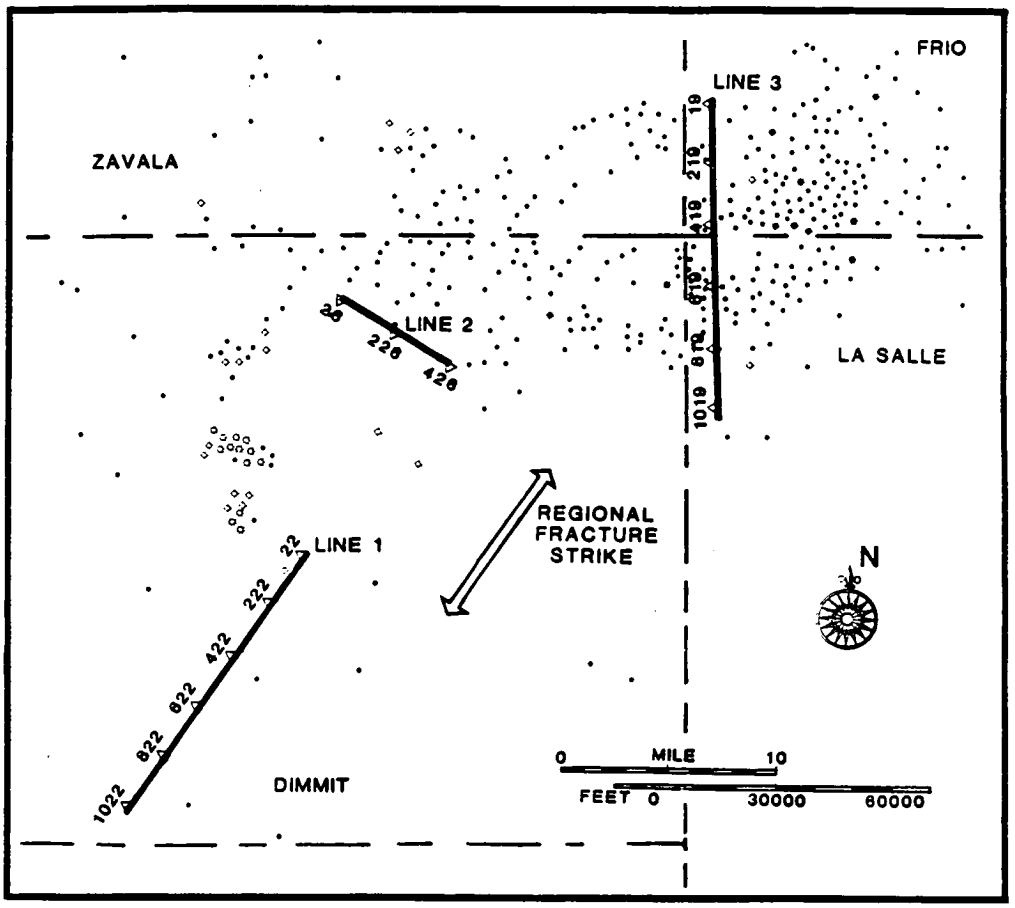

(b)

Figure 7.1 (continued)

(Stapp 1977). In the late 1970's, the interests in the Chalk were renewed by the sharp increase in the price of oil. Scott (1977) gave a good description of oil development in the Austin Chalk in that period. About 10 years later, interests in the Austin Chalk were re-kindled with the advent of horizontal drilling technology. 83% of all horizontal completions in the U.S. have taken place in the Austin Chalk trend in South and Central Texas (Mueller 1991). Kuich (1989) and Ames (1990) reviewed these activities.

The Austin Chalk is porous but impermeable. Consequently, reservoir development is almost wholly accessing fractures, and the success of drilling depends completely on identifying and penetrating highly fractured chalk (Kuich 1989; Mueller 1991). Since the hydrocarbon accumulation in the Austin Chalk is not in conventional anticlinal or fault traps, methods normally used for prospect definition can not be applied (Scott 1977). In 1986, in order to verify the use of shear-wave splitting as an exploration tool for defining fracture systems in sedimentary basins, Amoco Production Company acquired several lines of multi-component shear-wave reflection data in Dimmit, Frio, and La Salle Counties in South Texas. The Austin Chalk trend offers a natural laboratory for this kind of experiment.

Over the last few years, observations and applications of shear-wave splitting have become well-documented and established both in sedimentary basins (Crampin 1985a, 1985b; Crampin *et al.* 1986; Alford 1986b; Thomsen 1988; etc.) and in many other areas of the crust (Crampin *et al.* 1985). Crampin and Lovell (1991) review these developments. Brodov *et al.* (1990) and Cliet *et al.* (1991) correlated shear-wave splitting with oil production rates in a multi-offset three-component VSP survey in the Romashkino Field, Russia, and Mueller (1991) identified lateral fracture concentrations from the differential amplitudes of split shear-waves in the Giddings Field of Central Texas. Davis and Lewis (1990) and Lewis *et al.* (1991) also correlated the degree of shear-wave splitting with oil production in a three-dimensional and three-component reflection survey in Silo Field, Wyoming. Here, I present

another example demonstrating how the degree of shear-wave splitting can be correlated with oil production in the Austin Chalk in South Texas.

The Chapter compares the characteristics of shear-waves on three survey lines including the variations of amplitude and velocity and of polarization and time delay; discusses the processing sequences for different situations; and examines the effects of different processing techniques on evaluating shear-wave splitting. I will first summarize the geological history of the Austin Chalk in South Texas, then discuss the data acquisition system, data characteristics, and processing procedures.

7.2 GEOLOGY AND FRACTURES IN AUSTIN CHALK

Regional geology and sedimentology of the Austin Chalk has been reviewed by Weeks (1945), Seewald (1967), and Dravis (1979). The producing wells along the trend of the Austin Chalk are shown in Figure 7.1a. The chalk outcrops in the north-west edge of the map in Figure 7.1a, and dips into the subsurface towards the south-east. In Dimmit, Zavala, Frio and La Salle counties, the chalk is located at 8,000-10,000 ft depth below surface with a thickness of 700-1000 ft (Scott 1977; Stapp 1977). Structures in the chalk strike north-east, parallel with others in the Gulf Coast subsiding basin.

The Austin Chalk was formed from a fine-grained carbonate mud containing skeletal remains of algae (Corbett *et al.* 1987; Stapp 1977). The skeletal remains of the algae (coccospheres), and their disarticulated pear-shaped skeletal plates (coccoliths) were desposited in great thicknesses under quiet water conditions (Stapp 1977). Chalks deposited in deep water show fewer fluctuations in rock physics and have widespread uniform facies, while chalks deposited in shallow water suffer fluctuations and rapid changes. The outcrops of Austin Chalk are believed to have been deposited in shallow water, whereas the chalk in the subsurface, as found in Dimmit, Zavala, Frio, and La Salle counties, is believed to have been deposited in deep water

environments (Stapp 1977) and uniform facies are expected.

The porosity in the Austin Chalk trend varies both along strike and dip. In outcrops, the porosity may be as high as 30%, but in the subsurface, the porosity may be as low as 6% (Corbett *et al.* 1987). With such low-porosity in the subsurface, the rocks can neither take up nor give up fluid of any kind without fracturing (Scott 1977). Chalks usually have high porosity following deposition, but this gradually decreases with depth of burial. As the chalk loses porosity and packs down to a brittle rock, it easily fractures in response to tension. According to Scott (1977), the Austin Chalk was deposited on a relatively flat surface which, in response to subsequent deposition of great thicknesses of Tertiary sands and shales, became downwarped. It is this downwarping that stretched the Austin Chalk and created one set of fractures, known as textural fractures (Stapp 1977). They are not directly related to faulting. Since the stretching was uniform and along the dip direction of the structure, the strike of these textural fractures are usually vertical cracks parallel to the strike of the structure (Scott 1977).

The other major fracture system in the Upper Cretaceous Austin Chalk is fault related (Stapp 1977; Reaser and Collins 1988). The structural setting and the trend were determined by the Gulf Coast subsiding basin, and modified by the Balcones, Luling, Mexia, and Talco fault zones (Reaser and Collins 1988). Faulting through the Austin Chalk trend is characterized by normal faults. As all large subsurface faults in the Cretaceous strata have similar displacement and there is no evidence of a difference in age between the fault zones (Corbett *et al.* 1987), all movements are assumed to be contemporaneous and the regional stress field is assumed to be uniform. Consequently, the fault-related fractures strike parallel to the structural strike and are expected to be uniformly distributed.

Although, as suggested above, the strike of fractures in the chalk is expected to be uniform, the fracture intensity in dipmeter logs and field

mapping is not uniform. This is probably due to minor differences in the local stress and variations of the content of skeletal algae remains, so that fracturing is marginally easier in some areas than in others (Scott 1977; Stapp 1977; Corbett *et al.* 1987). Thus, fractures form clusters and swarms in the Chalk. These swarms of fractures are major exploration targets for horizontal drilling (Kuich 1989; Mueller 1991).

Figure 7.1b shows the locations of the survey lines and well distributions. Line 1, striking N39°E, is parallel to the strike of the subsurface faults and subsurface fractures. As shown in Figure 7.1b, there were no significant exploration wells drilled in this area of south-west Dimmit. Line 2, striking N50°W, is approximately perpendicular to the fracture strike; Line 3, striking approximately north-south, is at about 39° to the fault and fracture strike. These two lines are located near the intersection of Dimmit, Zavala, Frio and La Salle Counties, where the area had been very heavily drilled (Figure 7.1b). Significant oil fields operated near the intersection area are the Pearsall Field in Frio County (Champion 1936) and the Big Well Field in Dimmit and Zavala Counties (Layden 1976). Recent horizontal drilling in the Austin Chalk was also mainly carried out in this area (Kuich 1989, Ames 1990, Mueller 1991).

7.3 ACQUISITION SYSTEM AND DATA CHARACTERISTICS

7.3.1 Field data acquisition

The data were acquired in early 1986 with 242-channel recording (121 inline channels and 121 crossline channels) for two horizontal sources (one inline source and one crossline source), referred to as a four-component shear-wave survey (Alford 1986a). Tests for the four-component survey were performed along Line 1 (Figure 7.1b) to determine optimum field acquisition parameters. Group spacing was chosen as 110 ft initially, and was changed to 165 ft after observing enormous ground roll in the test records acquired with 110 ft spacing. The group array contained 24 geophones, and geophone

spacing within the group was also changed from 9.5 ft to 14 ft after testing. The split spread was designed with the source centred at the spread. The inline source array contained six horizontal vibrators with 82.5 ft spacing; the crossline source array contained three horizontal vibrators with 165 ft spacing. The sweep frequency was 8-32 Hz and the sweep length was 22s, and 12 sweeps per vibrator point were taken. The vibrators were orientated into the inline and crossline direction alternately, but spread layout, directions and locations of geophones were fixed for each source direction. Table 7.1 summarizes all the acquisition parameters.

7.3.2 Shot data matrix

Figure 7.2 shows one shot record from each survey line illustrating the changes in field data for different line azimuths. Each shot record has four-components, which are displayed in a data matrix with common source component as rows and common receiver component as columns, where inline components are marked *X* and crossline *Y*. Figure 7.2 shows such shot data matrices for each of the three lines. The shot data matrices of both Line 1 and Line 2 (Figures 7.2a and 7.2b) show strong coherent shear-wave events in the diagonal elements but almost no coherent signal in the off-diagonal elements. In contrast, in the data matrix of Line 3 (Figure 7.2c), there are strong coherent shear-wave events with approximately equal energy in both diagonal and off-diagonal elements. This illustrates the effects of shear-wave splitting in a structure having azimuthal anisotropy with uniform symmmetry directions, specifically, orthorhombic symmetry with vertical and horizontal planes of symmetry. Lines 1 and 2 are parallel to the vertical planes of symmetry, so that inline source excites inline receiver, and crossline source excites crossline receiver, and there is no cross-coupling. Line 3, in an intermediate direction, causes the shear-wave source excitations to split and there is strong cross-coupling.

TABLE 7.1: Acquisition parameters.

RECEIVER GROUP:
Group spacing: 165 ft;
Group length: 330 ft;
Phones/group: 24;
Geophone groups centred on the station;
Inline and cross-line receiver groups co-located.
SPREAD:
Split spread shooting with 121 geophone groups;
Spread length: 19800 ft;
Far offset: 9900 ft;
60 geophone groups to each side.
SOURCE:
Inline source array: 6 vibrators with 82.5 ft spacing;
Crossline source array: 3 vibrators with 165 ft spacing;
Source array centred on the station;
Sweep frequency: 8-32 Hz;
Sweep length: 22 seconds;
Number of sweeps per vibrator point: 12.
RECORDING:
Recording length: 30 seconds;
Sampling interval: 2 ms;
No notch filter;
Shot every second station;
Maximum CDP fold: 31.

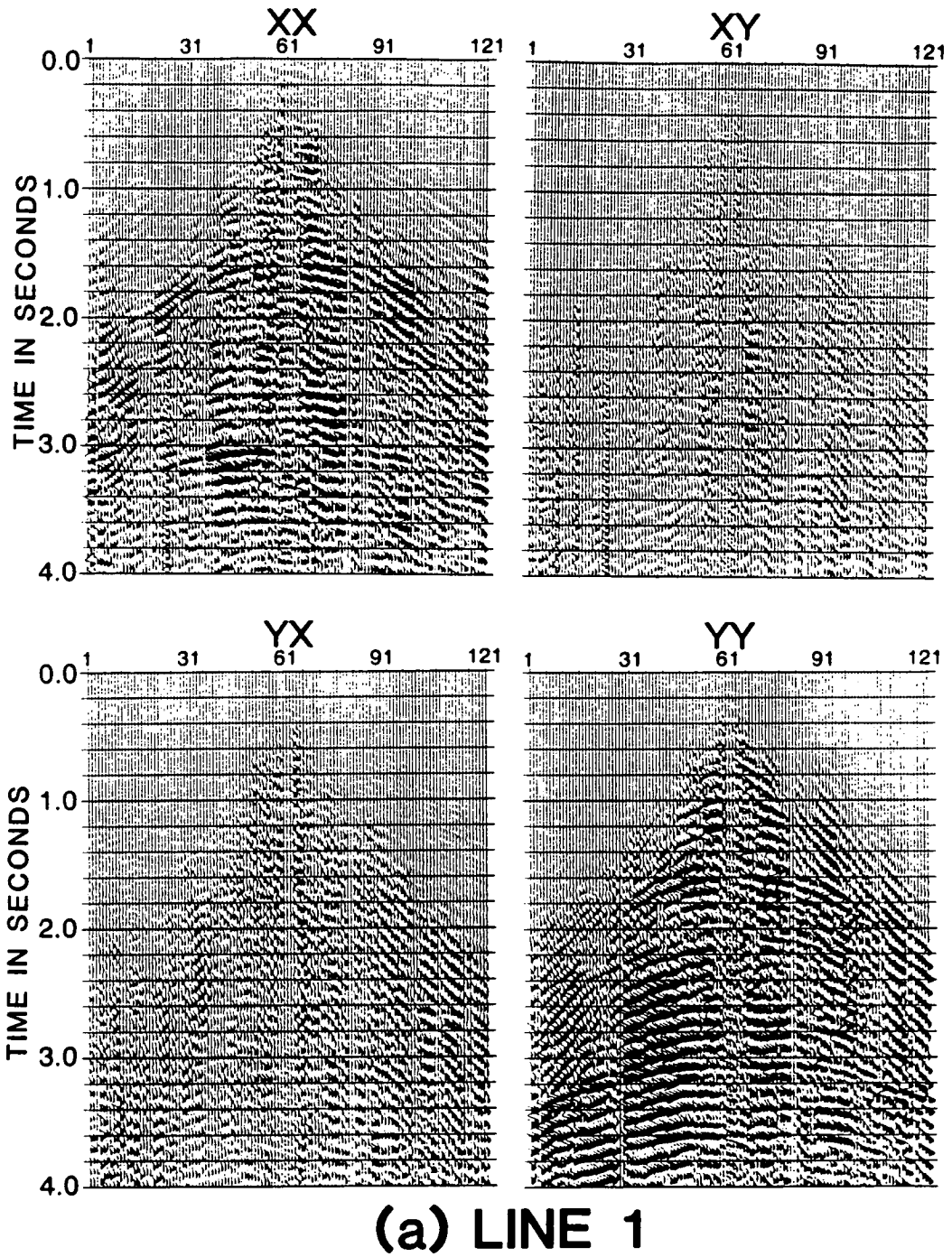

Figure 7.2. Comparison of shot data matrix selected from the three lines: (a) shot 161 at station #690, Line 1; (b) shot 50 at #275, Line 2; (c) shot 33 at #160, Line 3.

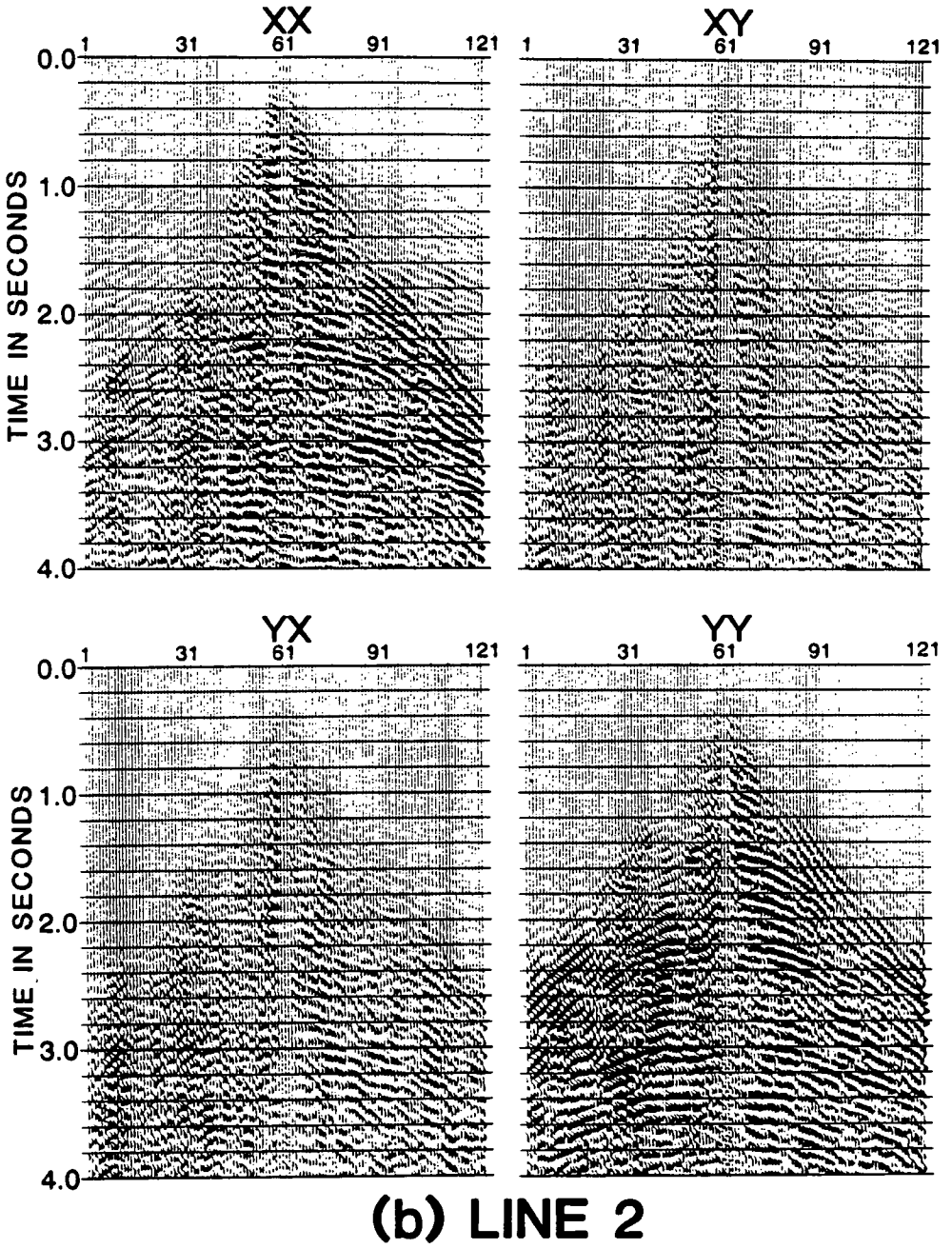

Figure 7.2 (continued)

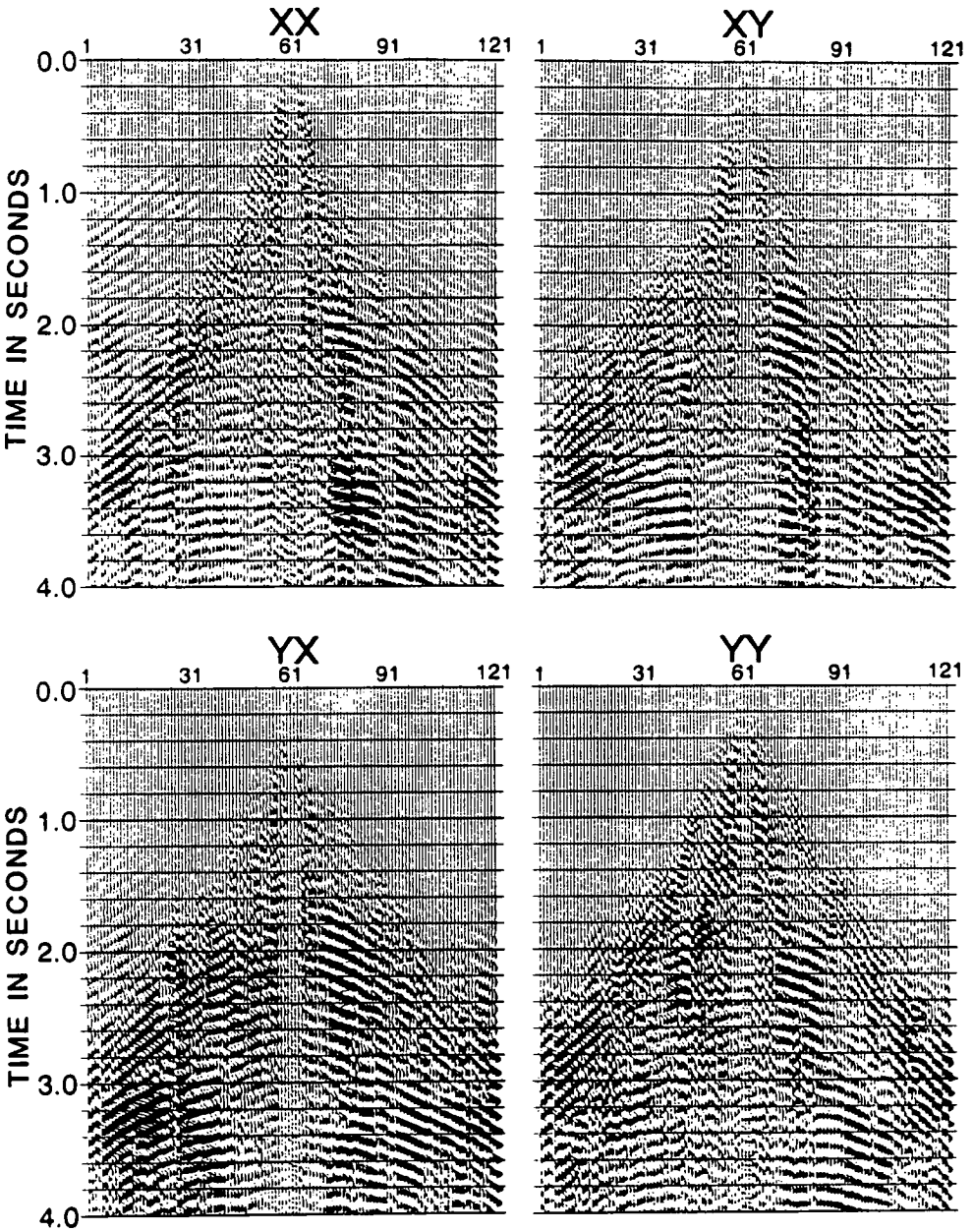

Figure 7.2 (continued)

7.3.3 Instantaneous polarizations

Chapters 4 and 5 (Li and Crampin 1990b, 1990d, 1991c, 1991d) presented the complex-component analysis of shear-wave splitting, in which I calculated instantaneous polarizations and used colour-coded displays to interpret the variations of polarization. Here, I examine the characteristics of instantaneous polarizations in survey lines with different azimuths. Figures 7.3a and 7.3b show the instantaneous polarizations of *X*- and *Y*-sources from the data matrix of Line 1 (Figure 7.2a) and the data matrix of Line 3 (Figure 7.2c). The instantaneous polarizations of Line 2 show similar features to Line 1, and are not shown, here.

Figure 7.3a shows the instantaneous polarizations of the *X*-source calculated from the *XX* and *XY* components of the shot data matrix of Line 1 (Figure 7.2a) showing dominant green events and indicating inline polarizations of about 0°. The corresponding polarizations of the *Y*-source in Figure 7.3b, calculated from the *YX* and *YY* components of Line 1 (Figure 7.2a), show dominant red events, indicating crossline polarizations of about 90°. The polarizations appear source-dependent, there are no common polarizations from different source orientations and there is no shear-wave splitting. In contrast, the instantaneous polarizations of the *X*- and *Y*-sources of Line 3 in Figures 7.3c and 7.3d, respectively, calculated from the data matrix in Figure 7.2c, show coherent common blue events indicating polarizations of about -51°, and also show some indications of weak red-orange events indicating polarizations of about 39°. In this case, the polarizations are source-independent and fixed in the space giving approximately the same spatial polarizations as Lines 1 and 2. Note that the radial direction is north-south. This is a typical example of shear-wave splitting with a line orientated intermediate to the symmetry planes of azimuthal anisotropic media.

Figure 7.3. Instantaneous polarizations calculated by the complex component analysis from (a) the *XX*- and *XY*-components in Figure 7.2a, Line 1; (b) the *YX*- and *YY*-components in Figure 7.2a, Line 1; (c) the *XX*- and *XY*-components in Figure 7.2c, Line 3; (d) the *YX*- and *YY*-components in Figure 7.2c, Line 3. Positive angles in the scale indicate the polarizations measured clockwise from the radial direction, and negative ones indicate the polarizations measured anticlockwise.

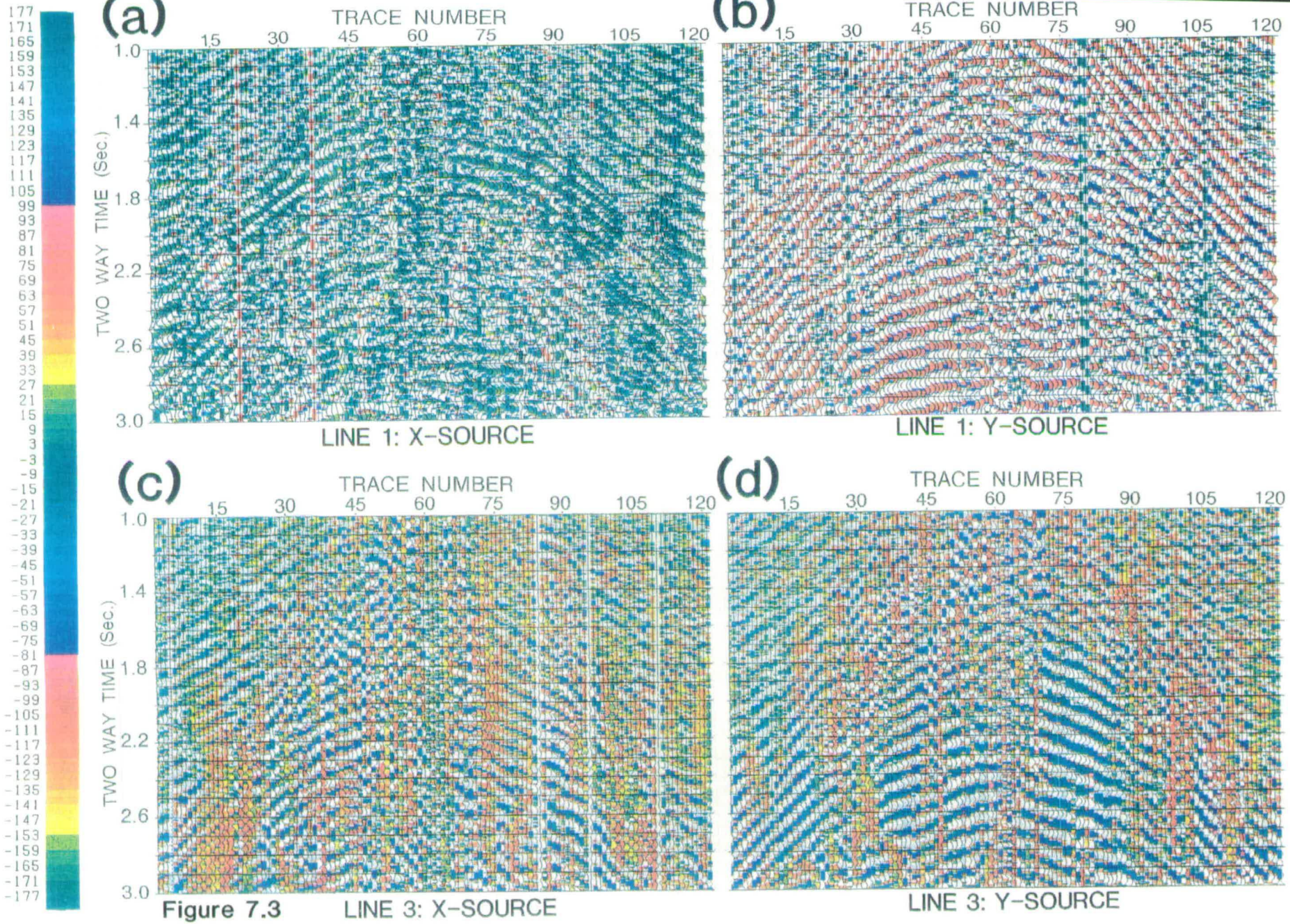
(a)
TRACE NUMBER
15 30 45 60 75 90 105 120
TWO WAY TIME (Sec.)
1.0 1.4 1.8 2.2 2.6 3.0
LINE 1: X-SOURCE
(b)
TRACE NUMBER
15 30 45 60 75 90 105 120
LINE 1: Y-SOURCE
(c)
TRACE NUMBER
15 30 45 60 75 90 105 120
TWO WAY TIME (Sec.)
1.0 1.4 1.8 2.2 2.6 3.0
LINE 3: X-SOURCE
(d)
TRACE NUMBER
15 30 45 60 75 90 105 120
LINE 3: Y-SOURCE
177 171 165 159 153 147 141 135 129 123 117 111 105 99 93 87 81 75 69 63 57 51 45 39 33 27 21 15 9 3 -3 -9 -15 -21 -27 -33 -39 -45 -51 -57 -63 -69 -75 -81 -87 -93 -99 -105 -111 -117 -123 -129 -135 -141 -147 -153 -159 -165 -171 -177

Figure 7.3

7.4 PROCESSING LINES 1 AND 2

Lines 1 and 2 are, respectively, parallel and perpendicular to the presumed crack strike. Figures 7.2a, 7.2b, and 7.3a show that the two split shear-waves are separated, so that the components can be processed separately using conventional techniques (Lynn and Thomsen 1990; Li and Crampin 1991a; Mueller 1991). As the off-diagonal elements contain very little signal energy (Figures 7.2a and 7.2b), they can be omitted at an early processing stage. Table 7.2 summarizes the conventional processing sequence used for processing Lines 1 and 2. In case of shear-wave splitting, once the split shear-waves are separated, the separated components can also be processed using the conventional processing sequences (Lewis *et al.* 1991)

Note that it is not strictly correct that conventional processing techniques are appropriate for separated shear-waves in anisotropic media, since even when the polarizations are separated, the velocities of the two shear-waves will be different and will vary with offset. This means that stacking CDP gathers at constant moveout velocities are not strictly appropriate (Li and Crampin 1990a, 1990c, 1992b; see also Chapter 2), although the effects in many circumstances may be negligible. Chapter 2 (Li and Crampin 1990a, 1990c, 1992b) suggested velocity and moveout equations for CDP gathers in anisotropic media. Also note that the effect of varying moveout velocities are thought to be negligible in Lines 1, and 2, and conventional processing has been used.

7.4.1 Robust average scaling (RAS)

Amplitude balancing is usually necessary in processing vibrator data. Traces at small offsets typically have large amplitudes which decrease sharply with increasing offset, and a trace-by-trace amplitude scaling to balance amplitudes is often needed. Such simple trace-by-trace amplitude scaling tends to alter the relative amplitudes between different components. However, relative amplitudes must be preserved for extracting polarization angles, or

TABLE 7.2. Conventional processing sequences.

DATA EDITING:
Geometry input;
Trace editing;
Data statics using velocity 3000 ft/s.
VELOCITY AND RESIDUAL STATICS:
CDP sort;
Velocity analysis;
NMO correction;
Four-component scaling: balancing trace by off-diagonal elements;
Stacking: form pilot traces for statics estimation;
Residual statics picking;
Solve for surface consistent residual statics;
Iterate above sequence.
FINAL STACKING:
CDP sort;
NMO correction;
Robust average scaling (RAS);
Residual statics application;
Stack;
Display.

investigating the amplitude variation between the faster and slower split shear-waves. A four-component scaling can maintain the relative amplitudes among the components, but cannot properly balance the amplitudes between traces from the same component within the same shot record or CDP gather. To overcome this problem, an optimum amplitude-balancing technique, called robust average scaling (RAS) has been used (see Table 7.2).

The conventional algorithm for amplitude balancing scales the maximum or average amplitude of every trace to a given reference level within a shot record, or CDP gather. Since this reference level is irrelevant to the true amplitude level of a trace, the relative amplitudes among different components can be freely changed by applying such scaling. If the reference level is the true amplitude level of the stacked trace of a CDP gather and every un-stacked trace in the gather is scaled to this reference level, the amplitudes between traces within the CDP gather are balanced, and the relative amplitudes among different components are also preserved.

This can be realized with one iteration. I first correct for normal moveout, and stack the unbalanced CDP gather, and calculate the average amplitude of this stacked trace. Secondly, I take this average amplitude as an optimum estimation of the true amplitude level of the CDP gather, and use it as the reference level to balance the NMO-corrected CDP gather. After it is balanced, the CDP gather is stacked again. This sequence is called robust average scaling or RAS. Figure 7.4 shows a comparison of CDP stacking results with and without applying robust average scaling. The data are selected from the *XX* component in Line 1. Comparing Figure 7.4a with 7.4b shows that the continuity of events and the signal to noise ratio are both improved after applying RAS.

7.4.2 Statics and velocity analysis

In addition to amplitude scaling, reflection surveys also require

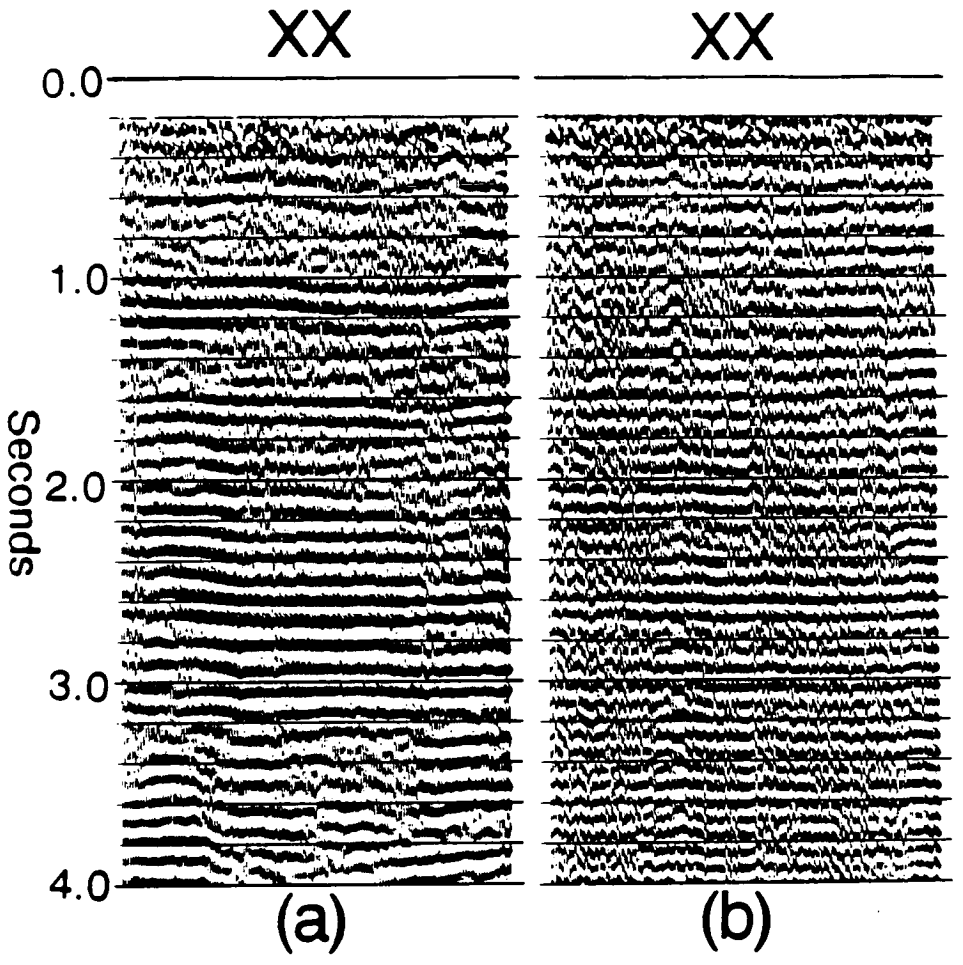

Figure 7.4. Effects of robust average scaling (RAS): (a) stacking with applying RAS; (b) stacking without applied RAS. Data selected from *XX* component of Line 1.

corrections for statics. In order to measure time delays correctly, we need to maintain the relative time shifts between different components. To simplify the problem, it is often assumed that the faster and slower split shear-waves have the same field statics and the same residual statics, although, since shear-wave splitting is due to the polarizations reacting differently to the anisotropic structure, this assumption can only be a first-order estimate. Assuming equal statics, the problem is to ensure that the same statics are applied to all components. Here a constant velocity of 3000ft/s was used for field data statics, and residual statics was derived from the *YY* components. The velocity and statics sequence was iterated once to refine the pilot traces for picking the residual statics (see Table 7.2).

Velocity analysis is also a common problem in reflection data processing. The faster and slower split shear-waves have different stacking velocities (Thomsen 1988; Li and Crampin 1990a, 1990c; 1992b; see also Chapter 2), and it may be necessary to carry out two separate passes of velocity analysis for *S1* and *S2*, as we did here. Figure 7.5 shows the average differences of *S1* and *S2* stacking velocities for the three lines. As shown in Figure 7.5, the differences in the stacking velocities of Line 1 are generally small, and it is not necessary to use two separate velocity-sets for *S1* and *S2* in processing Line 1. However, the differential stacking velocities in Line 2 are large, particularly after 1.5 seconds, and two separate velocity-sets are necessary in processing Line 2.

7.4.3 Final stacked results

After obtaining satisfactory stacking velocities and residual statics, we can follow the final stacking sequence in Table 7.2. For Line 1, which is parallel to the assumed strike, the *XX* component contains the faster split shear-wave (*S1*), and the *YY* component contains the slower split shear-wave (*S2*). Carrying out the final stacking sequence separately for *XX*- and *YY*-components, we can obtain the final stacked *S1* and *S2* sections for Line 1, as shown in

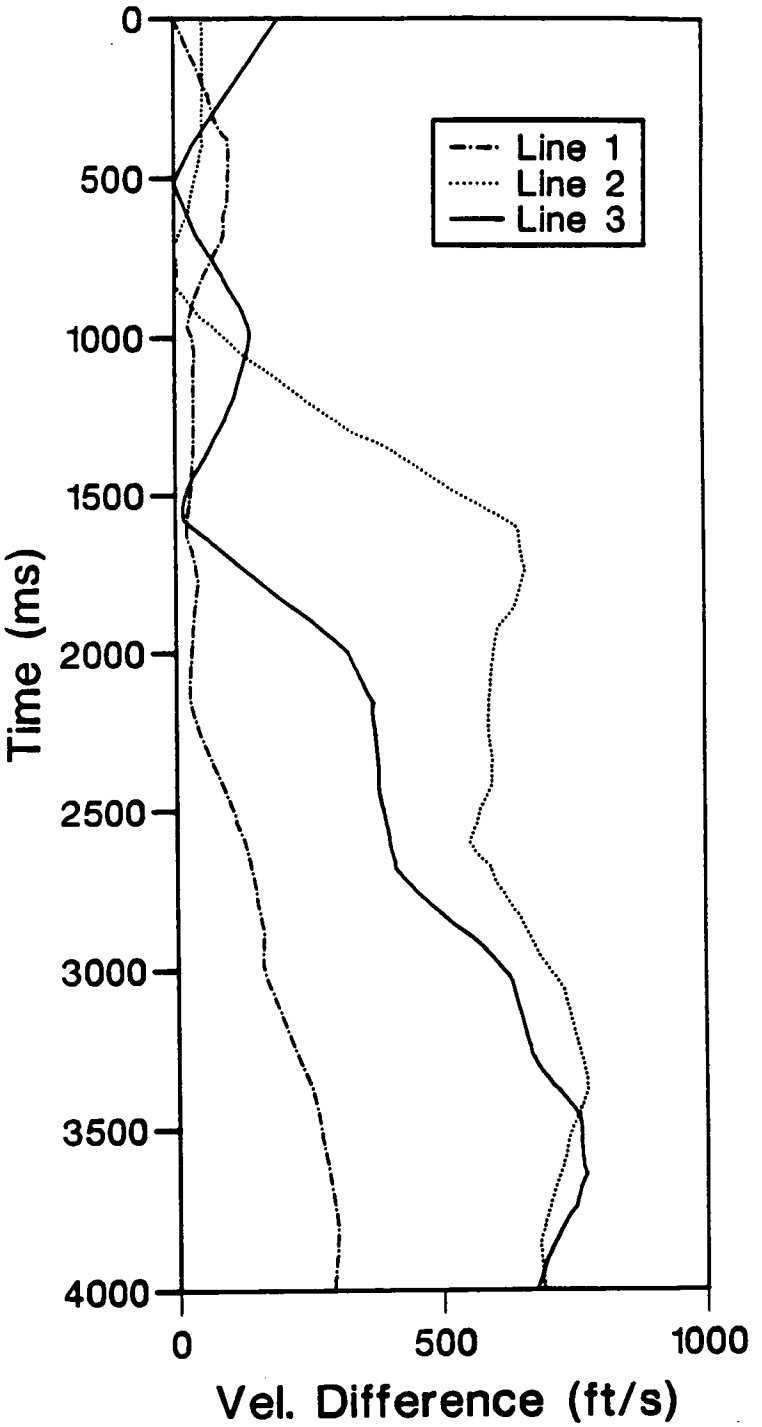

Figure 7.5. Comparison of average differential stacking velocities between the faster and slower split shear-waves along the three reflection lines: Line 1 - broken line; Line 2 - dotted line; and Line 3 - solid line.

Figures 7.6a and 7.6b, respectively. For Line 2, which is perpendicular to the crack strike, the *XX* component is the *S2* component, and *YY* component is the *S1* component. Similar to Line 1, the final stacked *S1* and *S2* sections can be obtained by two separate passes of the final stacking sequence in Table 7.2. The results are shown in Figures 7.6c and 7.6d. Comparison of Lines 1 and 2 in Figure 7.6 shows that the overall data quality of Line 2 is not as good as that of Line 1.

7.5 PROCESSING LINE 3

Line 3 shows pronounced shear-wave splitting. Separating split shear-waves provides an extra challenge in addition to the problems discussed above. The conventional technique for separating shear-wave splitting in reflection surveys is numerical rotation of the horizontal components of the record section to minimize the energy in the cross diagonal elements of the data matrix (Alford 1986b), and similar results can be obtained by rotating analytically (Murtha 1988, 1989). Li and Crampin (1991b, 1992a; see also Chapter 6) suggest a flexible linear-transform technique as an alternative to the conventional rotation techniques. Here, both the rotation technique and the linear transform method are used in processing Line 3 in order to evaluate their merits and to establish an optimum sequence for processing shear-wave reflection data in the presence of anisotropy.

7.5.1 Rotation analysis

The process of rotation analysis can be summarized as follows. Firstly, the data editing sequence in Table 7.2 is applied to all the four components. Secondly, the velocity and statics sequence in Table 7.2 is applied to the *YX* component (crossline source and inline receiver), or *XY* component (inline source and crossline receiver), to determine the stacking velocities and residual statics. Note that the *XY* and *YX* components should be approximately equal in noise-free azimuthal anisotropic media containing uniform symmetry (same

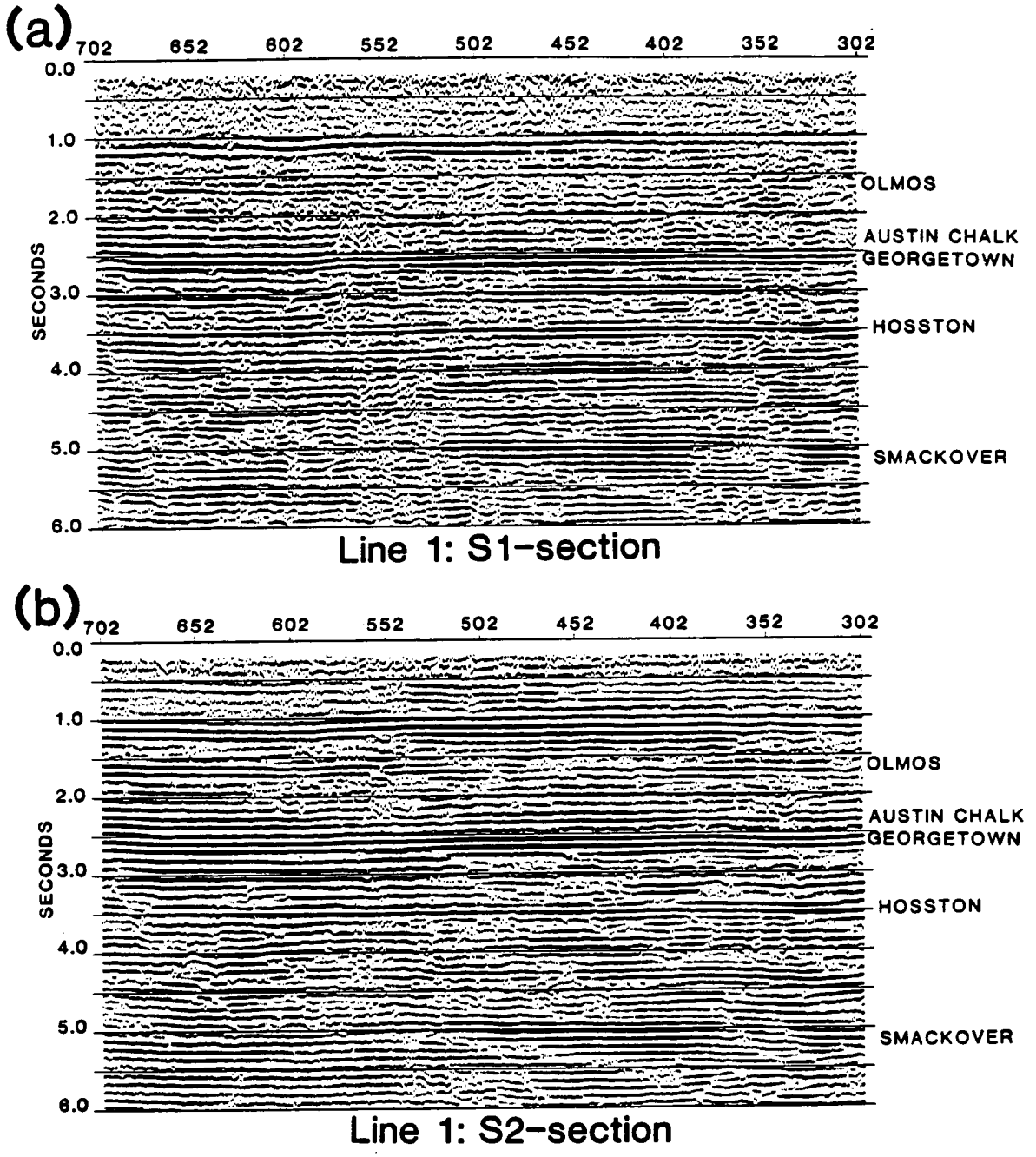

Figure 7.6. Final stacked *S1*- and *S2*-sections using the processing sequence in Table 7.2. Line 1: (a) *S1*-section (*XX*-component); (b) *S2*-section (*YY*-component); Line 2: (c) *S1*-section (*YY*-component); (d) *S2*-section (*XX*-component).

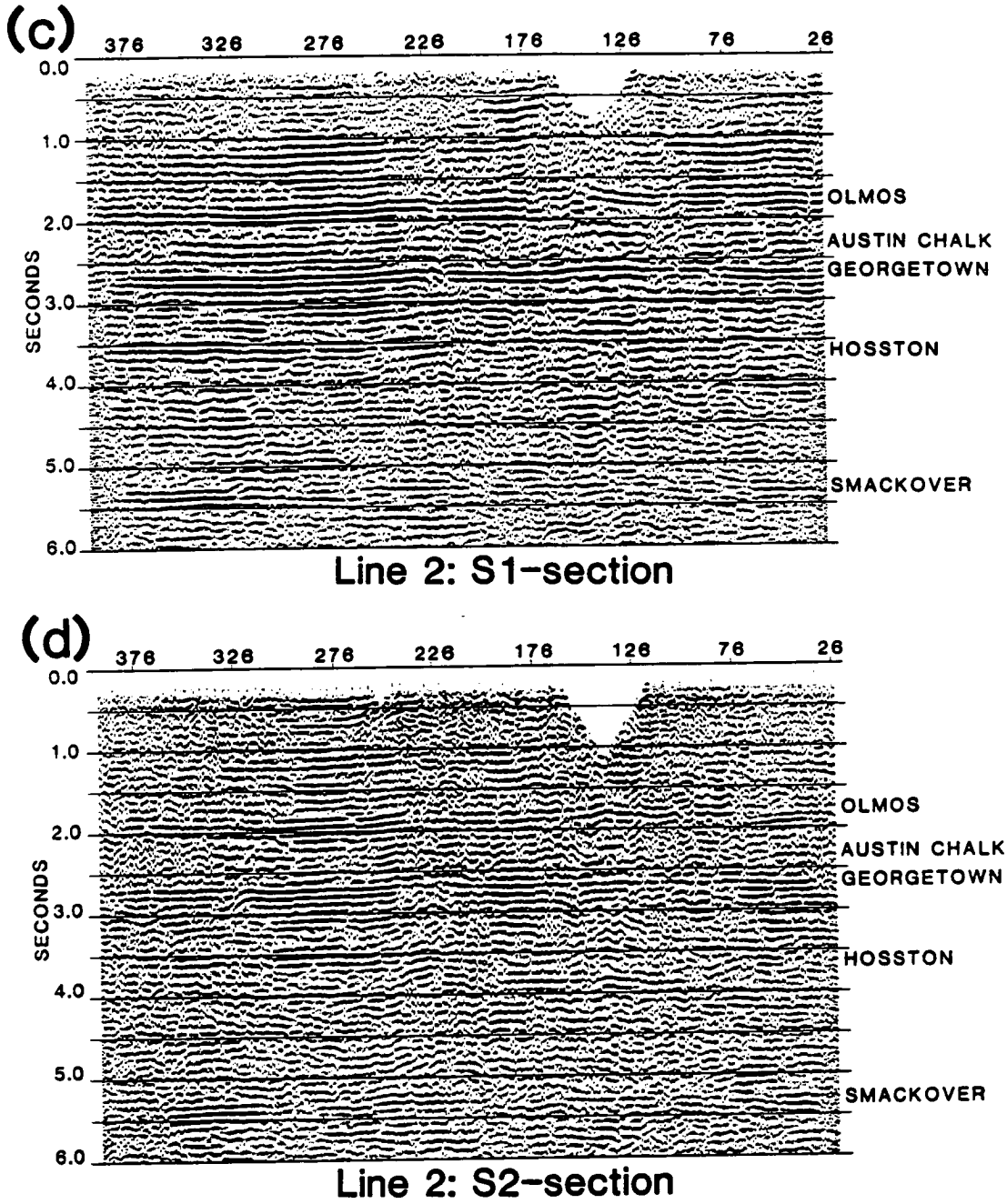

Figure 7.6 (continued)

orientation of cracks) throughout the depth range (Figure 7.2c). Thus, only a single pass of the velocity and statics sequence is needed to choose off-diagonal elements for preparing stacked data matrices for rotation. Thirdly, the rotation sequence in Table 7.3 is applied to all four components separately. At this stage, the stacked data matrix can be used to determine the rotation angle, and this angle is used to rotate the shot data matrix to separate the four-component data into two-component *S1* and *S2* data sets. Finally, the velocity and statics sequence and the final stacking sequence in Table 7.2 are applied to the *S1* and *S2* components separately, and the final stacked *S1* and *S2* sections are then obtained.

Figure 7.7 shows a portion of the stacked data matrix for Line 3 after the third stage of processing. The split shear-waves are mixed together and mistie of events may not be observed in the data matrix. For example, events appear at 2.0 seconds in components *XX* and *XY*, events appear at 3.0 seconds in components *YX* and *YY*. Figure 7.8 shows the polarization angles measured from the stacked data matrix using the linear transform technique (Note that in conventional rotation analysis, polarization angle is determined by rotation scanning). The dotted line shows the measurements from the data window over the Austin Chalk, and solid line shows those from the whole data. The two measurements are generally consistent. Before station #600, the rotation angles are consistent and have an average of about around 39°; after #600, the measurements are more scattered because of poor data quality. Thus the rotation angle can be choosen as 39° for separating the four-component data into *S1* and *S2* datasets. The final stacked *S1* and *S2* sections are shown in Figure 7.9. Overall comparison of Figure 7.7 with Figure 7.9 shows that the continuity of events in the *S1* and *S2* sections is improved, and mistie of events is observed, as events at 2.0 and 3.0 seconds show.

TABLE 7.3. Processing sequences for separating split shear-waves: comparison of rotation technique with linear-transform technique.

ROTATION SEQUENCE:
CDP sort;
NMO correction;
Robust average scaling;
Residual statics application;
Stack;
Rotation angle estimation: rotation analysis, or other technique;
Apply rotation angle to shot data;
Separate data into *S1* and *S2* data sets.
LINEAR-TRANSFORM TECHNIQUE:
Apply linear-transform to shot data;
Separate data into *S1* and *S2* polarization data sets.

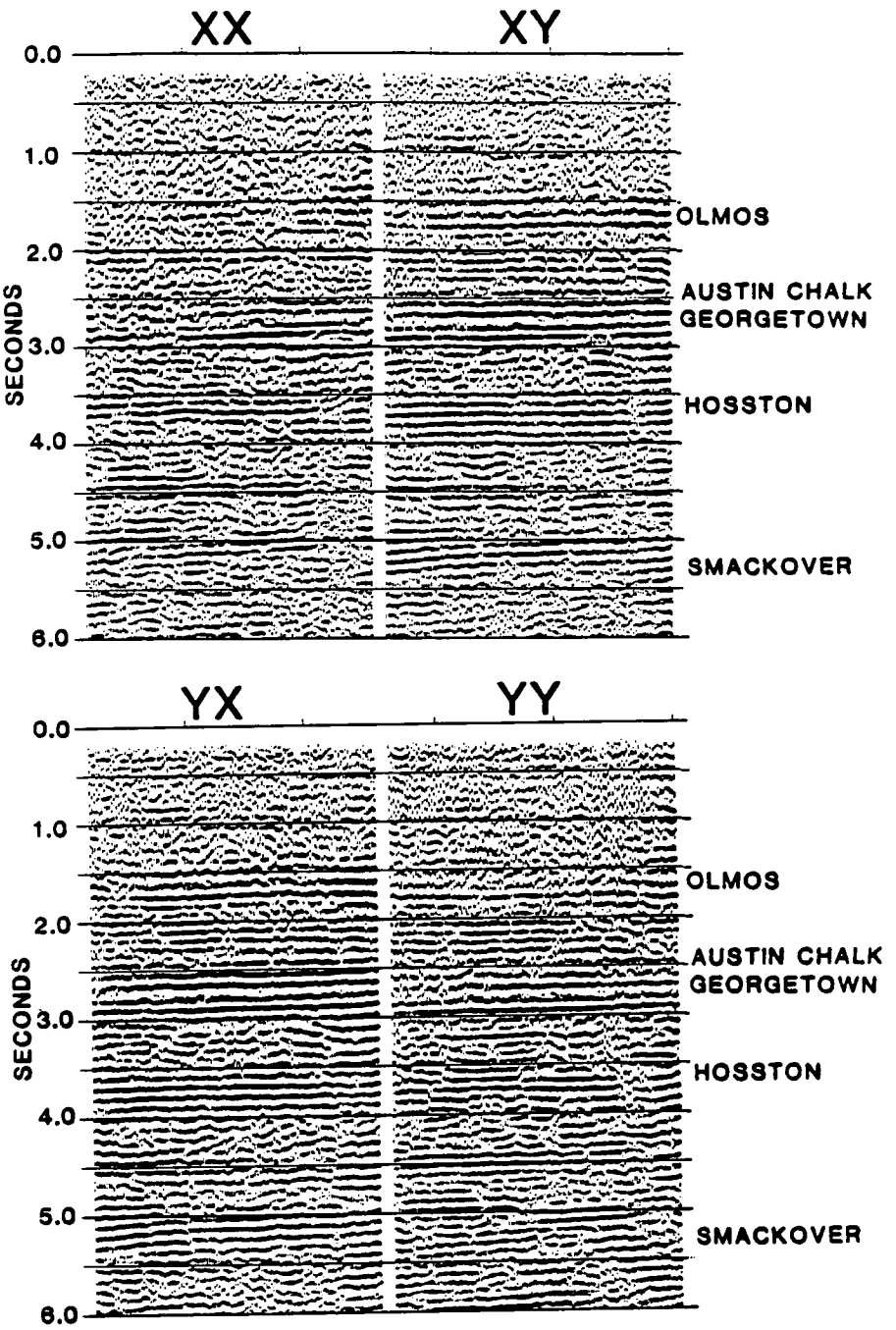

Figure 7.7. Stacked data matrix from Line 3 using the processing sequence in Table 7.3.

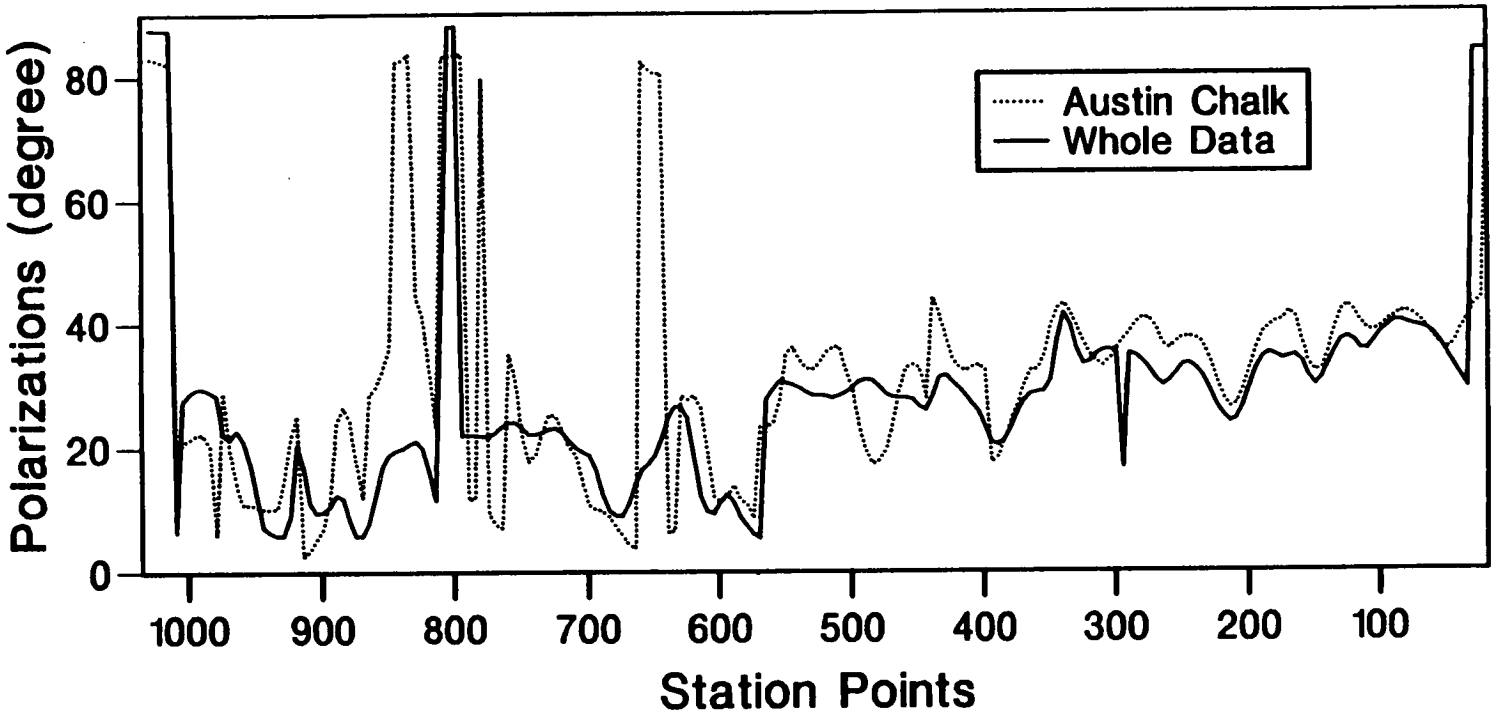

Figure 7.8. Polarization angles measured from the stacked data matrix in Figure 7.7 using the linear-transform technique (Li and Crampin 1991b, 1992a; also see Chapter 6): dotted line, measured from the bottom of the Austin Chalk; solid line, measured from the whole data set.

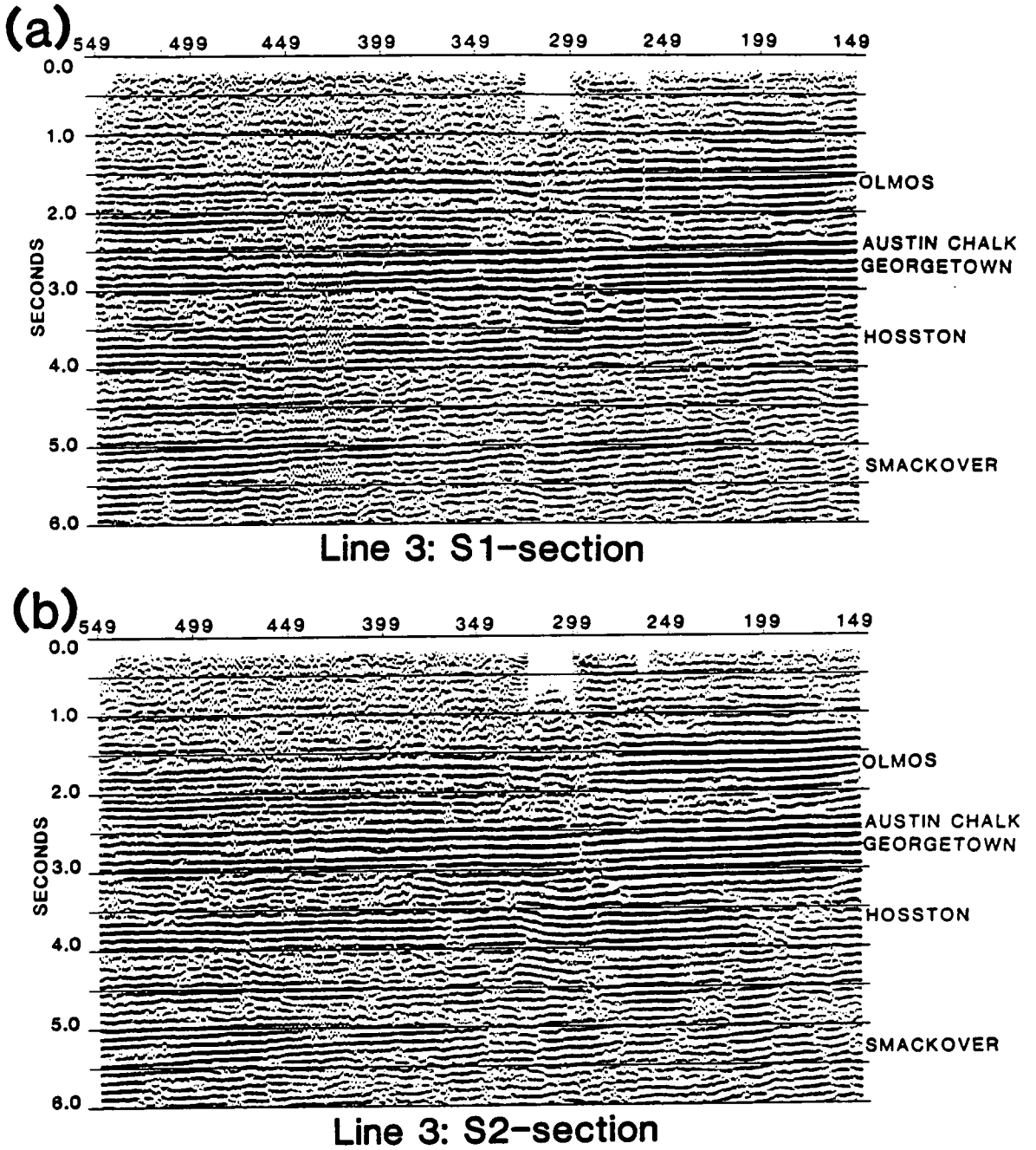

Figure 7.9. Final stacked data of Line 3 using the rotation process described in the text. The rotation is chosen as 39°. (a) *S1*-section of the fast split shear-wave; (b) *S2*-section of the slower split shear-waves.

7.5.2 Linear-transform technique (LTT)

The process involving LTT is straightforward. Firstly, as before, the data editing sequence is applied to all four components. Secondly, the LTT sequence in Table 7.3 is applied to the shot data matrix to transform the four components into the three LTT components: *S1*; *S2*; and the component of polarization logs (see Chapter 5; also Li and Crampin 1990d; 1991d). Thirdly, the velocity and statics sequence and the final stacking sequence in Table 7.2 are applied separately to the *S1*, *S2* and polarization components to give the final stacked *S1*, *S2*, and polarization sections.

Figure 7.10a shows the *S1* and *S2* shot records after applying LTT to the data matrix in Figure 7.2c. For comparison, the results of the rotation process are shown in Figure 7.10b. Comparison of Figure 7.10a with 7.10b shows that *S1* and *S2* records obtained by LTT are as good as those obtained by the rotation technique. Figure 7.11 shows the comparison of the residual energy after LTT with the energy after rotation, where *S3* represents the sum of the off-diagonal elements in the shot data matrix after applying LTT or rotation. Overall comparison of Figure 7.11a with Figure 7.11b shows that the residual energy after LTT (Figure 7.11a) is smaller than the residual energy after rotation (Figure 7.11b). This indicates that the split shear-waves are better optimized by LTT than by rotation.

Figure 7.12 shows final stacked *S1* and *S2* sections of the LTT. Comparison of Figure 7.12 with the stacked sections using the rotation technique in Figure 7.9 shows that overall quality of the final stacked sections using LTT is slightly better than those using the rotation process: for example compare the events between 3.5 to 4.0 seconds at stations between #399 and #499.

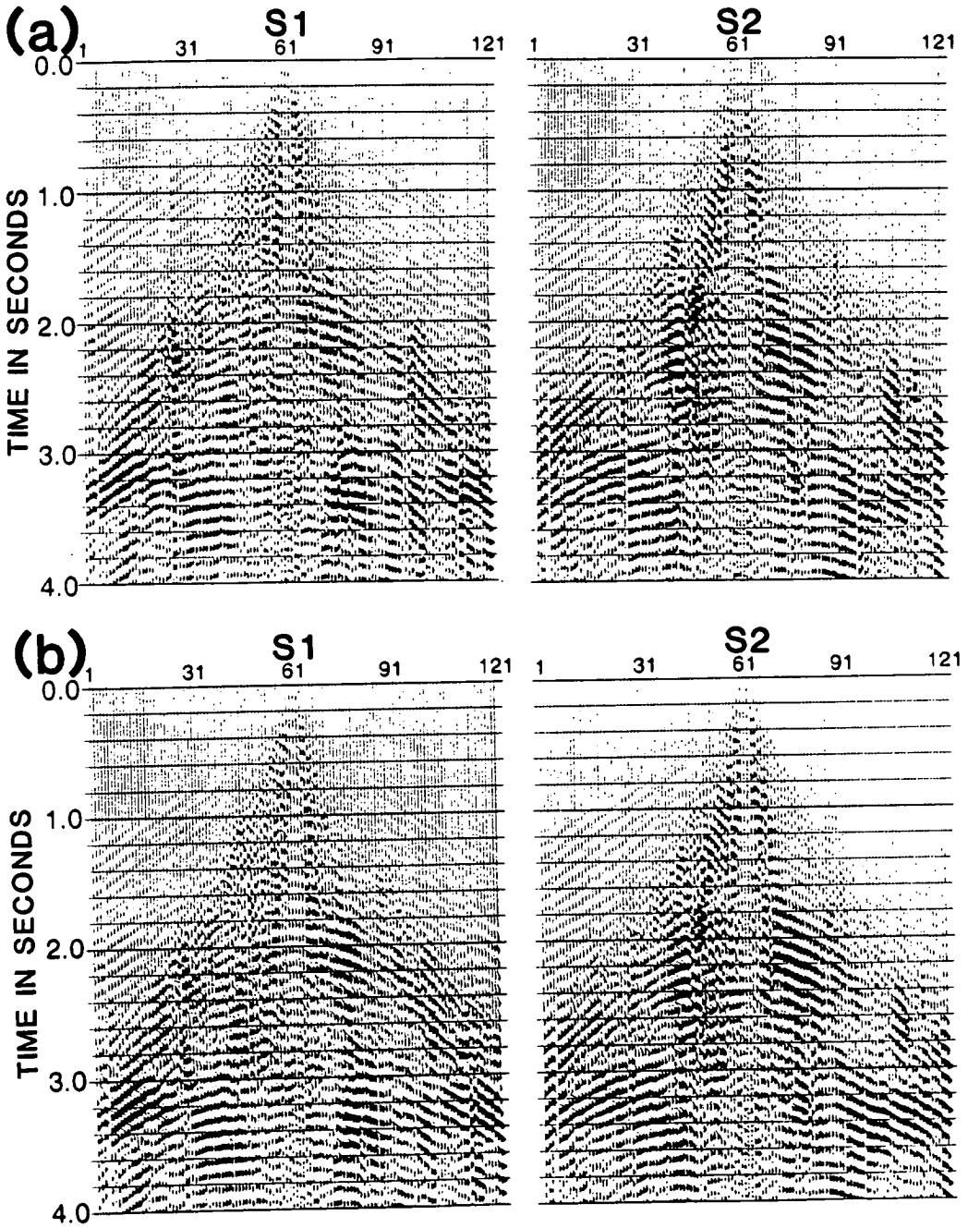

Figure 7.10. Comparison of *S1* and *S2* components of the split shear-waves calculated from the shot data matrix of Figure 7.2c using: (a) the linear-transform technique; and (b) the rotation technique with 39° rotation angle.

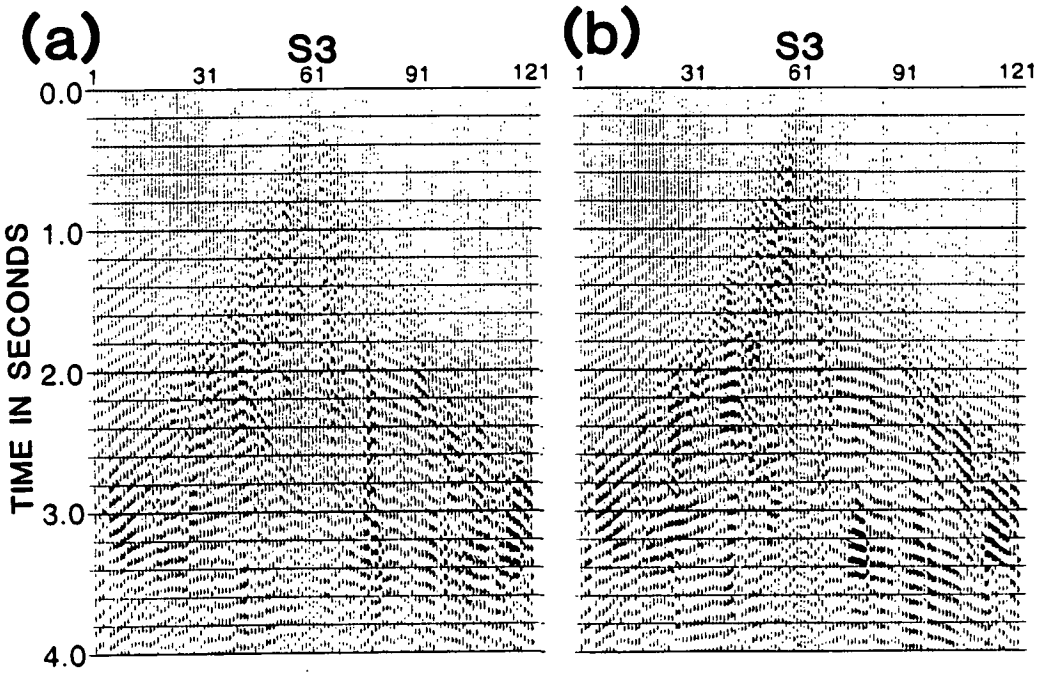

Figure 7.11. Comparison of the residual energy in the off-diagonal elements in the data matrix of Line 3 after split shear-waves are optimized: (a) after applying linear transform technique to the shot data matrix in Figure 7.2c; and (b) after applying 39° rotation to the shot data matrix in Figure 7.2c.

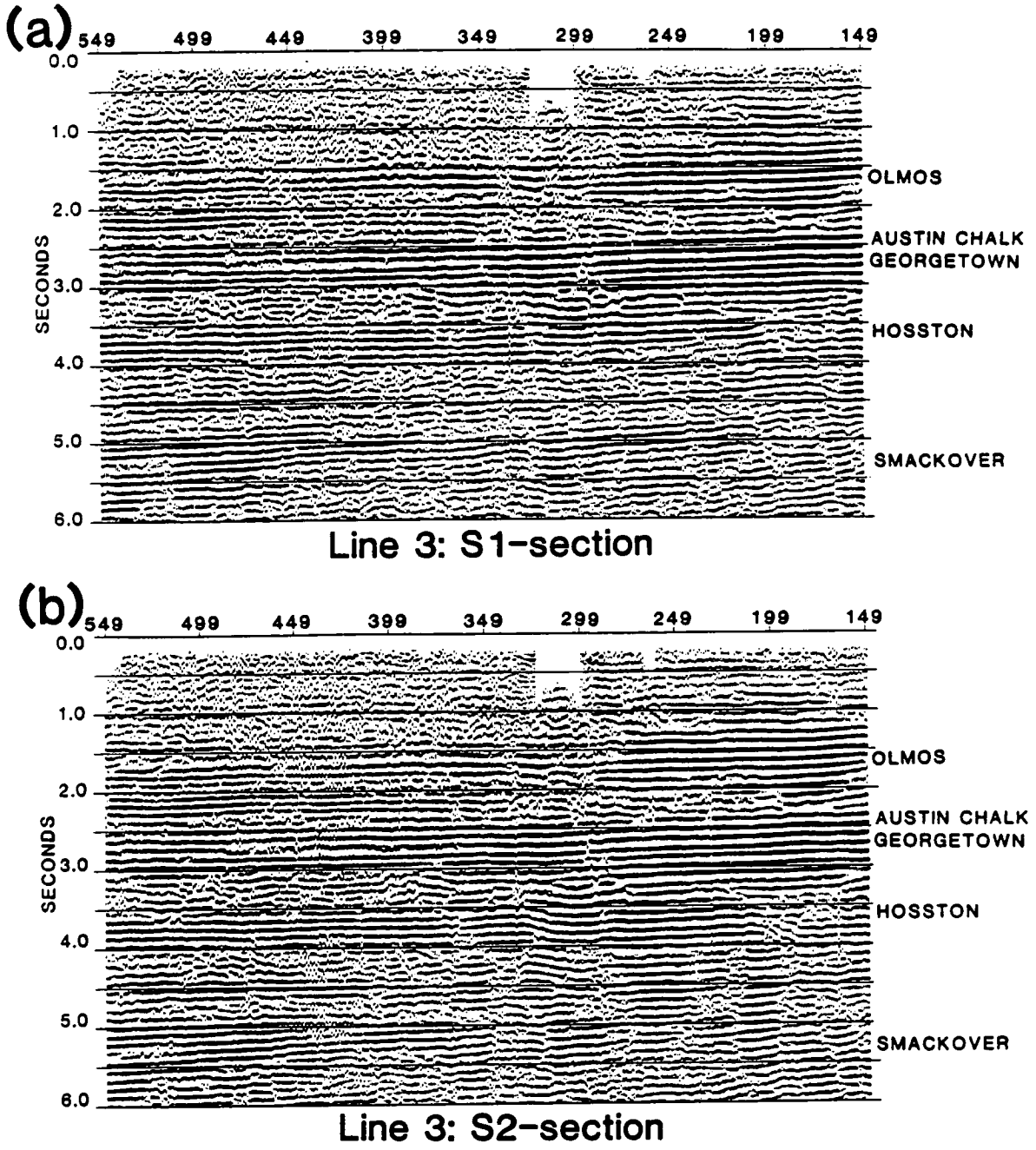

Figure 7.12. Final stacking results of Line 3 obtained by the linear transform process described in the text. (a) *S1*-section of the faster split shear-wave; and (b) *S2*-section of the slower split shear-waves.

7.5.3 Stacked polarization section

After applying LTT to separate the *S1*- and *S2*-waves, we can also obtain the component of polarization logs (Li and Crampin 1990d, 1991d; see also Chapter 5). Applying polarization filters (Li and Crampin 1991d; see also Chapter 5) and following the velocity and statics sequence and the final stacking sequence in Table 7.2, I can obtain the stacked polarization section or *polarization logs*. Such polarization logs with colour coded displays can be used to interpret lateral and vertical variations of polarization and subsurface structure.

Figures 7.13a and 7.13b compare polarization logs of shots from Lines 1 and 3. The polarization log of Line 1 (Figure 7.13a) shows two events, green (a radial polarization of 0°) and red (a transverse-horizontal polarization of 90°), indicating that *SV* and *SH* polarizations from the source are preserved. This implies either a plane-layered isotropic structure or, as here, an anisotropic structure where the reflection lines are along directions of vertical symmetry planes. The polarization log of Line 3 in Figure 7.13b shows blue and orange events with polarizations of -39° and 51° from the radial direction.

In reflection data, the polarizations may change with offset, as shown in Figure 7.13b. Such changes may be due to the variations expected for different directions of propagation through an anisotropic symmetry system. However, in most cases the polarization change is caused by random noise, or coherent noise such as interaction with converted *P*-waves from the effects of the shear-wave window (Evans 1984; Booth and Crampin 1985). In such cases, particularly if the noise falls into the same frequency band as the signal it may be very difficult to eliminate, and directly stacking CDP gathers may degrade the polarizations, as demonstrated by Li and Crampin (1989). Processing the data with polarization logs resolves this problem.

Since the polarization of noise almost always differs from the polarization

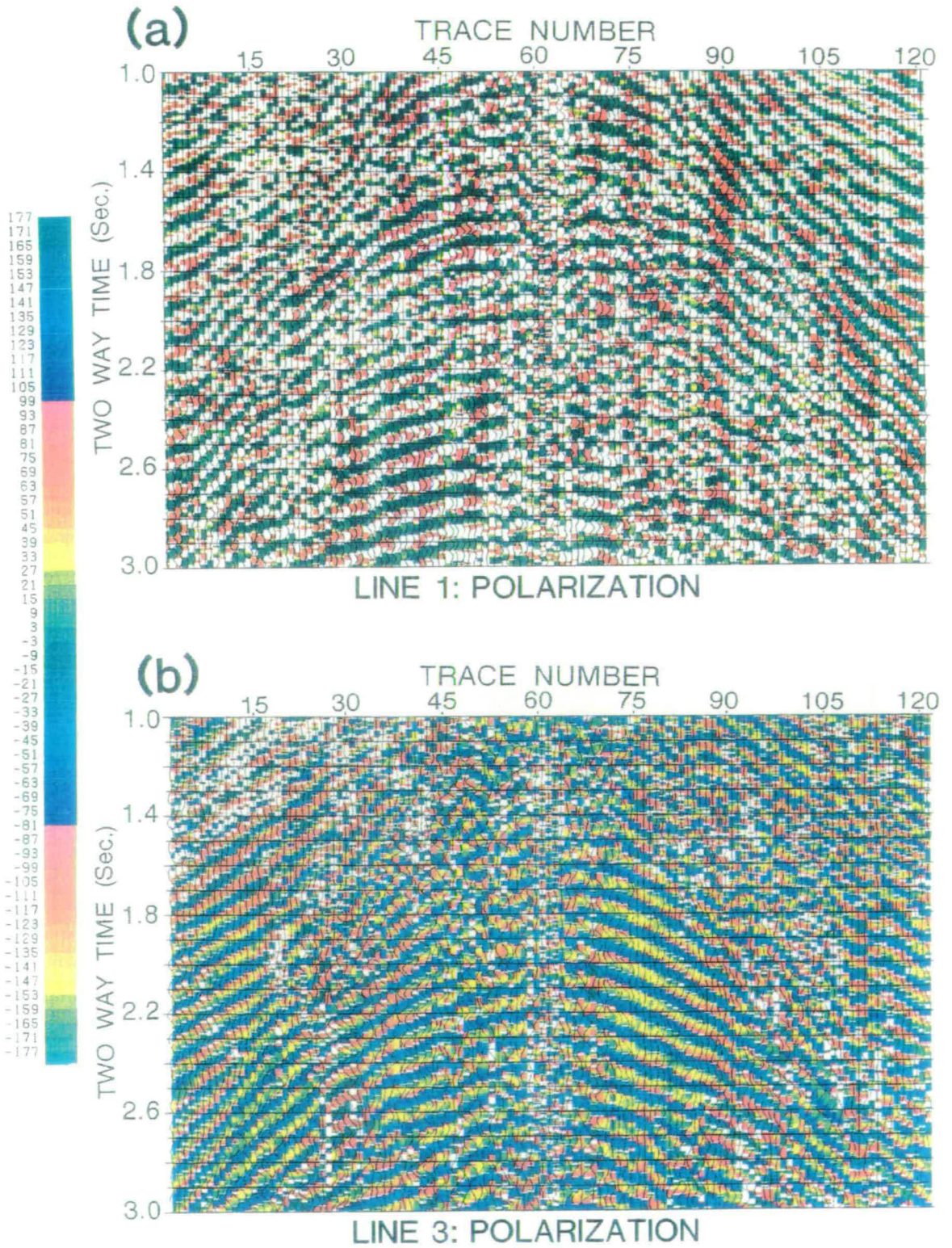

Figure 7.13. Polarization logs after applying the linear transform technique to shot data matrices in (a) Figure 7.2a, Line 1; (b) Figure 7.2c, Line 3. The colour scale is same as in Figure 7.3.

of the signal, the noise polarization can be easily eliminated by applying polarization filters before stacking. The polarization filter may be designed as an orthogonal fan filter as shown in Chapter 5 (Li and Crampin 1991d) in order to enhance orthogonal shear-wave motions. Here in processing the polarization component of Line 3, a polarization filter of 5° to 85° is applied to all the shot polarization records. The final stacked polarization log of Line 3 is shown in Figure 7.14 corresponding to the sections in Figure 7.9 and Figure 7.12. Note that a backgound green polarization (0°) appears in Figure 7.14. This is because after stacking, the polarization angles of non-coherent events are attenuated towards 0°, and the polarization colours are hence shifted towards green. Polarization logs of Lines 1 and 2 are not shown here because there is no shear-wave splitting in these two lines.

Both structural and anisotropic information can be obtained from polarization logs as suggested by Li and Crampin (1990b, 1990d, 1991c, 1991d; see also Chapters 4 and 5). Firstly, polarization logs of shear-waves can be used to image the subsurface structure, like the amplitude and phase of seismic waves. This is because shear-wave reflections from the same interface at adjacent stations tend to show similar polarizations, as shown in Figures 7.13 and 7.14. Comparing Figure 7.14 with Figures 7.9 and 7.12 shows that overall features of the subsurface structure in the polarization logs are similar to those in the amplitude sections, and most events in polarization logs have better continuity than those in the amplitude sections.

Secondly, lateral and vertical variation of polarizations can be determined from the polarization logs. As shown in Figure 7.14, from right to left and from top to bottom, dominant blue and weak red-orange colours appear on almost all major polarization events; and there are almost no polarization changes in Figure 7.14, which agrees with the geological and geophysical evidence about the crack strike in the area, as reviewed previously. The polarizations can be estimated from the blue and red-orange events, which represent two approximately orthogonal motions -51° degrees and 39° degrees

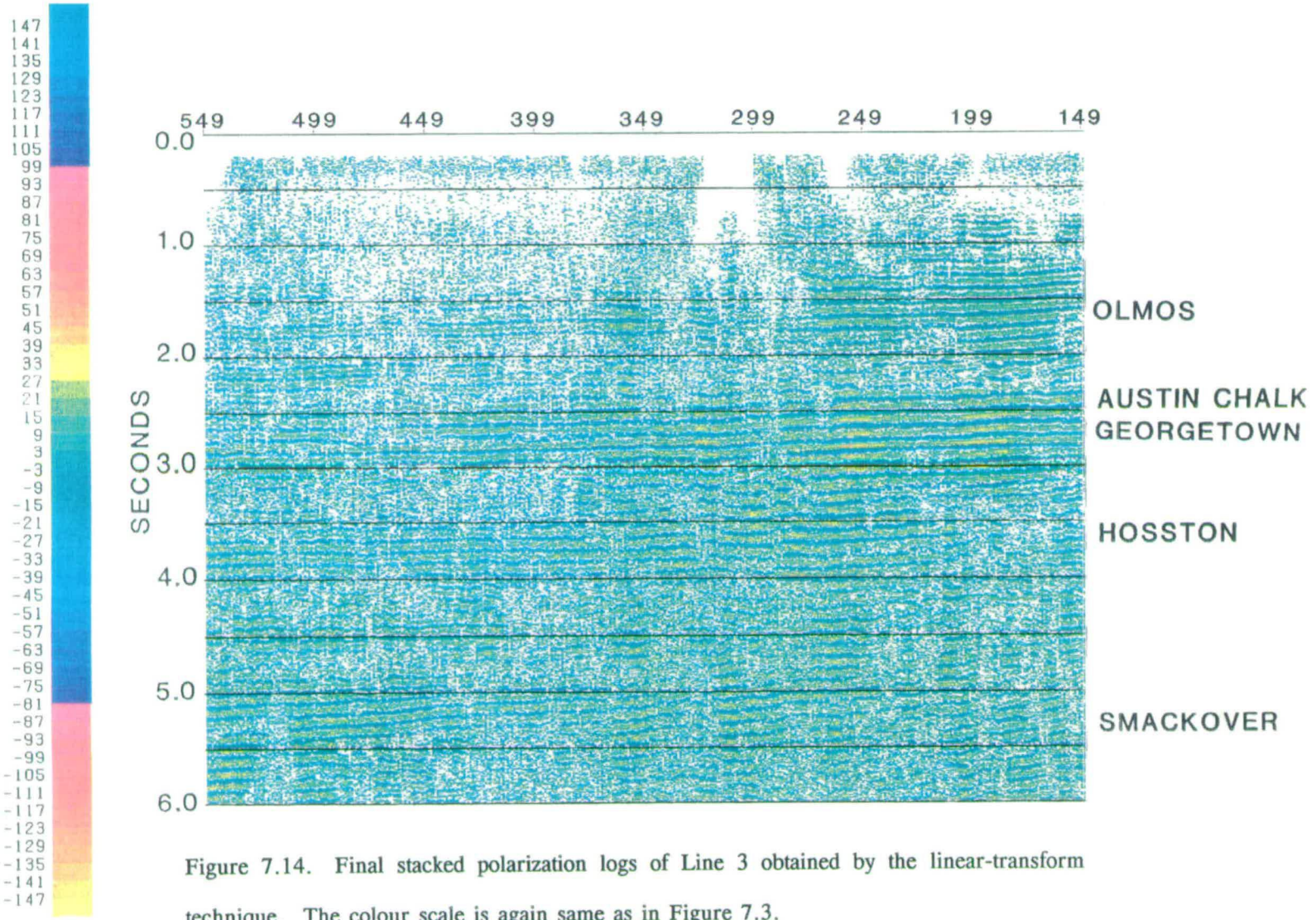

Figure 7.14. Final stacked polarization logs of Line 3 obtained by the linear-transform technique. The colour scale is again same as in Figure 7.3.

from the radial direction (north-sourth): N51°W and N39°E, repectively.

7.6 VARIATION OF SHEAR-WAVE ATTRIBUTES

Several shear-wave attributes have been used to characterize shear-wave anisotropy. These include differential stacking velocity, polarization variation, amplitude variation, mistie of events in *S1* and *S2* sections, and cumulative time delay. Among these, polarization, event mistie and cumulative time delay are the most reliable and commonly used attributes. Other attributes can aid the interpretation, but are often more subtle and more complicated to interpret. The polarization variation in the three reflection lines and its applications have been discussed above. Here, I examine the variations of the other attributes in the three reflection lines.

7.6.1 Differential stacking velocity

Figure 7.5 shows the comparison of average differential stacking velocities of the faster and slower shear-waves in the three lines. The differential stacking velocities increase with depth. Before 1.0 seconds, velocity differences in the three lines are all small and negligible. After 1.0 seconds, the difference in Line 1 (the broken line) remains small, while the difference in Line 2 (dotted line) sharply increases until 1.5 seconds, and the difference in Line 3 gradually increases after 1.5 seconds. Note that the turning points on the curves of the differential velocity correspond to strong coherent events in the stacked sections as seen in Figures 7.6, and 7.12. In summary, Line 1 shows the least variation in differential stacking velocity, whereas Line 2 shows the most, and Line 3 is intermediate between the other two.

7.6.2 Mistie of events

Figure 7.15 shows a comparison of stacked *S1* and *S2* sections for the three lines to display the mistie of events. The events in the *S1* and *S2*

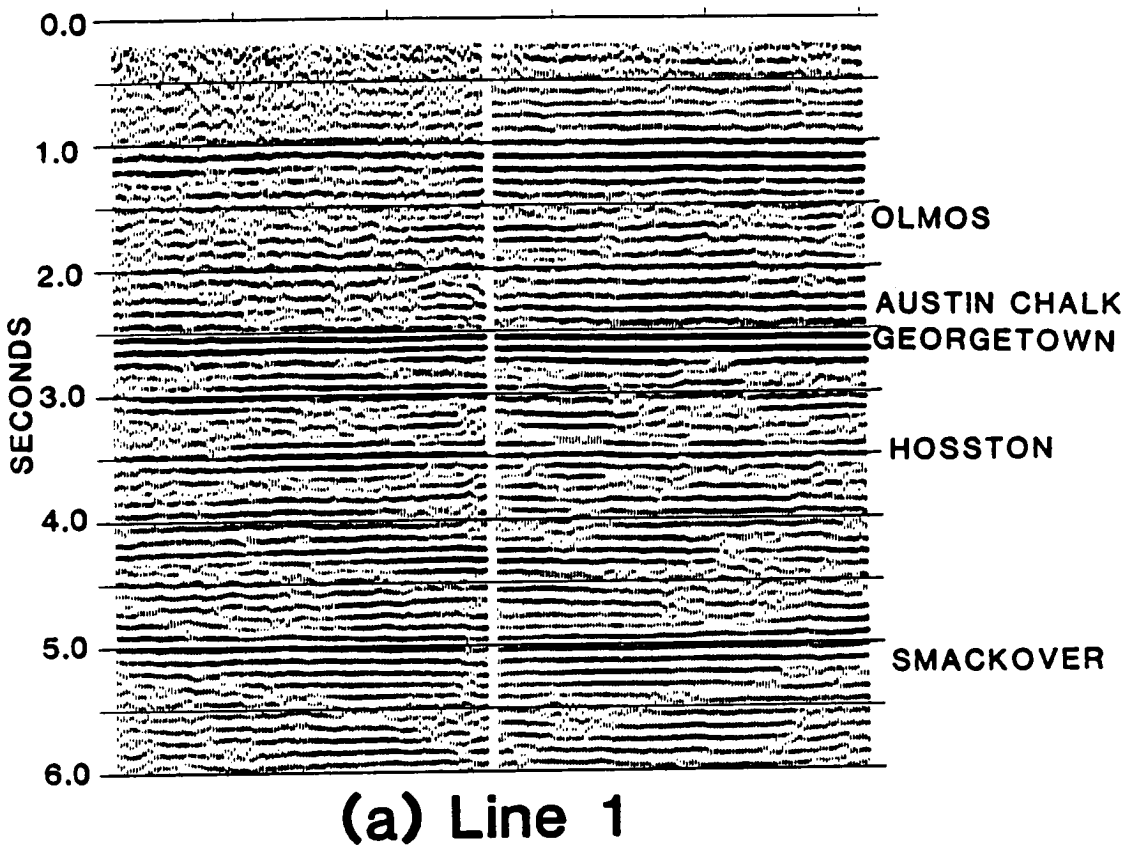

Figure 7.15. Comparison of mistie of events between faster (left panel) and slower (right panel) split shear-waves in the final stacked sections. (a) Line 1; (b) Line 2; (c) Line 3.

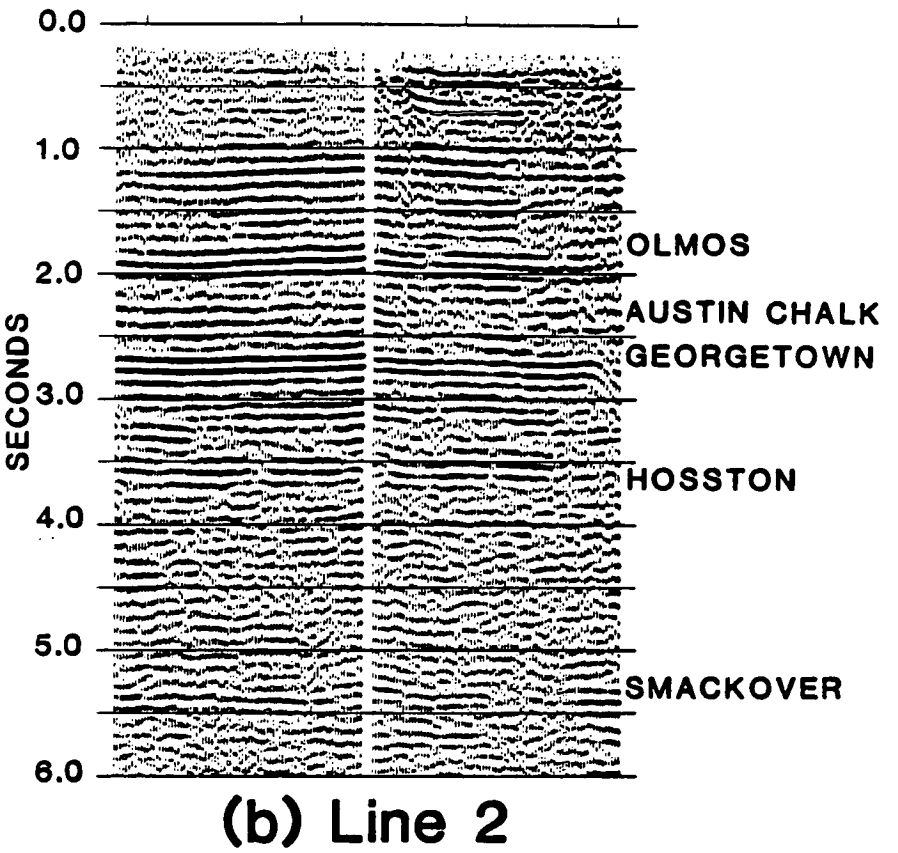

Figure 7.15 (continued)

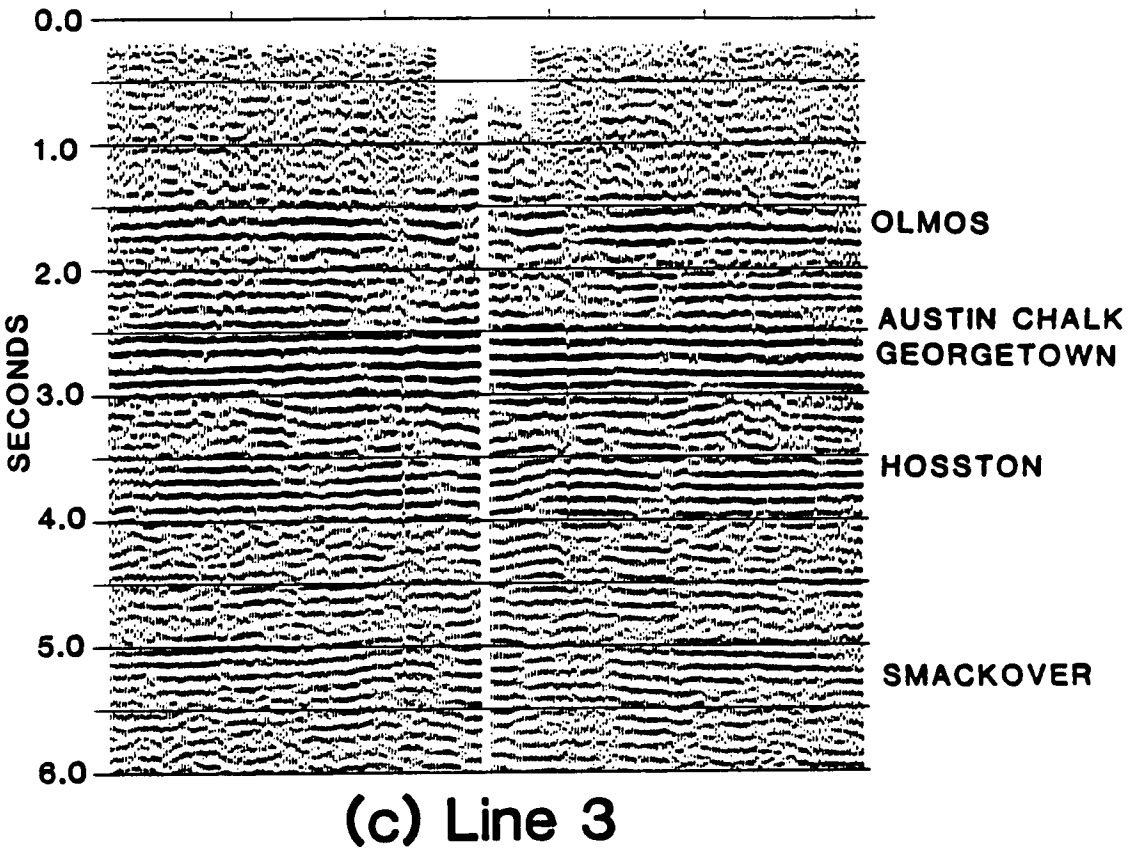

Figure 7.15 (continued)

sections of Line 1 (Figure 7.15a) tie very well and almost no mistie can be observed. Mistie of events in the stacked *S1* and *S2* sections can be observed in Lines 2 and 3 in Figures 7.15b and 7.15c, respectively. The reflection events in Line 2 corresponding to the Olmos Sandstone have a mistie of about 10-15 ms by visual examination, while reflection events at the Georgetown formation have a mistie of 20-40 ms. Larger misties can also be observed in Line 3.

7.6.3 Amplitude variation

Overall amplitude variations in the three lines can be compared in the stacked sections in Figures 7.6, and 7.12. The shallow events above 1.6 seconds in the *S2* section of Line 1 (Figure 7.6b) show slightly better continuity than those in the *S1* section (Figure 7.6a). For deeper events at 2.0 seconds and below, events in both *S1* and *S2* sections in Figures 7.6a and 7.6b show similar amplitudes and similar continuity. Events in both shallow and deeper parts of the *S1* section of Line 2 in Figure 7.6c show stronger amplitudes and better continuity than those in the *S2* section in Figure 7.6d. In Line 3, no obvious variations of differential amplitudes in *S1* and *S2* sections (Figure 7.12) can be observed, and the overall features of *S1* and *S2* sections are similar in Figures 7.9 and 7.12.

To examine the differential amplitude variations in more detail, we window the *S1* and *S2* sections over the Austin Chalk and Georgetown in Figure 7.16. The windowed *S1* and *S2* sections for Line 1 are shown in Figure 7.16a; for Line 2 in Figure 7.16b; and for Line 3 in Figure 7.16c. The windowed *S1* and *S2* sections of Line 1 show similar amplitude features to those in Figures 7.6a and 7.6b. The windowed *S1* and *S2* sections of Line 2 show significant difference between *S1* and *S2* both in magnitude of amplitudes and in continuity of events. The windowed *S1* and *S2* sections of Line 3 show subtle changes in magnitude and continuity of events for *S1* and *S2* arrivals, which are not shown in the sections in Figures 7.9 and 7.12. As in Figure

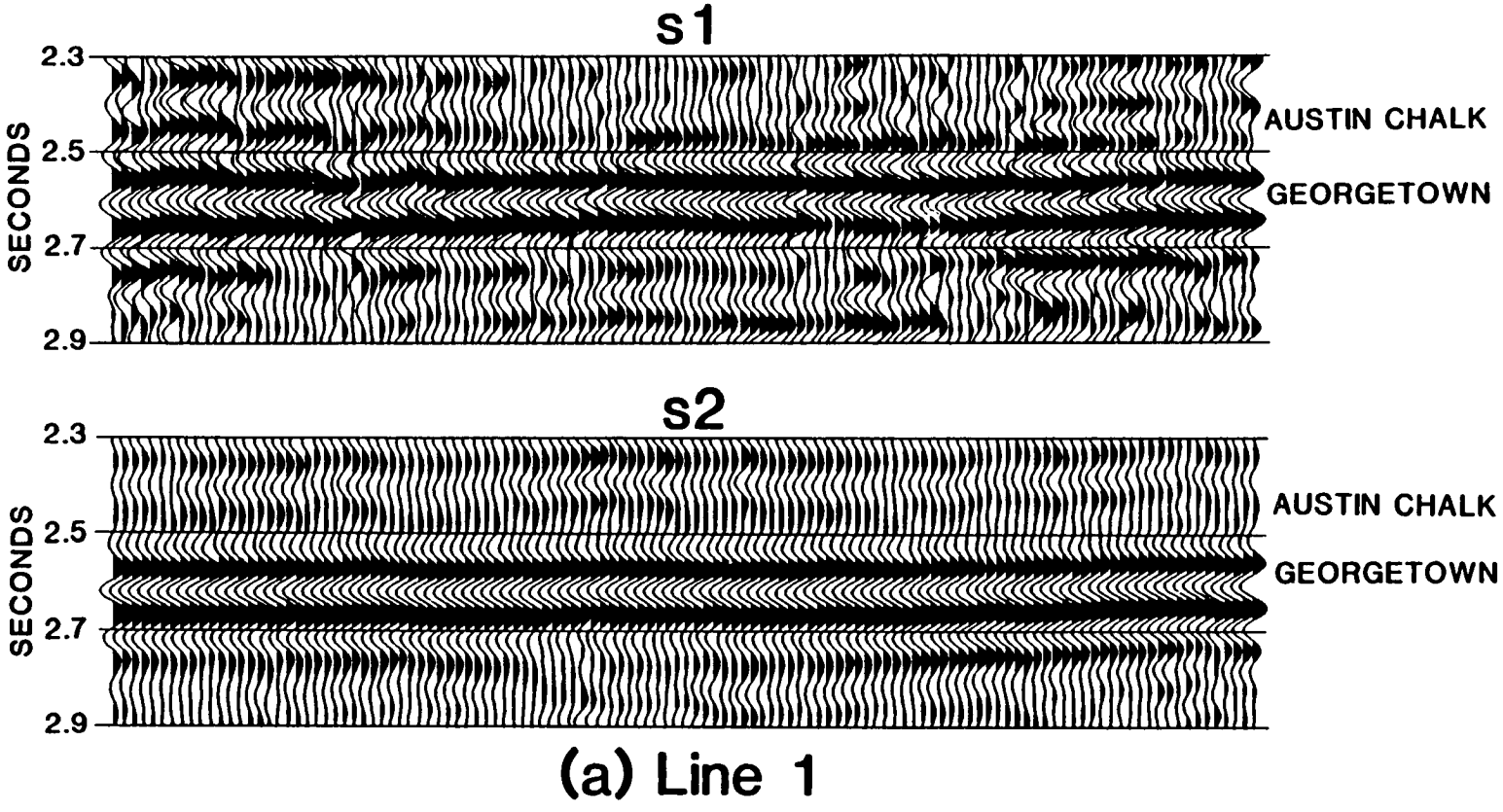

Figure 7.16. Comparison of amplitude variation between the faster and slower split shear-waves in the windowed final stacked *S1* and *S2* sections. (a) Line 1; (b) Line 2; (c) Line 3.

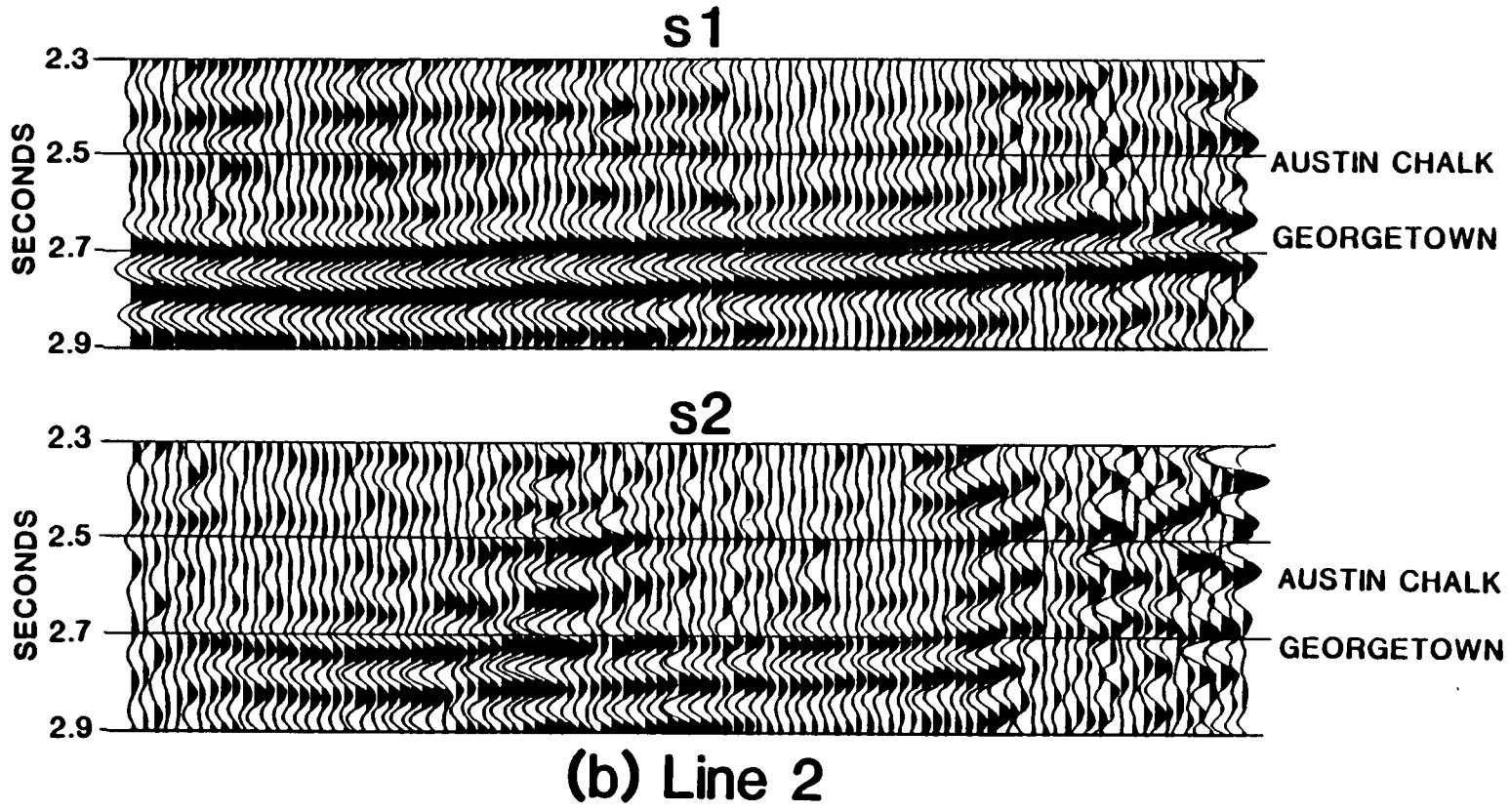

Figure 7.16 (continued)

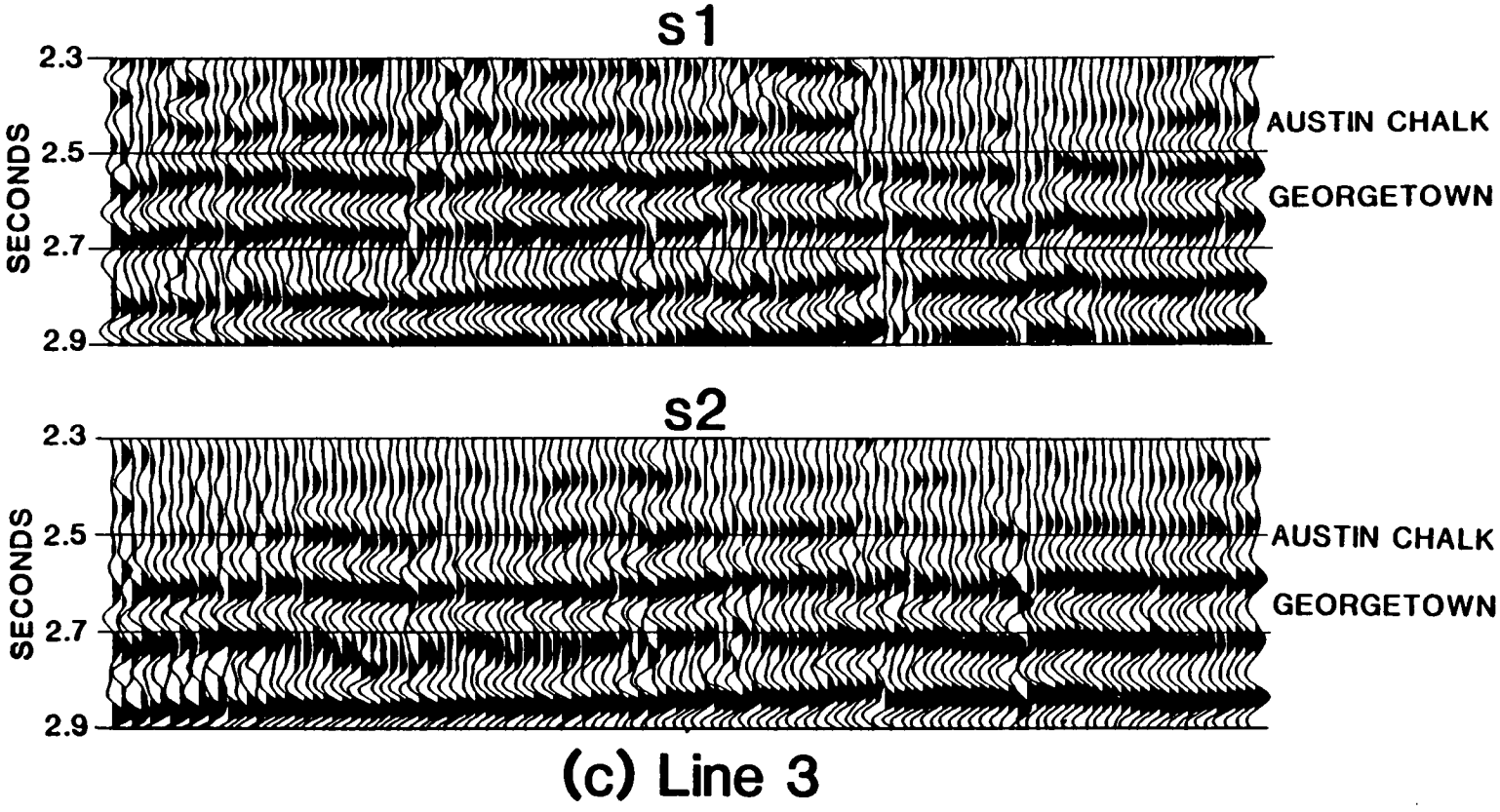

Figure 7.16 (continued)

7.16c, the events corresponding to the Austin Chalk in *S1* section show slightly larger amplitude and better continuity than those in the *S2* section. There are also some subtle changes in events at 2.7 seconds. Comparing Figures 7.16b and 7.16c shows that the variation in amplitude in Line 3 is not as significant and obvious as in Line 2.

7.6.4 Time delay variation

The mistie of events shown in Figure 7.15 demonstrates the variation of time delays in the three lines. To quantify the time delays, Figure 7.17 shows the cross-correlation of the *S1* and *S2* sections from the Georgetown formation immediately underneath the Austin Chalk and are the cumulative time delays from the surface. Time delays above the Austin Chalk are difficult to measure principally due to lack of quality events. The three lines represent the delays in the three survey lines 1, 2, and 3 with increasing average delays of about 10 and 25 ms for Lines 1 and 2, and for Line 3, 50 ms for stations from #1 to #400, decreasing to about 35 ms at station #1000.

We take the ratio of the time delay to the travel time of the raypath to estimate the percentage shear-wave anisotropy. The Georgetown formation appears at about 2.5 seconds as shown in Figures 7.6, and 7.12. Thus the shear-wave anisotropy is less than 0.5% for Line 1, and about 1.5% for Line 2, and varies from 2.5% to 1.5% from north to south along Line 3.

7.7 INTERPRETATION AND CORRELATION

7.7.1 Variation of shear-wave anisotropy

As indicated by the mistie of events (Figure 7.15) and measured from the time delays (Figure 7.17), the average anisotropy in Line 1 is small, less than a half percent. This is consistent with variations in other attributes such as the small differential stacking velocities in Figure 7.5 and the small differential

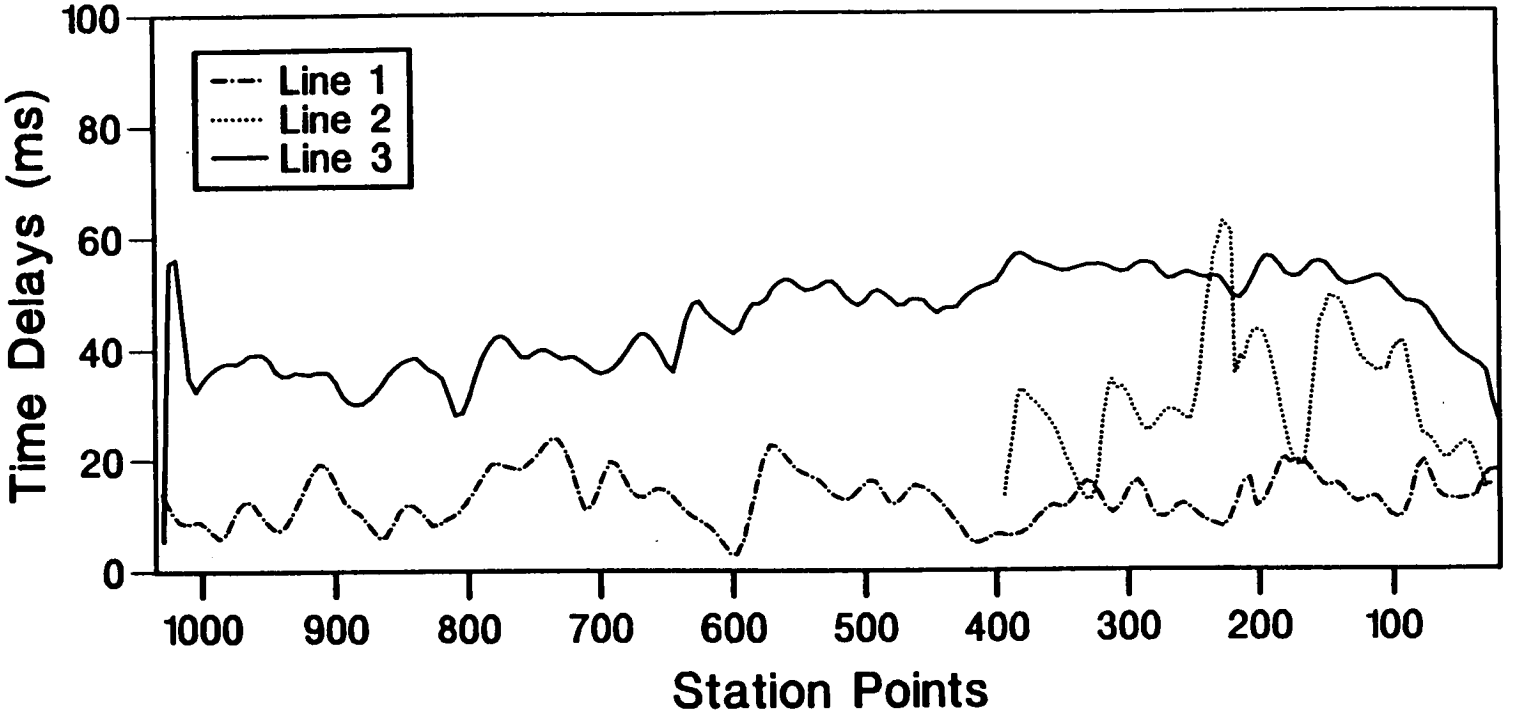

Figure 7.17. Comparison of time delays between the faster and slower split shear-waves measured from the Georgetown formation immediately underneath the Austin Chalk in the stacked sections of the three reflection lines in Figures 7.6, and 7.12: Line 1 - broken line; Line 2 - dotted line; and Line 3 - solid line.

amplitude variations in Figure and 7.16a. There is an increasing trend of anisotropy for Lines 2 and 3. The average anisotropy is 1.5% in Line 2 and varies from 1.5 to 2.5% along Line 3. This is also consistent with variations in differential stacking velocity and differential amplitude in Figures 7.5, and 7.16b and 7.16c.

There are, however, two exceptions to the trend of variation of attributes described above. The first is that the reflection events in the shallow part of the *S2* section of Line 1 show slightly stronger amplitudes and better continuity than the corresponding events in *S1* section (see Figures 7.6a, 7.6b and 7.16a). The second is that Line 2 shows a slightly larger differential velocity (Figure 7.5) and differential amplitude (Figure 7.16b) than Line 3 (Figure 7.16c). These appear to contradict the increasing mistie of events in Figure 7.15 and time delays in Figure 7.17.

Both exceptions are probably caused by the presence of coherent noise in the *XX* element of the data matrix, particularly in the shallow part. The shallow part of the *XX* element contains more coherent noise, particularly converted waves and surface waves, than the shallow part of the *YY* element as shown in Figure 7.2. Note that converted waves have higher stacking velocity than primary shear-wave reflections. Thus the presence of these converted waves in the shallow part of the component will distort the stacking velocity and amplitude variation depending on the quality of the primary shear-wave reflections. Also note that as the line azimuth changes, such noise may shift from one component to the other.

For the cause of the first exception, we should note that since Line 1 is parallel to the crack strike, the *XX* element is the *S1* component. The faster split shear-wave, and appearance of events in the shallow part of *S1* section and the stacking velocity of the *S1* component are thus affected by the presence of converted waves and surface waves. These distortions are small, because the overall data quality of Line 1 is good. For the second exception, because Line

2 is perpendicular to the crack strike, the *S2* component is the *XX* component. The presence of converted waves and other noise in the shallow part of the *S2* section has two effects. The stacking velocity of the *S2* component will shift towards the stacking velocity of the converted waves, if the data quality is not good enough to separate them, so that the differential stacking velocity will be further increased. [Note that the differential stacking velocity is a measurement of apparent anisotropy. The slower split shear-wave tends to have a larger stacking velocity than the faster split shear-wave (Thomsen 1988; Li and Crampin 1990a).] The other effect is that noise will degrade the stacking results of the slower split shear-wave and increase the differential amplitude between the faster and slower split shear-waves.

7.7.2 Correlation with oil production

Variation of anisotropy in the three lines can be approximately correlated with oil production. Figure 7.1b shows the well locations in the study area. Few wells have been drilled near Line 1, and the line is over tens of miles away from neighbouring production fields, but Line 2 is at the edge of the Pearsall and Big Wells field operating in Frio and Northern Dimmit and Southern Zavala and there are some ten wells within a mile of the line. Line 3 is through the centre of the Pearsall Field, and many tens of producing wells have been drilled along, or near the line. Comparing Figure 7.1b with Figure 7.17 shows that the overall oil production along or near the three reflection lines approximately correlates with the anisotropy (time delays) observed along the three lines, where Line 1 with smallest time delays has little production nearby; Line 2 with intermediate time delays shows intermediate production; and Line 3 with largest time delays has largest production nearby.

Variation of anisotropy along Line 3 can also be correlated to oil production along or near the line. Figure 7.18 shows the well distribution within 1 mile either side of the line. Most wells are distributed in the northern part of the line with station numbers below #700. There are only two

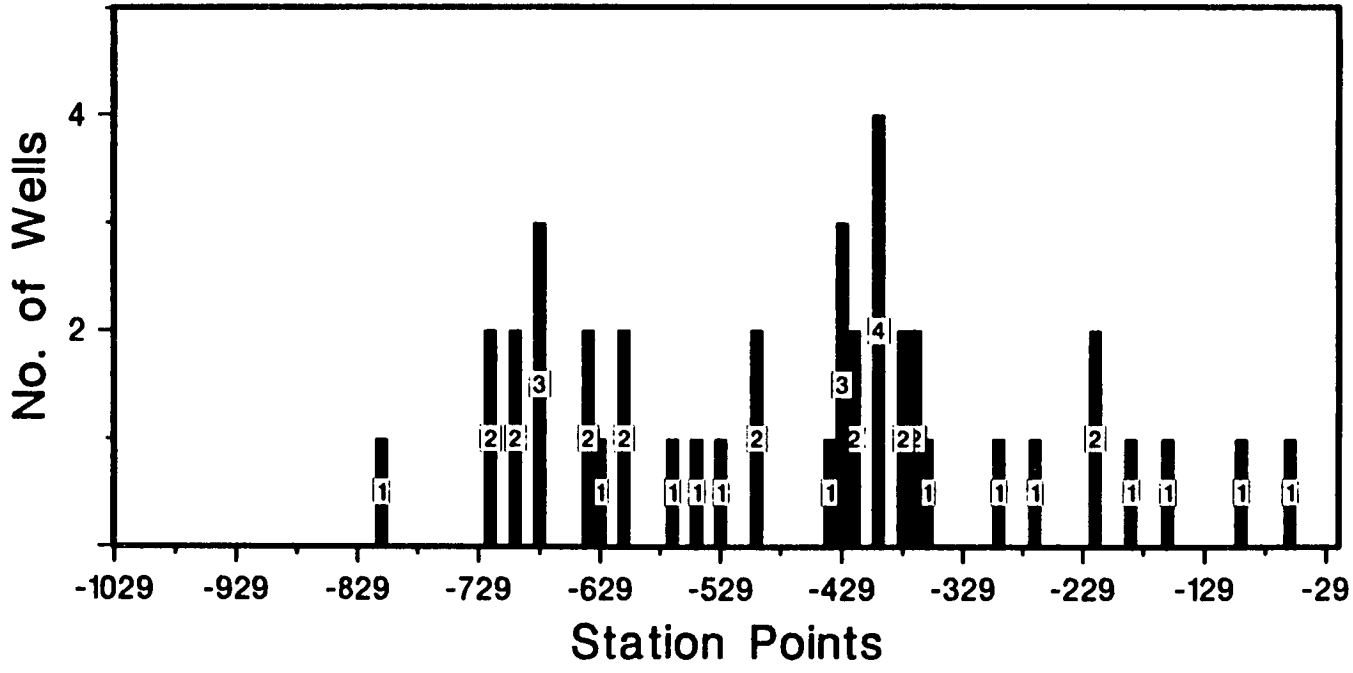

Figure 7.18. Distribution of producing wells within 1 mile either side of Line 3.

wells at the northern end (station numbers less than #100), and only one well at the southern end of the line (numbers greater than #800). The variation of time delays along Line 3 in Figure 7.17 shows similar variation. In the northern part (numbers less than #100), the delay rapidly builds up up to 55 ms, remains at about the same level until #400, and then uniformly decreases to about 35 ms at #1000 towards the south. Thus the trend of variation of time delays broadly correlates with the overall trend of well distribution along the northern part of the line.

The overall trend of the variation in the polarization log of Line 3 in Figure 7.14 may also be correlated with the oil production along the line. Corresponding to a high production area from #399 to #449, the polarizations are more scattered with white background in the lateral variations, and corresponding to major oil plays in the Austin Chalk, the polarization events are less continuous and often broken in vertical variations. Following Mueller (1991), this indicates areas of fractured chalk where good production may be expected. We should point out that such variations are subtle and complicated, and only when the nature of such variations of polarization are better understood, from more case studies, can such interpretation be confidently made.

In summary, shear-waves in the three reflection lines show typical features of shear-wave splitting. The variation of anisotropy in the three lines can be correlated to the commercial oil production in the study area. Variation of anisotropy along Line 3 can be also correlated with oil production along the line. High production areas and major oil plays are found to be associated with scattered polarizations and broken polarization events in the stacked polarization logs.

7.8 DISCUSSION

Detailed correlations of the amount of shear-wave splitting with oil

production in individual wells (Brodov *et al.* 1990; Cliet *et al.* 1991; Mueller 1991) and individual areas (Lewis *et al.* 1991) have been published elsewhere. This paper demonstrates that the overall degree of anisotropy, as quantified by the percentage of differential shear-wave velocity along reflection surveys that are tens of miles in length, can be broadly correlated with the overall amount of oil production nearby. When such correlations refer to the Austin Chalk (this study and Mueller 1991), where production is dominated by wells penetrating fractures in this porous but low permeability formation, the correlations again confirm the close association of shear-wave anisotropy with subsurface cracks and fractures.

Although it is difficult to quantify because of noise and poor quality arrivals, the increasing trend of anisotropy from Lines 1 to 2 and 3 appears to be present throughout the whole rockmass not just in the neighbourhood of the productive Austin Chalk. The same trend of anisotropy is certainly present in the Olmos Sandstone above the chalk, and may be present below the Austin Chalk and the Georgetown formation, but the arrivals are of lower quality. Certainly the anisotropy of the Austin Chalk is associated with large fractures, but the apparent pervasive anisotropy throughout the rockmass is probably caused by extensive-dilatancy anisotropy or EDA, rather than widespread distributions of large fractures. EDA is the distribution of stress-aligned fluid-filled cracks, microcracks, and preferentially oriented pore-space present in most types of rock, which causes shear-wave splitting in a wide variety of geological formations (Crampin and Lovell 1991).

The correlation of the trend of anisotropy throughout the rockmass with oil production and fractures in the Austin Chalk suggests that the geological conditions creating fractures in the chalk also align cracks and microcracks throughout the rockmass. Note that EDA-cracks are strain- and stress-induced alignments of existing fluid-filled inclusions that are present in most rocks, especially sedimentary formations. Such re-alignments of existing fluid-filled inclusions can take place at much lower levels of stress and strain deformation

than the high stresses required to open new fractures, and can be caused by a variety of mechanisms, not just elastic deformation (Crampin and Lovell 1991).

7.9 CONCLUSIONS

The shear-waves in the three reflection lines show typical characteristics of shear-wave splitting in both shot data matrix and colour displays of instantaneous polarization logs. The overall fracture orientation is N39°E in the study area, agreeing with other geological and geophysical results. In areas in which commercial oil production is absent, the average time delay of the split shear-waves is less than 10 ms, corresponding to about 0.5% anisotropy or less. In areas close to major production fields, the average delay is about 30-40 ms, corresponding to about 1.5% shear-wave anisotropy. In major production areas, the delay is up to 50 to 60 ms, corresponding to about 2.5% anisotropy. Other features in the three survey lines, such as differential amplitudes of the faster and slower split shear-waves, and differential stacking velocities, show similar trends of variations as the anisotropy and oil production vary, but these variations are more subtle, complicated and sometimes difficult to interpret compared with variations of time delays of split shear-waves.

The use of the complex component analysis and the linear transform technique simplifies the processing sequence of shear-wave reflection data in the presence of anisotropy. It allows the generation of both stacked amplitude and stacked polarization sections of split shear-waves. Not only can lateral variation of polarizations, which are often associated with lateral variation of crack geometry, be identified from the polarization section, but subsurface structures can also be better imaged by shear-wave polarizations compared with conventional amplitude images. High production areas and major oil plays are found to be associated with scattered polarizations and broken polarization events in the stacked polarization section.

CHAPTER EIGHT

SUMMARY OF ACHIEVEMENTS AND FINDINGS AND FUTURE WORK

8.1 SUMMARY

The results of this thesis can be classified into three groups: theoretical development, processing techniques, and case studies. The achievements and findings can be summarized as follows.

8.1.1 Theoretical development

1. Approximate velocity equations in symmetry planes of weakly anisotropic solids have been extended to off-symmetry planes to meet the needs of real data. The modified equations are good approximations up to approximately 10% anisotropy in symmetry planes and 6% in off-symmetry planes.

2. The moveouts of faster and slower split shear-waves in CMP gathers, or shot records, from a single interface of weak anisotropy can be separated into hyperbolic moveouts and residual moveouts. The residual moveout is proportional to the amount of anisotropy in the medium concerned and to the spread length of the acquisition geometry.

3. Expressions have been derived for calculating plane shear-wave reflection and transmission coefficients at vertical incidence at an interface separating two cracked (anisotropic) media with different crack strikes. These expressions can be used to examine the effects that changing crack strike and crack density has

on shear-wave amplitudes.

4. For an interface with high velocity-contrasts, the effects of crack strike varying with depth can be neglected in processing shear-wave splitting. For an interface with low velocity-contrasts, the amplitude ratio of the off-diagonal elements in the data matrix after separation of split shear-waves can be used to extract anisotropic information.

8.1.2 Processing techniques

5. Complex component analysis has been developed for displaying and identifying shear-wave splitting in multi-component seismic data. The technique allows calculation of shear-wave attributes such as instantaneous polarizations and instantaneous amplitudes for two-component seismic data, and shear-wave splitting sections (SWS-sections), and polarization logs for four-component data.

6. These shear-wave attributes can be displayed as colour-coded time-versus-offset seismic sections, so that any polarization anomaly can be continuously followed both vertical and laterally. This can aid the identification and interpretation of shear-wave splitting and the stratigraphic interpretation of reflection events in seismic sections.

7. A linear-transform technique has been developed for quantifying shear-wave splitting in four-component seismic data. The technique transforms the four-component data by four linear transforms so that the complicated shear-wave motion is linearized in a wide variety of circumstances.

8. The linear-transform technique allows various attributes to be measured, including the polarizations and time delays of split shear-waves, as well as downhole geophone orientations. It also allows the time series of the faster and slower split shear-waves to be separated deterministically, and such

separation can be implemented before stacking in reflection surveys.

8.1.3 Case studies

9. The data were acquired by Amoco Production Company in Dimmit, La Salle, and Frio Counties in South Texas. These included three reflection lines with different azimuths in areas of varying oil production. The purpose of the survey was to verify the use of shear-wave splitting in characterizing fractured reservoirs.

10. The case studies confirm that the use of complex component analysis and the linear transform technique can simplify the processing sequence of shear-wave reflection data in the presence of anisotropy, and allows the generation of both stacked amplitude and stacked polarization sections (polarization logs) of split shear-waves.

11. Polarizations of split shear-waves tend to be remarkably coherent in polarization sections. The polarization section images both vertical and lateral variations of polarizations, and also images subsurface structures better than conventional amplitude sections.

12. High oil production area and fracture zones of reservoirs are found to be associated with scattered polarizations and broken polarization events in the stacked polarization sections. Thus, it is possible to use polarization sections to identify fracture zones associated with fractured hydrocarbon reservoirs.

13. The degree of anisotropy can be broadly correlated with the oil production in the survey area. Other features in the survey lines, such as differential amplitudes of the faster and slower split shear-waves, and differential stacking velocities, show similar trends of variations as the anisotropy and oil production vary.

8.2 FUTURE WORK

During 1990 and 1991, major progress has been made in understanding, interpreting and processing shear-wave splitting, with direct applications to hydrocarbon production, and a possible application to monitoring stress changes before earthquakes, about which Crampin and Lovell (1991) provided a comprehensive review. Crampin and Lovell (1991) also identified major areas of application of shear-wave splitting and major future developments. Here, I summarize necessary future work with respect to shear-wave splitting in reflection surveys, as a continuation of the work described in this thesis.

8.2.1 3-D polarization image of subsurface structures

Three-dimensional (3-D) and three-component (3-C) reflection data have been acquired to study anisotropy for reservoir characterization (Lewis *et al.* 1991; Kramer 1991). Research can be carried out to further develop complex component analysis to investigate the 3-D polarization image in characterizing structural and anisotropic variations.

8.2.2 Anisotropic velocity analysis and residual moveouts

In addition to the work in Chapter 2, several other studies have been published recently about velocity and travel time equations in anisotropic media with hexagonal symmetry (Sena 1991; Berge 1991). Case studies can be undertaken to estimate shear-wave residual moveouts and vertical and horizontal velocities in anisotropic media, and to investigate their application to improving CDP stacking results and interpreting anisotropic information. Ideal datasets would be 3-D or 2-D multi-component data with horizontal interfaces.

8.2.3 Effects of anisotropy and heterogeneity

To aid the processing and interpretation of shear-wave splitting in areas

with complex geological structures, it is necessary to develop a practical algorithm for calculating synthetic seismograms for models containing dipping and curved interfaces, so that structure-induced effects on shear-wave splitting can be compared with effects of anisotropy in order to identify and separate these kinds of effects.

8.2.4 Near-surface effects

Shear-wave polarizations observed at the surface may differ from those at depth if the crack orientation changes with depth. The reflection coefficients in Chapter 3 and the linear-transform technique in Chapter 6 can help to estimate and eliminate the effects of the near-surface (Macbeth, Li, Crampin, and Mueller 1992). Refining algorithms need be developed and case studies should be made to verify these techniques.

8.2.5 Multi-component deconvolution

Deconvolution is one of the most efficient techniques for enhancing seismic data quality in conventional seismic data processing (Yilmaz 1987). However, it is not recommended in processing shear-wave splitting, because possible phase distortions are likely to be introduced during deconvolution. Kramer (1991) proposed a three-component deconvolution for processing VSP data which can improve the data quality while preserving shear-wave splitting. Four-component deconvolution can be designed for reflection data, which fulfil the same purose (Li and Macbeth, personal communication).

8.2.6 Integrated studies

Recently, there has been an increase in using crosshole surveys. Guided waves have a dominant energy in most crosshole seismic data (Lou and Crampin 1991b). Lou and Crampin (1991a, 1991b, 1992) studied the effects of anisotropy on guided waves and investigated their applications to monitoring

enhanced oil recovery operations. An integrated study of reflection surveys, VSPs, and crosshole surveys will be of importance for reservoir characterization and development.

In conclusion, understanding shear-wave propagation and observations of shear-wave splitting in the Earth's crust are fundamental advances for seismology. In this thesis, I developed suitable techniques for processing shear-wave splitting in controlled source seismology, and I have shown that the degree of shear-wave splitting can be correlated with oil production. I have also demonstrated that areas of high oil production and high fractured zones are associated with scattered polarizations and broken polarization events in polarization sections. These features are directly related to hydrocarbon determination. However, one is clearly only just beginning to understand and use the phenomenon of shear-wave splitting. As shear-wave technology together with study of shear-wave splitting further develops, it will bring an interesting future for shear-wave exploration in the search for hydrocarbon resources.

APPENDIX A
DERIVATION OF MOVEOUT EQUATION (2-8)

Letting $\phi = 0°$ and $90°$ in equation (2-5) gives:

$$1/v^2_v = a_0 + a_1 + a_2 + a_3 + a_4; \text{ and} \tag{A-1}$$

$$1/v^2_h = a_0; \tag{A-2}$$

where v_v and v_h are the vertical and horizontal velocities, respectively, for any type of body waves, in Figure 2.1.

Substituting equation (2-5) into equation (2-7) gives:

$$\begin{aligned} t^2 &= 4z^2[a_0 + a_1\cos\phi + a_2\cos^2\phi + a_3\cos^3\phi + a_4\cos^4\phi]/\cos^2\phi; \\ &= 4z^2(a_0/\cos^2\phi + a_2 + a_4\cos^2\phi) + 4z^2(a_1 + a_3\cos^2\phi)/\cos\phi. \end{aligned} \tag{A-3}$$

Note that

$$\begin{aligned} 2z\tan\phi &= x; \text{ and} \\ 1/\cos\phi &= 1/(1-\sin^2\phi)^{1/2} \\ &= 1 + (\sin^2\phi)/2 + (3\sin^4\phi)/8 + (15\sin^6\phi)/48 + R_n; \end{aligned} \tag{A-4}$$

where R_n is the residual error term and, for incidence angles less than $30°$, R_n is less than 0.0014, and can be neglected. (High order terms may be introduced for higher incidence angles.) Note also that $\sin\phi$ is the ratio of spread length of acquisition geometry to the length of the ray path and may be called the *spread factor*. Substituting (A-4) into equation (A-3), omitting the error term R_n and making some suitable manipulations, gives:

$$t^2 = 4z^2(a_0+a_1+a_2+a_3+a_4) + x^2(a_0+a_1/2-a_3/2-a_4) + \\ + x^2(-a_1/2+a_3/2+a_4)\sin^2\phi + x^2(3a_1-a_3)/8\sin^2\phi + \\ + x^2(-a_1+a_3)/16\sin^4\phi - x^2(5a_1/16+a_3/4)\sin^6\phi + \\ + x^2(5a_3/16)\sin^8\phi. \qquad \text{(A-5)}$$

Equation (A-5) is a general moveout equation for weak anisotropy which is accurate to the second order in the amount of anisotropy and third order in the spread factor $\sin\phi$. It can be further manipulated. First the normal moveout velocity can be calculated as:

$$1/v^2_{nmo} = \lim_{x\to 0}(dt^2/dx^2) = a_0 + a_1/2 - a_3/2 - a_4. \qquad \text{(A-6)}$$

Substituting equations (A-1), (A-2) and (A-6) into (A-5), and omitting the higher order terms of $\sin^4\phi$, $\sin^6\phi$ and $\sin^8\phi$ gives:

$$t^2 = 4z^2/v^2_v + x^2/v^2_{nmo} + x^2(1/v^2_h - 1/v^2_{nmo})\sin^2\phi + x^2(3a_1-a_3)/8\sin^2\phi \\ = t^2_0 + x^2/v^2_{nmo} + x^2(1/v^2_h - 1/v^2_{nmo})\sin^2\phi + t^2_{off}\sin^2\phi; \qquad \text{(A-7)}$$

where

$$t^2_0 = 4z^2/v^2_v; \text{ and}$$
$$t^2_{off} = x^2(3a_1 - a_3)/8. \qquad \text{(A-8)}$$

Note that coefficients a_1 and a_3 are associated with velocity variations in off-symmetric planes. As discussed previously, if angle $\alpha = 0°$ in equation (2-5) is also in a plane of vertical symmetry, coefficients a_1 and a_3 will be zero. Thus $3a_1-a_3$ must be small compared to other terms in equation (A-7). Omitting term $t^2_{off}\sin^2\phi$ in equation (A-7) gives equation (2-8).

APPENDIX B
DERIVATION OF REFLECTION AND TRANSMISSION COEFFICIENTS

B.1 STRESS-STRAIN RELATIONSHIP

Figure B.1 shows schematically an anisotropic material with orthorhombic symmetry formed from a combination of PTL and EDA anisotropy. A shear-wave entering such a material necessarily splits into two phases with different speeds and different polarizations (Crampin 1981). For near-vertical propagation, the faster split shear-wave is polarized parallel to the crack strike and the slower split shear-wave perpendicular to the crack strike. A right-handed coordinate system is assumed as shown in Figure B.1, where x_1 is parallel to the crack normal, x_2 is parallel to the crack strike, and x_3 is vertical downwards. This system may be called the natural coordinate system of a cracked material. The stress-strain relation can be written as (Crampin 1981):

$$\begin{bmatrix} \sigma_{11} \\ \sigma_{22} \\ \sigma_{33} \\ \sigma_{23} \\ \sigma_{31} \\ \sigma_{12} \end{bmatrix} = \begin{bmatrix} c_{11} & c_{12} & c_{13} & 0 & 0 & 0 \\ c_{12} & c_{22} & c_{23} & 0 & 0 & 0 \\ c_{13} & c_{23} & c_{33} & 0 & 0 & 0 \\ 0 & 0 & 0 & c_{44} & 0 & 0 \\ 0 & 0 & 0 & 0 & c_{55} & 0 \\ 0 & 0 & 0 & 0 & 0 & c_{66} \end{bmatrix} \begin{bmatrix} \varepsilon_{11} \\ \varepsilon_{22} \\ \varepsilon_{33} \\ \varepsilon_{23} \\ \varepsilon_{31} \\ \varepsilon_{12} \end{bmatrix}; \tag{B-1}$$

where σ_{ij} and ε_{ij} $(i,j=1, 2, 3)$ are stress and strain tensors, respectively; and c_{ij} $(i,j=1,2,\ldots,6)$ are elastic constants. Using u_1, u_2 and u_3 to represent the

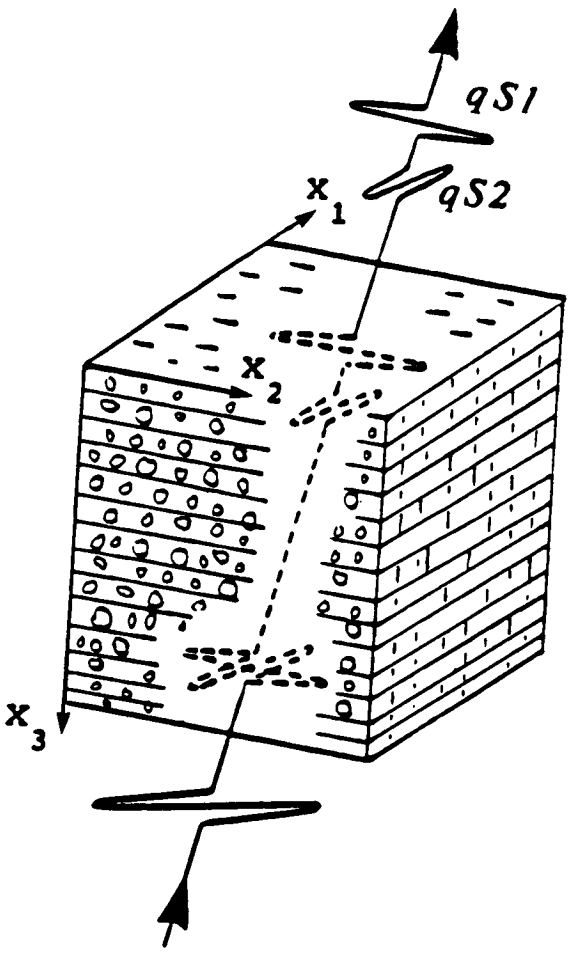

Figure B.1. A schematic illustration showing shear-wave propagation in an anisotropic medium with orthorhombic symmetry formed from a combination of PTL and EDA anisotropy, with the coordinate system used in the study.

displacements along the corresponding axes gives:

$$\varepsilon_{ij} = \partial u_i/\partial x_j + \partial u_j/\partial x_i, \text{ if } i \neq j; \text{ and}$$
$$\varepsilon_{ij} = \partial u_i/\partial x_j; \qquad \text{if } i=j. \tag{B-2}$$

B.2 ELASTIC CONSTANTS

Take x_1, x_2 and x_3 as the local natural coordinate system of Medium 1, and x'_1, x'_2 and x'_3 as the local natural coordinate system of Medium 2. In Medium 1, one has (Crampin 1981):

$$c_{44} = \rho_1 V^2_{11};$$
$$c_{55} = \rho_1 V^2_{21};$$
$$\sigma_{32} = c_{44}\varepsilon_{32}; \text{ and}$$
$$\sigma_{31} = c_{55}\varepsilon_{31}. \tag{B-3}$$

Similarly, in Medium 2, one has:

$$c'_{44} = \rho_2 V^2_{12};$$
$$c'_{55} = \rho_2 V^2_{22};$$
$$\sigma'_{32} = c'_{44}\varepsilon'_{32}; \text{ and}$$
$$\sigma'_{31} = c'_{55}\varepsilon'_{31}; \tag{B-4}$$

where the primed variables are parameters of Medium 2 in its local natural coordinate system.

B.3 BOUNDARY CONDITIONS

I take the local coordinate system of Medium 1 as the global coordinate system, and plane $x_3=0$ as the interface. The boundary conditions can be written as:

$$
\begin{aligned}
&u_2|^1_{x3=0} = u_2|^2_{x3=0};\\
&u_3|^1_{x3=0} = u_3|^2_{x3=0};\\
&\sigma_{31}|^1_{x3=0} = \sigma_{31}|^2_{x3=0}; \text{ and}\\
&\sigma_{12}|^1_{x3=0} = \sigma_{12}|^2_{x3=0};
\end{aligned}
\tag{B-5}
$$

where $|^1$ denotes parameters referring to Medium 1, and $|^2$ denotes parameters referring to Medium 2, and all measurements are under the global coordinate system.

B.4 COORDINATE TRANSFORM

As the global coordinate system is that of Medium 1, one needs to apply a coordinate transform to the parameters of Medium 2. The transform is a horizontal rotation from system (x'_1, x'_2) to (x_1, x_2), as shown Figure B.2, where $\Delta\alpha$ is the crack strike difference between Medium 1 and 2. $\Delta\alpha$ is positive if it is measured anticlockwise from the x_2 direction (crack strike of Medium 1), and negative if measured clockwise. Thus, it has:

$$
\begin{aligned}
&x_3 = x'_3;\\
&u_1 = u'_1\cos\Delta\alpha + u'_2\sin\Delta\alpha;\\
&u_2 = u'_2\cos\Delta\alpha - u'_1\sin\Delta\alpha;\\
&\sigma_{31} = \sigma'_{31}\cos\Delta\alpha + \sigma'_{32}\sin\Delta\alpha; \text{ and}\\
&\sigma_{32} = \sigma'_{32}\cos\Delta\alpha - \sigma'_{31}\sin\Delta\alpha;
\end{aligned}
\tag{B-6}
$$

where the un-primed variables are measurements in the global coordinate system (x_1, x_2, x_3), and the primed variables are measurements in the local natural coordinate system (x'_1, x'_2, x'_3).

B.5 qS1 AT NORMAL INCIDENCE

In this case, the displacements in Medium 1 under the global coordinate

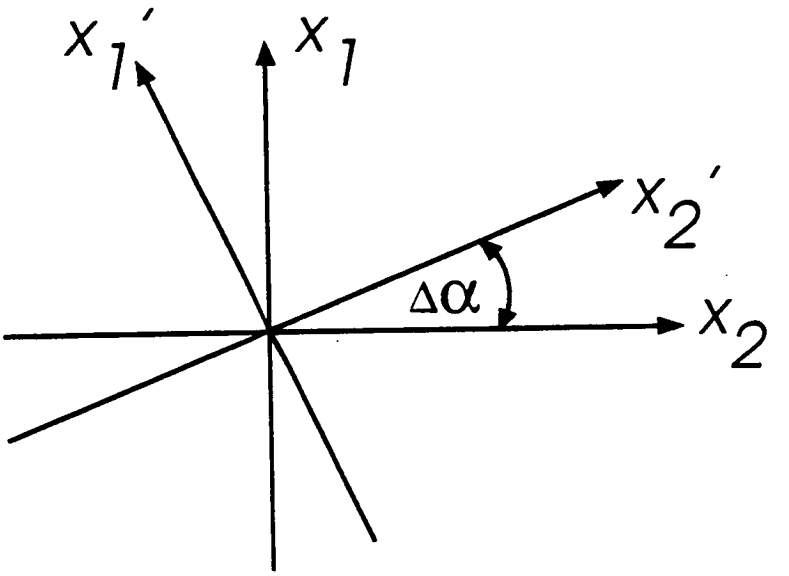

Figure B.2. Coordinate transform from a local natural coordinate system (x'_1, x'_2) to the global coordinate system (x_1, x_2) for a horizontal rotation of $\Delta\alpha$.

system can be written as:

$$u_1 = A_2 \exp[i\omega(t + x_3/V_{21})];$$
$$u_2 = A_0 \exp[i\omega(t - x_3/V_{11})] + A_1 \exp[i\omega(t + x_3/V_{11})]; \text{ and}$$
$$u_3 = 0; \qquad \text{(B-7)}$$

where ω is the angular frequency; and i is the square root of -1. Substituting (B-7) into equations (B-2) and (B-3) gives the stresses σ_{31} and σ_{32} in Medium 1 under the global coordinate system as:

$$\sigma_{31} = \rho_1 V_{21} A_2 (i\omega) \exp[i\omega(t + x_3/V_{21})]; \text{ and}$$
$$\sigma_{32} = \rho_1 V_{11} (i\omega)\{-A_0 \exp[i\omega(t - x_3/V_{11})] + A_1 \exp[i\omega(t + x_3/V_{11})]\}. \qquad \text{(B-8)}$$

Similarly, the displacements u'_1, u'_2 and u'_3 in Medium 2 under its local natural coordinate system can be written as:

$$u'_1 = A_4 \exp[i\omega(t - x'_3/V_{22})];$$
$$u'_2 = A_3 \exp[i\omega(t - x'_3/V_{12})]; \text{ and} \qquad \text{(B-9)}$$
$$u'_3 = 0.$$

Substituting (B-9) into equations (B-2) and (B-4) gives the stresses σ'_{31} and σ'_{32} in Medium 2 under its local natural coordinate system as:

$$\sigma'_{31} = \rho_2 V_{22} A_4 (-i\omega) \exp[i\omega(t - x'_3/V_{22})]; \text{ and}$$
$$\sigma'_{32} = \rho_2 V_{12} A_3 (-i\omega) \exp[i\omega(t - x'_3/V_{12})]. \qquad \text{(B-10)}$$

Substituting (B-9) and (B-10) into equation (B-6), the displacements u_1 and u_2 and stresses σ_{31} and σ_{32} in Medium 2 under the global coordinate system can be written as:

$$u_1 = A_4 \exp[i\omega(t - x_3/V_{22})] \cos\Delta\alpha +$$
$$+ A_3 \exp[i\omega(t - x_3/V_{12})] \sin\Delta\alpha; \text{ and}$$

$$u_2 = A_3\exp[i\omega(t-x_3/V_{12})]\cos\Delta\alpha - \\ - A_4\exp[i\omega(t-x_3/V_{22})]\sin\Delta\alpha; \qquad \text{(B-11)}$$

$$\sigma_{31} = \rho_2 V_{22} A_4(-i\omega)\exp[i\omega(t-x_3/V_{22})]\cos\Delta\alpha + \\ + \rho_2 V_{12} A_3(-i\omega)\exp[i\omega(t-x_3/V_{12})]\sin\Delta\alpha, \text{ and}$$

$$\sigma_{32} = \rho_2 V_{12} A_3(-i\omega)\exp[i\omega(t-x_3/V_{12})]\cos\Delta\alpha - \\ - \rho_2 V_{22} A_4(-i\omega)\exp[i\omega(t-x_3/V_{22})]\sin\Delta\alpha. \qquad \text{(B-12)}$$

Substituting equations (B-7), (B-8), (B-11) and (B-12) into equation (B-5), noting that $x_3=0$ at the interface, and making some suitable manipulations, gives:

$$A_2 = A_4\cos\Delta\alpha + A_3\sin\Delta\alpha;$$
$$A_0 + A_1 = A_3\cos\Delta\alpha - A_4\sin\Delta\alpha;$$
$$\rho_1 V_{21} A_2 = -\rho_2 V_{22} A_4\cos\Delta\alpha - \rho_2 V_{12} A_3\sin\Delta\alpha; \text{ and}$$
$$\rho_1 V_{11}(A_1 - A_0) = \rho_2 V_{22} A_4\sin\Delta\alpha - \rho_2 V_{12} A_3\cos\Delta\alpha. \qquad \text{(B-13)}$$

Dividing equation (B-13) by A_0, then noting equation (3-2), gives:

$$r_{12} = t_{12}\cos\Delta\alpha + t_{11}\sin\Delta\alpha;$$
$$1 + r_{11} = t_{11}\cos\Delta\alpha - t_{12}\sin\Delta\alpha;$$
$$\rho_1 V_{21} r_{12} = -\rho_2 V_{22} t_{12}\cos\Delta\alpha - \rho_2 V_{12} t_{11}\sin\Delta\alpha; \text{ and}$$
$$\rho_1 V_{11}(r_{11} - 1) = \rho_2 V_{22} t_{12}\sin\Delta\alpha - \rho_2 V_{12} t_{11}\cos\Delta\alpha. \qquad \text{(B-14)}$$

Thus, expressions for r_{11}, r_{12}, t_{11}, and t_{12} can be obtained from equation (B-14) as shown in equations (3-3), (3-4), (3-5), and (3-6).

B.6 qS2 AT NORMAL INCIDENCE

In this case, again the displacements u and stresses σ_{31} and σ_{32} in Medium 1 can be written as:

$$u_1 = A_0 \exp[i\omega(t - x_3/V_{21})] + A_2 \exp[i\omega(t + x_3/V_{21})];$$
$$u_2 = A_1 \exp[i\omega(t + x_3/V_{11})]; \text{ and}$$
$$u_3 = 0; \qquad \text{(B-15)}$$

$$\sigma_{31} = \rho_1 V_{21}(i\omega)\{-A_0\exp[i\omega(t - x_3/V_{21})] + A_2\exp[i\omega(t + x_3/V_{21})]\}; \text{ and}$$
$$\sigma_{32} = \rho_1 V_{11} A_1 (i\omega)\exp[iw(t + x_3/V_{11})]. \qquad \text{(B-16)}$$

Note that the displacements and the stresses in Medium 2 for this case are the same as in the previous case. Substituting (B-11), (B-12), (B-15) and (B-16) into equation (B-5) and letting $x_3=0$ gives:

$$A_0 + A_2 = A_4\cos\Delta\alpha + A_3\sin\Delta\alpha;$$
$$A_1 = A_3\cos\Delta\alpha - A_4\sin\Delta\alpha;$$
$$\rho_1 V_{21}(A_2 - A_0) = -\rho_2 V_{22} A_4\cos\Delta\alpha - \rho_2 V_{12} A_3\sin\Delta\alpha; \text{ and}$$
$$\rho_1 V_{11} A_1 = \rho_2 V_{22} A_4\sin\Delta\alpha - \rho_2 V_{12} A_3\cos\Delta\alpha. \qquad \text{(B-17)}$$

Dividing (B-17) by A_0 and using equation (3-8) gives:

$$1 + r_{22} = t_{22}\cos\Delta\alpha + t_{21}\sin\Delta\alpha;$$
$$r_{21} = t_{21}\cos\Delta\alpha - t_{22}\sin\Delta\alpha;$$
$$\rho_1 V_{21}(r_{22} - 1) = -\rho_2 V_{22} t_{22}\cos\Delta\alpha - \rho_2 V_{12} t_{21}\sin\Delta\alpha; \text{ and}$$
$$\rho_1 V_{11} r_{21} = \rho_2 V_{22} t_{22}\sin\Delta\alpha - \rho_2 V_{12} t_{21}\cos\Delta\alpha. \qquad \text{(B-18)}$$

Thus, expressions for r_{22}, r_{21}, t_{22} and t_{21} can be obtained from equation (B-18), following equations (3-9), (3-10), (3-11), and (3-12).

APPENDIX C
DERIVATIONS OF EQUATIONS (6-2), (6-4) AND (6-6)

C.1 DERIVATION OF EQUATION (6-2)

As shown in Figure C.1a, a source vector **F** with signature $F(t)$ is decomposed into two subsources **F1** and **F2** with signatures $F1(t)$ and $F2(t)$, respectively. Given $F(t)$ and angles γ_1 and γ_2, $F1(t)$ and $F2(t)$ can be uniquely determined. In the upper triangle of Figure C.1a, according to the sine rule of the triangle geometry, and noting $\gamma = 180° - (\gamma_1 + \gamma_2)$, one has:

$$F(t)/\sin[180° - (\gamma_1 + \gamma_2)] = F1(t)/\sin\gamma_2; \text{ or}$$
$$F(t)/\sin(\gamma_1 + \gamma_2) = F1(t)/\sin\gamma_2. \qquad \text{(C-1)}$$

Similarly, in the lower triangle of Figure C.1a, one has:

$$F(t)/\sin(\gamma_1 + \gamma_2) = F2(t)/\sin\gamma_1. \qquad \text{(C-2)}$$

Solving (C-1) and (C-2) gives:

$$F1(t) = F(t)\sin\gamma_2/\sin(\gamma_1 + \gamma_2); \text{ and}$$
$$F2(t) = F(t)\sin\gamma_1/\sin(\gamma_1 + \gamma_2). \qquad \text{(C-3)}$$

If source **F** is decomposed as shown Figure 6.1a, in terms of angles α' and β', angles γ_1 and γ_2 in Figure C.1a can be expressed as:

$$\gamma_1 = 90° - \alpha';$$
$$\gamma_2 = \beta' - 90°; \text{ and}$$

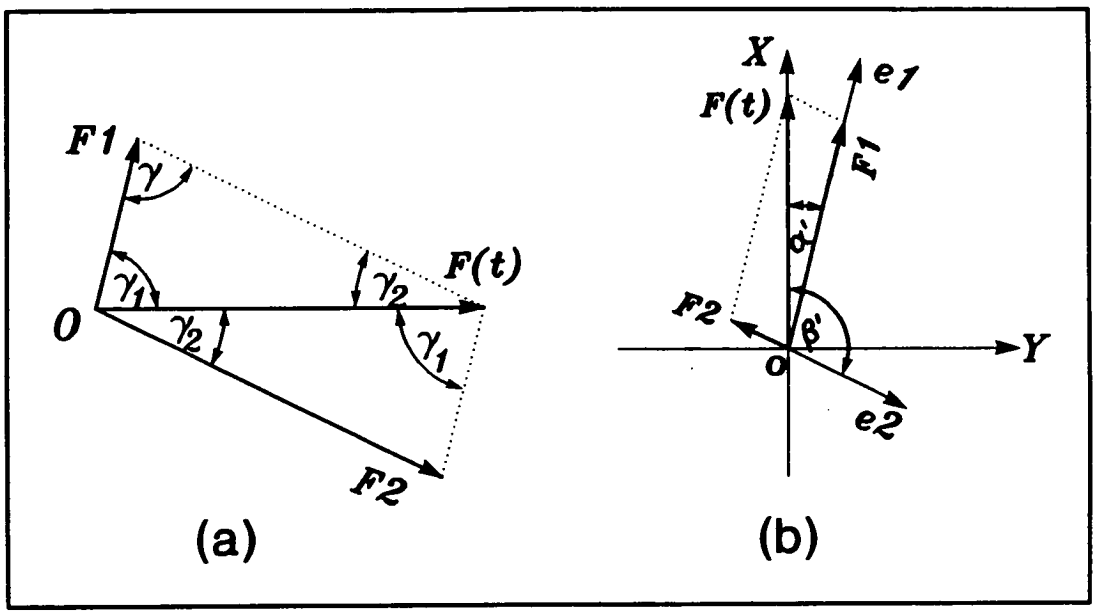

Figure C.1. Geometrical decomposition: (a) decomposition of a source vector F; (b) decomposition of inline *X*-source.

$$\gamma_1+\gamma_2 = \beta'-\alpha'. \qquad \text{(C-4)}$$

Substituting (C-4) into (C-3) and making some suitable manipulations give equation (6-2).

C.2 DERIVATION OF EQUATION (6-4)

Before equation (6-4) can be derived, I first introduce expressions for *qS1(t)* and *qS2(t)*, then discuss the decomposition of inline *X*-source.

C.2.1 Expressions of qS1(t) and qS2(t)

By definition, *qS1(t)* and *qS2(t)* are the amplitudes of the faster and slower split shear-waves, respectively, at a geophone position when source **F** is polarized along **e1** and **e2** directions, respectively. Thus following Thomsen (1988), *qS1(t)* and *qS2(t)* can be written as:

$$qS1(t) = p1(t)*F(t); \text{ and}$$
$$qS2(t) = p2(t)*F(t); \qquad \text{(C-5)}$$

where *p1(t)* and *p2(t)* are the medium response of faster and slower split shear-waves, respectively, which embodies geometric spreading, attenuation, reflectivity, etc. Equation (C-5) is also referred to as the deconvolution model of a seismic trace (Yilmaz, 1987).

C.2.2 Inline source decomposition

If source **F** is polarized along inline *X* direction, **F** can be decomposed as shown Figure C.1b. Similar to the derivation of equation (6-2), the two subsources in Figure C.1b can be written as:

$$F1(t) = F(t)\sin\beta'/\sin(\beta'-\alpha'); \text{ and}$$

$$F2(t) = - F(t)\sin\alpha'/\sin(\beta'-\alpha'); \qquad \text{(C-6)}$$

respectively, where the minus sign in $F2(t)$ represents the fact that **F2** in Figure C.1b is polarized along the opposite direction of **e2**.

C.2.3 Equation (6-4)

If one decomposes the *X*-source as shown Figure C.1b, according to the principle of superposition, the amplitudes of the faster and slower split shear-waves excited by *X*-source are equivalent to the amplitudes of faster and slower split shear-waves excited by subsources **F1** and **F2**. Note that in a homogeneous medium as shown Figure 6.1, a source polarized along **e1** direction will only excite faster split shear-waves, and a source polarization along **e2** direction will only excite slower split shear-waves (Crampin, 1981; Thomsen 1988). Thus the amplitudes of the faster and slower split shear-waves excited by subsources **F1** and **F2** can be written as:

$$p1(t)*F1(t) = [p1(t)*F(t)]\sin\beta'/\sin(\beta'-\alpha'); \text{ and}$$
$$p2(t)*F2(t) = - [p2(t)*F(t)]\sin\alpha'/\sin(\beta'-\alpha'); \qquad \text{(C-7)}$$

respectively. Substituting equation (C-5) into (C-7) gives equation (6-4).

C.3 DERIVATION OF EQUATION (6-6)

Equation (6-6) can be derived similarly. Figure 6.1a shows the decomposition of the *Y*-source with signature $F(t)$, and equation (6-2) shows the two subsources. Thus, the amplitudes of the faster and slower split shear-wave excited by *Y*-source can be written as

$$p1(t)*F1(t) = - [p1(t)*F(t)]\cos\beta'/\sin(\beta'-\alpha'), \text{ and}$$
$$p2(t)*F2(t) = [p2(t)*F(t)]\cos\alpha'/\sin(\beta'-\alpha'), \qquad \text{(C-8)}$$

respectively. Substituting equation (C-5) into (C-8) gives equation (6-6).

APPENDIX D
ANALYSIS OF LINEAR MOTION

A shear-wave is said to be linearly polarized if the trajectory of the particle motion is a straight line. Such linear motion has simple mathematical properties which make it easy to measure polarization attributes from a linear motion.

Figure D.1 shows a linear motion in the horizontal plane. The arrow marks the initial direction of the particle motion; $A(t)$ is the displacement at time t; $x(t)$ and $y(t)$ are the projections of $A(t)$ on to the two horizontal axes; and α is the angle that the initial motion makes with the x-axis. I define $A(t)$ as positive when particle displacement on the side of the origin towards direction α, and negative when particle displacement is on the other side of the origin; α is defined over the range $-\pi$ to π, positive when it is measured clockwise from the x-direction, and negative when it is measured anti-clockwise. It gives:

$$x(t) = A(t)\cos\alpha; \text{ and}$$
$$y(t) = A(t)\sin\alpha; \text{ or} \qquad \text{(D-1)}$$
$$\tan\alpha = y(t)/x(t); \qquad \text{(D-2)}$$

where it is assumed that α is time invariant. Note that $A(t)$ can be positive, or negative. This is different from the conventional usage where $A(t)$ is usually positive and α is a function of time. Also note that if α is a function of time and $A(t)$ is constant, equation (D-1) will represent a circular motion.

Under the above definitions, the purpose of analysis of a linear motion is

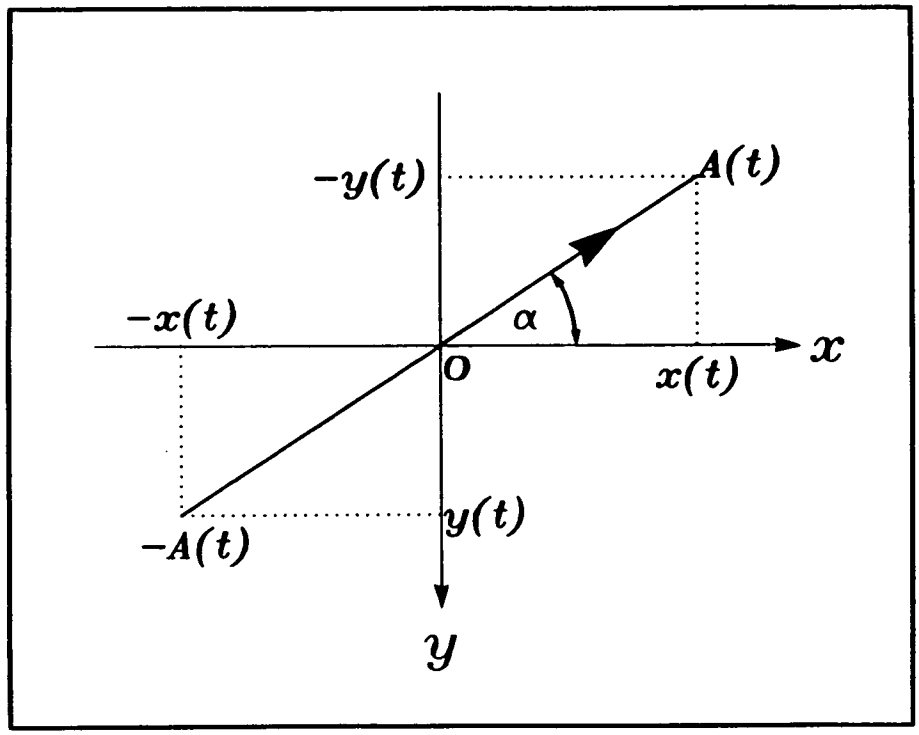

Figure D.1. Geometry of a linear motion.

to determine angle α and time series $A(t)$, given time series $x(t)$ and $y(t)$. Before approaching this problem, I first discuss some mathematical properties of a linear motion.

D.1 MATHEMATICAL PROPERTIES

Some useful properties can be immediately derived from equation (D-1) and Figure D.1. [Note that if a shear-wave motion has a displacement $A(t)$, it will be referred as "motion $A(t)$".]

D.1.1 Zero crossing

If motion $A(t)$ is a linear motion, $x(t)$, $y(t)$, and $A(t)$ have zero crossings at the same time.

D.1.2 Sign functions and polarities

If motion $A(t)$ is a linear motion, sign functions s_x, s_y, s_A:

$$\begin{aligned} s_x &= x(t)/|x(t)|, \text{ if } x(t) \neq 0.0; \\ s_y &= y(t)/|y(t)|, \text{ if } y(t) \neq 0.0; \quad \text{and} \\ s_A &= A(t)/|A(t)|, \text{ if } A(t) \neq 0.0; \end{aligned} \tag{D-3}$$

have the following relations:

$$\begin{aligned} s_A &= s_x, \quad \text{if} \quad \pi/2 > \alpha > -\pi/2; \\ &= -s_x, \quad \text{if} \quad -\pi/2 > \alpha \geq -\pi, \text{ or, } \pi \geq \alpha > \pi/2; \text{ and} \end{aligned} \tag{D-4}$$

$$\begin{aligned} s_A &= s_y, \quad \text{if} \quad \pi > \alpha > 0; \\ &= -s_y, \quad \text{if} \quad 0 > \alpha > -\pi. \end{aligned} \tag{D-5}$$

In other words, time series $A(t)$ either has the same, or reverse polarity as $x(t)$, or $y(t)$. If one allows a polarity difference, s_A can be uniquely determined

from $x(t)$, or $y(t)$ without knowing angle α. Note that equations (D-4) and (D-5) are valid for all time samples of a linear motion.

D.1.3 Eigenvalues and eigenvectors

Form covariance matrix **C**

$$\mathbf{C} = \begin{bmatrix} Var[x] & Cov[x,y] \\ Cov[x,y] & Var[y] \end{bmatrix}; \tag{D-6}$$

where $Var[x]$ and $Var[y]$ are respectively the variances of $x(t)$ and $y(t)$, and $Cov[x,y]$ is the covariances of $x(t)$ and $y(t)$ over a specified time window. Suppose that $x(t)$ and $y(t)$ have N samples over a specified time window. Thus $Var[x]$, $Var[y]$ and $Cov[x,y]$ can be written as [see equation 19.3-2 in Kanasewich (1981)]:

$$Var[x] = (1/N) \sum_i (x_i-\mu_x)^2;$$

$$Var[y] = (1/N) \sum_i (y_i-\mu_y)^2; \text{ and}$$

$$Cov[x,y] = (1/N) \sum_i (x_i-\mu_x)(y_i-\mu_y); \tag{D-7}$$

where

$$\mu_x = (1/N) \sum_i x_i; \textit{ and}$$

$$\mu_y = (1/N) \sum_i y_i; \tag{D-8}$$

and are, respectively, the mean values of time series $x(t)$ and $y(t)$ over the specified time window.

If motion $A(t)$ is a linear motion, the smaller eigenvalue of matrix **C** is zero (Kanasewich, 1981). Let λ be the non-zero, or the larger eigenvalue of **C**, and $\mathbf{N} = (x_0, y_0)^T$ be the corresponding normalized eigenvector, where superscript T represents transpose. It then gives:

$$\tan\alpha = y_0/x_0. \tag{D-9}$$

D.2 ESTIMATING ANGLE α

For VSP data, processing shear-wave splitting often involves the direct shear-arrival. From equation (D-2), a quick estimation of polarization angle α can be made as the average angle over the time window of direct arrival, or the angle corresponding to the maximum value of $A(t)$ over the specific time window. But a more accurate and robust estimation of angle α is given by equation (D-9) by estimating eigenvalues and eigenvectors of the covariance matrix **C**. Because only a second order matrix is involved, the computing is still very fast.

For reflection data, processing shear-wave splitting often involves different shear-wave arrivals (events). Because it is often difficult to define time windows of all shear-arrivals accurately, a different approach is suggested here. First, angle α is calculated sample-by-sample (instantaneously) using equation (D-2) over the entire trace, then the instantaneous values are displayed in colour as Figure 6.7c. From colour sections, one not only can estimate angle

α, but also can identify shear-wave events as demonstrated by Figure 6.7c. Thus with an interactive interpretation tool (such as, interactive workstations), a good initial estimation of angle α can be made, and time windows of all shear-wave arrivals can also be defined, then more detailed estimations can be achieved using equation (D-9).

D.3 DETERMINING TIME SERIES A(t)

It is possible to find out a time invariant α by applying equations (D-6) and (D-9) over a whole trace, or a specific time window, then to determine $A(t)$ from:

$$A(t) = x(t)\cos\alpha + y(t)\sin\alpha. \qquad \text{(D-10)}$$

But one can use the mathematic properties of a linear motion to simplify the determination of $A(t)$ by allowing a polarity difference. Clearly the absolute values of $A(t)$ can be estimated as the square root of $(x^2 + y^2)$ from equation (D-1), and the only problem is to estimate the polarity of $A(t)$, or the sign function $s_A(t)$. From equations (D-4) and (D-5), there are only two solutions of $s_A(t)$ with a polarity difference. If one ignores the polarity difference, say, choosing a positive solution from (D-4), one has:

$$\begin{aligned} A(t) &= s_x\,[x^2(t)+y^2(t)]^{\frac{1}{2}} && \text{if } x \neq 0.0; \text{ and} \\ &= 0.0, && \text{if } x = 0.0. \end{aligned} \qquad \text{(D-11)}$$

[Note that, if one wishes, the polarity can be determined from angle α by applying equation (D-6) and (D-9) over a whole trace.]

In this way $A(t)$ can be determined sample by sample without knowing α. This involves only simple arithmetic, which can be easily implemented for processing trace-ordered seismic data. Note that the results of (D-11) may have a polarity difference to the exact solution. But if the polarities of all traces of $x(t)$ and $y(t)$ are consistent, the polarity differences are also consistent, or systematic for all traces. Thus, this polarity difference will not cause severe problems in further processing of time series $A(t)$. The real significance relies on that measurement of polarizations, such as angle α can often be allowed a 180° difference.

In most cases one can obtain satisfactory results using equation (D-11), as shown in Figure 6.5b, 6.6b and 6.7b, which are all determined in this way. Because of the speed and directness, this approach is particularly useful for determining the principal time series of pre-stack data for processing multi-component reflection data in the presence of anisotropy, as demonstrated by Figure 6.7b.

REFERENCES

Aki, K., and Richards, P.G., 1980. *Quantitative Seismology, theory and method*, **1**. W. H. Freeman and Com., San Francisco.

Alford, R.M., 1986a. Multisource multireceiver method and system for geophysical exploration. *European patent application no. 0 169 075*

Alford, R.M., 1986b. Shear data in the presence of azimuthal anisotropy: Dilley, Texas. *56th Annual International Meeting & Exposition, Society of Exploration Geophysics, 2-6 November, 1986, Houston, Expanded Abstracts*, 476-479.

Ames III, G.L., 1990. Oil and gas developments in south Texas in 1989. *The American Association of Petroleum Geologists Bulletin* **74**, no. 10B, 144-148.

Auld, B.A., 1973. *Acoustic fields and waves in solids*. New York, John Wiley and Sons, Inc.

Backus, G.E., 1962. Long-wave elastic anisotropy produced by horizontal layering. *Journal of Geophysical Research* **67**, 4427-4440.

Backus, G.E., 1965. Possible forms of seismic anisotropy of the uppermost mantle under oceans. *Journal of Geophysical Research* **70**, 3429-3439.

Berge, P.A., 1991. Estimating *SV*-wave stacking velocities for transversely isotropic solids. *Geophysics* **56**, 1596-1602.

Berryman, J.G., 1979. Long-wave elastic anisotropy in transversely isotropic media. *Geophysics* **44**, 846-917.

Booth, D.C. and Crampin, S., 1985. Shear-wave polarizations on a curved wavefront at an isotropic free-surface. *Geophysical Journal of the Royal Astronomical Society* **83**, 31-45.

Booth, D.C., Crampin, S., Evans, R. and Roberts, G., 1985. Shear-wave polarizations near the North Anatolian Fault —— I. Evidence for anisotropy-induced shear-wave splitting. *Geophysical Journal of the Royal Astronomical Society* **83**, 61-73.

Brodov, L., Kuznetsov, V., Tikhonov, A., Cliet, C., Marin, D. and Michon, D., 1990. Measurements of azimuthal anisotropy parameters for reservoir study. *Fourth International Workshop on Seismic Anisotropy, 2-6 July, 1990, Edinburgh, Abstracts.*

Buchbinder, G.G.R., 1985. Shear-wave splitting and anisotropy in Charlevoix seismic zone, Quebec. *Geophysical Research Letters* **12**, 425-428.

Bush, I. and Crampin, S., 1987. Observations of EDA and PTL anisotropy in shear-wave VSPs. *57th Annual International Meeting & Exposition, Society of Exploration Geophysics, 11-15 October, 1987, New Orleans, Expanded abstracts*, 646-649.

Bush, I. and Crampin, S., 1991. Paris Basin VSPs: case history establishing combinations of fine-layer (and matrix) anisotropy and crack anisotropy from modelling shear wavefields near point singularities. *Geophysical Journal International* **107**, 433-447.

Byun, B.S., Corrigan, D. and Gaiser, J.E., 1989. Anisotropic velocity

analysis for lithology discrimination. *Geophysics* **54**, 1564-1574.

Campden, D.A., 1990. *Modelling and analyzing VSPs for shear-wave anisotropy*. Ph.D. Dissertation, University of Edinburgh.

Champion, O.R., 1936. The stratigraphy and structure of the Pearsall Field, Frio County, Texas. *American Association of Petroleum Geologists Bulletin* **20**, no. 11, 1514.

Cholet, J. and Richard, H., 1954. A test on elastic anisotropy measurement at Berraine. *Geophysical Prospecting* **2**, 232-246.

Cliet, Ch., Brodov, L., Tikhonov, A., Marin, D. and Michon, D., 1991. Anisotropy survey for reservoir definition. *Geophysical Journal International* **107**, 417-427.

Corbett, K., Friedman, M. and Spang, J., 1987. Fracture development and mechanical stratigraphy of Austin Chalk, Texas. *The American Association of Petroleum Geologists Bulletin* **71**, 17-28.

Crampin, S., 1966. Higher modes of seismic surface waves: propagation in Eurasia. *Bulletin of the seismological Society of America* **56**, 1227-1239.

Crampin, S., 1970. The dispersion of surface waves in multilayered anisotropic media. *Geophysical Journal of the Royal Astronomical Society* **21**, 387-402.

Crampin, S., 1977. A review of the effects of anisotropic layering on the propagation of seismic waves. *Geophysical Journal of the Royal Astronomical Society* **49**, 9-27.

Crampin, S., 1978. Seismic wave propagation through a cracked solid:

polarization as a possible dilatancy diagnostic. *Geophysical Journal of the Royal Astronomical Society* **53**, 467-496.

Crampin, S., 1981. A review of wave motion in anisotropic and cracked elastic media. *Wave Motion* **3**, 343-391.

Crampin, S., 1982. Comments on 'Possible forms of anisotropy of the uppermost mantle under oceans' by George E. Backus. *Journal of Geophysical Research* **87**, No. B6, 4636-4640.

Crampin, S., 1984a. An introduction to wave propagation in anisotropic media. *Geophysical Journal of the Royal Astronomical Society* **76**, 17-28.

Crampin, S., 1984b. Effective elastic-constants for wave propagation through cracked solids. *Geophysical Journal of the Royal Astronomical Society* **76**, 135-145.

Crampin, S., 1985a. Evidence for aligned cracks in the Earth crust. *First Break* **3**, No. 3, 12-15.

Crampin, S., 1985b. Evaluation of anisotropy by shear-wave splitting. *Geophysics* **50**, 142-152.

Crampin, S., 1987. Geological and industrial implications of extensive-dilatancy anisotropy. *Nature* **328**, 491-496.

Crampin, S., 1989. Suggestions for a consistent terminology for seismic anisotropy. *Geophysical Prospecting* **38**, 621-631.

Crampin, S., 1990. Alignment of near-surface inclusions and appropriate crack geometries for hot-dry-rock experiments. *Geophysical Prospecting* **38**, 621-631.

Crampin, S., 1991. Effects of singularities on shear-wave propagation in sedimentary basins. *Geophysical Journal International* **107**, 531-543.

Crampin, S., Booth, D.C., Evans, R., Peacock, S. and Fletcher, J.B., 1990. Changes in shear-wave splitting at Anza near the time of the North Palm Springs Earthquake. *Journal of Geophysical Research* **95**, 11197-11212.

Crampin, S., Bush, I., Naville, C. and Taylor, D.B., 1986. Estimating the internal structure of reservoirs with shear-wave VSPs. *The Leading Edge* **5**, No. 11, 35-39.

Crampin, S. and Booth, D.C., 1985. Shear wave polarizations near the North Anatolian Fault: II, interpretation in terms of crack-induced anisotropy. *Geophysical Journal of the Royal Astronomical Society* **83**, 75-92.

Crampin, S., Evans, R. and Üçer, S.B., 1985. Analysis of records of local earthquakes: the Turkish Dilatancy Projects (TDP1 and TDP2). *Geophysical Journal of the Royal Astronomical Society* **83**, 1-16.

Crampin, S., Evans, R., Üçer, S.B., Doyle, M., Davis, J.P., Yegorkina, G.V. and Miller, A., 1980. Observations of dilatancy-induced polarization anomalies and earthquake prediction. *Nature* **286**, 874-877.

Crampin, S. and Kirkwood, S.C., 1981. Velocity variations in systems of anisotropic symmetry. *Journal of Geophysics* **49**, 35-42.

Crampin, S. and Lovell. J.H., 1991. A decade of shear-wave splitting in the Earth's crust: what does it mean? what use can we make of it? and what should we do next? *Geophysical Journal International* **107**, 387-407.

Crampin, S. and Radovich, B., 1982. Interpretation of synthetic

common-depth-point gathers for a single anisotropic layer. *Geophysics* **47**, 323-335.

Daley, P.F. and Hron, F., 1979. Reflection and transmission coefficients for seismic waves in ellipsoidally anisotropic media. *Geophysics* **44**, 27-38.

Davis, T. and Lewis, C., 1990. Reservoir characterization by 3-D, 3-C seismic imaging, Silo Field, Wyoming. *The Leading Edge* **9**, No. 11, 22-25.

Douma, J., Den Rooijen H. and Schoking, F., 1989. Anisotropy detected in shallow clays using shear-wave splitting in a VSP survey. *51st Meeting and Technical Exhibition, European Association of Exploration Geophysicists, 29 May - 2 June, 1989, Berlin, Germany, Technical Program and Abstracts,* 141-142.

Dravis, J.J., 1979. *Sedimentology and diagenesis of the upper Cretaceous Austin Chalk formation, south Texas and northen Mexico.* Ph.D. Dissertation, Rice University, Houston.

Ensley, R.A., 1984. Comparison of *P*- and *S*-wave seismic data: A new method for detecting gas reservoirs. *Geophysics* **49**, 1420-1431.

Evans, R., 1984. Effects of the free surface on shear-waves. *Geophysical Journal of the Royal Astronomical Society* **76**, 165-172.

Guich, M.L., 1989. *Four-component rotation of 3-D shear wave data, Silo Field, Wyoming.* M.Sc. thesis, Colorado School of Mines.

Helbig, K., 1983. Elliptical anisotropy - its significance and meaning. *Geophysics* **48**, 825-832.

Horton, C.W., 1943. Secondary arrivals in a well & velocity survey. *Geophysics* **8**, 290-296.

Huang, D.J., 1989. The extraction of main characteristic parameters of seismic wave. *China Oil Geophysical Prospecting* **24**, 155-165.

Hudson, J.A., 1981. Wave speed and attenuation of elastic waves in a material containing cracks. *Geophysical Journal of the Royal Astronomical Society* **64**, 133-150

Hudson, J.A., 1982. Overall properties of a crack solid. *Mathematical Proceedings of the Cambridge Philosophical Society* **88**, 371-384.

Igel, H. and Crampin, S., 1990. Extracting shear wave polarizations from different source orientations: synthetic modelling. *Journal of Geophysical Research* **95**, 11283-11292.

Jolly, R.N., 1956. Investigation of shear waves. *Geophysics* **21**, 905-938.

Kanasewich, E.R., 1981. *Time sequence analysis in geophysics*. The University of Alberta Press.

Keith, C.M. and Crampin, S., 1977. Seismic body waves in anisotropic media. *Geophysical Journal of the Royal Astronomical Society* **49**, 181-243.

Kerner, C., Dyer, B. and Worthington, M., 1989. Wave propagation in a vertical transversely isotropic medium: field experiment and model study. *Geophysical Journal of the Royal Astronomical Society* **97**, 295-309.

Kramer, D., 1991. *Multicomponent vertical seismic profiles for reservoir characterization, South Casper Creek Field, Natrona County, Wyoming*. Ph.D. Thesis, Colorado School of Mines.

Kramer, D., Davis, T.L., 1991. Multicomponent vertical seismic profiles for reservoir characterization, South Casper Creek Field, Natrona County, Wyoming. *61st Annual International Meeting & Exposition, Society of Exploration Geophysics, 10-14 November, 1991, Houston, Expanded Abstracts* **1**, 383-386.

Krey, T. and Helbig, K., 1956. A theorem concerning anisotropy of stratified media and its significance for reflection seismics. *Geophysical Prospecting* **4**, 294-302.

Kuich, N., 1989. Seismic fracture identification and horizontal drilling: keys to optimizing productivity in a fractured reservoir, Giddings Field, Texas. *Transactions-Gulf Coast Association of Geological Societies* **39**, 153-158.

Layden, R.L., 1976. Big Well Field, Dimmit and Zavala Counties, Texas. *North American oil and gas fields*, Braunstein J. Eds, *The American Association of Petroleum Geologists Memoir* **24**, 145-156.

Lefeuvre, F., Winterstein, D., Meadows, M. and Nicoletis, L., 1991. Propagator matrix and layer stripping methods: A comparison of shear-wave birefringence detection on two data sets from Railroad Gap and Lost Hills Fields. *61st Annual International Meeting & Exposition, Society of Exploration Geophysics, 10-14 November, 1991, Houston, Expanded Abstract* **1**, 55-60.

Levin, F.K., 1978. The reflection, refraction, and diffraction of waves in media with an elliptical velocity dependence. *Geophysics* **43**, 528-537.

Levin, F.K., 1979. Seismic velocities in transversely isotropic media. *Geophysics* **44**, 918-936.

Lewis, C., 1989. *Three-dimensional multicomponent imaging of reservoir*

heterogeneity, Silo Field, Wyoming. Ph.D. Dissertation, Colorado School of Mines.

Lewis, C., Davis, T.L. and Vuillermoz, C., 1991. Three-dimensional multicomponent imaging of reservoir heterogeneity, Silo Field, Wyoming. *Geophysics* **56**, 2048-2056.

Li, X.-Y. and Crampin, S., 1989. Analyzing shear-wave splitting in three-component reflection survey. *Research Workshop on Recording and Processing Vector Wave Field Data, Society of Exploration Geophysics, 13-17 August, 1989, Snowbird, Utah, Technical Abstracts*, 114.

Li, X.-Y. and Crampin, S., 1990a. The dynamic and kinematic features of seismic shear-waves in the horizontally stratified anisotropic Earth. *The 14th United Kingdom Geophysical Assembly, Joint Association of Geophysics, 18-20 April, 1990, Plymouth, Abstracts, Geophysical Journal International* **101**, 292.

Li, X.-Y. and Crampin, S., 1990b. Complex analysis of shear-wave splitting. *52nd Meeting and Technical Exhibition, European Association of Exploration Geophysicists, 28 May - 1 June, 1990, Copenhagen, Denmark, Technical Program and Abstracts*, 95-96.

Li, X.-Y. and Crampin, S., 1990c. Dynamic and kinematic features of shear-waves in a horizontally stratified anisotropic Earth. *Fourth International Workshop on Seismic Anisotropy, 2-6 July, 1990, Edinburgh, Abstracts.*

Li, X.-Y. and Crampin, S., 1990d. Case studies of complex component analysis of shear-wave splitting. *60th Annual International Meeting & Exposition, Society of Exploration Geophysics, 23-27 September, 1990, San Francisco, Expanded Abstracts* **2**, 1427-1430.

Li , X.-Y. and Crampin, S., 1991a. Implementing pre-stack rotation for four-component shear-wave reflection data. *53rd Meeting and Technical Exhibition, European Association of Exploration Geophysicists, 26-30 May, 1991, Florence, Italy, Technical Program and Abstracts*, 554-555.

Li , X.-Y. and Crampin, S., 1991b. Linear-transform technique for analyzing shear-wave splitting in four-component seismic data. *61st Annual International Meeting & Exposition, Society of Exploration Geophysics, 10-14 November, 1991, Houston, Expanded Abstract* **1**, 51-54.

Li , X.-Y. and Crampin, S., 1991c. Complex component analysis of shear-wave splitting: theory. *Geophysical Journal International* **107**, 597-604.

Li , X.-Y. and Crampin, S., 1991d. Complex component analysis of shear-wave splitting: case studies, *Geophysical Journal International* **107**, 605-613.

Li , X.-Y. and Crampin, S., 1992a. Linear-transform techniques for processing shear-wave anisotropy in four-component seismic data. *Geophysics*, in press.

Li , X.-Y. and Crampin, S., 1992b. Approximations to shear-wave velocity and moveout in anisotropic media. *Geophysical Prospecting*, submitted.

Li , X.-Y. and Crampin, S., 1992c. Variation of reflection and transmission coefficients with crack strike and crack density in anisotropic media. *Geophysical Prospecting*, submitted.

Li , X.-Y., Crampin, S. and M.C. Mueller, 1992. Correlation of anisotropy with oil production: shear-wave splitting in reflection profiles in South Texas. *Geophysical Prospecting*, awaiting submission.

Liu, E., Crampin, S. and Roth, B., 1989. Detection of anisotropy by in-seam seismic channel waves. *51st Meeting and Technical Exhibition, European Association of Exploration Geophysicists, 29 May - 2 June 1989, Berlin, Germany, Technical Program and Abstracts*, 171.

Liu, E. and Crampin, S., 1990. Effects of the internal shear wave window: comparison with anisotropy induced splitting. *Journal of Geophysical Research* **95**, 11275-11281.

Liu, E., Crampin, S. and Yardley, G.S., 1990. Polarizations of reflected shear-waves. *Geophysical Research Letters* **17**, 1137-1140.

Lou, M. and Crampin, S., 1991a. Dispersion of guided waves in thin anisotropic waveguides. *Geophysical Journal International* **107**, 545-555.

Lou, M. and Crampin, S., 1991b. Seismic guided waves propagation in cracked thin-layer sedimentary reservoirs and its potential application in EOR monitoring by crosshole survey. *61st Annual International Meeting & Exposition, Society of Exploration Geophysics, 10-14 November, 1991, Houston, Expanded Abstracts* **2**, 846-849.

Lou, M. and Crampin, S., 1992. Modelling guided-waves in crosshole surveys in cracked and uncracked rock. *Geophysical Prospecting*, submitted.

Love, A.E.H., 1903. *A treatise on the mathematical theory of elasticity.* 1st edn. New York, Dover Publ. Inc.

Lynn, H.B. and Thomsen, L.A., 1986. Reflection shear-wave data along the principal axes of azimuthal anisotropy. *56th Annual International Meeting & Exposition, Society of Exploration Geophysics, 2-6 November, 1986, Houston, Expanded Abstracts*, 473-476.

Lynn, H.B. and Thomsen, L.A., 1990. Reflection shear-wave data collected near the principal axes of azimuthal anisotropy. *Geophysics* **55**, 147-156.

MacBeth, C. and Crampin, S., 1990. Comparison of signal processing techniques for estimating the effects of anisotropy in VSP data. *Geophysical Prospecting* **39**, 357-386.

MacBeth, C. and Crampin, S., 1991a. Examination of a spectral method for measuring the effects of anisotropy. *Geophysical Prospecting* **39**, 667-689.

MacBeth, C. and Crampin, S., 1991b. Automatic processing of seismic data in the presence of anisotropy. Geophysics **56**, 1320-1330.

MacBeth, C., Li, X.-Y., Crampin, S. and Mueller, M.C., 1992. Detecting lateral variability in crack parameters from surface data. In preparation.

MacBeth, C. and Yardley, G.S., 1991. Optimal estimation of crack strike. *Geophysical Prospecting*, submitted.

Martin, M.A. and Davis, T.L., 1987. Shear-wave birefringence: a new tool for evaluating fractured reservoirs. *The Leading Edge* **6**, No. 10, 22-25.

McCormack, M.D. and Tatham, R.H., 1991. *Shear-waves and anisotropy in exploration seismology*. SEG Special Publication.

Mueller, M.C., 1991. Prediction of lateral variability in fracture intensity using multicomponent shear wave surface seismic as a precursor to horizontal drilling. *Geophysical Journal International* **107**, 409-415.

Murtha, P.E., 1988. Estimation of the rotation transformation angle for shear-wave data acquired in azimuthally anisotropic regions. *Third International Workshop on Seismic Anisotropy, 31 May - 4 June, 1988,*

Berkeley, California, Abstract.

Murtha, P.E., 1989. Preliminary analysis of the ARCO multicomponent seismic group experiment. *Research Workshop on Recording and Processing Vector Wave Field Data, Society of Exploration Geophysics, 13-17 August, 1989, Snowbird, Utah, Abstracts.*

Musgrave, M.J.P., 1970. Crystal Acoustics. Holden-Day, San Francisco.

Naville, C., 1986. Detection of anisotropy using shear-wave splitting in VSP survey: requirements and application. *56th Annual International Meeting & Exposition, Society of Exploration Geophysics, 2-6 November, 1986, Houston, Expanded Abstracts,* 391-394.

Nicoletis, L., Client, C. and Lefeuvre, F., 1988. Shear-wave splitting measurements from multi-shot VSP data: *58th Annual International Meeting & Exposition, Society of Exploration Geophysics, 30 October - 3 November, 1988, Anaheim, Expanded Abstracts* **1**, 527-530.

Peacock, S., Crampin, S., Booth, D.C. and Fletcher, J.B., 1988. Shear-wave splitting in Anza seismic gap, Southern California: temporal variations as possible precursors. *Journal of Geophysical Research* **93**, 3339-3356.

Postma, G.W., 1955. Wave propagation in a stratified medium. *Geophysics* **20**, 780-806.

Raikes, S.A., 1991. Shear-wave characterization of the BP Devine Test Site, Texas. *61st Annual International Meeting & Exposition, Society of Exploration Geophysics, 10-14 November, 1991, Houston, Expanded Abstract* **1**, 65-68.

Reaser, D.F., and Collins, E.W., 1988. Style of faults and associated

fractures in Austin Chalk, northern extension of Balcones fault zone, Central Texas. *Transactions-Gulf Coast Association of Geological Societies* **38**, 267-276.

René, R.M., Fitte, J.L., Forsyth, P.M., Kim, K.Y., Murray, D.J., Walters, J.K. and Westerman, J.D., 1986. Multicomponent seismic studies using complex trace analysis. *Geophysics* **51**, 1235-1251.

Richards, T.C., 1960. Wide angle reflections and their application to finding limestone structures in the foothills of Western Canada. *Geophysics* **25**, 385-407.

Ricker, N. and Lynn, R.D., 1950. Composite reflections. *Geophysics* **15**, 30-49.

Schoenberg, M. and Douma, J., 1988. Elastic wave propagation in media with parallel fractures and aligned cracks. *Geophysical Prospecting* **36**, 571-590.

Scott, R.J., 1977. The Austin Chalk-Buda trend of south Texas. *Transactions-Gulf Coast Association of Geological Societies* **27**, 164-168.

Seewald, K.O., 1967. Stratigraphy of the Upper Cretaceous Austin Group, Central Texas. *Transactions-Gulf Coast Association of Geological Societies* **17**.

Sena, A.G., 1991. Seismic traveltime equations for azimuthally anisotropic and isotropic media: estimation of interval elastic properties. *Geophysics* **56**, 2090-2101.

Shearer, P.M. and Orcutt, J.A., 1985. Anisotropy in the oceanic lithosphere - theory and observation from the Ngendei seismic refraction experiment in

the south-west Pacific. *Geophysical Journal of the Royal Astronomical Society* **80**, 493-526.

Shih, X.R. and Meyer, R.P., 1990. Observation of shear-wave splitting from natural events: South Moat of Long Valley, Caldera, California, June 29 to August 12, 1982. *Journal of Geophysical Research* **95**, 11179-11195.

Snedden, J. W. and Kersey, D. G., 1982. Depositional environments and gas production trends Olmos sandstone, Upper Cretaceous, Webb County, Texas. *Transactions-Gulf Coast Association of Geological Societies* **32**, 497-518.

Spencer, T.W. and Chi, H.C., 1991. Thin-layer fracture density. *Geophysics* **56**, 833-843.

Squires, S.G., Kim, C.D.Y. and Kim, D.Y., 1989. Interpretation of total wave-field data over Lost Hills field, Kern County, California. *Geophysics* **54**, 1420-1429.

Stapp, W.L., 1977. The geology of the fractured Austin and Buda formations in the subsurface of south Texas. *Transactions-Gulf Coast Association of Geological Societies* **27**, 208-229.

Taner, M.T., Koehler, F. and Sheriff, R.E., 1979. Complex seismic trace analysis. *Geophysics* **44**, 1041-1063.

Taner, M.T. and Sheriff, R.E., 1977. Application of amplitude, frequency, and other attributes to stratigraphic and hydrocarbon determination. in *Seismic Stratigraphy - applications to hydrocarbon exploration*, ed. Payton, C.E., *A.A.P.G., Memoir* **26**, 301-327.

Tatham, R.H., 1982. V_p/V_s and lithology. *Geophysics* **47**, 336-344.

Thomsen, L.A., 1986. Weak elastic anisotropy. *Geophysics* **51**, 1954-1966.

Thomsen, L.A., 1988. Reflection seismology over azimuthally anisotropic media. *Geophysics* **53**, 304-313.

Thomsen, L.A., *et al.*, 1989. Comparison of anisotropic modelling codes: Anisotropic Modeling Collaboration. *Research Workshop on Recording and Processing Vector Wave Field Data, Society of Exploration Geophysics, 13-17 August, 1989, Snowbird, Utah, Technical Abstracts*, 4.

Uren, N.F., Gardner, G.H.F. and McDonald, J.A., 1990. Normal moveout in anisotropic media. *Geophysics* **55**, 1634-1636.

Weeks, A.W., 1945. Balcones, Luling, and Mexia fault zones in Texas. *The American Association of Petroleum Geologists Bulletin* **29**, 1733-1737.

White, J.E., Heaps, S.N. and Lawrence, A.L., 1956. Seismic waves from a horizontal force. *Geophysics* **21**, 715-723.

Wild, P., 1990. Report on anisotropic modelling collaboration: 1 - Model 1. *British Geological Survey, Technical Report* WL/90/4.

Wild, P. and Crampin, S., 1991. The range of effects of azimuthal isotropy and EDA-anisotropy in sedimentary basin. *Geophysical Journal International* **107**, 513-529.

Willis, H.A., Rethford, G.L. and Bielanski, E., 1986. Azimuthal anisotropy: Occurrence and effect on shear-wave data quality. *56th Annual International Meeting & Exposition, Society of Exploration Geophysics, 2-6 November, 1986, Houston, Expanded Abstracts*, 479-481.

Winterstein, D.F., 1986. Anisotropy effects in *P*-wave and *SH*-wave stacking velocities contain information on lithology. *Geophysics* **51**, 661-672.

Winterstein, D.F., 1990. Velocity anisotropy terminology for geophysicists. *Geophysics* **55**, 1070-1088.

Winterstein, D.F. and Hanten, J.B., 1985. Super critical reflections observed in *P*- and *S*-wave data. *Geophysics* **50**, 185-195.

Winterstein, D.F. and Meadows, M.A., 1990. Depth dependence of S-wave polarization azimuth near the San Andreas Fault. *4th International Workshop on Seismic Anisotropy, 2-6 July, 1990, Edinburgh, Abstract.*

Winterstein, D.F. and Meadows, M.A., 1991a. Shear-wave polarization and subsurface stress directions at Lost Hills field. *Geophysics* **56**, 1331-1348.

Winterstein, D.F. and Meadows, M.A., 1991b. Changes in shear-wave polarization azimuth with depth in Cymric and Railroad Gap Oil Fields. *Geophysics* **56**, 1349-1364.

Yardley, G., 1992. *Identification and characterization of fractured reservoirs using shear-wave anisotropy.* Ph.D. Dissertation, University of Edinburgh.

Yardley, G. and Crampin, S., 1990. Automatic determination of anisotropic parameters from shear-wave splitting in the Lost Hills VSP. *60th Annual International Meeting & Exposition, Society of Exploration Geophysics, 23-27 September, 1990, San Francisco, Expanded Abstracts* **2**, 1424-1426.

Yardley, G. and Crampin, S., 1991. Extensive-dilatancy anisotropy: relative information in VSPs and reflection surveys. *Geophysical Prospecting* **39**, 337-355.

Yardley, G.S., Graham, G. and Crampin, S., 1991. Viability of shear-wave amplitude versus offset studies in anisotropic media. *Geophysical Journal International* **107**, 493-503.

Yilmaz, Ö., 1987. *Seismic data processing*. SEG Publication, Tulsa.

Zeng, X. and MacBeth, C., 1992. Algebraic processing techniques for estimating shear-wave splitting in zero-offset VSP data: Theory. in preparation.

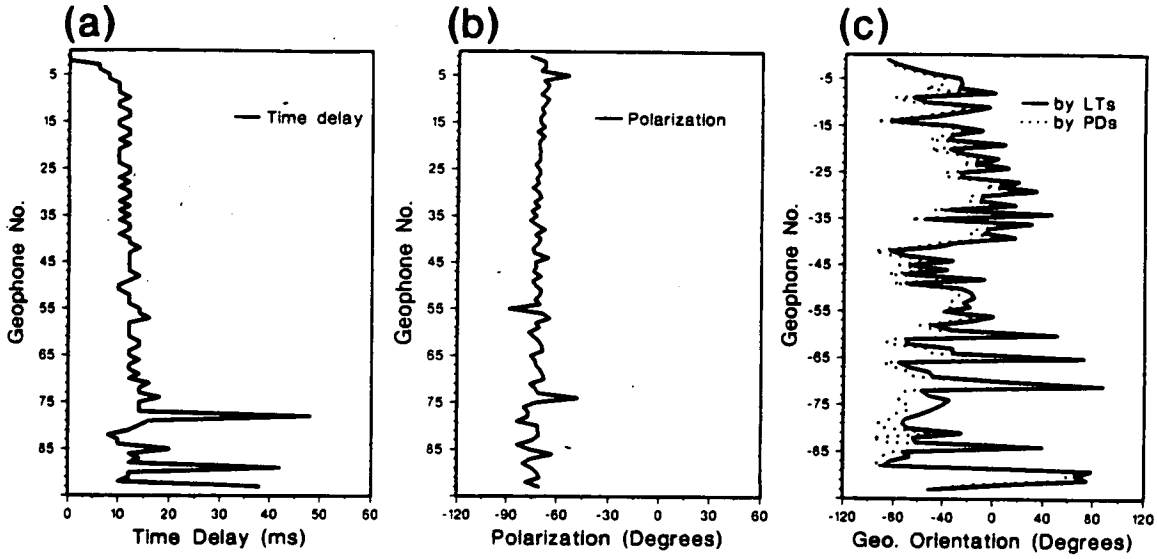

FIG. 3. Results of the zero-offset VSP in Figure 2. (a) measured time delays, (b) measured polarization direction of faster split shear waves; and (c) comparison of geophone orientations (x-direction) estimated by the linear transform technique (solid line) and by visual examination of polarization diagarms, PDs (dotted line), where both attributes are measured from the source X-direction.

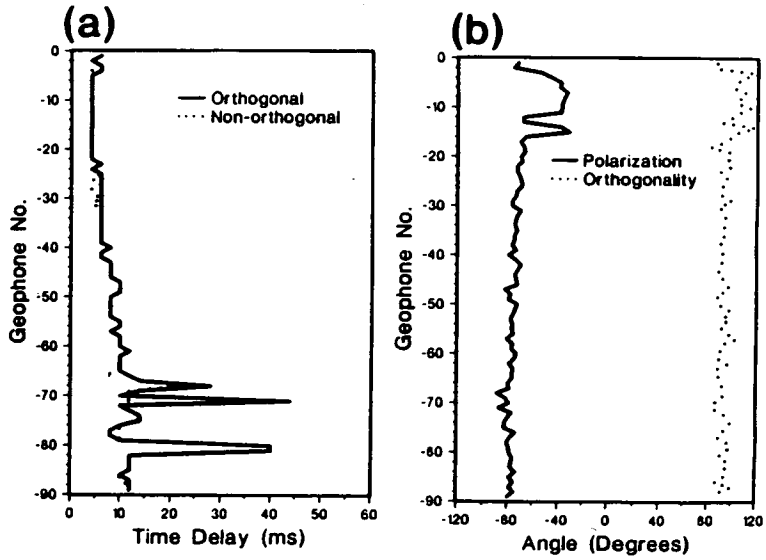

FIG. 4. Results of an offset VSP from BP. (a) comparison of time delay measured using the orthogonal algorithm (solid line); and using the non-orthogonal algorithm (dotted line); and (b) measured orthogonallity, angle between the two split shear-waves (dotted line), and polarization angles of the faster split shear-waves (solid line), where both attributes are measured from source X-direction.

Conclusions

Recorded shear-wave motion can be linearized in a variety of conditions by four linear transforms. This simplifies the processing of four-compoent shear-wave VSPs or reflection surveys in the presence of anistropy, and allows various attributes measured, regardless of the orthogonality of the split shear-waves. Comparing with conventional techniques, this linear transform technique is computing fast, flexible, and widely applicable.

Acknowledgements

We thank British Petroleum for making available the multi-component VSP data from its test site. We thank Gareth Yardley for providing the processed VSPs. This work was supported by the Sponsors of the Edinburgh Anisotropy Project, and the Natural Environment Research Council, and is published with the approval of the Director of the British Geological Survey (NERC).

References

Alford, R.M., 1986, Shear data in the presence of azimuthal anisotropy, Expanded Abstracts, 56th Int.SEG Meeting, Houston, 476-479.

Li, X.-Y., and Crampin, S., 1990., Case studies of complex component analysis of shear-wave splitting, Expanded Abstracts 60th Int.SEG Meeting, San Francisco, 2, 1427-1430.

Macbeth, C., and Crampin, S., 1991, Automatic processing of seismic data in the presence of anisotropy, Geophysics, in press.

Murtha, P.E., 1989, Preliminary analysis of the ARCO multicomponent seismic group experiment, Abstracts, SEG Research Workshop, Recording and Processing Vector Wave Field Data, Snowbird, 61-63.

Nicoletis, L., Client, C., and Lefeuvre, F., 1988, Shear-wave splitting measurements from multi-shot VSP data, Expanded Abstracts, 58th Int.SEG Meeting, Anaheim, 1, 527-530.

Squires, S.G., Kim, C.D., and Kim, D.Y., 1989, Interpretation of total wave-field data over Lost Hills field, Kern County, California, Geophysics, 54, 1420-1429.

Thomsen, L.A., 1988, Reflection seismology over azimuthally anisotropic media, Geophysics, 53, 304-313.

Winterstein, D.F., and Meadows, M.A., 1990, Changes in shear-wave polarization azimuth with depth in Cymric and Railroad gap Oil Fields, Expanded Abstracts, 60th SEG meeting, San Francisco, 2, 1435-1438.

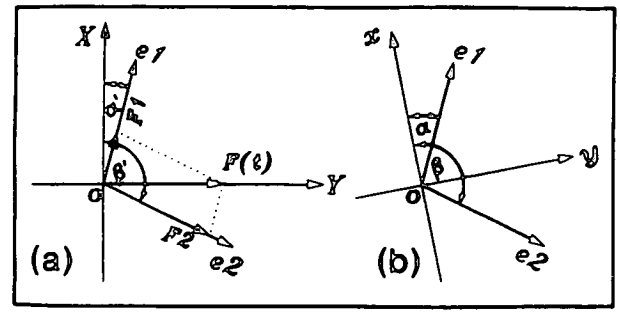

FIG. 1. Diagrams showing the acquisition geometry and coordinate system in the horizontal plane. (a) Source geometry, where X and Y are two orthogonal sources with signature $F(t)$, and **F1** and **F2** are two decompositions of the source vector **F**. (b) Geophone geometry, where x and y are two orthogonal geophones possibly in a different orientation from the source signals.

FIG. 2. Polarization diagrams (PDs) of a zero-offset VSP from BP, showing the linearity of the transformed motions: (a) in-line source (X-source), $s_{11}(t)$ and $s_{21}(t)$; (b) cross-line source (Y-source), $s_{12}(t)$ and $s_{22}(t)$; (c) transformed components, $\xi(t)=s_{11}(t)-s_{22}(t)$ and $\eta(t)=s_{12}(t)+s_{21}(t)$; and (d) transformed components $\zeta(t)=s_{11}(t)+s_{22}(t)$ and $\chi(t)=s_{12}(t)-s_{21}(t)$.

as in a zero-offset VSP. When the orientation of the downwell geophones is unknown, we can write $\beta = \pi/2 + \alpha$ and $\beta' = \pi/2 + \alpha'$, and the transformed components can be written as:

$$\xi(t) = [qS1(t) - qS2(t)] \cos(\alpha+\alpha');$$
$$\eta(t) = [qS1(t) - qS2(t)] \sin(\alpha+\alpha'); \quad (7)$$

$$\zeta(t) = [qS1(t) + qS2(t)] \cos(\alpha-\alpha'); \text{ and}$$
$$\chi(t) = -[qS1(t) + qS2(t)] \sin(\alpha-\alpha'). \quad (8)$$

Equations (7) and (8) show time series $V1(t) = qS1 + qS2$ and $V2(t) = qS1 - qS2$ are separated in the transformed components as linear motion, so we can easily estimate $V1$ and $V2$, and $\alpha+\alpha'$ and $\alpha-\alpha'$ from the transformed components. Hence, $qS1 = (V1 + V2)/2$ and $qS2 = (V1 - V2)/2$, and α and α' can be determined, and the orientation of the geophone can be estimated from $\alpha-\alpha'$.

NON-ORTHOGONAL SPLIT SHEAR-WAVES: In off-vertical incidence, the polarizations of the faster and slower split shear-wave in the horizontal plane may not be orthogonal. Such cases include offset-VSPs, and pre-stack data in reflection surveys. In all cases of non-orthogonallity, it is reasonable to assume that the orientation of geophone is same as the source, that is, $\alpha = \alpha'$, and $\beta = \beta'$, the results of the transformed components can be written as:

$$\xi(t) = [qS1(t) - qS2(t)] \sin(\alpha+\beta)/\sin(\beta-\alpha);$$
$$\eta(t) = -[qS1(t) - qS2(t)] \cos(\alpha+\beta)/\sin(\beta-\alpha); \quad (9)$$

$$\zeta(t) = qS1(t) + qS2(t); \text{ and}$$
$$\chi(t) = -[qS1(t) - qS2(t)] \cos(\beta-\alpha)/\sin(\beta-\alpha). \quad (10)$$

Again time series $V1 = qS1 + qS2$ and $V2 = qS1 - qS2$ are separated: $V1$ is directly given by component $\zeta(t)$, and $V2$ is a linear motion as in equation (9). Thus, the faster split shear-wave $qS1$ and polarization angle α, and the slower split shear-wave, $qS2$ and angle β can also be determined for non-orthogonal split shear-waves. Angle $\beta-\alpha$ is the angle between the faster and slower split shear-wave and is a measure of the orthogonallity of the split shear-waves.

Verification of the technique

To verify this technique, we demonstrate the linearity of the transformed time series in field VSPs. Figure 2 shows polarization diagrams (PDs, or hodograms) in the horizontal plane of a zero-offset VSP. PDs of the in-line (X-) source (the particle motion of s_{11} and s_{21}, 2a), and PDs of the cross-line (Y-) source (particle motion of s_{12} and s_{22}, 2b) are very elliptical and shear-wave splitting is difficult to identify. But almost all PDs of the transformed motions, $V2(t)$ (particle motion of $\xi = s_{11} - s_{22}$ and $\eta = s_{12} + s_{21}$, 2c) and PDs of $V1(t)$ (particle motion of $\zeta = s_{11} + s_{22}$ and $\chi = s_{12} - s_{21}$, 2d) are essentially linear as expected, despite the ellipticity of the original particle motion.

We also examined similar PDs in the horizontal plane of offset-VSPs, which showed similar features. In summary, although the particle motion of shear waves as recorded are frequently elliptical, the linear transforms of the sum and difference of the split shear-waves, $V1$ and $V2$, respectively, are linear. Consequently, the time series of the split shear-waves can be directly separated by recombining $V1$ and $V2$, regardless of the orthogonallity of split shear-waves.

Results

ZERO-OFFSET VSP: Results of a zero-offset VSP are presented. The results include principal time series of split shear-waves, polarizations and time delays of split shear-waves, and down well geophone orientations. Figure 3 shows some of the results: time delays, polarizations and geophone orientations. The results agree with analysis based on PDs by Yardley (private communication).

OFFSET VSP: Results of an offset VSP are presented, where the geophone orientation is determined from the polarizations of P-waves. Figure 4 shows some of the results: time delays, polarizations and orthogonalities. The time delays from assuming orthogonal polarizations (solid line, 4a) and non-orthogonal polarizations (dotted line, 4a) are almost identical, presumably because the polarizations are nearly orthogonal. The measured polarizations (solid line, Figure 4b) are similar to those of the zero offset VSP (Figure 3b). The orthogonallity (dotted line, Figure 4b) of the two split shear-waves are about the 90° line, as expected from the comparison of the delays in Figure 4a.

REFLECTION SURVEY: Results of the Lost Hills reflection data (Squires et al., 1989) will be presented. The results inculde separation into principal time series of the split shear-waves, measured from shot records, colour polarizations of split shear-waves, and final stacking section of principal time series. The colour polarization section can be used to identify laterall varation of anistropy and the stacking section is optimized.

Discussion

This technique recognizes the essential linearity of the shear-wave motion in the transformed coordinate system. These (four) linear transforms are deterministic and can be efficiently implemented. The technique allows unknown downwell geophone orientations to be used, where conventional rotation technique often fails (Figure 3). The technique also allows large offset data, where the split shear-waves may not be orthogonal in the horizontal plane (Figure 4). In reflection data, shear-wave polarization and amplitudes can be more easily measured from the transformed components. The technique can be extended to media where the effective polarizations changes with depth, and in this case, we can extrapolate the sources downwards into the lower layers, so that the medium between the extrapolated sources and the geophones is homogeous, as was demonstrated by Winterstein and Meadows (1990).

Linear-Transform Techniques for Analyzing Shear-Wave Splitting in Four-Component Seismic Data

BG2.5

Xiangyang Li and Stuart Crampin, Edinburgh Anisotropic Project, British Geological Survey, Scotland*

Summary

Most techniques for analyzing shear-wave splitting employ rotation procedures and tend to be computing intensive. Here, we present a fast linear-transform technique for analyzing shear-wave splitting in four-component seismic data (two source orientations recorded by two receivers). We transform the data by four linear transforms so that the shear-wave motion is linearized in a wide variety of conditions. Many properties of shear-waves can be easily estimated from the transformed components.

The technique allows various attributes to be measured, including the polarizations of faster split shear-wave, and the time delays between faster and slower split shear-waves, as well as allowing the time series of the faster and slower split shear-waves to be separated deterministically. In addition, with minimum assumptions, the geophone orientations can be estimated for zero-offset VSPs, and the polarizations of the slower split shear-waves can be estimated for offset VSPs. The time series of the split shear-waves can be separated before stack for reflection surveys. The technique has been successfully applied to a number of field VSPs and reflection data sets. Applications to a zero-offset VSP, an offset VSP, and a reflection dataset are presented to illustrate the technique.

Introduction

In a homogeous crack-induced anisotropic medium, caused, say, by a single set of parallel vertical cracks in an isotropic matrix rock, the recorded four-components can be expressed in terms of the properties of the uncracked matrix and the properties of the faster and slower split shear-waves. Thus, in principle, the properties of the matrix and the faster and slower split shear-waves can be determined from the recorded components.

Among the earliest studies of techniques for solving this inversion problem was the use of rotation analysis by Alford (1986) and Thomsen (1988). A number of similar rotation procedures have been developed by Nicoletis et al. (1988), Murtha (1989), Macbeth and Crampin (1991), and others. Most of these techniques employ rotation scanning procedures and tend to be computing intensive.

In an attempt to overcome some of these problems, we first developed complex component analysis (Li and Crampin, 1990) and now we prepose a new fast technique, which we call the linear-transform technique, for analyzing shear-wave splitting in four-component seismic data.

Basic definitions

Figure 1a shows the source geometry, and Figure 1b shows the surface projection of the geophone geometry, where **e1** and **e2** are two unit vectors representing the directions of faster and slower split shear-waves. The medium between the source and the first geophone, and between successive geophones, is assumed to be homogeous with a uniform distribution of cracks.

We define the principal time series $qS1(t)$ and $qS2(t)$ of the faster and slower split shear-waves, respectively, as the time series received at a geophone position when a source vector **F** is polarized along **e1** and **e2**, respectively, with signature $F(t)$. The concept of the principal time series was introduced by Alford (1986) and Thomsen (1988). Here, we give an alternative geometrical definition. We introduce two transformed time series $V1(t)$ and $V2(t)$ as the sum and difference, respectively, of the principal time series $qS1(t)$ and $qS2(t)$:

$$V1(t) = qS1(t) + qS2(t);$$
$$V2(t) = qS1(t) - qS2(t). \quad (1)$$

We define the four-component time series as $s_{ij}(t)$ recorded from X- and Y-sources (i = 1, 2) on x- and y-geophones (j = 1, 2). Following a similar approach to Alford (1986) and Thomsen (1988), The four components, $s_{ij}(t)$, can be written as:

$$s_{11}(t) = [qS1(t)\ \sin\beta'\cos\alpha - qS2(t)\ \sin\alpha'\cos\beta]/\sin(\beta'-\alpha');$$
$$s_{21}(t) = [qS1(t)\ \sin\beta'\sin\alpha - qS2(t)\ \sin\alpha'\sin\beta]/\sin(\beta'-\alpha');$$
$$s_{12}(t) = [-qS1(t)\ \cos\beta'\cos\alpha + qS2(t)\ \cos\alpha'\cos\beta]/\sin(\beta'-\alpha');$$
$$s_{22}(t) = [-qS1(t)\ \cos\beta'\sin\alpha + qS2(t)\ \cos\alpha'\sin\beta]/\sin(\beta'-\alpha'), \quad (2)$$

where α, β, α' and β' are the angles in Figure 1a and 1b. In cases where geophones and sources are orientated in the same direction ($\alpha=\alpha'$; $\beta=\beta'$) and the two shear-waves are orthogonal to each other ($\beta'-\alpha'=\pi/2$), these equations will reduced to Thomsen's equations (7), (8) and (9) (Thomsen, 1988).

Linear transform techniques

The four linear transforms are:

$$\xi(t) = s_{11}(t) - s_{22}(t); \quad (3)$$
$$\eta(t) = s_{21}(t) + s_{12}(t); \quad (4)$$
$$\zeta(t) = s_{11}(t) + s_{22}(t); \text{ and} \quad (5)$$
$$\chi(t) = s_{12}(t) - s_{21}(t). \quad (6)$$

[Linear transforms (3) and (4) were first used by Li and Crampin (1990) to calculate orientation logs in reflection surveys.] The results of the transformed components for orthogonal and non-orthogonal split shear-waves are discussed separately.

ORTHOGONAL SPLIT SHEAR-WAVES: The two split shear-waves in disributions of parallel vertical cracks can be assumed to be orthogonal to each other at vertical incidence,

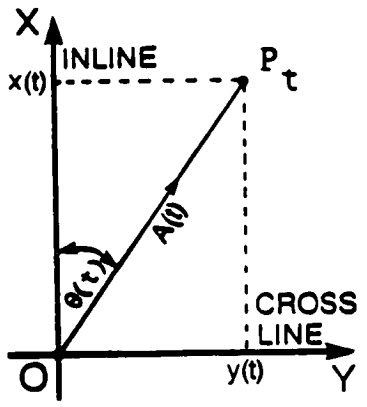

Figure 1. Coordinate system used for complex component analysis.

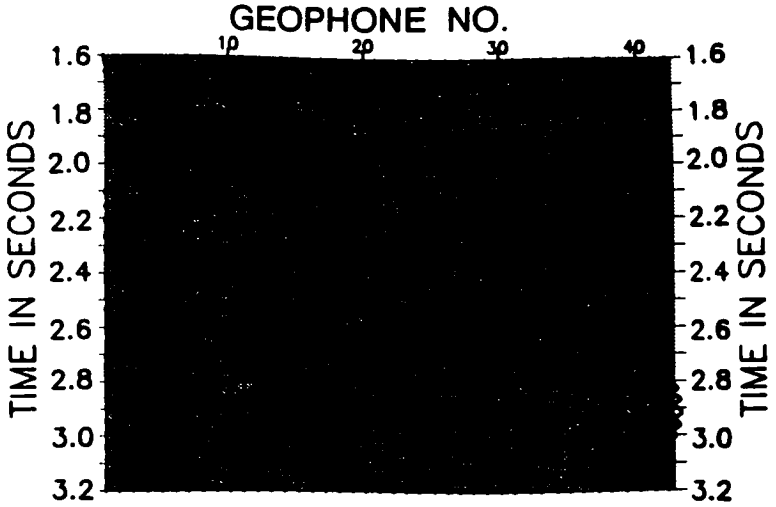

Figure 3. Colour display of Figure 2 (with grey shading for correspondence). Wiggle-traces of amplitude are superimposed on colour-coded phase signals.

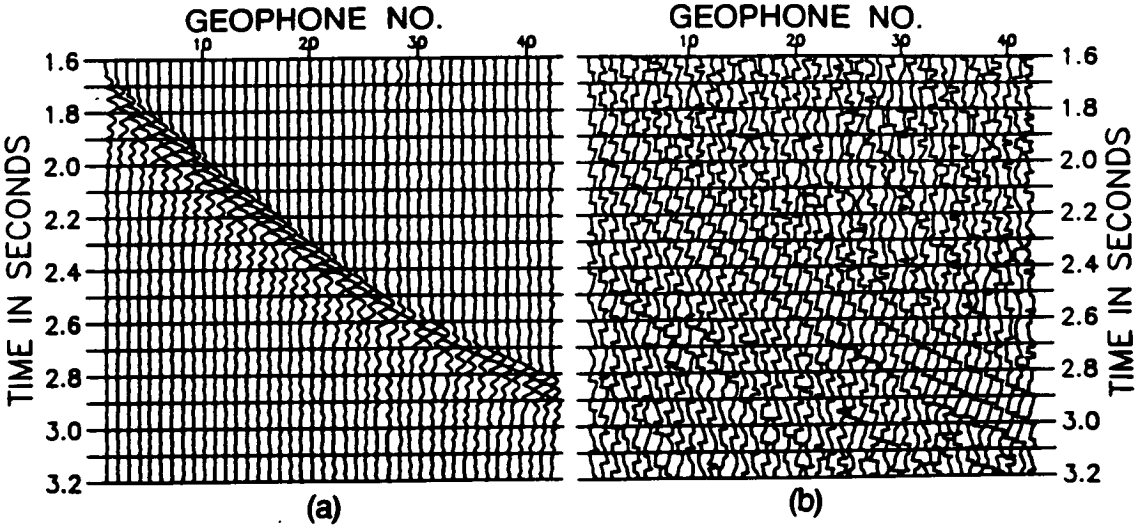

Figure 2. Complex component of *SH*-source from Lost Hills VSP: (a) instantaneous amplitude, and (b) instantaneous phase.

PARIS BASIN VSP - S_1 offset (Bush *et al* 1987): The quality of this data is not as good as the previous one, but shear-wave splitting can be recognized from two orthogonal elliptical motions on the polarization diagrams. On the colour section of complex component, two orthogonal effective polarization angles (the phase angle at the time when instantaneous amplitude has a local maximum) can be clearly identified from the changing of colour. This first effective angle is not the polarization angle of the leading shear-wave. The difficulty, in this case, is that the signals are elliptical and are difficult to evaluate except by fullwave synthetic modelling (Bush *et al.* 1987)

LOST HILLS REFLECTION SURVEY: Two colour sections of a CMP gather are presented. These displays can be used, not only to identify shear-wave splitting at near-offset traces, but also to examine the variation of angle of polarization along the hyperbola. The shear-wave window at the surface for each hyperbola can also be determined. This is important for stacking CMP gathers, because stacking traces, which do not show similar polarizations will distort the characteristics of the shear-wave splitting. Orientation logs are also presented.

DISCUSSION

The attributes calculated from the complex component are values associated with time at a point. Thus both variation of waveforms and variation of polarizations can be followed continuously either along time direction, or along offset direction (Figs. 2(a, b)). The use of colour improves the identification and quantification of such variations, and makes it possible to carry out stratigraphic and anisotropic interpretation on displays of complex attributes(Fig. 3). Orientation log offers another way to determine polarization angle of the leading shear-wave.

CONCLUSIONS

We conclude from our study that the treatment of the two horizontal components in multi-component shear-wave data as a complex component allows the calculation of instantaneous attributes of amplitude, phase, and frequency. Four-component data can be transformed to two-component data using linear transforms, which allows the calculation of orientation logs. This technique of complex component analysis can aid stratigraphic interpretation and identification and estimation of shear-wave splitting from seismic sections, and may aid hydrocarbon determination.

ACKNOWLEDGMENTS

This work was supported by the Edinburgh Anisotropy Project and the Natural Environment Research Council and is published with the approval of the Director of the British Geological Survey (NERC).

REFERENCES

Alford, R.M. 1986, Shear data in the presence of azimuthal anisotropy: Dilley, Texas. Expanded Abstracts, 56th SEG meeting, Houston, 476-479.

Bush, I. and Crampin, S. 1987, Observations of EDA and PTL anisotropy in shear-wave VSPs. Expanded abstracts, 57th SEG meeting, New Orleans, 646-649.

Crampin, S. 1981, A review of wave motion in anisotropic and cracked elastic-media. Wave Motion 3, 343-391.

Crampin, S. 1985a, Evidence for aligned cracks in the Earth crust. First Break 3, No. 3, 12-15.

Crampin, S. 1985b, Evaluation of anisotropy by shear-wave splitting. Geophysics 50, 142-152.

Crampin, S. 1987, Crack porosity and alignment from shear-wave VSPs. *in* Danbom, S., and Domenico, S.N., Eds., Shear-wave exploration: Geophysical Developments, 1, SEG Special publication, 227-251.

Crampin, S. and Atkinson, B.K. 1985, Microcracks in the Earth's crust. First Break 3, No. 3, 16-20.

Justice, M.G., McCormick, M.D. and Lee, S.S. 1987, Anistropy in the Morrow formation of Southeast New Mexico. *in* Danbom, S., and Domenico, S.N., Eds., Shear-wave exploration: Geophysical Developments, 1, SEG Special publication, 154-164.

Squires, S.G., Kim, C.D.Y. and Kim, D.Y. 1989, Interpretation of total wave-field data over Lost Hills field, Kern County, California. Geophysics, 54, 1420-1429.

Taner, M.T., Koehler, F. and Sheriff, R.E. 1979, Complex seismic trace analysis. Geophysics 44, 1041-1063.

Thomsen, L.A., 1988, Reflection seismology over azimuthally anisotropic media, Geophysics, 53, 304-313.

Willis, M.A., Rothford, G.L. and Bielanski, E. 1986, Azimuthal anisotropy: occurence and effect on shear-wave data quality. Expanded Abstracts, 56th SEG Meeting, Houston, 479-481.

Winterstein, D.F. 1986, Anisotropy effects in *P*-wave and *SH*-wave stacking velocities contain information on lithology. Geophysics, 51, 661-672.

Case Studies of Complex Component Analysis of Shear-Wave Splitting

SN3.2

Xiangyang Li and Stuart Crampin, British Geological Survey, Scotland*

SUMMARY

In multi-component reflection and VSP surveys, the two horizontal components can be taken as the real and imaginary parts of a complex component. This transforms multi-component data from conventional Cartesian coordinates to polar coordinates, and allows the calculation of instantaneous amplitude, instantaneous phase, and instantaneous frequency. We call this technique complex component analysis.

These instantaneous attributes convey information about both the variation of waveforms and the variation of polarizations. Thus complex component analysis can help to evaluate the effects of anisotropy in *in situ* rocks in terms of the polarization of fast split shear-wave and the delay between two split shear-waves. Furthermore, complex component analysis of shear-waves is a natural extension of complex trace analysis of *P*-wave data sets, when only the real part of the complex trace is recorded. By this extension, complex component analysis can aid stratigraphic interpretation.

After giving the basic definitions of a complex component, we present three examples of field data to demonstrate the use of the technique in stratigraphic interpretation and anisotropic interpretation. The results are colour-coded diagrams, which will be shown at the meeting but are not included in the abstract.

INTRODUCTION

Over the last decade, the use of multi-component seismic data to evaluate the effects of anisotropy has become comparatively common within the industry. Alford (1986), Winterstein (1986), Justice *et al.* (1987), and Thomsen (1988) evaluate anisotropy from seismic sections. Crampin (1981, 1985b, and 1987) and co-authors determine crack orientation and crack density in the *in situ* rockmass from analysis of polarization diagrams.

Seismic sections, displaying three components separately in time-versus-offset plots, accentuate the variation of waveforms, and analysis of such sections is the principal technique for stratigraphic interpretation. Polarization diagrams, displaying the data in the displacement plane over a time window, stress the variation of particle motion, and are principally used to analyze shear-wave splitting.

Transformation of seismic data from one form to another is common in seismic data processing. Complex component analysis transforms multi-component data from conventional Cartesian coordinates to polar coordinates in the horizontal plane (it can be easily extended to other planes). Such transform retains the local significance of both variation of waveforms and variation of particle motion by calculating the instantaneous amplitude, instantaneous phase, and instantaneous frequency. These quantities, referred to as seismic attributes (following Taner *et al.* 1979, although they have quite different physical meanings), can be presented in conventional seismic time-versus-offset displays coded by colour.

Thus complex component analysis can be used to evaluate the effects of anisotropy in terms of the polarization of leading shear-wave and the delay between the two split shear-waves. Furthermore, complex component analysis of shear-waves is an extension of complex trace analysis of *P*-waves and can assist in stratigraphic interpretation and possibly in hydrocarbon determination.

DEFINITIONS

We assume a multi-component shear-wave data set with the inline, $x(t)$, and crossline, $y(t)$, recording geometry shown in Fig. 1. The horizontal displacement of a shear-wave, Pt, has amplitude $A(t)$, and angle $\theta(t)$ to the inline direction, so that:

$$x(t) = A(t)\cos\theta(t); \text{ and} \quad (1)$$

$$y(t) = A(t)\sin\theta(t). \quad (2)$$

We take $x(t)$ and $y(t)$ as the real and imaginary parts of a complex signal:

$$z(t) = x(t) + i\,y(t); \quad (3)$$

and solve for A and θ for any x and y, giving:

$$A(t) = [x^2(t) + y^2(t)]^{\frac{1}{2}} = |z(t)|; \text{ and} \quad (4)$$

$$\theta(t) = \arctan[y(t)/x(t)], \text{ defined for } \pm 180°; \quad (5)$$

where $A(t)$ is the *instantaneous amplitude*; $\theta(t)$ is the *instantaneous phase*, following Taner *et al.* (1979).

The rate of change of the time-dependent phase gives a time-dependent frequency:

$$\phi(t) = d\theta(t)/dt; \quad (6)$$

where $\phi(t)$ is the *instantaneous frequency*.

PHYSICAL SIGNIFICANCE

INSTANTANEOUS AMPLITUDE: The instantaneous amplitude in equation (4) is a measure of the distance between the moving particle and its equilibrium position. Local maxima of instantaneous amplitude indicate the largest distance of the particle from its equilibrium position, and may help in identifying the onset

of the shear-wave signal and the interference of split shear-waves.

INSTANTANEOUS PHASE: The instantaneous phase in equation (5) is a measure of the deviation of the moving particle from the inline direction. The variation of the phase represents the variation of the polarization direction of the split shear-waves. The first arrival is polarized in a direction fixed by the path through the anisotropy, so that the instantaneous phase tends to remain constant until the arrival of the slower split shear-wave. The shape of the phase signal is a combination of rectangular and 'semi-triangular' shapes, which corresponds to the combination of linear and elliptical motion in polarization diagrams when shear-wave splitting occurs. Thus phase display can help to identify and quantify shear-wave splitting in both seismic reflection and VSP data sets.

INSTANTANEOUS FREQUENCY: The instantaneous frequency in equation (6) is a measure of the rate of change of instantaneous phase. If the instantaneous phase is constant, the instantaneous frequency will be zero. Thus at the time of the shear-wave splitting, the frequency display is expected to show a low frequency shadow. This, if observed, may be a good indicator for a cracked oil reservoir, or gas accumulation. Since most hydrocarbon reservoirs contain inclusions and show some form of shear-wave splitting (Willis et al., 1986), the frequency display may be of special significance for hydrocarbon determination.

SHEAR-WAVE SPLITTING

Shear-wave splitting is almost universally observed in the Earth's crust (Crampin 1985a; Crampin and Atkinson 1985, etc.). To study this phenomenon, not only multi-component receivers but also multi-component sources have been used to generate four-component (Alford, 1986; and Thomsen, 1988) and nine-component data sets (Squires *et al.* 1989).

Equations (1) to (6) are defined for two-component shear-wave data. We use two techniques to apply complex component analysis to four-component data:

(1) Calculating the complex components of *SH*- and *SV*-sources separately. Features which diagnose shear-wave splitting or stratigraphic variation usually occur in some consistent, systematic way. Thus the two data sets are expected to give similar features, which will enhance interpretation.

(2) Calculating the transformed complex component of *SH*- and *SV*-sources. Following Thomsen (1988), the four components can be written as:

$$s_{11}(t) = s_1(t_1)\cos^2\theta + s_2(t_2)\sin^2\theta; \quad (7)$$

$$s_{22}(t) = s_1(t_1)\sin^2\theta + s_2(t_2)\cos^2\theta; \text{ and} \quad (8)$$

$$s_{12}(t) = s_{21}(t) = [s_1(t_1) + s_2(t_2)]\sin\theta\cos\theta; \quad (9)$$

where $s_1(t_1)$ and $s_2(t_2)$ are, respectively the fast and slower split shear-wave signals, and θ is the crack strike measured from the inline direction. Linear transforms of:

$$\xi(t) = s_{11}(t) - s_{22}(t); \text{ and} \quad (12)$$

$$\eta(t) = s_{12}(t) + s_{21}(t); \quad (13)$$

can be used to transform four-component data to two-component data. Equations (7), (8) and (9) give:

$$\tan 2\theta = \eta(t)/\xi(t); \quad (14)$$

which implies the instantaneous phase of the two component data $\xi(t)$ and $\eta(t)$ is a measure of the crack (or fracture) strike in the media. Thus we call it an *orientation log*.

COLOUR DISPLAY

The use of colour in displaying seismic data is extremely effective in improving the perceptibility of subsurface features, as demonstrated by Taner *et al.* (1979). Colour codes used for complex component analysis need to be different from those used for complex trace analysis. The basic scheme for display in complex component analysis superimposes a wiggle-trace of amplitude on the colour-coded phase, where the colours repeat every 180°. Thus, phase values with a difference of 180° or -180° will be coded with the same colour, since the linear motion is independent of the orientation of the anisotropy.

EXAMPLES

LOST HILLS VSP: The Lost Hills VSP is a total wavefield nine-component data set of high quality (Squires *et al.* 1989). The initial linear-motion can be observed in polarization diagrams of the primary shear-waves at most geophone depths, and the shape of the phase is a combination of rectangular shapes and semi-triangular shapes (Fig. 2b). The colour-section of two horizontal components of *SV* and *SH* sources are both presented. The sections are colour-coded phases superimposed by wiggle-traces of amplitude (Fig. 3 with grey shading for correspondence). Corresponding to the onset of the shear-waves, there is a rectangle of constant colour from which the polarization of the leading shear-wave can be determined, and delay can be determined from the duration of this rectangle. The two source orientations show consistent results. The orientation logs will be also presented.

Geophys. J. Int. (1991) **107**, 597–604

Complex component analysis of shear-wave splitting: theory

Xiang-Yang Li[1,2] and Stuart Crampin[1]

[1] *Edinburgh Anisotropy Project, British Geological Survey, Murchison House, West Mains Road, Edinburgh* EH9 3LA, *UK*
[2] *Department of Geology and Geophysics, University of Edinburgh, James Clerk Maxwell Building, Edinburgh* EH9 3JZ, *UK*

Accepted 1991 June 12. Received 1991 June 11; in original form 1991 January 8

SUMMARY

The use of complex arithmetic is a natural way to treat vectorially polarized data, where the real and imaginary components can be taken as two perpendicular axes. This transforms multicomponent data from conventional Cartesian coordinates to polar coordinates, and allows the calculation of instantaneous amplitude and instantaneous polarization. We call this technique complex component analysis. Wave motion can be represented by instantaneous attributes which show distinct features characteristic of the type of wave motion. It is particularly informative to examine shear-wave splitting by instantaneous attributes. The instantaneous amplitude of shear-wave splitting has a number of local maxima, and the instantaneous polarization has a combination of rectangular and semitriangular shapes. Shear-wave splitting can be identified from displays of instantaneous amplitude and polarization, where the polarization of the faster split shear wave and the delay between the two split shear waves can be quantified from colour-coded displays. The instantaneous attributes can be displayed as wiggle-lines of amplitude superimposed on a colour-coded polarization, where the use of colour improves the indentification and quantification of shear-wave splitting.

Key words: complex components, instantaneous amplitude, instantaneous polarization, shear-wave splitting.

1 INTRODUCTION

Shear-wave splitting occurs along almost all ray paths in the uppermost 10 to 20 km of the Earth's crust (Crampin 1985a, 1987; Crampin & Atkinson 1985), including most sedimentary basins (Alford 1986; Willis, Rethford & Bielanski 1986). We present a technique (Li & Crampin 1990a, 1990b), which we shall call *complex component analysis*, to analyse shear-wave splitting in multicomponent reflection and VSP surveys.

René *et al.* (1986) extended complex trace analysis (Taner & Sheriff 1977; Taner, Koehler & Sheriff 1979) to multicomponent data. They defined the complex multicomponent trace with real orthogonal components and imaginary (quadrature) components derived by application of the Hilbert transform to the corresponding real components. They then defined several polarization attributes including phase difference, reciprocal ellipticity and tilt angle. They applied the technique to multicomponent walkaway seismic data to characterize ambient noise and source-generated waves.

Here, we directly define the two horizontal components of multicomponent reflection and VSP surveys as the real and imaginary parts of a complex component. This transforms multicomponent data from conventional Cartesian coordinates to polar coordinates, and allows the calculation of instantaneous amplitude and instantaneous polarization. These quantities, referred to as seismic attributes (following Taner *et al.* 1979), can be presented in conventional seismic time-versus-offset displays in which colour is used to quantify the polarizations of the shear waves.

Three major applications of such complex component analysis can be envisaged as follows.

(1) Anisotropic interpretation. Attributes can assist in the rapid recognition and identification of shear-wave splitting in seismic sections, and in extracting shear-wave polarizations and delays from seismic data for interpretation in terms of the crack- and stress-geometry throughout the reservoir.

(2) Stratigraphic interpretation. Seismic attributes provide further information about the location and analysis of faults, discontinuities, unconformities, and other geological features, as demonstrated by Taner *et al.* (1979).

(3) Hydrocarbon determination. Attributes can assist in recognizing and interpreting bright spots, with particular application to the relative brightness of differential shear-wave amplitude. Such bright spots are likely to be

associated with hydrocarbon accumulations in oriented cracks and fractures. Attributes can also help in interpreting fracture zones, and identifying lateral variation of fracture intensity, which may be related to preferential permeability.

This paper presents the theory of complex component analysis of shear-wave splitting. The paper suggests techniques for estimating the behaviour of shear waves, and demonstrates the significance of instantaneous attributes in identifying and evaluating shear-wave splitting.

2 SIGNIFICANCE OF THE COMPLEX COMPONENT

2.1 Definitions

We assume a multicomponent shear-wave data set with the horizontal in-line $x(t)$ and cross-line $y(t)$ recording geometry shown in Fig. 1. We may write the horizontal displacement of a shear wave (or any seismic wave), with vector displacement P_t, amplitude $A(t)$ and angle to the inline direction $\theta(t)$, as

$$x(t) = A(t) \cos \theta(t) \tag{1}$$

and

$$y(t) = A(t) \sin \theta(t). \tag{2}$$

Thus, $x(t)$ and $y(t)$ can be considered as the real and imaginary parts of a complex signal $z(t) = x(t) + iy(t)$, where i is the square root of -1. In this way, the method of complex trace analysis of single component data (Taner & Sheriff 1977; Taner *et al.* 1979) can be extended to multicomponent data without using the Hilbert transforms (René *et al.* 1986). Solving for A and θ for any x and y, we have

$$A(t) = [x^2(t) + y^2(t)]^{1/2} = |z(t)|, \tag{3}$$

$$\theta(t) = \arctan [y(t)/x(t)], \tag{4}$$

defined for $\pm 180°$; where $A(t)$ is the *instantaneous amplitude*; and $\theta(t)$ is the *instantaneous polarization.*

2.2 Physical significance

In addition to the attributes described above, the wavetrain also contains information about instantaneous frequency, apparent polarity, energy distribution, and waveform, which can also be extracted from complex components (Taner *et al.* 1979; Huang 1989). Each piece of information has a particular significance and application in exploration seismology, and in reservoir characterization and development. Here, we shall only discuss instantaneous amplitude and instantaneous polarization.

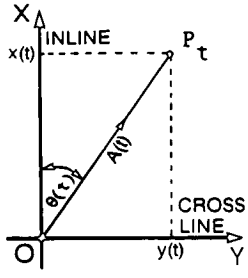

Figure 1. Diagram showing the coordinate system for complex component analysis. P_t is the horizontal displacement of a shear wave at time t with amplitude $A(t)$ and angle $\theta(t)$ to the inline direction, and $x(t)$ and $y(t)$ are the coordinates of the two horizontal components in a Cartesian coordinate system.

Instantaneous amplitude

The instantaneous amplitude in equation (3) is a measure of the distance between the moving particle and its equilibrium position. Instantaneous amplitude may have its maximum at points other than at peaks or troughs of the two individual horizontal components. Local maxima of instantaneous amplitude indicate the largest distance of the particle from its equilibrium position, and may help in identifying the onset of the shear-wave signal and the interference of split shear waves without rotating seismogram axes.

Instantaneous polarization

The instantaneous polarization in equation (4) is a measure of the polarization direction of the moving particle relative to the polarization direction of the source. Since the polarization is independent of amplitude, it may give clear particle motion directions even for weak arrivals as long as they are coherent signals. Thus, instantaneous polarization may be a good indicator of discontinuities, faults, pinchouts, and angularities, as demonstrated in similar circumstances by Taner *et al.* (1979).

The variation of the instantaneous polarization of recorded split shear waves represents the variation of the direction of the particle motion of the split shear waves. The first arrival of the split shear waves is polarized in a direction fixed by the ray path through the anisotropic rock (Crampin 1981), so that the instantaneous polarization tends to remain constant until the arrival of the slower split shear wave. Thus the polarization display, and associated amplitude display, can help to identify and quantify shear-wave splitting in both seismic reflection and VSP data sets.

2.3 Represention of wave motion

Figures 2(a) and (b) show the seismograms and instantaneous amplitude and polarization attributes of eight typical wave motions: linear, elliptical, and shear-wave splitting with six different time delays. Fig. 3 shows corresponding polarization diagrams (hodograms) of the particle motion. Since any shear-wave motion in the horizontal plane can be considered as either linearly, or elliptically polarized (or some combination thereof in shear-wave splitting), we first discuss these two characteristic types of wave motion.

Linear wave motion

WM1 in Figs 2 and 3 show typical linear motion, that can be written as

$$y(t) = x(t) \tan \alpha, \tag{5}$$

where $x(t)$ and $y(t)$ are the displacements in the x and y directions, respectively; α is the angle the polarization

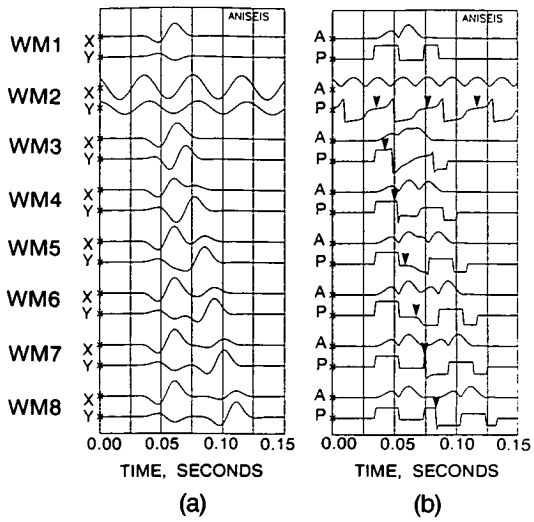

Figure 2. Seismograms and instantaneous attributes of eight typical wave motions. WM1 is linear motion, WM2 is elliptical, and WM3 to WM8 show shear-wave splitting with time delays increasing from 8 ms (WM3) to 48 ms (WM8) for a 40 Hz signal. (a) Horizontal component seismograms, X inline and Y crossline; (b) displays of instantaneous amplitude (A) and polarization (P). Arrows on WM2 mark the position of the effective polarization angle, and arrows on WM3 to WM8 mark the points where the polarization changes direction at the onset of the second split shear-wave arrival.

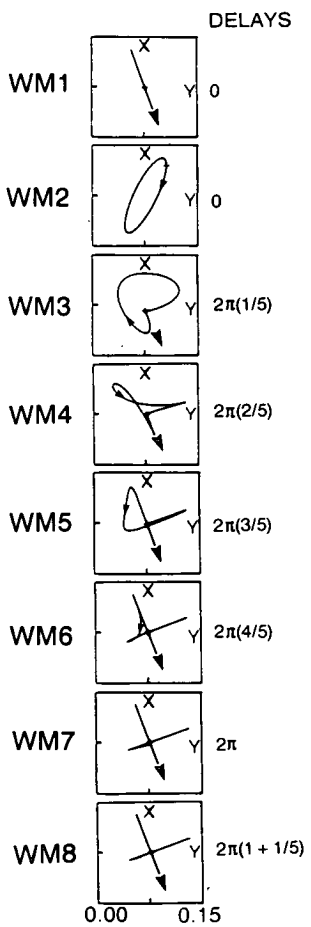

Figure 3. Polarization diagrams of the eight typical wave motions in Fig. 2. The small arrows mark the direction of motion, and the large arrows mark the initial polarization directions.

makes with the inline direction. In Fig. 2, α is chosen as 160° measured from the instantaneous polarization direction to the inline direction:

$$\theta(t) = \begin{cases} \alpha = 160°, & x(t) < 0, \\ 0, & x(t) = 0, \\ \alpha - \pi = 160° - 180° = -20°, & x(t) > 0. \end{cases} \tag{6}$$

We see that the instantaneous polarization of linear motion is a series of rectangular shapes. The important features to note are as follows.

(1) The height or depth of the initial rectangle from the base line is the polarization angle of the linear motion at that point, and the height or depth of the next rectangle is the polarization angle less 180°. Note that there is only one rectangle unless the signal is more than half a cycle long.

(2) The width of the rectangle is the half period of the wave motion, independent of the number of cycles in the waveform (as long as the signal contains at least half a cycle). Thus, the angle of polarization given by the instantaneous polarization in Fig. 2(b) is 160°, and the instantaneous amplitude has two local maxima. The final narrower rectangle in WM1, Fig. 2(b), is a result of the low-amplitude tail of the wavelet used in Fig. 2(a).

Elliptical motion

The elliptical motion WM2 in Figs 2(a) and 3 can be represented by

$$y(t) = a \sin \omega t, \qquad x(t) = b \cos(\omega t + \phi), \tag{7}$$

where a and b are the peak amplitudes in y and x components (WM2, Fig. 2a), respectively; ω is the angular frequency, here taken to be $2\pi \times 40$, say, for a 40 Hz signal, and ϕ is a phase shift, here taken to be 20°.

The elliptical motion in Fig. 2(b) gives a varying instantaneous polarization of repeated characteristic shapes, which we call 'semitriangular'. The polarization angle of the ellipse (the direction of semimajor axis, also called the effective polarization angle) can be determined by combining the instantaneous amplitude displays. The maximum amplitude occurs when the particle displacement is at the long axis of the ellipse. Thus, the angle at the time where the amplitude has a local maximum is an effective polarization angle. (Note, however, that this is not usually coincident with the polarization directions of either of the split shear waves.) There is also another feature which can be used to determine the polarization angle of the ellipse. When the particle motion is at the maximum, the polarization has a smooth variation which forms a step in the instantaneous polarization [marked with arrowhead in WM2, Fig. 2(b)]. The polarization angle can be estimated from the amplitude of this step.

The features discussed above can be used to determine the type of wave motion. Wholly rectangular shapes indicate linear motion (or well-separated split shear waves), and semitriangular shapes indicate some form of elliptical motion. Note that if black and white plots of instantaneous polarization, as in Fig. 2(b), were to be routinely used to determine polarization angles, the polarization would need to be plotted at a larger scale so that the values of the

polarization would be easily read. More effective displays will be discussed below.

3 SHEAR-WAVE SPLITTING

The most characteristic features of shear waves in anisotropic structures are the polarization anomalies in the 3-D waveforms resulting from shear waves splitting into phases which propagate with different polarizations and different velocities (Crampin 1978, 1981; Crampin & Booth 1985). The polarization patterns of shear-wave splitting can be represented by the interference of two linear motions with (typically) similar waveforms but different polarization directions and separated by a time delay. The interference of these signals results in a combination of linear and elliptical waveforms, or two linear waveforms if the time delay between the two split shear waves is large enough to separate the signals. The patterns of particle motion vary with the delay and particle-motion polarizations of the two split shear waves.

We examine a variety of characteristic wavetypes. Without loss of generality, we assume in this paper that the two split shear-wave polarizations are polarized orthogonally.

3.1 Polarization patterns

The six polarization patterns, WM3 to WM8 in Fig. 3, are characteristic of shear-wave splitting with a range of delays: from WM3 to WM8, the delay linearly increases from 8 to 48 on a 40 Hz signal (phase delays from 72° to 432°, respectively). At the onset of the faster split shear waves, the polarizations are linear. At the onset of the slower shear waves, the polarizations either change smoothly to elliptical motion or change abruptly to further linear motion in different directions, if the delays between the two split shear waves are sufficiently large. When the delays between the split shear waves are less than half a cycle (as in WM3 and WM4, Fig. 3), the polarizations change smoothly with elliptical patterns of polarization, and the underlying characteristic cruciform patterns are barely discernible. As the delays increase beyond half a period (WM5 and WM6), the polarizations change more sharply, and the cruciform patterns become clearer. When the delays are equal to the period of the wave (WM7), or greater (WM8), the polarizations change abruptly, and the patterns are wholly cruciform.

3.2 Instantaneous attributes

Figure 2(b) shows corresponding instantaneous attributes of amplitude (A) and polarization (P) of the seismograms in Fig. 2(a) and polarization diagrams in Fig. 3.

WM3 and WM4

The amplitude has three local maxima, and the polarization starts with a step equal to the polarization angle of the first arrival. The polarization then remains constant until the slower wave arrives, when it changes smoothly. If the change can be identified [marked by arrowheads in WM3 and WM4. Fig. 2(b)], the arrival time and polarization direction of the slower split shear wave and the delay between the two split shear waves can also be determined. The overall feature of the instantaneous polarization of shear-wave splitting is a combination of rectangular and semitriangular shapes.

WM5 and WM6

The amplitude has four local maxima, and the polarization is again a combination of rectangular and semitriangular shapes. The polarization change on arrival of the slower shear wave has been marked by arrows in Fig. 2(b), but is subtle and difficult to identify reliably.

WM7 and WM8

The amplitude has four clear local maxima, and the polarization has wholly rectangular shapes. The polarization directions and the delay can be determined easily.

To summarize: as the delay increases, the number of local maxima of instantaneous amplitude increases, and the shape of instantaneous polarization changes from a combination of rectangular and semitriangular shapes to a combination of purely rectangular shapes. Thus, shear-wave splitting can be identified from displays of instantaneous amplitude and polarization, and the polarization direction can be easily and accurately determined when the delays are sufficiently large. The delays are easy to determine when the delays are large, but may be difficult to determine when the delays are less than a cycle. We shall see that colour displays of the attributes are more informative.

4 COLOUR DISPLAYS

The use of colour in displaying seismic data has been shown to improve the perceptibility of subsurface features (Taner *et al.* 1979). Fig. 4 shows the colour codes used for displays of instantaneous polarization in this paper. Code (a) contains a series of contrasting colours, useful for identifying the exact value of the polarization; and (b) a series of continuous colours, useful for recognizing shear-wave splitting on a larger scale. Note that the colours repeat every 180°. Thus, if the polarization values have a difference of ±180°, they will be coded with the same colour, allowing for the ±180° difference between the positive and negative values of the polarization of linear motion.

Figure 5 is the colour display of Fig. 2(b), showing the colour-coded polarization angle in the contrasting colours of code (a) superimposed on a wiggle trace of instantaneous amplitude. This type of display aids estimation of the parameters of shear-wave splitting:

(1) The colour-coded polarization quantifies the polarization direction by reference to the colour key. For example WM1 is a wholly red colour, which represents 162° ± 3° (or −18° ± 3°), where we use the angle (colour) D to represent the range $D - 3° <$ to $\leq D + 3°$. From the shape of the polarization curve we know the angle is 162° ± 3°.

(2) The onset of the slower arrival can be easily identified by the change of the uniform (red) to the varying colours of elliptical motion in WM3 to WM7, or the uniform (black)

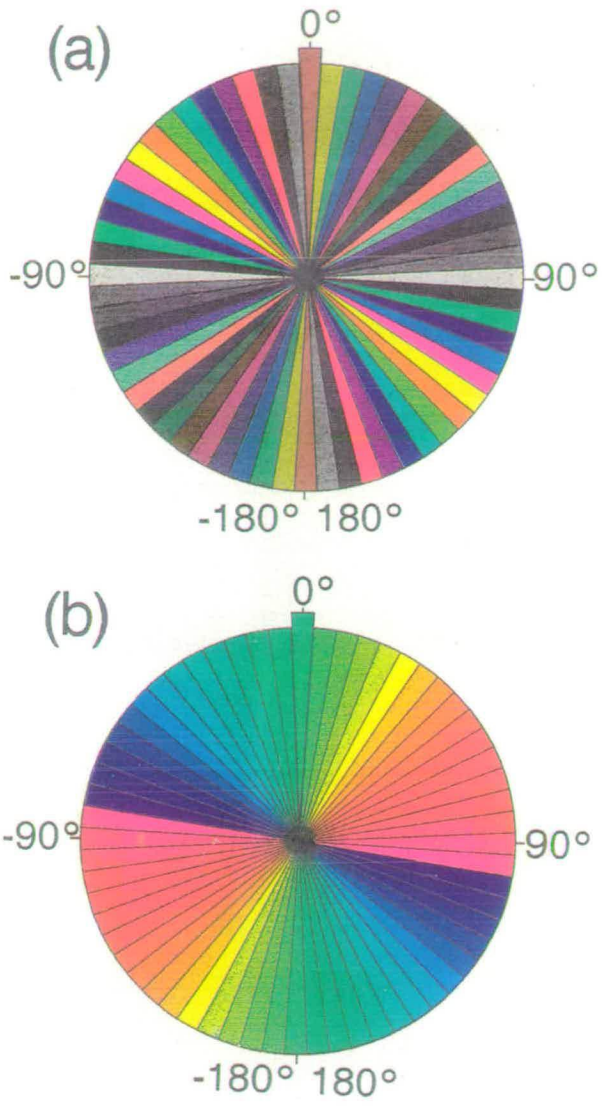

Figure 4. Colour codes for polarization displays: (a) contrasting colour-code; (b) continuous colour-code.

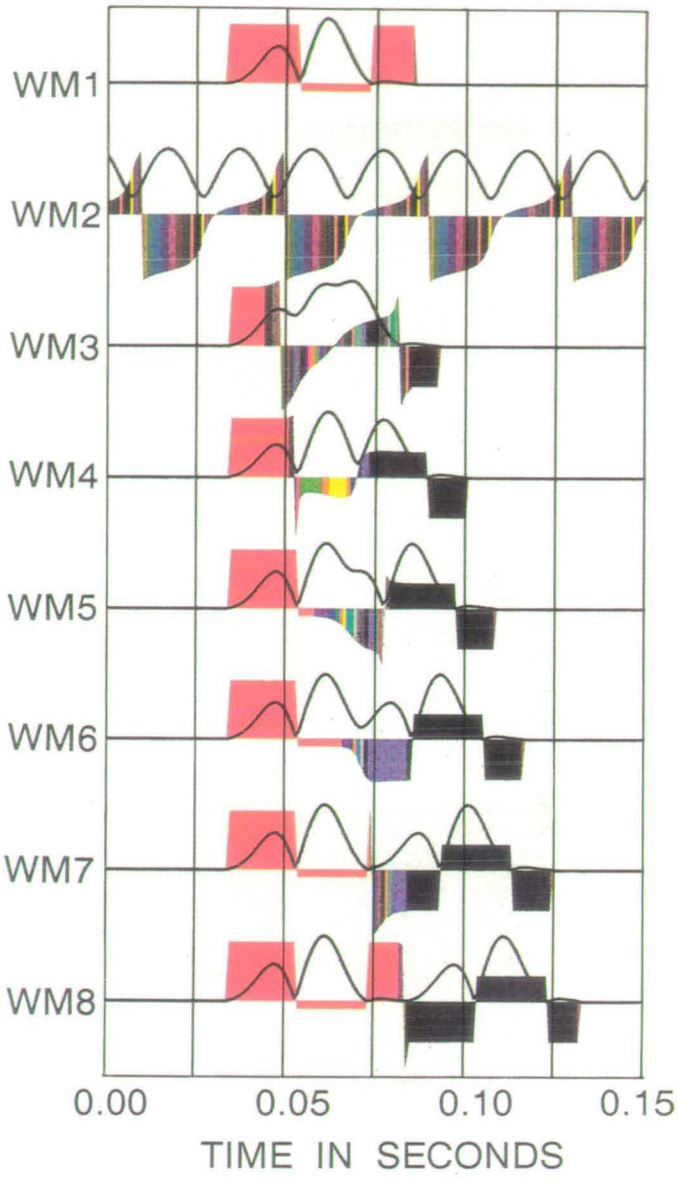

Figure 5. The colour-coded display of Fig. 2(b), where a wiggle line of instantaneous amplitude is superimposed on the colour-coded instantaneous polarization.

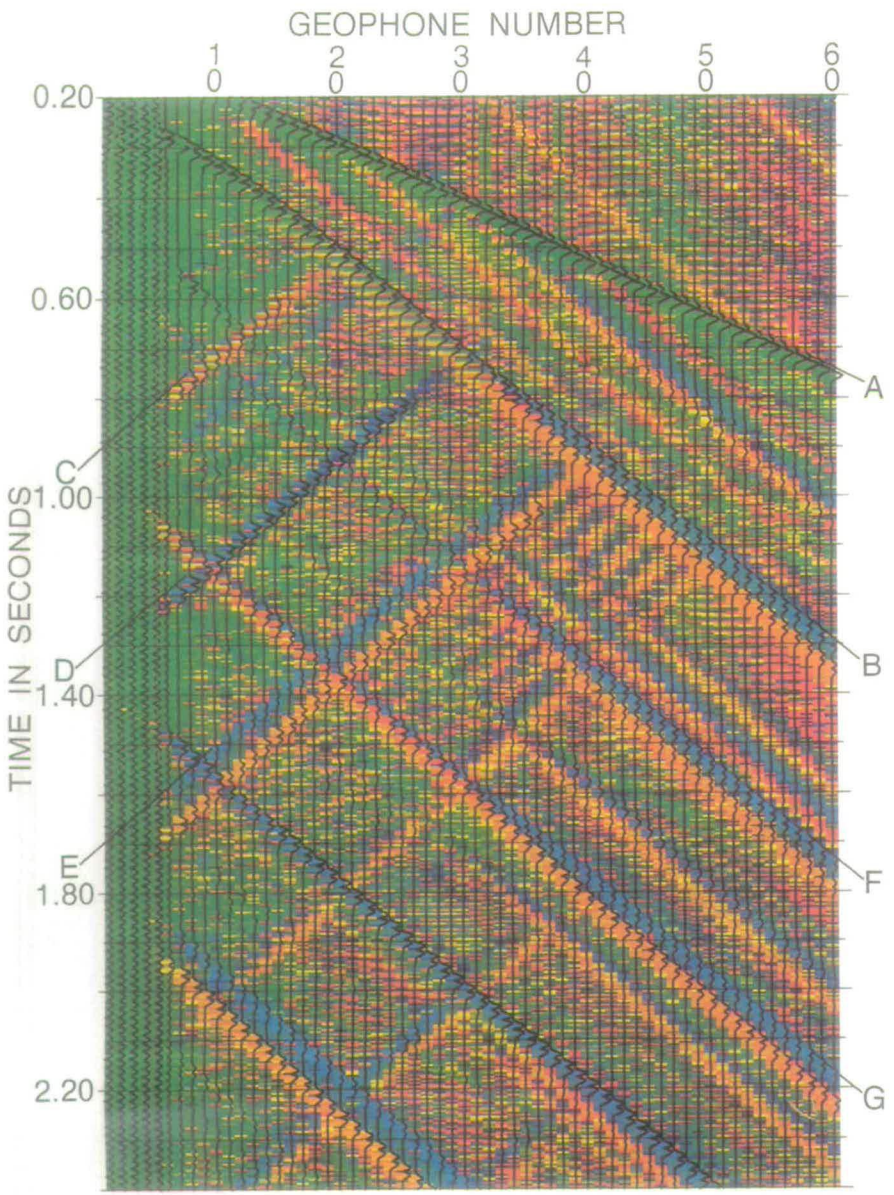

Figure 7. Colour display of instantaneous polarization and amplitude derived from the VSP data in Fig. 6(b). The colour-coded instantaneous polarization is superimposed on wiggle lines of instantaneous amplitude. Letters A–G mark significant arrivals mentioned in the text.

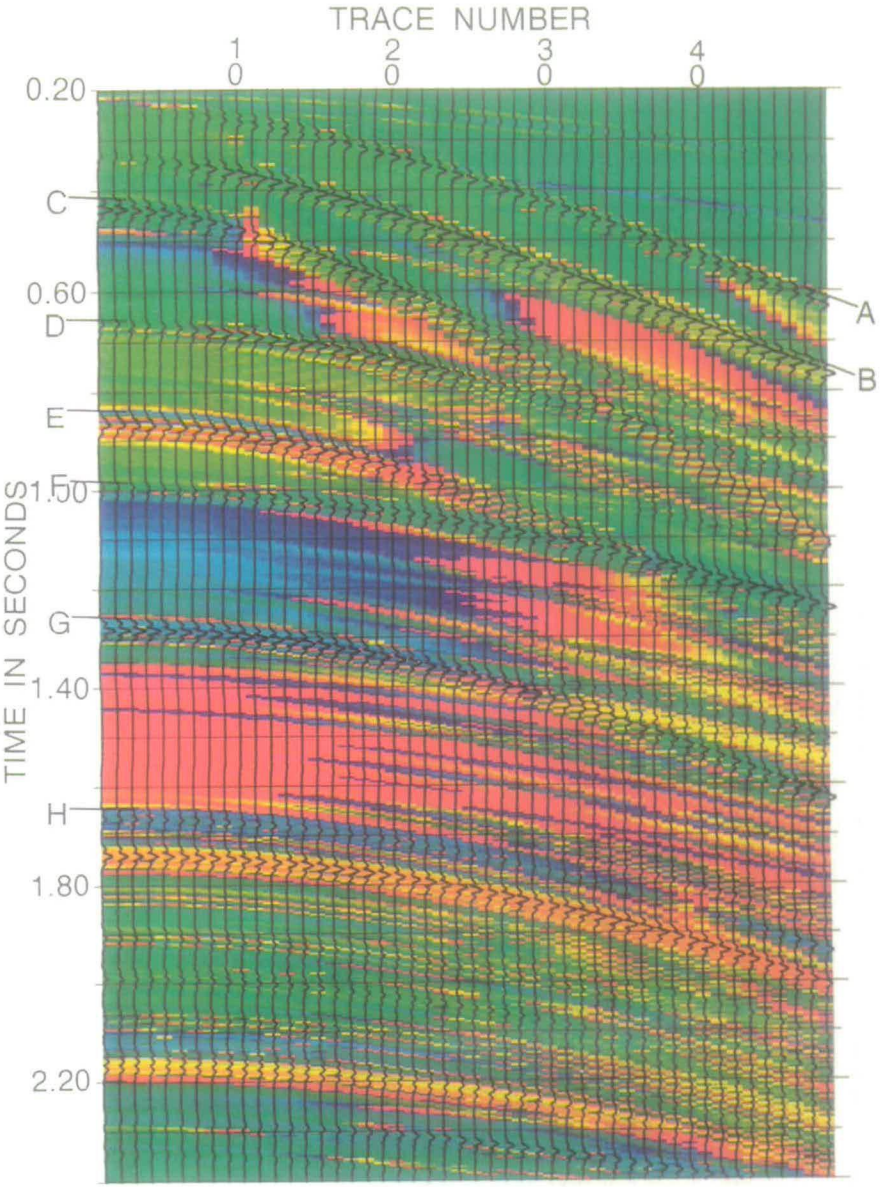

Figure 8. Colour displays of instantaneous polarization and amplitude derived from the CMP gathers of Fig. 6(c). Letters A–H mark significant arrivals mentioned in the text.

colour representing perpendicular motion ($72° \pm 3°$ or $-108° \pm 3°$).

(3) The difference between the linear motion. WM1 and the shear-wave splitting with a delay of more than a cycle, WM8, is clearly demonstrated by the colour. WM1 has a single colour which implies no change of polarization (or a change of $\pm 180°$); whereas WM8 has two different colours (separated by approximately 90°), which implies two approximately orthogonal linear motions.

In applying these techniques to seismograms with incoherent or signal-generated noise, the use of the continuous colour code is recommended for identifying shear-wave splitting, although the contrasting colour code may be required for estimating values of polarization. In the following examples, the polarization is coded by the continuous code (b). Two examples are used to demonstrate the significance and application of instantaneous attributes to anisotropic interpretations.

5 APPLICATIONS

5.1 AMC model and data

The data used are a synthetic VSP and a CMP gather from the response of the Edinburgh Anisotropy Project (Wild 1990) to the Anisotropic Modelling Collaboration of Thomsen *et al.* (1989). A number of research groups are contributing to the Anisotropic Modelling Collaboration (AMC) to calculate full wave synthetic seismograms in specified VSPs and CMPs in a given anisotropic multilayered model (Thomsen *et al.* 1989). Fig. 6(a), adapted from Wild (1990), shows a schematic diagram of Model 1 (AMC1) used in this study (note that only every second three-component geophone is marked in the figure). The crack strike is east–west in each anisotropic layer. The model features a strongly anisotropic layer from 1500 to 2000 m depth, simulating highly fractured reservoir rocks.

The collaboration calculated a full nine-component (inline, crossline, and vertical sources recorded by inline, crossline, and vertical receivers) offset VSP, and a variety of nine-component reflection lines, as indicated in Fig. 6(a). Only one source component, the inline component, of both the VSP, at an offset of 500 m and an azimuth of N45°E, and the 2400 m reflection line data, again at an azimuth of N45°E, are analysed here. Fig. 6(b) shows the two horizontal components of the VSP excited by the inline source located at S_V in Fig. 6(a). Cruciform patterns of particle motion in the polarization diagrams from primary downward propagating shear waves (polarization diagrams c and d) are observed within and below the simulated

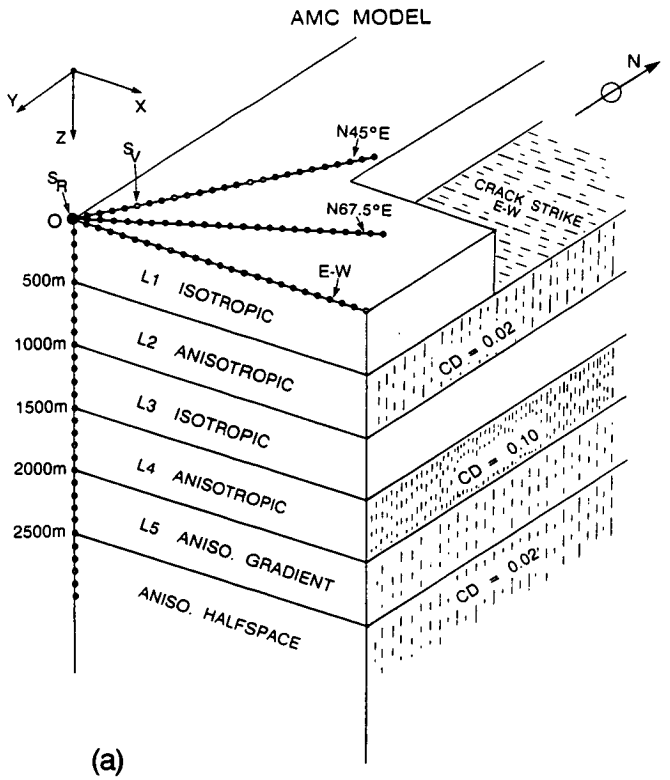

Figure 6. (a) The structure and geometry of the AMC model. The dots along survey lines represent every second geophone of 50 m geophone spacing. (b) The two horizontal components of the VSP data for the inline source orientation. The offset is 500 m at an azimuth of N45°E. Note noise on the first five in-line source components. Some selected polarization diagrams are shown. Number on top right corner of the polarization diagrams is the geophone number at the time interval marked below. Arrows drawn on particle motions are in the same notation as Fig. 3. R1 to R4 are reflected shear waves from Layers L1 to L4, respectively. M1 to M4 are the multiples of the primary downward propagating shear wave. The four particle motions on the left are selected from the primary downgoing shear waves, and on the right from the reflected shear waves. (c) The two horizontal components of the reflection line at an azimuth of N45°E for the inline source orientation with some selected polarization diagrams. Symbols drawn on the diagrams have the same notation as (b). Those on the left are selected from the reflected shear waves R1, R2, R3 and R4 at geophone 1 (near offset), and on the right from the same event-arrivals but at geophones at larger offsets where the polarizations have changed.

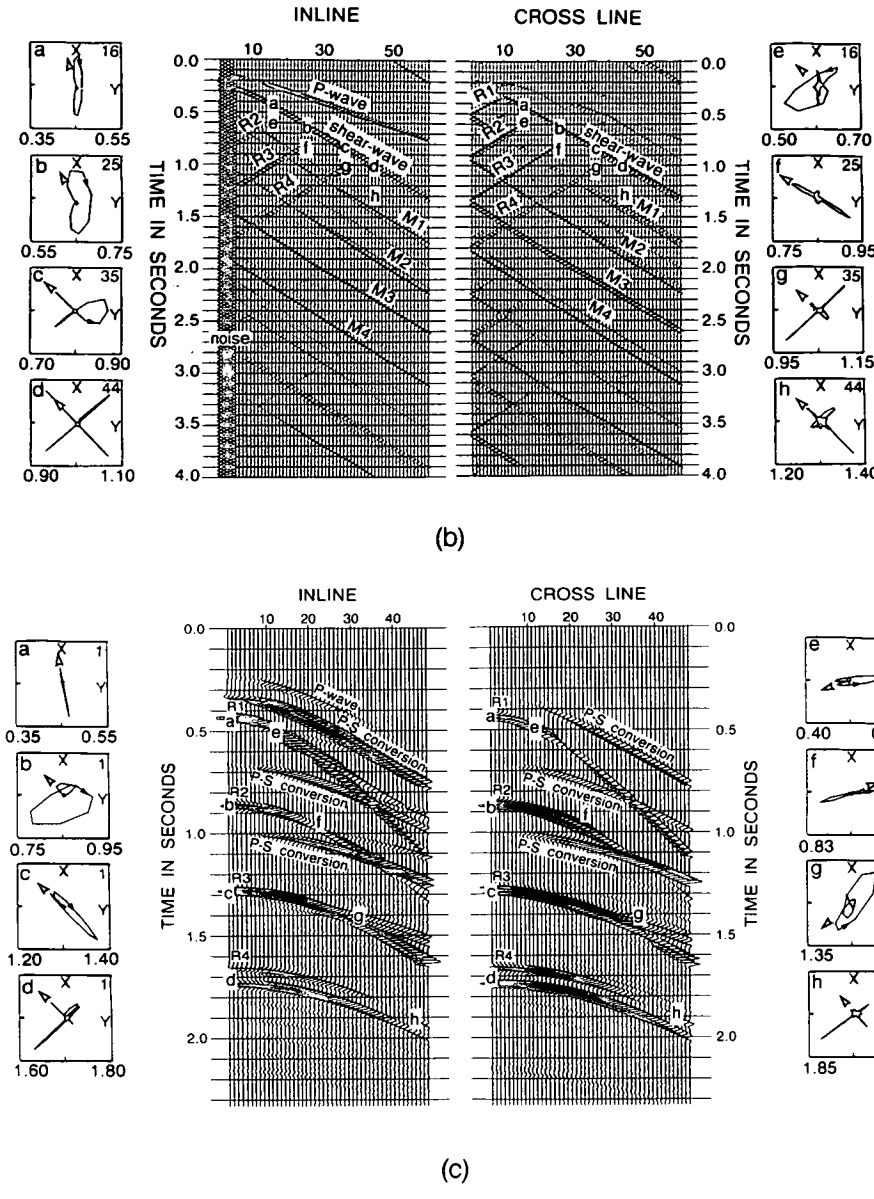

Figure 6. (*continued*)

fractured reservoir (Layer L4); the delays between the downward shear waves gradually increase with increasing geophone depth. Fig. 6(c) shows the two horizontal components of the CMP gather excited by the inline source located at S_R in Fig. 6(a). Polarization diagrams of the shear-wave reflection from the bottom of the reservoir (event R4; polarization diagrams d and h) have cruciform polarizations and show strong shear-wave splitting.

5.2 Analysis of the VSP

Figure 7 shows the colour-coded display for the instantaneous polarization of the VSP data in Fig. 6(b), with a superimposed wiggle trace of instantaneous amplitude. The display contains a large amount of relatively easily interpretable information. A few major items in the interpretation of the display are summarized as follows.

(1) Event A corresponds to the *P*-wave arrival in Fig. 6(b). The whole waveform of the instantaneous amplitude is covered by a single green colour, implying linear motion with a polarization angle of $0° \pm 3°$ (or $\pm 180 \pm 3°$).

(2) Event B is the direct shear wave. Shear-wave splitting can be clearly identified by the shape of polarization curve containing two rectangles of blue ($132° \pm 3°$ or $-48 \pm 3°$) and orange ($42° \pm 3°$ or $-138° \pm 3°$) representing orthogonal or nearly orthogonal motion. The polarization direction of the faster shear wave is represented by the blue rectangle ($-48° \pm 3°$ or $132° \pm 3°$), and the magnitude of the delay can be estimated from the duration of the blue rectangle. Below geophone 30, at the top of layer L4, the duration of the blue rectangle gradually increases, showing the delay between the split shear waves increasing with depth in the strongly anisotropic reservoir.

(3) Event C corresponds to R2, a reflection from the

bottom of L2. Shear-wave splitting can also be identified by the change of colours from blue to orange. Because the delay is small, this change is subtle and can only be clearly seen at geophones 9, 10, 11, and 12, where there is a narrow band of blue.

(4) Event D corresponds to R3, a reflection from the bottom of L3. The blue rectangle covering the waveform indicates linear motion with a polarization angle of $132° \pm 3°$ (or $-48 \pm 3°$).

(5) Event E corresponds to R4, a reflection from the bottom of L4. The waveforms of instantaneous amplitude are dominated by two rectangles of blue and orange, and the shear-wave splitting can be identified and parameters estimated as for the direct shear wave.

(6) Events F and G correspond to M1 and M2, respectively, multiples of the primary down shear wave. The shape of the polarization curve and the variation of colour show the same features as those of the direct shear wave.

5.3 Analysis of the CMP gathers

Figure 8 shows the instantaneous attributes of Fig. 6(c) displaying colour-coded polarization data superimposed by wiggle lines of instantaneous amplitudes. The instantaneous attributes of CMP gathers have two applications.

First, as discussed in the VSP data, the attributes of the CMP gathers can be used to identify the type of shear-wave motion in reflected waves, as follows.

(1) Events A and F, describing the *P*-wave reflections from the bottom of layers L1 and L3, respectively, show linear motion as they are both dominated by a single light green ($0° \pm 3°$ or $\pm 180° \pm 3°$) and dark green ($174° \pm 3°$ or $-6° \pm 3°$) colours, respectively.

(2) Events C and G (corresponding to R1 and R3, shear-wave reflections from the bottom of layers L1 and L3, respectively) are also linear motions at near offset and are dominated by one major colour: event C by the background green ($0° \pm 3°$ or $\pm 180° \pm 3°$), and G by blue ($132° \pm 3°$ or $-48° \pm 3°$).

(3) Events E and H, corresponding to R2 and R4, are shear-wave reflections from the bottom of L2 and L4, respectively, and at near offsets both show shear-wave splitting which can be recognized by the shape of the polarization curve and the variation of colour from blue to orange. The polarization and delay can be determined in the same way as discussed for the VSP data. The delay of event E is small as indicated by the narrow blue rectangle, but the delay of event H is large as it traverses the strongly anisotropic L4 on both downgoing and upgoing rays.

Secondly, the attributes of CMP gathers contain information about the effective shear-wave window at the free surface (Booth & Crampin 1985) for each shear-wave reflection:

(1) The polarization of the shear wave changes with offset, as demonstrated by the variation of colour. For example, event B (a *P–S* conversion from the bottom of layer L1) starts with background green colour at near offset, then changes to a light green at middle offset, and becomes yellow at far offset, indicating an approximate 30° change in polarization as the angle of incidence on the reflecting interface varies (Liu & Crampin 1990). In contrast, the polarization of the *P*-wave is relatively unaffected by the variation of offsets as shown by events A and F.

(2) 'Critical angles' at internal interfaces can also be identified, where one of the shear waves has zero reflection amplitude as the offset increases (Liu & Crampin 1990). For incidence on the reflecting interface smaller than this angle, the colour of the instantaneous polarization remains constant (or only shows gradual change), but at the critical angle the colour indicates a 90° polarization (phase) change. For example, the change due to the critical angle for reflection from Layer 1 for event C is at geophone 12 (the colour suddenly changes from green to red, indicating a 90° change), and the critical angle for reflection from Layer 2 for event E is at geophone 22. Similarly, there are critical angles for event G at geophone 28, and elsewhere.

Effects of the shear-wave window are difficult to observe because of the interference of multiply reflected and converted waves. Note that effects of the first 'critical angle' at internal reflections typically cause a comparatively simple change in polarization direction, and hence a change in the instantaneous polarization (Liu & Crampin 1990), whereas the shear-wave window at the surface usually causes much more complicated effects (Crampin & Booth 1985).

Identifying the offset at which the polarization of each shear-wave arrival changes polarity is important for stacking the CMP gather. Conventional stacking of split shear waves, where the polarizations and delays change markedly with offset, will tend to distort and degrade the characteristics of the split shear waves unless appropriate techniques are used (Li & Crampin 1989). Such changes of polarity occur both at critical reflections at internal interfaces (Liu & Crampin 1990), and at the surface shear-wave window (Booth & Crampin 1985).

6 DISCUSSION AND CONCLUSIONS

We have suggested a technique for the complex component analysis of shear-wave data by transforming the displacements from Cartesian to polar coordinate systems. The use of colour provides a technique for displaying the large amount of information contained in the shear wavetrain (Crampin 1985b) in a form which is similar to many conventional time-versus-offset displays, and which could easily be assimilated into conventional stratigraphic analysis.

The VSP example shows how the technique can help in analysing and estimating shear-wave splitting continuously as it varies with depth. The results of pre-stack reflection data show how shear-wave splitting can be traced along both time and offset directions, and reveals the potential for applying these techniques to post-stack data, so that much of the stratigraphic and anisotropic interpretation can be made on a single display of complex attributes. Although the instantaneous attributes were defined for vertical propagation, at wider angles they can be used to identify the various critical angles at the surface and at internal interfaces, which are critical for any stacking of shear-wave data in anisotropic structures (Li & Crampin 1989).

We conclude that the treatment of the two horizontal components in multicomponent shear-wave data as a complex variable allows convenient displays of instantaneous amplitude and polarization. The colour display of

these attributes allows the identification of shear-wave splitting and permits estimates of shear-wave polarizations and delays in seismic sections. The examples in this paper aim to demonstrate the concept of the complex component analysis of shear-wave splitting and the potential application of colour displays of instantaneous attributes. We suggest these colour displays provide a flexible format for recognising and parametrizing shear-wave splitting. Further developments and case studies are presented by Li & Crampin (1990b, 1991).

ACKNOWLEDGMENTS

The synthetic seismograms were calculated with the ANISEIS package of Applied Geophysical Software Inc. and Macro Ltd. We thank David C. Booth and Colin MacBeth for their comments on the manuscript. This work was supported by the Edinburgh Anisotropy Project and the Natural Environment Research Council, and is published with the approval of the Director of the British Geological Survey (NERC).

REFERENCES

Alford, R. M., 1986. Shear data in the presence of azimuthal anisotropy: Dilley, Texas, *56th Ann. Int. SEG Mtg, Houston, Expanded Abstracts*, pp. 476–479.

Booth, D. C. & Crampin, S., 1985. Shear-wave polarizations on a curved wavefront at an isotropic free-surface, *Geophys. J. R. astr. Soc.*, **83**, 31–45.

Crampin, S., 1978. Seismic wave propagation through a cracked solid: polarization as possible dilatancy diagnostic, *Geophys. J. R. astr. Soc.*, **53**, 467–496.

Crampin, S., 1981. A review of wave motion in anisotropic and cracked elastic-media, *Wave Motion*, **3**, 343–391.

Crampin, S., 1985a. Evidence for aligned cracks in the Earth crust, *First Break*, **3**, 3, 12–15.

Crampin, S., 1985b. Evaluation of anisotropy by shear-wave splitting, *Geophysics*, **50**, 142–152.

Crampin, S., 1987. Geological and industrial implications of extensive-dilatancy anistropy, *Nature*, **328**, 491–496.

Crampin, S. & Atkinson, B. K., 1985. Microcracks in the Earth's crust, *First Break*, **3**, 3, 16–20.

Crampin, S. & Booth, D. C., 1985. Shear wave polarizations near the North Anatolian Fault: II, interpretation in terms of crack-induced anisotropy, *Geophys. J. R. astr. Soc.*, **83**, 75–92.

Huang, D. J., 1989. The extraction of main characteristic parameters of seismic wave, *China Oil Geophys. Prosp.*, **24**, 155–165.

Li, X.-Y. & Crampin, S., 1989. Analyzing shear-wave splitting in three-component reflection survey, *SEG Res. Workshop. Recording and Processing Vector Wave Field Data, Snowbird, 13–17 August, 1989, Technical Abstracts*, p. 114.

Li, X.-Y. & Crampin, S., 1990a. Complex component analysis of shear-wave splitting: theoretical studies, *Fourth Int. Workshop on Seismic Anisotropy, Edinburgh 2–6 July, 1990, Abstracts*, British Geological Survey.

Li, X.-Y. & Crampin, S., 1990b. Case studies of complex component analysis of shear-wave splitting, *60th Ann. Int. SEG Mtg, San Francisco, Expanded Abstracts*, vol. 2, pp. 1427–1430.

Li, X.-Y. & Crampin, S., 1991. Complex component analysis of shear-wave splitting: case studies, *Geophys. J. Int.*, this issue.

Liu, E. & Crampin, S., 1990. Effects of an internal shear wave window: comparison with anisostropy induced splitting, *J. geophys. Res.*, **95**, 11 275–11 281.

René, R. M., Fitte, J. L., Forsyth, P. M., Kim, K. Y., Murray, D. J., Walters, J. K. & Westerman, J. D., 1986. Multicomponent seismic studies using complex trace analysis, *Geophysics*, **51**, 1235–1251.

Taner, M. T. & Sheriff, R. E., 1977. Application of amplitude, frequency, and other attributes to stratigraphic and hydrocarbon determination, *AAPG Mem.*, **26**, 301–327.

Taner, M. T., Koehler, F. & Sheriff, R. E., 1979. Complex seismic trace analysis, *Geophysics*, **44**, 1041–1063.

Thomsen, L. *et al.*, 1989. Comparison of anisotropic modelling codes: Anisotropic Modeling Collaboration, *SEG Res. Workshop, Recording and Processing Vector Wave Field Data, Snowbird, 13–17 August, 1989, Technical Abstracts*, p. 4.

Wild, P., 1990. Report on anisotropic modelling collaboration: 1—Model 1, *Tech. Report WL/90/4*, British Geological Survey.

Willis, H. A., Rethford, G. L. & Bielanski, E., 1986. Azimuthal anisotropy: occurrence and effect on shear-wave data quality. *56th Ann. Int. SEG Mtg, Houston, Expanded Abstracts*, pp. 479–481.

Geophys. J. Int. (1991) **107**, 605–613

Complex component analysis of shear-wave splitting: case studies

Xiang-Yang Li[1,2] and Stuart Crampin[1]

[1] *Edinburgh Anisotropy Project, British Geological Survey, Murchison House, West Mains Road, Edinburgh* EH9 3LA, *UK*
[2] *Department of Geology and Geophysics, University of Edinburgh, James Clerk Maxwell Building, Edinburgh* EH9 3JZ, *UK*

Accepted 1991 June 12. Received 1991 June 11; in original form 1991 January 8

SUMMARY

Complex component analysis has been applied to four shear-wave data sets: a four-component single-offset VSP in the Lost Hills, Kern County; a multi-offset single-source two-component VSP in the Paris Basin; a four-component reflection line in the Lost Hills; and an in-seam crosshole survey at German Creek Mine, Australia. In all cases, the polarization of the faster split shear wave (or channel wave) can be assessed from the colour-coded record sections of the seismic attributes. In particular, the source-independent coherent polarization on the colour sections of the complex components of in-line and cross-line sources allows the shear-wave polarization angle to be determined without need for rotation of the instrument and source axes. We conclude that complex component analysis can aid identification and estimation of shear-wave splitting from seismic sections, help stratigraphic interpretation, and simplify the processing sequence of multicomponent reflection data in the presence of anisotropy.

Key words: case studies, complex component analysis, shear-wave splitting.

1 INTRODUCTION

Over the last decade, the use of multicomponent shear-wave data to evaluate the effects of anisotropy has become comparatively common within the hydrocarbon industry. Alford (1986), Justice, McCormick & Lee (1987), Thomsen (1988), and Winterstein & Meadows (1990) evaluate anisotropy from seismic sections of reflection surveys and vertical seismic profiles by rotating source and geophone axes synchronously. Crampin *et al.* (1986) and Bush & Crampin (1987) and co-authors determine crack orientation and crack density in the *in situ* rockmass from analysis of polarization diagrams (PDs), or hodograms. Recently, some important applications have been recognized: Mueller (1990) identified fracture zones in the Austin Chalk from variations of shear-wave splitting, and Brodov *et al.* (1990) correlated production rates with the degree of anisotropy in shear-wave VSPs at different wells in an oil field with variable production rates between wells.

Seismic sections, displaying seismograms in time-versus-offset plots, accentuate the relative arrival times of the various phases, and analysis of such arrival times is the principal technique for stratigraphic interpretation. Up to now, one of the commonest techniques for estimating shear-wave splitting from nine-component, or four-component, record sections is by synchronous rotation of horizontal source and geophone axes, in order to separate and identify the polarizations of the shear-wave splitting (Alford 1986). (Nine-component sections are three separate source components recorded by three-component geophones, and four-component sections are two horizontal source components recorded by two horizontal geophones.) The principal alternative technique for analysing shear-wave splitting is by analysing PDs (polarization diagrams), which display the data in the displacement plane over an appropriate time window, and display directly the variation of the waveforms and polarizations of the particle motion (Crampin 1978).

Transformation of seismic data from one configuration to another (time domain, frequency domain, FK-space, etc.) is common in seismic data processing. Complex component analysis transforms multicomponent data from conventional Cartesian coordinates to polar coordinates in the horizontal plane (it can be extended to other planes). Such transformations retain the local significance of both variation of waveforms and variation of particle motion by calculating the instantaneous amplitude and instantaneous polarization. Such complex component analysis can be used to evaluate the effect of anisotropy in terms of the polarization of the leading split shear wave and the delay between the two split shear waves, and allows these parameters to be displayed similar to conventional record sections.

This paper applies the complex component analysis techniques of Li & Crampin (1990a, b, 1991) to four field data sets: a four-component vertical seismic profile (VSP) in

Lost Hills, Kern County, a two-component VSP in the Paris Basin, a four-component reflection profile in Lost Hills, and a three-component in-seam (crosshole) seismic survey from the German Creek Mine, Australia. (Note that the Lost Hills recordings were nine-component data sets, although only four components will be analysed here.) Application of complex component analysis to field data confirms the theoretical promise of Li & Crampin (1991), and reveals new insights into the technique.

We outline the calculation of complex components of four-component seismic data, discuss necessary pre-processing procedures, and present the four case studies.

2 CALCULATION OF COMPLEX COMPONENTS

The technique of complex component analysis of shear-wave splitting is presented by Li & Crampin (1991), who illustrated the ideas with two-component synthetic shear-wave data. However to study shear-wave splitting, multicomponent receivers and multicomponent sources have been used to generate four-component (Alford 1986; Thomsen 1988) and nine-component data sets (Squires, Kim & Kim 1989).

Li & Crampin (1991) defined complex component analysis for two-component shear-wave data. We apply these techniques to further multicomponent data in the following three ways.

(1) Calculate and display the complex components of in-line and cross-line sources separately by equations (1) to (4) of Li & Crampin (1991). (Hereafter, in-line, and cross-line will be referred to as IL, and XL, respectively.) Features which diagnose shear-wave splitting or stratigraphic variation typically display systematic behaviour, so that data sets from orthogonally polarized source components are expected to display consistent features, which will enhance and confirm interpretations.

(2) Calculate and display the shear-wave splitting section (SWS section). Let $\theta_x(t)$ and $\theta_y(t)$ be the instantaneous polarizations of the IL, (x), and XL, (y), source, respectively. The absolute differential polarization angle $d(t)$ between θ_x and θ_y can be calculated as

$$d(t) = |\theta_x(t) - \theta_y(t)|. \tag{1}$$

A filter operator $f(t)$ can be defined as

$$f(t) = \begin{cases} 1, & \text{if } d(t) \le d_0, \\ 0, & \text{if } d(t) > d_0, \end{cases} \tag{2}$$

where d_0 is a threshold value. The combined polarization $\Theta(t)$ can be written as

$$\Theta(t) = [\theta_x(t) + \theta_y(t)]f(t)/2. \tag{3}$$

Equations (1), (2), and (3) show that $\Theta(t)$ will specify any common polarization which appears on both IL and XL sections. The existence of a common polarization at the onset of the shear-wave arrival among different source orientations suggests shear-wave splitting, where the common polarization is the alignment of the leading split shear wave. Thus, we call $\Theta(t)$ the instantaneous polarization of shear-wave splitting; and the corresponding display is called the shear-wave splitting section (SWS section).

(3) Calculate and display the transformed complex component of IL and XL sources. Following Thomsen (1988), the four components can be written as

$$s_{11}(t) = s\,qS1\,(t)\cos^2\theta + s\,qS2\,(t)\sin^2\theta, \tag{4}$$

$$s_{22}(t) = s\,qS1\,(t)\sin^2\theta + s\,qS2\,(t)\cos^2\theta, \tag{5}$$

$$s_{12}(t) = s_{21}(t) = [s\,qS1\,(t) - s\,qS2\,(t)]\sin\theta\cos\theta, \tag{6}$$

where $s\,qS1\,(t)$ and $s\,qS2\,(t)$ are the fast and slow split shear-wave signals, $qS1$, and $qS2$, respectively. s_{ij} are the recorded seismograms, where i is the receiver component, and j is the source component; subscript 1 is the IL component, and 2 the XL component; and θ is the crack strike measured from the IL direction. Linear transforms of

$$\xi(t) = s_{11}(t) - s_{22}(t), \tag{7}$$

$$\eta(t) = s_{12}(t) + s_{21}(t), \tag{8}$$

can be used to transform four-component data to two-component data. Equations (4), (5) and (6) give

$$\tan 2\theta = \eta(t)/\xi(t), \tag{9}$$

showing that the instantaneous polarization of the two-component data $\xi(t)$ and $\eta(t)$ is a measure of polarization of the leading split shear-wave, which we call the *orientation log*. In the absence of lithology- or layer-induced anisotropy, this instantaneous polarization is the strike of the cracks (or fractures) in the rockmass (Crampin 1981). Equation (9) can also be derived from the $\tan 4\theta$ expression of rotation angle based on the minimization of the sum of squares of the off-diagonal terms over a time window in the data matrix (Murtha 1988).

3 DATA PROCESSING

The aim of data processing is to improve data quality while preserving the characteristics of shear-wave splitting. Processing data prior to complex component analysis often involves the following.

(1) Use of band-pass filtering to improve the signal–noise ratio. If the passband is properly selected, by simple spectral analysis, for example, the characteristics of shear-wave splitting will not be affected (Campden 1990). Fig. 1 shows the PDs of the downgoing shear wave in the Lost Hills VSP before (Fig. 1a) and after (Fig. 1b) a 2–25 Hz band-pass filter, showing that the polarization is preserved.

(2) Use of FK-filtering to separate the upgoing and downgoing wavefields. The FK-filter is preferred for separating seismic wave fields without the degradation resulting from median-filters, or other separation methods (Campden 1990). Fig. 2(a) shows PDs before FK- and median-filtering of the Paris Basin VSP data; Fig. 2(b) shows PDs after FK-filters, and Fig. 2(c) after median-filters. The PDs show almost no difference after FK-filters, but have significant differences after median-filters.

(3) Use of polarization filtering to improve the image of colour sections of complex components by muting out noise with intermediate polarizations. Fig. 3 shows the definition of polarization filter. Like a fan filter, it passes the principal and orthogonal polarizations, in order to preserve the

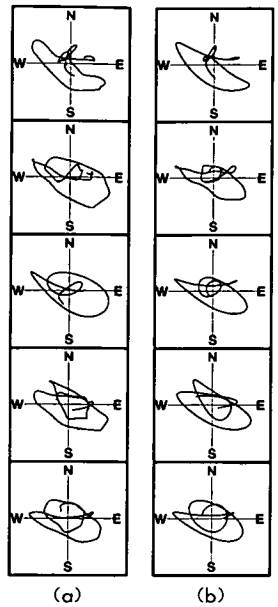

Figure 1. Polarization diagrams: (a) before and (b) after a 2–25 Hz bandpass filter. Data are from Lost Hills VSP.

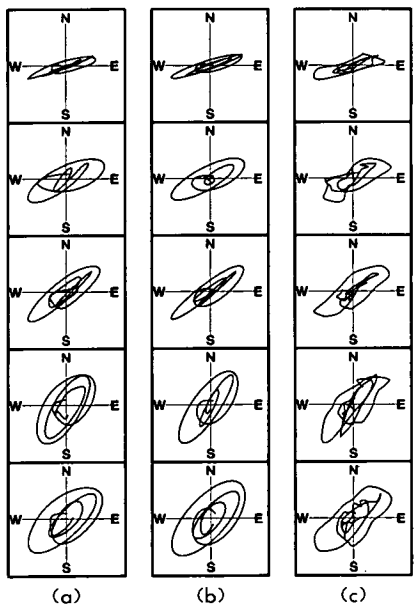

Figure 2. Comparison of FK-filter and median-filter: (a) PDs before FK- and median-filter; (b) PDs after FK-filter; and (c) PDs after median-filter. Data are from Paris Basin VSP.

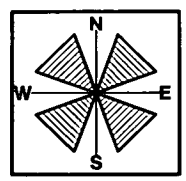

Figure 3. Geometry of polarization filter for north–south or east–west polarized shear-waves, where the polarizations within the shading areas are muted.

characteristics of shear-wave splitting. The passband should be as wide as possible, around the principal and orthogonal polarizations. Selected PDs can be used to determine the passband. A front mute is often applied in conjunction with the polarization filter. Note that zero is a meaningful polarization value, and to implement the polarization filter, when $\theta(t)$ is outside the passband, we set $\theta(t)$ to a specific value which represents the background colour of display media. Also note that the improved colour image accentuates the principal polarizations, whether they are shear waves, converted waves, or *P*-waves.

Figure 4(a) shows colour overlays of instantaneous amplitudes and polarizations from the Lost Hills VSP before applying polarization filters, where although polarization variations can be followed, the rainbow of colours may be misleading. From the PDs in Fig. 4(b), we can identify an initial polarization about N54°E ± 3° and effective polarization (main ellipse) is about N42°W ± 3°. Thus a passband from N15°E to N75°E is appropriate. After applying the designed filter, the section accentuates the principal shear-wave polarizations (Fig. 4d), from which the variation of polarization can be more easily followed.

4 CASE STUDIES

We use four field data sets to illustrate the application of complex component analysis in a variety of different recording situations.

4.1 Lost Hills nine-component VSP

This example aims to illustrate the use of complex component analysis for analysing shear-wave splitting for four-component VSP data. The Kim-Tech Lost Hills VSP is a total wavefield nine-component data set of high quality (Squires *et al.* 1989), but in this analysis we shall use only the four horizontal components. The two horizontal sources are oriented north and east. The source offset is 500 ft (150 m) west of the well and there are 42 geophones with 100 ft (30 m) spacing. The first geophone is located at depth 3600 ft (1100 m). Consequently, the incidence angle is comparatively small and most of the shear-wave energy is in the horizontal plane. The initial linear motion can be observed in PDs of the primary shear waves at most geophone depths (Fig. 4b). Note that we use terms such as north–south (NS) source, and east–west (EW) source for VSPs of small offset, where the IL and XL terms of the reflection survey are less relevant.

Figure 4(b) shows some selected colour PDs in which the particle motions are superimposed on colour pies which represent the colour scale used in this study. The initial polarization direction indicated by arrowheads is corresponding to a red–orange colour, indicating N54°E ± 3°.

Figures 4(c) and (d) show the attribute displays of the north–south and east–west sources, marked as NS and EW sections, respectively. At the onset of the shear wave, indicated by arrowheads, almost the same red–orange colour band appears on all geophones on both NS and EW sections. [Note that there are minor colour changes of about 6° in these first arrivals, which are believed to be due to the interference of split shear waves (Yardley & Crampin 1990).] The existence of a similar colour band means the

polarization of the onset shear wave is fixed in space, independent of the source orientations, and is diagnostic of shear-wave splitting. Thus, the polarization of the faster split shear wave is represented by the red–orange band, and the time delay between the split shear waves by the duration of the band. This band is about 50 ms wide at the shallowest depths, and as depth increases, the duration of the band slightly decreases, indicating a decrease in the time delays. As mentioned above, the red–orange colour indicates 54°E ± 3°, which agrees with the results of Yardley & Crampin (1990).

A similar decrease in delays in a multi-offset VSP at a neighbouring site in the Lost Hills Field has been interpreted by Winterstein & Meadows (1990) as indicating a change in crack orientation with depth. Similarly, Squires *et al.* (1989) have interpreted a negative delay in a nine-component reflection survey through the Lost Hills site we are analysing as a 90° change in crack orientation. However, shear-wave point singularities are believed to be commonly situated near vertical ray paths in sedimentary basins (Crampin 1991; Wild & Crampin 1991), as a result of combinations of matrix and crack anisotropies. Thus, an alternative explanation for the decrease in delays may be that the directions of the ray paths through a uniform crack orientation vary with depth so that they cross a point singularity. The upper ray paths on one side of a point singularity would build up a delay, whereas the lower ray paths on the other side, with a nearly 90° change in effective polarization (Crampin 1991), would reduce the delay.

At the shear-wave onset on both Figs 4(c) and (d), the instantaneous polarization shows a constant band of colour, where the instantaneous polarizations have rectangular shapes. After this band, the instantaneous polarizations show a smooth change of colour, with semitriangular shapes. These characteristic combinations of rectangular and semitriangular shapes are diagnostic of shear-wave splitting and confirm the theoretical results of Li & Crampin (1991).

Figure 4(e) shows SWS sections calculated from the NS section (Fig. 4c) and the EW section (Fig. 4d) using equations (1), (2) and (3), where only arrivals which have similar polarizations on both source sections are displayed. Following the onset of shear waves, Fig. 4(e) shows a red–orange colour band. The colour of the band represents the polarization of the faster split shear wave, and the duration of the band represents the dealy between the two split shear waves.

Figure 4(f) shows the orientation logs from equations (7), (8) and (9). As with the SWS sections, the red–orange colour at the onset of the shear waves indicates the polarization of the faster split shear waves, and the duration of the band indicates the delay; however, with this display, the interference of split shear waves is separated. Fig. 4(f) shows two simple polarizations: a red–orange polarization, the polarization of the faster split shear wave, and a blue polarization, the polarization of the slower split shear wave.

We have demonstrated three types of display for processing shear-wave splitting in four-component VSP data by complex component analysis: (1) colour sections of complex component attributes from different source orientations to examine the coherency and duration of instantaneous polarizations; (2) SWS sections; and (3) orientation logs.

4.2 Paris Basin VSP

This Paris Basin VSP was a multi-offset single source VSP recorded on two horizontal geophones (Bush & Crampin 1987). We shall process only the S1 offset at 272 m. This case history is presented to demonstrate the application of complex component analysis to two-component seismic data. In addition to showing how complex component analysis can be used to interpret shear-wave splitting, we also show how it can aid stratigraphic interpretation. Preliminary processing included: applying a band pass filter of 5–50 Hz; and FK-filter to separate the downgoing and upgoing wavefields; and prior to display, applying a polarization filter of N15°E–N75°E.

Enlargements of the PDs in Fig. 5(a) show a very small initial orientation of a blue colour, indicating N42°W ± 3°. This is less obvious than the first arrival in the Lost Hills VSP (Fig. 4b) because of the smaller time delays in the Paris Basin data. The effective polarization (polarization of the main ellipse) changes from red (N78°E ± 3°) to orange yellow (N42°E ± 3°).

Figure 5(b) shows the instantaneous amplitude and polarization of the downgoing wavefield. On the onset of the shearwave, the polarization starts with a band of blue colour, indicated by arrowheads, which has a rectangular shape. The polarization colour smoothly changes following the constant blue band, and has semitriangular shapes. These characteristic shapes suggest shear-wave splitting. This blue band and the following colour pattern changes appear at all geophone depths, showing consistency and coherency, which enhances the interpretation. The time delay and polarization can be interpreted from the blue band, which is about 20 ms wide and increases with depth. This example of two-component data analysis also confirms the theoretical promise of Li & Crampin (1991).

Figures 5(c) and (d) demonstrate the application of complex component analysis in stratigraphic interpretation. Fig. 5(c) shows the colour section of the instantaneous amplitude and polarization of the upgoing wavefield. Reflections from the same interface tend to have coherent polarizations at adjacent geophones when there is shear-wave splitting. [Reflections of shear waves at isotropic/isotropic interfaces at wider offsets display systematic changes of polarization with incidence angle due to differences in the reflection coefficients of *SH*- and *SV*-wave components (Liu, Crampin & Yardley 1990).] This coherency of polarization can help identify reflection events. As shown on Fig. 5(c), the events can be easily identified and traced back to the reflectors following the variation of polarization colours. A variation of polarization from red (N78°E ± 3°) to yellow orange (N42°E ± 3°) can be observed from shallow reflections to deep reflections; Bush & Crampin (1987) model this as the effects of combination of thin-layer and crack anisotropy.

Processing the upgoing wavefield further, we shift to two-way time, and apply a corridor stack, to obtain the VSP log in Fig. 5(d). Fig. 5(d) shows instantaneous polarization superimposed on wiggle-lines of instantaneous amplitude. Colour displays of instantaneous polarization appear to display better continuity of shear-wave reflections than amplitude displays. In addition, the polarization offers additional criteria in correlating VSPs with stacked sections.

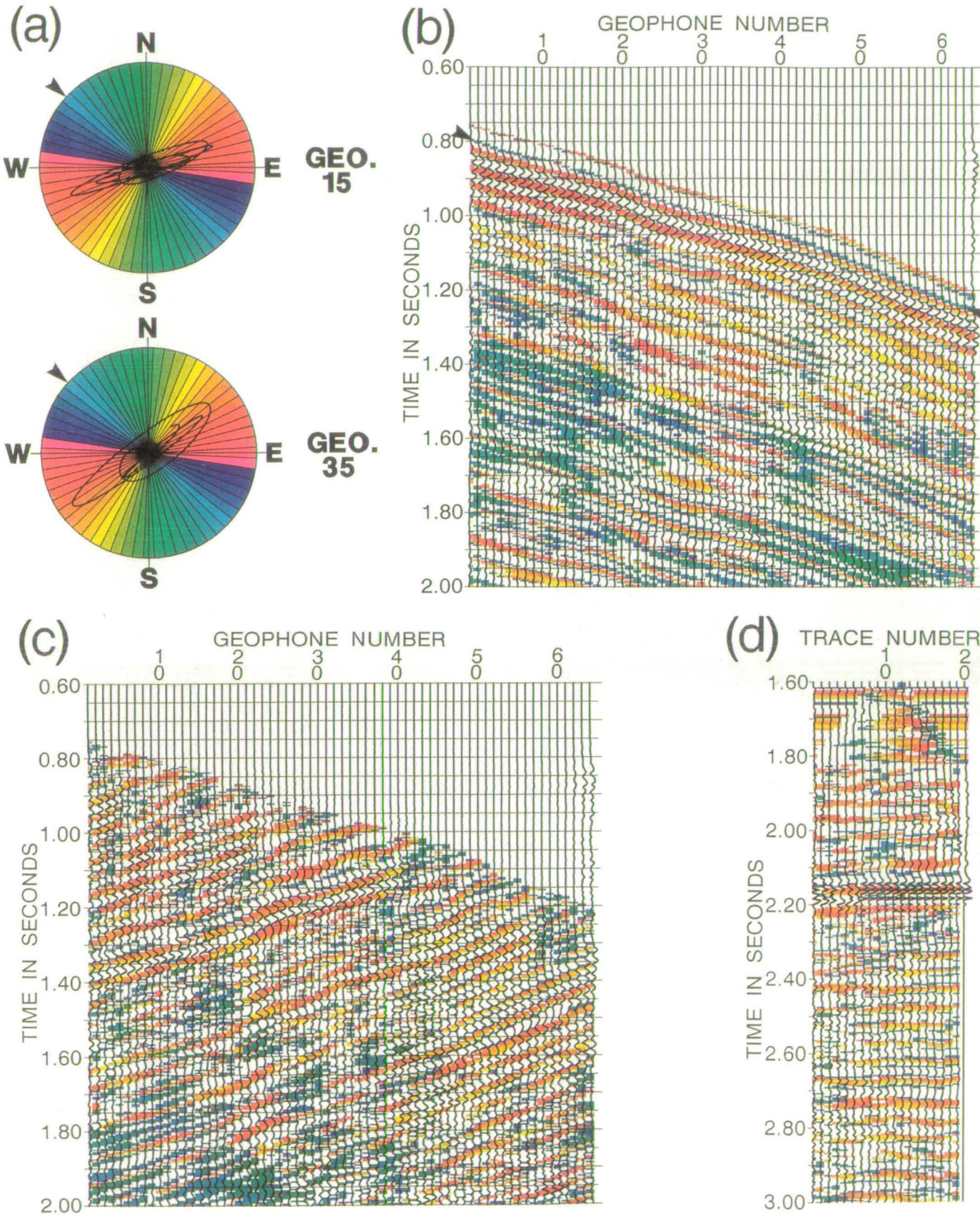

Figure 5. Results of Paris Basin VSP: (a) selected PDs in the horizontal plane with notation of Fig. 4(b); (b) colour section of the instantaneous amplitude and polarization of downgoing shear waves; (c) colour section of the instantaneous amplitude and polarization of upgoing shear waves; and (d) VSP log obtained by shifting upgoing waves to two-way time and stacking.

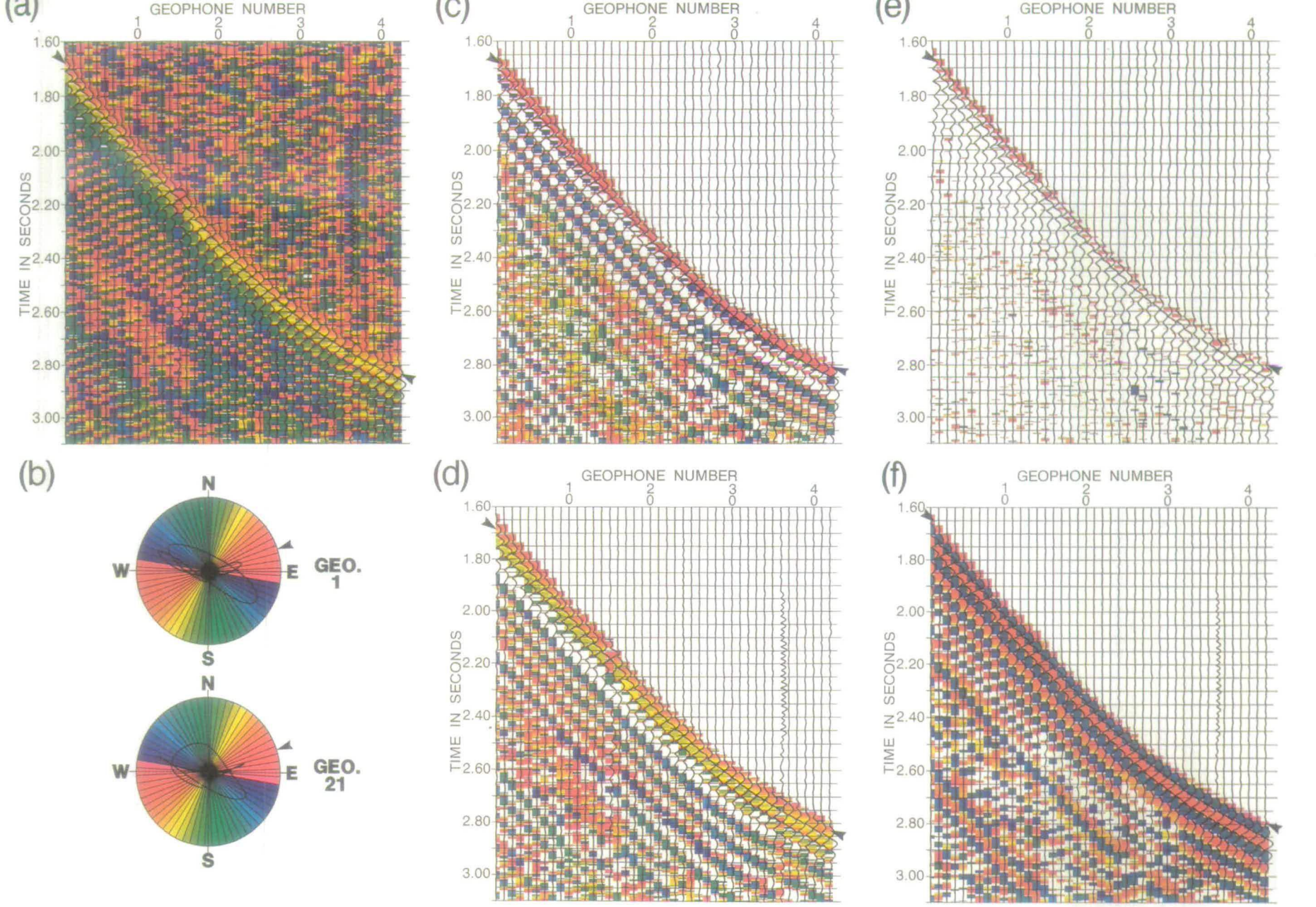

Figure 4. Processing the Kim-Tech Lost Hills VSP. (a) Colour section of the complex components of EW source: instantaneous polarization superimposed on wiggle-lines of instantaneous amplitude of the north–south source of Lost Hill VSP before polarization filter. (b) Selected PDs of north–south source component in the horizontal plane with geographical coordinates, where the colour pie shows the colour scale used in this study. (c) Colour section of the instantaneous amplitude and polarization of NS source; (d) Colour section of the instantaneous amplitude and polarization of EW source; (e) SWS section, which combines the common polarizations in the EW section (c) and NS section (d); (f) orientation logs of the EW and NS sections of the Lost Hill VSP.

Thus, the characteristic shape and coherency of polarizations between adjacent geophones are the major criteria for interpreting shear-wave splitting in two-component VSP data. The coherency of polarizations also improves the continuity of reflection events and hence the image of subsurface structure.

4.3 Lost Hills reflection profile

We apply complex component analysis to four-component reflection profiles in the Kim-Tech Lost Hills data set to analyse shear-wave splitting and aid stratigraphic interpretation. We examine the pre-stack common shot records. This avoids possible data degradation introduced by inappropriate data processing, such as stacking of varying shear-wave polarizations (Li & Crampin 1989). It also avoids possible source inconsistences in CMP gathers, such as unequal source strengths and different configurations of source arrays subject to acquisition conditions (Lewis 1989). Prior to display we have applied a band pass filter and a fan polarization filter as in the Lost Hills VSP discussed above. The effects of these processing procedures on the characteristics of shear-wave splitting can be neglected if the choice of parameters is optimal.

Figure 6(a) shows the data matrix of a selected shot. *XX* stands for horizontal *X* source (first *X*) and horizontal *X* receiver (second *X*) component; *XY* stands for *X* source and *Y* receiver component; etc. We can identify a major reflection event at 1.60 s at the middle trace (trace 60), marked with A. Fig. 6(b) shows some selected PDs, where shear-wave splitting can barely be identified from the PDs because of the interference of shear waves and existence of noise. Fig. (6c) shows the colour section of the instantaneous amplitude and polarization calculated from *XX* and *XY*, which we call the *X* section; Fig. 6(d) shows the section from *YX* and *YY* (the *Y* section). Fig. 6(e) shows the orientation log. The features and interpretations of these sections are summarized below.

(1) The shapes of polarization in Figs 6(c) and (d) are difficult to interpret. As a result, we cannot analyse shear-wave splitting in reflection data in the same way as in VSP data. Similarly, PDs show few diagnostic features of shear-wave splitting.

(2) Variations of polarization with incidence angle are also difficult to interpret. In noise-free data, as the incidence angle reaches the internal shear-wave window of an interface (Liu & Crampin 1990), polarizations show sudden changes, which can be identified on the colour section of the complex component (Li & Crampin 1990a, 1991). Sudden changes of individual polarization can easily be identified in real data, such as event A on the *Y* section (Fig. 6d) at trace 67, and trace 83. However, these changes are most likely to be caused by interference with ambient noise caused by air wave, groundroll, random noise, etc., but might also be

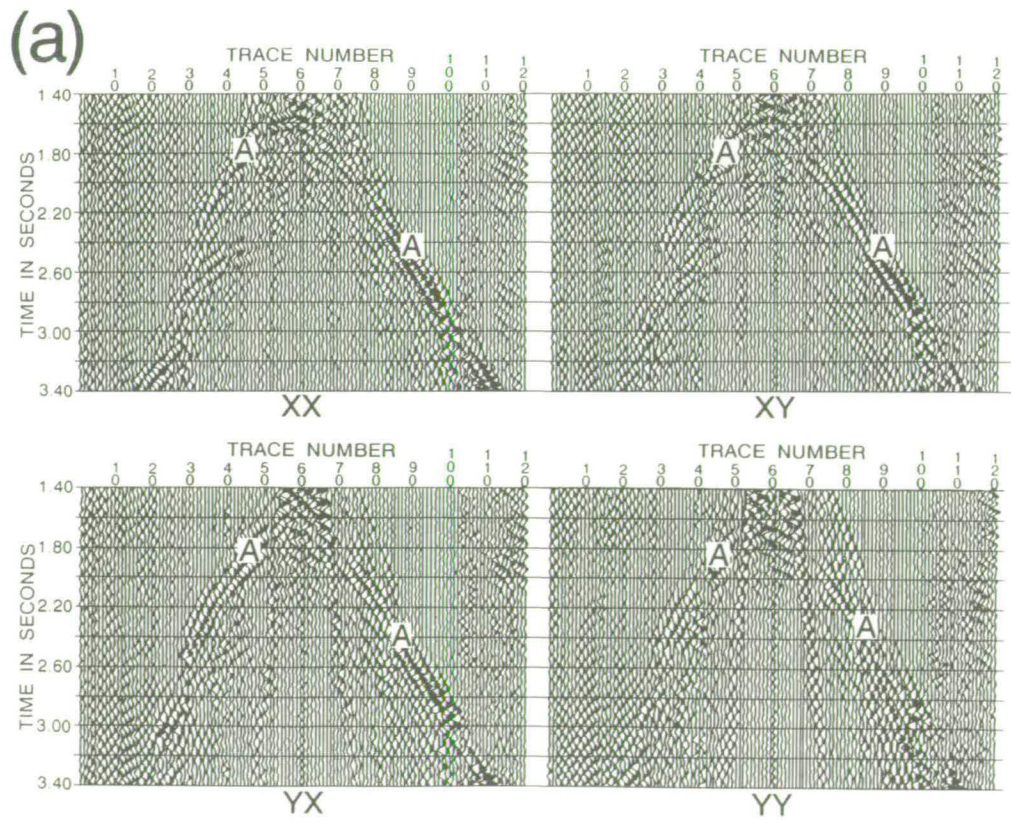

Figure 6. Results of Lost Hill reflection survey: (a) data matrix of a selected record (record 137), and *X* stands for in-line, and *Y* for cross-line; *XX* stands for *X* source (first *X*) and *X* receiver (second *X*), and *XY* for *X* source and *Y* receiver, etc.; (b) selected PDs of *XX* and *XY* components; (c) *X* section, the colour section of the instantaneous amplitude and polarization of *XX* and *XY*; (d) *Y* section, that of *YX* and *YY*; (e) orientation logs.

caused by the effects of an internal shear-wave window (Liu & Crampin 1990). Since most of reflective interfaces are well below the surface, it is reasonable to assume that the angle of incidence is sufficiently small that all reflections are within internal shear-wave windows.

(3) Although polarization variations of individual traces are difficult to interpret, Figs 6(c) and (d) show that polarizations of the same reflection events appear to be coherent, as is observed in VSPs. For example, event A of the *X* section (Fig. 6c) has a coherent blue polarization on higher traces than 60 where the source is located. Because the interfaces are dipping (Squires *et al.* 1989), the arrivals for event A at lower traces than 60 are contaminated with the direct arrival. Coherent polarizations appear also on other events such as the event at 2.6 s and trace 35 at the *X* section (Fig. 6c), etc. This coherency of polarizations helps to indentify shear-wave events, and Figs 6(c) and (d) show better continuity of reflection than Fig. 6(a).

(4) Figures 6(c) and (d) also show that there are coherent polarizations independent of source orientations on the two colour sections, as observed in VSPs. For examples, event A in the *Y* section (Fig. 6d) has a same coherent blue colour as in the *X* section (Fig. 6c). There are several similar events. The same coherent colour (polarization) on different events, independent of source orientations, can most directly be interpreted as indicating shear-wave splitting, and can be used to identify shear-wave splitting. The coherent colour represents the polarization angle of the leading shear wave. In this case, the coherent colour is blue, indicating N42°W ± 3°. This observation can be used to determine the pre-stack rotation angles before synchronous rotation in processing multicomponent reflection shear-wave data in the presence of anisotropy. Thus the processing of shear-wave data in the presence of anisotropy can be simplified by omitting post-stack rotation analysis which is now a conventional procedure for determining the rotation angle.

(5) Figure 6(e) shows that orientation logs of the reflection data improves the continuity of reflection events and separates the interference of the split shear waves. The variations of polarization in Fig. 6(e) can be more easily followed than in Figs 6(c) and (d). The blue colour of the polarization of leading split shear-wave arrivals appears on all events, and the polarization of the slower split shear wave can also be identified as a red–orange colour. Note there is a lateral change of anisotropy in the Lost Hills line; the polarizations of the leading split shear wave at this shot position have a different orientation from those at location of VSPs, as was also found by Squires *et al.* (1989). The SWS section of the reflection data is less informative than that of the VSPs, because of noise and shear-wave interference, and is not shown here.

To summarize, the attribute sections of reflection data have a more complex nature than those of VSPs. Characteristic rectangular shapes of polarizations are difficult to determine with confidence, hence analysing shear-wave splitting in reflection data cannot be carried out in the same way as in VSPs. We are able to indentify shear-wave splitting and determine the polarization of leading split shear waves, by examining the coherency of polarization between geophones and different source orientations. This makes it possible to determine polarization angles for pre-stack data without a post-stack rotation analysis. Orientation logs improve the continuity of reflection events and separate the interference of split shear waves, allowing the optimum rotation angle to be more easily determined. SWS sections of reflection data are less informative than those of VSP data.

4.4 German Creek crosshole data

The example is given to demonstrate how complex component analysis can help examine polarization variation in crosshole surveys. This is an in-seam seismic data set acquired from German Creek Mine in Australia. Fig. 7(a) shows the acquistion geometry on the horizontal plane (G. S. Turner, private communication). There are 33 source points, and two fixed three-component geophones, marked as G1 and G2. The polarizations of wave modes received at the geophone are expected to be different at different source positions. By examining such variation of polarizations it is possible to locate the cleats and determine cleat directions in coal seams (Liu, Crampin & Roth 1989). To identify the type of wavemodes and to recognize the polarization variations, we plot out seismograms and PDs of the horizontal components. In practice, this is time-consuming and difficult to keep objective. Complex component analysis can help overcome these difficulties.

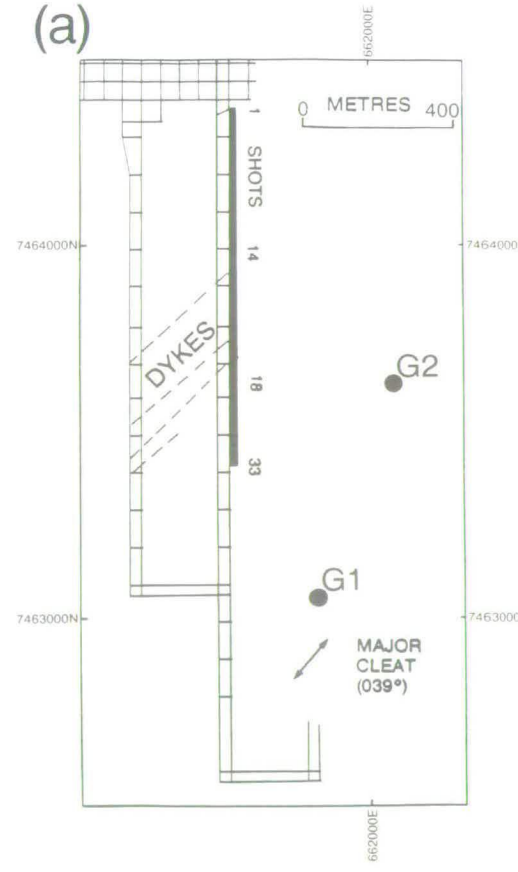

Figure 7. Results of German Creek Mine data: (a) plan of acquisition geometry; (b) colour section of the instantaneous amplitude and polarization of the two horizontal components at geophone G1; (c) colour section of the instantaneous amplitude and polarization of the two horizontal components at geophone G2. Letters mark the significant events.

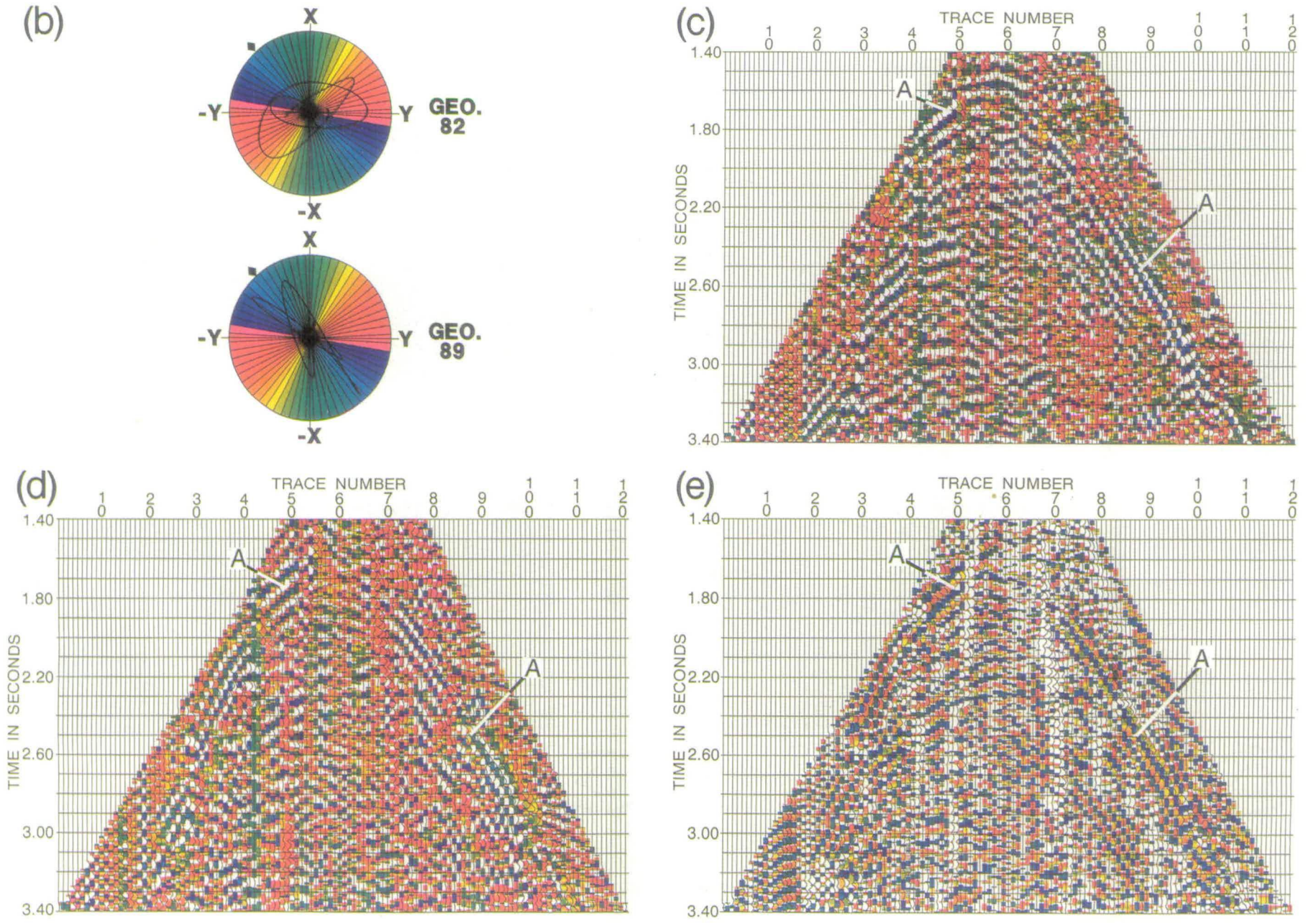

Figure 6. (*continued*)

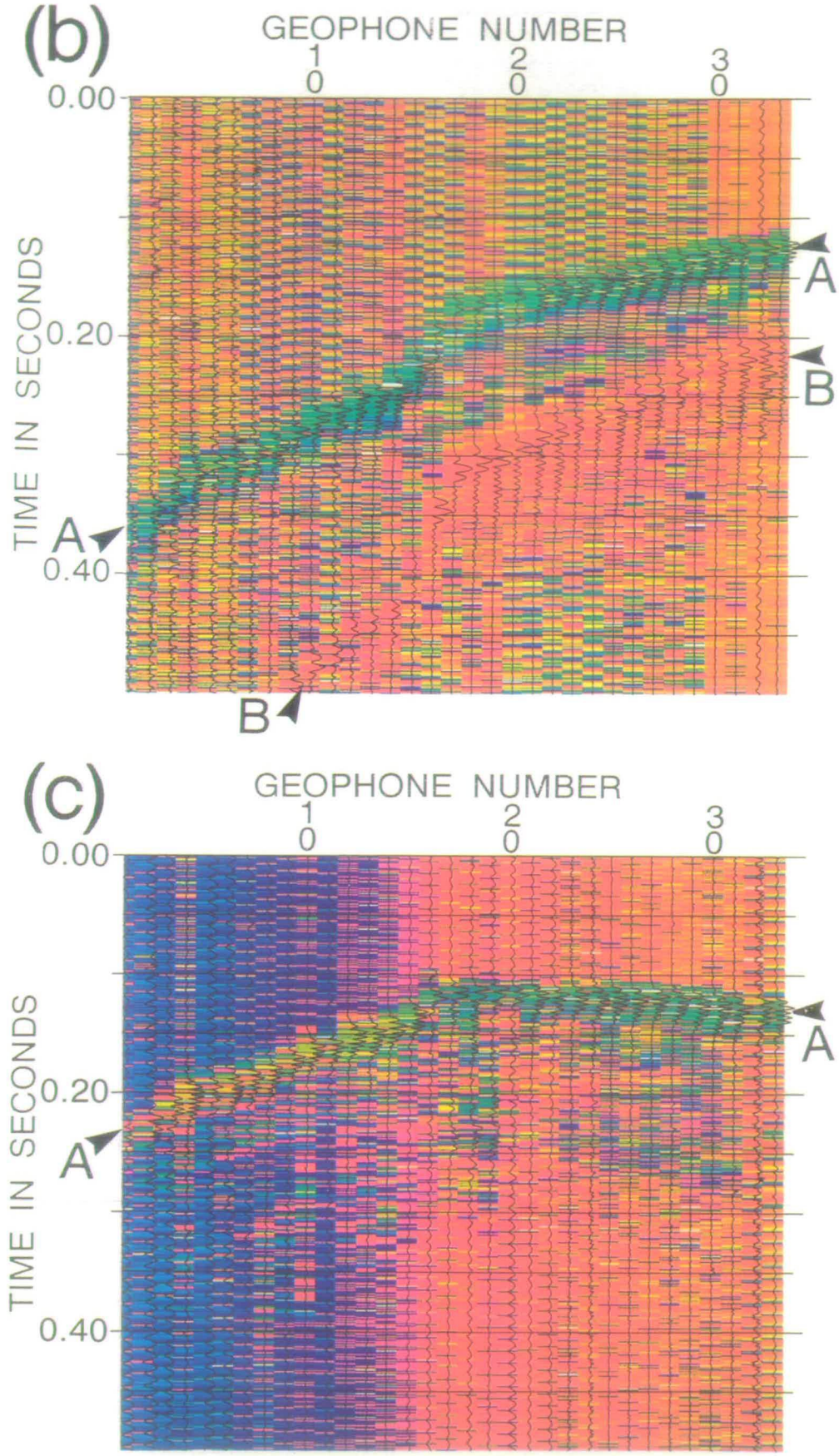

Figure 7. (*continued*)

Figure 7(b) shows the colour section of instantaneous polarizations superimposed on wiggle traces of instantaneous amplitude received at G1. Two modes can be identified with different characteristic colours. A is a *P*-wave mode, which has a constant green polarization (N0°E ± 3°) at all source positions. B is a shear-wave mode with a red polarization (N78°E ± 3°) at lower source numbers, but gradually changes to red–orange (N54°E ± 3°) at higher source numbers. Fig. 7(c) shows the colour displays of waves received at G2. Wave mode A has yellow green polarizations (N18°E ± 3°) at lower source numbers, then changes to pure green polarization (N0°E ± 3°). Thus, mode A is *P*-wave mode, and the change of polarization is due to the change of angle of azimuth of the travel path. This crosshole data set demonstrates that complex component analysis offers an easy way to examine polarization variations in many configurations.

5 DISCUSSION

The above case studies show the following phenomena.

(1) The VSPs confirm that the instantaneous polarization of shear-wave splitting shows characteristic combinations of rectangular and semitriangular shapes (Li & Crampin 1990a, 1991), which can be used to analyse shear-wave splitting in colour sections of complex components.

(2) Complex component analysis is further developed in four-component seismic data. The Lost Hills VSP shows that calculating and displaying SWS sections and orientation logs provides direct information about shear-wave splitting. In SWS sections, shear-wave arrivals showing shear-wave splitting are characterized by a coherent colour band in which the colour represents the polarization of the leading shear wave and the width of the band represents the delay between the split shear waves. In orientation logs, the polarization of a split shear wave is coded by colour plots, and the colour band of the leading split shear wave represents the delay between the split shear waves.

(3) It is observed that the polarizations of split shear waves are remarkably coherent. Consequently, complex component analysis is comparatively robust in the presence of noise.

The polarizations of the leading direct shear wave in VSPs tend to be consistent, and coherent among adjacent geophones. In isotropic examples, the polarization is source dependent, whereas in anisotropy, it is fixed in the symmetry direction and independent of source orientations.

The polarizations of reflected shear waves are more complicated than VSPs, and are dependent on source and incidence angle. Outside the shear-wave window, the polarizations are not coherent among adjacent traces regardless of source orientation and presence or absence of anisotropy. Within the shear-wave window at the free surface, in an isotropic rockmass, the polarizations are also varied and shear-wave polarizations are not usually orientated parallel to source axes (Liu *et al.* 1990); but in anisotropy, the polarizations are fixed and independent of source orientations. If the receiver axes are orientated parallel to source orientations, coherency of polarization among traces received within the shear-wave window can aid in identifying reflection events.

Techniques that take advantage of the coherency of signals are frequently robust in the presence of noise. A reasonable amount of noise could modify the polarization shape of individual geophone or trace, but barely disturb the coherent polarization variation as a whole. Thus, the behaviour of shear waves as indicated by complex component analysis will be preserved in the presence of noise as demonstrated by the Lost Hills reflection data.

(4) Complex component analysis of pre-stack data can be used to determine the rotation angle for source–geophone rotation for multicomponent reflection data. Source–geophone rotation has now become a conventional processing procedure for multicomponent reflection data, as demonstrated by Alford (1986). Murtha (1989), Squires *et al.* (1989), and others. To apply source–geophone rotation, a post-stack rotation analysis (Alford 1986; Squires *et al.* 1989) is often required to determine the optimum rotation angle. If post-stack rotation analysis is used, often the data have to be processed twice in order to get satisfactory results (M. C. Mueller, Amoco, private communication). The data are first stacked without rotation to apply post-stack rotation analysis, then stacked again with pre-stack rotation using the angle determined from rotation analysis. Murtha (1988) derived an analytic $\tan 4\theta$ expression of rotation angle for reflection data without the rotation scanning procedure. This can also be achieved by complex component analysis.

The purpose of rotation analysis is to determine the optimum rotation angle which best separates the energy of the two shear-wave arrivals. The process depends on the coherency of the polarization. This optimum angle is the source-independent coherent polarization in the colour sections of complex components. Thus, instead of using post-stack rotation analysis, we can use complex component analysis of pre-stack data to determine the optimum rotation angle. We only need to calculate the complex components and display colour sections, and to find the coherent polarization that is independent of source orientation and appears on all major reflection events. This procedure is much simpler than rotation analysis.

By calculating orientation logs, the interference of split shear waves is resolved, and the determination of optimum angles for source–geophone rotation becomes more reliable, as demonstrated by the Lost Hills reflection data. There are two dominant coherent polarizations orthogonal to each other in logs. Thus, pre-stack rotation can be easily and efficiently implemented, and lateral variation of rotation angle along the survey line can be examined as we change the location of orientation logs.

(5) The German Creek crosshole data confirm that both variation of waveforms and variation of polarizations can be followed continuously either along time direction, or along offset direction (Li & Crampin 1990a, 1991), and complex component analysis provides a useful tool for cases where identification of wave types and recognition of polarization variations are essential.

(6) In summary, complex component analysis is a simple, robust, and effective technique for analysing shear-wave anisotropy in VSPs and reflection surveys. In the past, two methods have been used to examine shear-wave anisotropy in VSPs and reflection surveys: polarization analysis, and rotation analysis. Polarization analysis (analysis of polarization diagrams) relies principally on the shape of individual

polarization pattern and is a straightforward technique; while rotation analysis is mainly based on the coherency of whole polarizations and is relatively robust in the presence of noise, but would be difficult to apply if the crack orientations change with depth. Both techniques are time-consuming. In contrast, complex component analysis allows both for the shape of individual polarization and the coherency of whole polarizations. Thus, complex component analysis retains the advantages of both techniques, but has fewer disadvantages. it can also be applied to cases where crack orientations change with depth. We suggest that complex component analysis could well become a routine procedure in analysing shear-wave anisotropy for VSPs and reflection surveys.

6 CONCLUSIONS

The field data confirms that instantaneous polarizations of shear-wave splitting have diagnostic shapes which are combinations of rectangular and semitriangular shapes (Li & Crampin 1991). The technique is developed for multisource component seismic data. Four-component data can be used to calculate shear-wave splitting sections (SWS sections) or transformed to calculate orientation logs. Complex component analysis of four-component shear-wave reflection data allows the optimum rotation angle between adjacent geophones and different sources to be determined before stacking without source–geophone rotation. Finally, polarizations of split shear waves tend to be remarkably coherent. This coherency helps us to identify and estimate shear-wave splitting, and aids the stratigraphic interpretation of reflection events in VSPs and reflection surveys.

We conclude from our study that the theoretical promise of Li & Crampin (1990a, 1991) is confirmed by case studies, and complex component analysis can be further developed into four-component VSPs and reflection surveys. This technique of complex component analysis can aid identification and estimation of shear-wave splitting in VSPs and reflection surveys, help stratigraphic interpretation, and simplify the processing procedures for analysing four-component reflection shear-wave data in the presence of anisotropy.

ACKNOWLEDGMENTS

We thank the French VSP Consortium for approval to use the Paris Basin VSP, and the Australian Coal Industry Research Laboratories Ltd for approval to use the German Creek data. This work was supported by the Edinburgh Anisotropy Project and the Natural Environment Research Council and is published with the approval of the Director of the British Geological Survey (NERC).

REFERENCES

Alford, R. M., 1986. Shear data in the presence of azimuthal anisotropy, *56th Ann. Int. SEG Mtg, Houston, Expanded Abstracts*, pp. 476–479.

Brodov, L., Kuznetsov, V., Tikhonov, A., Cliet, C., Marin, D. & Michon, D., 1990. Measurements of azimuthal anisotropy parameters for reservoir study, *Fourth Int. Workshop on Seismic Anisotropy, Edinburgh 2–6 July, 1990, Abstracts*, British Geological Survey.

Bush, I. & Crampin, S., 1987. Observations of EDA and PTL anisotropy in shear-wave VSPs, *57th Ann. Int. SEG Mtg, New Orleans, Expanded Abstracts*, pp. 646–649.

Campden, D. A., 1990. Modelling and analyzing VSPs for shear-wave anisotropy, *PhD dissertation*, University of Edinburgh.

Crampin, S., 1978. Seismic wave propagation through a cracked solid; polarization as a possible dilatancy diagnostic, *Geophys. J. R. astr. Soc.*, **53,** 467–496.

Crampin, S., 1981. A review of wave motion in anisotropic and cracked elastic-media, *Wave Motion*, **3,** 343–391.

Crampin, S., 1991. Effects of point singularities on shear-wave propagation in sedimentary basins, *Geophys. J. Int.*, this issue.

Crampin, S., Bush, I., Naville, C. & Taylor, D. B., 1986. Estimating the internal structure of reservoirs with shear-wave VSPs, *The Leading Edge*, **5,** 11, 35–39.

Justice, M. G., McCormick, M. D. & Lee, S. S., 1987. Anisotropy in the Morrow formation of Southeast New Mexico, in *Shear-Wave Exploration: Geophysical Developments, 1*, SEG Special Publication, pp. 154–164, eds Danbom, S. & Domenico, S.N.

Lewis, C., 1989. Three-dimensional multicomponent imaging of reservoir heterogeneity, Silo Field, Wyoming, *PhD dissertation*, Colorado School of Mines.

Li, X.-Y. & Crampin, S., 1989. Analyzing shear-wave splitting in three-component reflection survey, *SEG Res. Workshop, Recording and Processing Vector Wave Field Data, Snowbird, 13–17 August, 1989, Technical Abstracts*, p. 114.

Li, X.-Y. & Crampin, S., 1990a. Complex component analysis of shear-wave splitting: theoretical studies, *Fourth Int. Workshop on Seismic Anisotropy, Edinburgh 2–6 July, 1990, Abstracts*, British Geological Survey.

Li, X.-Y. & Crampin, S., 1990b. Case studies of complex component analysis of shear-wave splitting, *60th Ann. Int. SEG Mtg, San Francisco, Expanded Abstracts*, vol. 2, pp. 1427–1430.

Li, X.-Y. & Crampin, S., 1991. Complex component analysis of shear-wave splitting: theory, *Geophys. J. Int.*, this issue.

Liu, E. & Crampin, S., 1990. Effects of the internal shear-wave window: comparison with anisotropy induced splitting, *J. geophys. Res.*, **95,** 11 275–11 281.

Liu, E., Crampin, S. & Roth, B., 1989. Detection of anisotropy by in-seam seismic channel waves, Presented at the *51th Ann. Int. EAEG Mtg, Berlin.*

Liu, E., Crampin, S. & Yardley, G., 1990. Polarizations of reflected shear waves, *Geophys. Res. Lett.*, **17,** 1137–1140.

Mueller, M. C., 1990. Prediction of lateral variability in fracture intensity using multicomponent shear wave surface seismic as a precursor to horizontal drilling, *Fourth Int. Workshop on Seismic Anisotropy, Edinburgh 2–6 July, 1990, Abstracts*, British Geological Survey.

Murtha, P. E., 1988. Estimation of the rotation transformation angle for shear-wave data acquired in azimuthally anisotropic regions, *Third Int. Workshop on Seismic Anisotropy, Berkeley, 31 May–4 June, 1988, Abstracts.*

Murtha, P. E., 1989. Preliminary analysis of the ARCO multicomponent seismic group experiment, *SEG Res. Workshop, Recording and Processing Vector Wave Field Data, Snowbird, 13–17 August, 1989, Abstracts.*

Squires, S. G., Kim, C. D. & Kim, D. Y., 1989. Interpretation of total wave-field data over Lost Hills field, Kern County, California, *Geophysics*, **54,** 1420–1429.

Taner, M. T., Koehler, F. & Sheriff, R. E., 1979. Complex seismic trace analysis, *Geophysics*, **44,** 1041–1063.

Thomsen, L. A., 1988. Reflection seismology over azimuthally anisotropic media, *Geophysics*, **53,** 304–313.

Wild, P. & Crampin, S., 1991. The range of effects of azimuthal isotropy and EDA-anisotropy in sedimentary basins, *Geophys. J. Int.*, this issue.

Winterstein, D. F. & Meadows, M. A., 1990. Correlation of shear-wave polarization with subsurface stress direction at Lost Hills Field, *Fourth Int. Workshop on Seismic Anisotropy, Edinburgh, 2–6 July, 1990, Abstracts*, British Geological Survey.

Yardley, G. & Crampin, S., 1990. Automatic determination of anisotropic parameters from shear-wave splitting in the Lost Hills VSP, *60th Ann. Int. SEG Mtg, San Francisco, Expanded Abstracts*, pp. 1424–1426.

NOTE ADDED IN PROOF

Since this paper was submitted further papers have been included in this issue. This means that more appropriate references for Brodov *et al.* (1990), Bush & Crampin (1987), and Mueller (1990) in the text are now Brodov *et al.* (1991), Bush & Crampin (1991), and Mueller (1991), given below.

REFERENCES

Brodov, L. U., Tikhonov, A. A., Chesnokov, E. M., Tertychnyi, V. V. & Zatsepin, S. V., 1991. Estimating physical parameters of cracked–porous oil reservoirs by inverting shear-wave splitting, *Geophys. J. Int.*, this issue.

Bush, I. & Crampin, S., 1991. Paris Basin VSPs: case history establishing combinations of fine-layer (or lithologic) anisotropy and crack anisotropy from modelling shear wavefields near point singularities, *Geophys. J. Int.*, this issue.

Mueller, M. C., 1991. Prediction of lateral variability in fracture intensity using multicomponent shear-wave surface seismic as a precursor to horizontal drilling in the Austin Chalk, *Geophys. J. Int.*, this issue.